

**DOUBLY-FED INDUCTION
GENERATOR WIND TURBINE
MODELLING, CONTROL AND
RELIABILITY**

A thesis submitted to The University of Manchester

for the degree of Doctor of Philosophy

in the Faculty of Engineering and Physical Sciences

2014

TING LEI

School of Electrical and Electronic Engineering

List of Contents

List of Contents	1
List of Tables	6
List of Figures	7
List of Abbreviations	13
Abstract	15
Declaration	16
Copyright Statement	17
Acknowledgement	18
List of Symbols	19
Chapter 1. Introduction	23
1.1. Project background	25
1.2. Research objectives	25
1.3. Thesis outline	26
Chapter 2. Literature Review	29
2.1. Introduction	29
2.2. Reliability of power electronic converters in wind turbines – an overview	29
2.3. Development and challenge	31
2.4. Components and properties	34
2.4.1. Semiconductor switches	35
2.4.2. Capacitors	37
2.5. Reliability of converters - past survey results	38
2.6. Failure causes and mechanisms	40
2.6.1. Possible failures in a voltage source converter	40
2.6.2. Control unit failures	41
2.6.3. Capacitor failures	41
2.6.4. Power semiconductor failures	43
2.7. Reliability prediction and condition monitoring technique for power converters	46

2.7.1. General concept	46
2.7.2. Parameter-based CM	47
2.7.3. Model-based CM	48
2.7.4. Model integration technique for CM	52
2.8. Conclusions	52
Chapter 3. Modelling and Control of DFIG Wind Turbine System	54
3.1. An overview of the DFIG wind turbine system	54
3.1.1. Mechanical system	54
3.1.2. Generator	54
3.1.3. Converter	55
3.1.4. Transformer	56
3.1.5. Crowbar	57
3.1.6. Overall control systems	57
3.2. Mechanical system representation	60
3.2.1. Aerodynamic model	60
3.2.2. Shaft model	61
3.3. Steady state DFIG model	64
3.3.1. Steady state equivalent circuit	65
3.3.2. Steady state power flow	66
3.4. Dynamic DFIG model	67
3.4.1. Space vector representation	67
3.4.2. Dq0 transformation	69
3.5. Implementation of the vector control	71
3.5.1. Rotor-side converter control	71
3.5.2. Grid-side converter control	73
3.6. Converter and dc-link model	74
3.7. Wind turbine control	75
3.7.1. Operating curve description	75
3.7.2. Per unit transformation of the mechanical parameters	79
3.7.3. Pitch control strategies	81
3.8. Conclusions	82

Chapter 4. Mathematical Modelling for Detailed Analysis of the Control Systems	84
4.1. Power and current control loops	84
4.1.1. Mathematical model of the RSC current loops	84
4.1.2. Mathematical model of the RSC power loops	86
4.1.3. Mathematical model of the GSC current loops	88
4.2. Small signal analysis of the dc-link control	89
4.2.1. State feed-back model derivation	89
4.2.2. Dynamic stiffness analysis at different operating points	93
4.3. Small signal analysis of the pitch control system	95
4.3.1. State feed-back model derivation	96
4.3.2. Open-loop response verification	100
4.4. Pitch controller design based on linear model	101
4.4.1. Proportional – only (P) controller	103
4.4.2. Proportional and integral (PI) controller	106
4.4.3. Proportional integral and derivative (PID) controller	108
4.4.4. Model verification	110
4.4.5. Gain scheduling	111
4.5. Conclusions	115
Chapter 5. Controller Coordination to Improve Fault Ride-through Capability	117
5.1. Introduction	117
5.2. RSC current control strategy for improving stability in small dips	117
5.2.1. DFIG behaviour under voltage dips	117
5.2.2. Demagnetizing current injection	119
5.2.3. Influence of controller tuning	123
5.2.4. Stability improvement by coordinated dq-controller tuning	127
5.3. Improvement of dc-link control for limiting the voltage fluctuations	130
5.3.1. Bandwidth coordination	130
5.3.2. Feed-forward compensation	132
5.4. Active crowbar protection for severe voltage dip	133
5.4.1. Crowbar activating strategy	133
5.4.2. Setting of the RSC control during crowbar activation	134

5.4.3.	Simulation results	135
5.5.	Controller coordination to reduce shaft oscillations	137
5.5.1.	RSC outer loop controller tuning – generic control strategy	138
5.5.2.	RSC outer loop controller tuning – additional damping control	139
5.5.3.	Coordination with the pitch control	142
5.5.4.	Proposed control strategy for fault ride-through	143
5.6.	Conclusions	147
 Chapter 6. Using Improved Power Electronics Modelling and Turbine Control to Improve Asset Management		 149
6.1.	Review of the recent reliability studies for the wind turbine power converter	150
6.1.1.	Thermal cycling affected by operating point	150
6.1.2.	Impact of different control strategies	151
6.1.3.	Impact from other factors	151
6.2.	Modelling considerations	152
6.2.1.	Power module in wind energy	152
6.2.2.	Power module selection	154
6.3.	Power loss calculation	156
6.3.1.	Operating states of the three – phase inverter	157
6.3.2.	Conduction loss	160
6.3.3.	Switching/reverse recovery loss	162
6.3.4.	Implementation – switched model	165
6.3.5.	Implementation – switch averaged model	166
6.3.6.	Verification with SemiSel	169
6.4.	Thermal network	171
6.4.1.	Concept of power device thermal model	171
6.4.2.	Thermal network development for SKiiP module	172
6.4.3.	Circuit transformation from Foster to Cauer network	173
6.4.4.	Spatial resolution analysis	175
6.4.5.	Full thermal network	176
6.5.	WTPC thermal capabilities under different conditions	179
6.5.1.	Steady-state thermal cycling	179
6.5.2.	Transient thermal response under electric torque over-load	181

6.5.3. System performance under grid voltage drop	183
6.5.4. System performance under variable wind speeds	186
6.6. Synchronous point enhancement through the modified controller	189
6.7. Conclusions	196
Chapter 7. Conclusions and Recommendations for Further Work	198
7.1. Power converter reliability and failure mechanisms	198
7.2. DFIG wind turbine modelling and mathematical analysis	198
7.3. Controller coordination to improve fault ride-through capability	199
7.4. Power converter thermal modelling	201
7.5. Suggestions for further work	202
7.6. Associated publications	202
References	204
Appendix A. DFIG Wind Turbine Model Parameters	213
Appendix B. DFIG Controller Tuning and Model Verification	218
Appendix C. Pitch Controller Tuning and Simulation Results	224

List of Tables

Table 3.1	Aerodynamic parameters of 5MW wind turbine (data based on Repower 5MW wind turbine)	76
Table 3.2	Turbine mechanical parameters	80
Table 3.3	Important operating points on the strategy curve	81
Table 4.1	Controller parameters at different operating points derived from linear model	111
Table 5.1	Three controller settings of the RSC current loops	129
Table 5.2	Threshold values of crowbar activation	134
Table 6.1	Performances evaluation of the three control strategies	151
Table 6.2	IGBT modules for wind turbines from two manufacturers	153
Table 6.3	Performance comparison of three SKIIP modules under various loads	156
Table 6.4	Power loss and device switching states	160
Table 6.5	Coefficients for conduction loss characteristic	162
Table 6.6	Parameters used for the switching energy equations	164
Table 6.7	Device temperature evolution with time under different steps in torque demand from a nominal operating point	181

List of Figures

Figure 1.1	Installed capacity of the UK renewables in seven years	23
Figure 2.1	Normalised failure rate of subsystems and assemblies in variable speed wind turbines from multiple manufacturers	30
Figure 2.2	Normalised hours lost per turbine per year due to faults in subsystems and assemblies in variable speed wind turbines	31
Figure 2.3	Trends of WTs with power electronics in the last 30 years	32
Figure 2.4	Dominant wind turbine concepts with power converter (a) DFIG Wind turbine with partial-scale power converter; (b) Wind turbine with full-scale power converter; (c) Market share of the WTs in 1.5-3 MW	32
Figure 2.5	General circuit construction of a 2L-BTB-VSC	35
Figure 2.6	Current and voltage limits for commonly used semiconductor switches (a) with (b) switching frequencies and (c) application area	35
Figure 2.7	IGBT packaging structures. (a) WBI module; (b) PPI module	36
Figure 2.8	Failure distribution of each component in a power converter	38
Figure 2.9	Component failures in power converters, (a) Failure distribution, (b) Fragile components claimed in an industrial survey	39
Figure 2.10	Converter components failure prediction from Relia-Wind FMEA	39
Figure 2.11	Possible fault locations in a back-to-back converter	40
Figure 2.12	Software-related failure mode hierarchy	41
Figure 2.13	Links of causes, failure mechanisms and failure modes in aluminium electrolytic capacitor	41
Figure 2.14	Weak points in WBI module regarding lifetime	45
Figure 2.15	Common package-related failure mechanisms, (a) Bond wire lift-off propagation, (b) Solder fatigue - crack and void formation	46
Figure 2.16	End-of-life behaviour of a MPPF capacitor	48
Figure 2.17	IGBT lifetime prediction in wind turbine applications	52
Figure 3.1	Schematic diagram of a typical DFIG wind turbine	54
Figure 3.2	Two other transformer connection types	56
Figure 3.3	Schematic diagram of the crowbar circuit	57

Figure 3.4	Overall control structure of the DFIG wind turbine	58
Figure 3.5	Two-mass wind turbine shaft system	63
Figure 3.6	Steady state equivalent circuit of the DFIG – one phase representation	65
Figure 3.7	Directions of the power flow in the DFIG model	67
Figure 3.8	Reference frames with transformation angles of DFIG	68
Figure 3.9	Stator flux orientation	71
Figure 3.10	Generic control of the rotor-side converter	72
Figure 3.11	Circuit construction of the grid-side converter	73
Figure 3.12	Reference frames with grid voltage orientation	74
Figure 3.13	Generic control of the grid-side converter	74
Figure 3.14	Schematic diagram of the full-switched and switch-averaged converter models	75
Figure 3.15	Operational strategies of a 5 MW wind turbine.	78
Figure 3.16	Alternative control method for the tracking the characteristic curve	79
Figure 3.17	Pitch controller with actuator and gain scheduling	81
Figure 4.1	Current control loops of the rotor-side converter	85
Figure 4.2	Power control loops of the rotor-side converter	87
Figure 4.3	Current control loops of the grid-side converter	88
Figure 4.4	Configuration of the current flow in the dc-link system	89
Figure 4.5	Non-linear block diagram of the dc-link control system	90
Figure 4.6	Small signal block diagram of the dc-link control system	91
Figure 4.7	Dc-link responses to a 1 pu torque step from the nominal operating point, with different damping values ($f_n = 10\text{Hz}$)	92
Figure 4.8	Verification of the dc-link model	93
Figure 4.9	Dc-link dynamic stiffness to power disturbance at varying V_{dco} and i_{g_q0}	94
Figure 4.10	Dc-link ripples at 50Hz power oscillation	94
Figure 4.11	Simulation of the lumped and 2-mass shaft systems	95
Figure 4.12	Small signal model of the 2-mass shaft wind turbine mechanical system	98
Figure 4.13	Block diagram of closed loop pitch control system	99
Figure 4.14	Open-loop plant model verification	100

Figure 4.15	Root-locus plot of the characteristic function $1+kG(j\omega)_{op}$ with marginally stable points	101
Figure 4.16	Bode diagram of the open-loop transfer function $G(s)$	103
Figure 4.17	Step responses to a 1 m/s wind speed step from nominal pint ($V_w=13\text{m/s}$, $\Delta\Omega_G=122.5$ rad/s), with different controller gains	104
Figure 4.18	Frequency response of the actuator for $\tau_i=0.2\text{s}$	105
Figure 4.19	Frequency response of the PI controller with $k_p=2$, $k_i=5$	107
Figure 4.20	Frequency response of the PID controller with $k_p=315$, $k_i=56$, $k_d=1$	109
Figure 4.21	Step responses of PID controller with increasing k_d	109
Figure 4.22	Frequency responses of the open-loop system with the three controllers	110
Figure 4.23	Verification between linear model and the PSCAD non-linear model at five operating points	111
Figure 4.24	Step responses at different operating points without gain scheduling	112
Figure 4.25	Sensitivity of the turbine aerodynamic torque versus pitch angle	113
Figure 4.26	Step responses at different operating points with gain scheduling	114
Figure 4.27	Comparison of the three pitch controllers under 10% wind turbulence	114
Figure 4.28	Comparison of the three pitch controllers under 20% wind turbulence	115
Figure 5.1	Demagnetizing current injectio	121
Figure 5.2	Calculation of the natural flux	121
Figure 5.3	Variation of the total flux and natural flux in a voltage dip	122
Figure 5.4	Original rotor current without compensation and the calculated demagnetizing current in d-q reference frame (50% voltage drop at full speed)	122
Figure 5.5	Improvement by injecting demagnetizing current at 30Hz controller bandwidth	123
Figure 5.6	Phasor diagram using PI controller. Left: predominant integral action, Right: predominant proportional action	124
Figure 5.7	Changing of the dominant control action with the increase of bandwidth	125
Figure 5.8	Comparison of different controller bandwidths in a 50% voltage dip	126

Figure 5.9	Plots of the stability function versus controller bandwidths with different damping ratios with $\omega_m=1.17$ pu (left) and rotor speeds with $\xi=1.2$ (right)	127
Figure 5.10	Natural flux and the induced rotor current result from the two controller settings	128
Figure 5.11	Relative positions of the natural flux and the induced rotor current in d-q reference frame for the two controller settings	128
Figure 5.12	Response comparison of the three controllers	130
Figure 5.13	Dc-voltage responses to a torque step under different controller bandwidths	131
Figure 5.14	Responses of the dc-link control under 30% voltage dip for three different bandwidths	131
Figure 5.15	Control strategy of the dc-link using feed-forward compensation	132
Figure 5.16	Impact of feed-forward compensation on dc-link control	132
Figure 5.17	PSCAD circuit construction for crowbar activation	134
Figure 5.18	Control scheme of the RSC during crowbar activation	135
Figure 5.19	Simulation of active crowbar protection under a full voltage dip	136
Figure 5.20	Simulation of active crowbar protection under 50% voltage dip	137
Figure 5.21	Mechanical oscillations using different time constants for T_e – loop response to 1 Nm torque step	139
Figure 5.22	Three-layer cascaded wind turbine mechanical control system	140
Figure 5.23	Root-loci of the system characteristic function with damping control	141
Figure 5.24	Responses to a 1m/s step in wind speed with different controller gains for the damping control	141
Figure 5.25	Root-locus of the pitch control system	143
Figure 5.26	Responses of pitch controller to a 1m/s step in wind speed	143
Figure 5.27	Bandwidth allocations for several main control-loops in DFIG wind turbine system	144
Figure 5.28	Strategy of the damping control	145
Figure 5.29	Improvement through damping control without crowbar engagement under 40% voltage dip	146
Figure 5.30	Improvement through damping and crowbar coordinated control	147
Figure 6.1	Interactions within the joint model for stress analysis	150

Figure 6.2	Diagram of a three phase inverter	157
Figure 6.3	Waveforms in pulse-width-modulation	158
Figure 6.4	Four quadrant operating states for one leg	160
Figure 6.5	Conduction loss and current dependency obtained by curve fitting	162
Figure 6.6	Typical waveforms of IGBT turn-on and Diode turn-off	163
Figure 6.7	Characteristics of switching loss at two different temperatures	165
Figure 6.8	Schematic diagram of IGBT power loss prediction using PWM switched model	166
Figure 6.9	Schematic diagram of the loss prediction using the switch-averaged model	167
Figure 6.10	Device power losses obtained from (a) switched model and (b) switch-averaged model	168
Figure 6.11	Comparison of the losses predicted by switched and averaged models at different turbine operating speeds	169
Figure 6.12	Verification of PSCAD/EMTDC models at different rotor speeds (below rated operating point)	170
Figure 6.13	Verification of the PSCAD/EMTDC models at different torque demands (over-load condition)	170
Figure 6.14	Mean device junction temperature obtained from SemiSel, (a) below the nominal operating point; (b) torque over-load conditions	171
Figure 6.15	Two equivalent thermal networks	172
Figure 6.16	Three-phase inverter and the circuit construction in one SKiiP module	172
Figure 6.17	Device thermal network and power loss dissipation in one 'fold'	173
Figure 6.18	Transient characteristics obtained from the equivalent circuits	175
Figure 6.19	Basic structure with the thermal resistance share of each layer in a common power module	176
Figure 6.20	Spatial resolution of the derived Cauer network	176
Figure 6.21	Full Cauer network including the power devices and the heat-sink	177
Figure 6.22	Loss distributions (a) instantaneous loss in the Foster network, (b) loss variations in the Cauer network during system start-up	178
Figure 6.23	Transient temperature obtained from the two full thermal networks during system start-up	179
Figure 6.24	Transient temperatures at the internal nodes in the Cauer network	179

Figure 6.25	Average temperature and corresponding variations at different rotor speeds	181
Figure 6.26	Transient thermal responses under different torque steps	182
Figure 6.27	Converter electrical and thermal responses under 40% grid voltage drop with RSC d-q loop at 10Hz	184
Figure 6.28	Converter electrical and thermal responses under 40% grid voltage drop with RSC d-loop 10Hz and q-loop 150Hz	185
Figure 6.29	800s wind variations with 10% turbulence	186
Figure 6.30	RSC electrical and thermal responses under 10% wind turbulences	187
Figure 6.31	Magnified graph of the RSC electrical and thermal performances	188
Figure 6.32	GSC electrical and thermal responses under 10% wind turbulences	189
Figure 6.33	Modified controller avoiding synchronous operating point	190
Figure 6.34	Rotor speed, electrical and mechanical torque from the generic and the modified controller	191
Figure 6.35	RSC electrical and thermal responses under 10% wind turbulences using the modified controller	192
Figure 6.36	Magnified graph of the RSC performances in the first controller transition	193
Figure 6.37	Magnified graph of the RSC performances in the second controller transition	194
Figure 6.38	GSC electrical and thermal performances under 10% wind turbulences using the modified controller	195

List of Abbreviations

BTB (topology)	Back To Back (topology)
CM	Condition Monitoring
CPM	Constant Power Mode
CTE	Coefficient of Thermal Expansion
CTM	Constant Torque Mode
DBC (substrate)	Direct Bounded Copper (substrate)
DFIG	Doubly Fed Induction Generator
FEA	Finite Element Analysis
FMEA	Failure Mode and Effect Analysis
FSM	Full Switched Model
GM	Gain Margin
GSC	Grid Side Converter
GTO (thyristor)	Gate Turn Off (thyristor)
HVDC (transmission)	High Voltage Direct Current (transmission)
IGBT	Insulated Gate Bipolar Transistor
IGCT	Integrated Gate Commuted Thyristor
MIMO	Multi-Inputs Multi-Outputs
MOSFET	Metal Oxide Semiconductor Field Effect Transistor
MPPF	Metalized Polypropylene Film
MPT	Maximum Power Tracking
MTBF	Mean Time Between Failures
NPC (topology)	Neutral Point Clamped (topology)
NTC (thermistor)	Negative Temperature Coefficient (thermistor)
O&M	Operation and Maintenance
PCT	Phase Controlled Thyristor
PHM	Prognosis and Health Management
PLL	Phase Locked Loop
PM	Phase Margin
PMSG	Permanent Magnet Synchronous Generator
PPI	Press Pack IGBT

PWM	Pulse Width Modulation
RSC	Rotor Side Converter
SAM	Switch Averaged Model
SOA	Safe Operating Area
THD	Total Harmonic Distortion
TIM	Thermal Interface Material
VSC	Voltage Source Converter
VSI	Voltage Source Inverter
WBI	Wire Bonded IGBT
WRIG	Wound Rotor Induction Generator
WTPC	Wind Turbine Power Converter

Abstract

The trend of future wind farms moving further offshore requires much higher reliability for each wind turbine in order to reduce maintenance cost. The drive-train system and power electronic converter system have been identified as critical subassemblies that are subject to higher failure rates than the other subassemblies in a wind turbine. Modern condition monitoring techniques may help schedule the maintenance and reduce downtime. However, when it comes to offshore wind turbines, it is more crucial to reduce the failure rates (or reduce the stresses) for the wind turbines during operation since the harsh weather and a frequently inaccessible environment will dramatically reduce their availability once a failure happens. This research examines the mechanical, electrical and thermal stresses in the sub-assemblies of a doubly-fed induction generator (DFIG) wind turbine and how to reduce them by improved control strategies.

The DFIG control system (the rotor-side and the grid-side converter control) as well as the wind turbine control system are well established. The interactions of these control systems have been investigated. This research examines several further strategies to reduce the mechanical and electrical stresses. The control system's coordination with the protection schemes (crowbar and dc-chopper) during a grid fault is presented as well. An electro-thermal model of the power converter has been developed to integrate with the DFIG wind turbine model, for the evaluation of the thermal stresses under different operating states and control schemes.

The main contributions of this thesis are twofold. A first contribution is made by providing all the control loops with well-tuned controllers in a more integrated methodology. The dynamics of these controllers are determined from their mathematical models to minimize the interferences between different control-loops and also to reduce the electrical transients. This thesis proposes a coordination strategy for the damping control, pitch control and crowbar protection which significantly reduces the mechanical oscillations. On the other hand, an integrated model of the wind turbine and converter electro-thermal system is established that can illustrate the performance integration with different control strategies

Declaration

No portion of the work referred to in this thesis has been submitted in support of an application for another degree or qualification of this or any other university or other institute of learning.

Copyright Statement

- i.** Copyright in text of this thesis rests with the author. Copies (by any process) either in full, or of extracts, may be made only in accordance with instructions given by the author and lodged in the John Rylands University Library of Manchester. Details may be obtained from the librarian. This page must form part of any such copies made. Further copies (by any process) of copies made in accordance with such instructions may not be made without the permission (in writing) of the author.

- ii.** The ownership of any intellectual property rights which may be described in this thesis is vested in The University of Manchester, subject to any prior agreement to the contrary, and may not be available for use by third parties without the written permission of the University, which will prescribe the terms and conditions of any such agreement.

- iii.** Further information on the conditions under which disclosures and exploitation may take place is available from the Head of School of Electrical and Electronic Engineering.

Acknowledgement

First and foremost, I would like to express my sincere gratitude to my supervisor Prof. Mike Barnes and my advisor Prof. Sandy Smith for their inspiration, support and invaluable guidance. I am grateful to Prof. P. J. Tavner for his guidance, discussions and assistance in providing the data. I must thank Prof. Bill Leithhead, Dr. Adam Stock and Dr. Sung-ho Hur. from Strathclyde University for their collaboration in this research. And finally, I shall also thank Andy Cross from Semikron Ltd for his explanations about their product which is important to this research

Thanks are due to the IT-support staff and the administrative staff in the department for making life easier. Also thanks go to my fellow Ph.D. students for sharing their knowledge and for their good companionship.

I wish to acknowledge the School of Electrical and Electronic Engineering of the University of Manchester and EPSRC for their financial support in my PhD study.

Finally, to my parents and my best friends, for their eternal support and encouragement, filling my heart with love and strength and also make this whole process full of joy.

List of Symbols

Superscripts

s	Stationary reference frame with respect to the stator windings
r	Rotor reference frame
e	Excitation reference frame, synchronously rotating with the stator voltage
*	Reference quantity of the controller
\wedge	Peak quantity

Subscripts

0	Steady state operating point, or initial conditions, or zero component ¹
s	DFIG stator circuit quantity
r	DFIG rotor circuit quantity
g	DFIG grid-side converter circuit quantity
d, q	Direct and quadrature axes
σ	Leakage quantity
CB	Rotor crowbar quantity
a, b, c	Electrical phases in three-phase system
n, f	Natural and forced components in a grid voltage drop
a	Aerodynamic quantity ¹
r	Lumped rotor quantity ¹
s	Shaft quantity ¹
T, G	Turbine rotor and generator rotor quantities
th	Thermal network-related quantity
Tr, D, hs	IGBT, Diode and Heat-sink quantity

Electrical variables and DFIG machine parameters

$\bar{V}, \bar{E}, \bar{I}, \bar{\psi}$	Phasors of the supplied voltage, induced emf, induced current and flux
v, i	Instantaneous voltage and current quantities
e_g, v_g	Terminal voltages at the GSC converter and the network connecting point

¹ Context-Specific!

T_e	Electromagnetic torque
P, Q, S	Active, reactive power and apparent power
R_r, R_s	Rotor and stator resistance
R_{gsc}	Coupling resistance to grid circuit
L_r, L_s	Rotor and stator self-inductance
$L_{\sigma r}, L_{\sigma s}, L_m$	Rotor leakage, stator leakage and magnetizing inductance
L_{gsc}	Coupling self-inductance grid circuit
σL_r	Operational transient inductance
N_r, N_s	Effective number of coil turns per phase rotor and stator winding
n	Rotor to stator turns ratio
pp	Magnetic pole pair number
s	Slip
ω_s, ω_r	Synchronous frequency and the slip frequency in rad/s (electrical)
ω_m	Rotor speed in rad/s (electrical)
f_s	Synchronous frequency in Hz
μ	Angle of the excitation frame with respect to the stationary frame
γ	Angle of the rotor frame with respect to the excitation frame
θ_r	Angle of the rotor frame with respect to the stationary frame
m_a	Amplitude modulation ratio
δ	Duty cycle
v_{con}, v_{tri}	Control signal and triangular signal

Mechanical and wind turbine aerodynamic variables

T_a, T_m	Aerodynamic torque and mechanical torque
P_{mech}	Mechanical power
ρ	Air density
R	Turbine rotor diameter ¹
C_p	Performance coefficient or power coefficient
λ	Tip – speed ratio
β	Blade pitch angle

k_{opt}	Optimum torque coefficient
v_w	Wind speed
J or H	Mechanical moment of inertia in [$kg \cdot m^2$] or [s]
Ω_m	Mechanical rotor speed
G	Gear box ratio
D_T, D_G, D_r	Mechanical damping of the turbine rotor, generator rotor and the lumped rotor
D_s	Mechanical shaft mutual damping
K_s	Mechanical shaft stiffness or spring constant
T_s	Reaction torque between high speed shaft and low speed shaft
θ_s	Twisting angle between high speed shaft and low speed shaft
γ	Aerodynamic torque sensitivity with respect to the rotor speed
ζ	Aerodynamic torque sensitivity with respect to the pitch angle
η	Aerodynamic torque sensitivity with respect to the wind speed
Δ	Small deviations of a quantity with respect to original operating point

Electro-thermal model parameters

T	Temperature
T_j, T_a	Power device junction temperature and ambient temperature ¹
T_{tr}, T_d, T_s	Temperature of IGBT, diode and heat-sink ¹
T_U, T_L	Upper and lower IGBT
D_U, D_L	Upper and lower diode
E_{on}, E_{off}, E_{rr}	Energy loss during device turn-on, turn-off or reverse recovery
$P_{Tr,con}, P_{D,con}$	IGBT and Diode conduction power loss
$P_{Tr,sw}, P_{D,sw}$	IGBT and Diode switching power loss
f_{sw}	PWM switching frequency in Hz
V_{CE}, V_F	IGBT collector-emitter voltage drop and diode forward voltage drop
I_C, I_F	IGBT collector current and diode forward conducting current

Control parameters

k_p, k_i, k_d	Proportional, integral & derivative controller gain values
ω_n	Natural (un-damped) frequency in rad/s
ω_c, θ_c	Cross-over frequency and the corresponding controller phase angle
ξ	Damping ratio
τ	Time constant of system response
τ_{cl}	Time constant of the closed control loop response
ϕ_m	Phase margin
t_{ss}	Time to reach steady state
E_{ssv}, E_{ssv}	Steady state position error and velocity error

Chapter 1. Introduction

In order to achieve low carbon generation, the European Union (EU) has set the target that 27 % of its total energy will come from renewables by 2030, for which the UK is required to provide 15% of its energy from renewables by 2020. Wind energy is evaluated to be the cheapest electricity technology after 2020 as a wind turbine consumes no fuel and produces zero CO₂ during its lifetime after installation and apart from decommissioning. From 1995 to 2011, the EU wind industry has had an annual growth of 15.6%. With an average of 20 wind turbines being installed every day, it is the fastest growing energy source. As seen in Figure 1.1, the installed capacity of wind energy saw a continuous increase and has largely exceeded other renewable sectors in the past six years. The development of the offshore wind is catching up with the onshore wind in recent years and will still see major growth in the coming years [1].

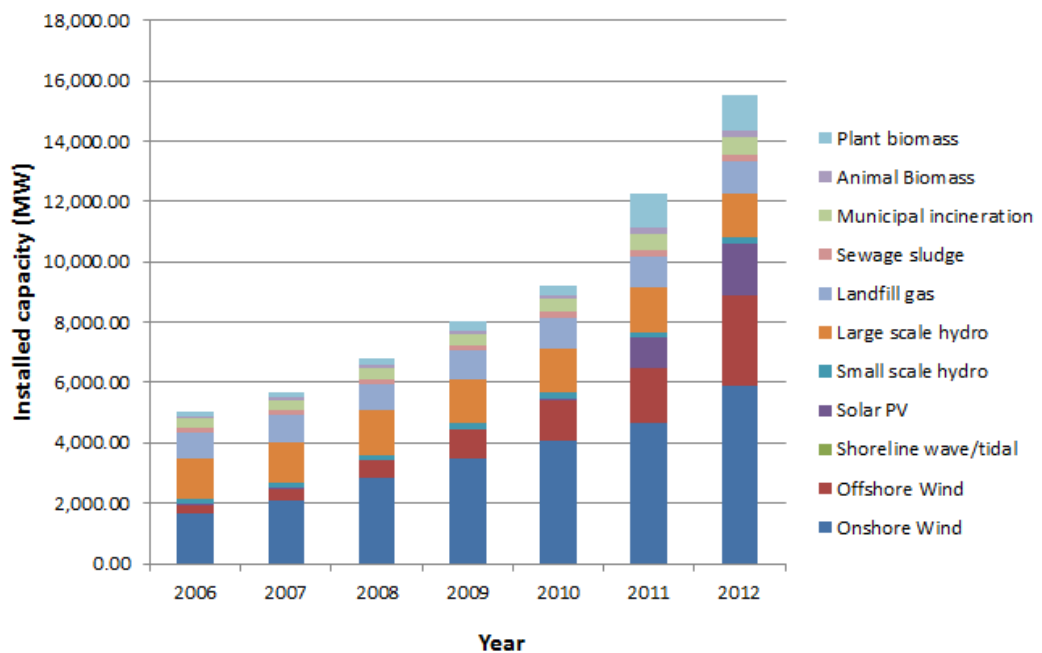


Figure 1.1 Installed capacity of the UK renewables in seven years [1]

The EU's policy requires that future wind farms go offshore in favour of acquiring more wind energy resource, and also to avoid some limitations and environmental impacts of on shore wind turbines [2]. This tendency requires ever larger wind turbines to be established due to economy considerations (civil engineering cost per MW reduces for larger turbines). Multi-megawatt wind turbines dominate the current market and their sizes will continuously increase for all manufacturers [3]. However, the cost of operation

and maintenance (O&M) is substantially higher offshore and the accessibility is usually restricted by the weather. Therefore pursuing maintenance free operation by improving reliability is especially important for reducing the cost of offshore wind turbines.

Variable speed wind turbines, with their many advantages compared to conventional fixed speed wind turbines, are a very promising technology for large wind farms and have lately dominated the yearly installation of total wind turbines. Among these, the DFIG wind turbine with a multiple-stage gear box still has the largest market share [4, 5]. An alternative wind turbine configuration for offshore applications is the direct-drive permanent-magnet synchronous generator (PMSG). It is becoming more and more attractive in recent years as the costs decrease and performance improves. Some major players in wind energy generation such as Vestas Wind Energy Systems and General Electric choose to use the DFIG technology, while some others like Siemens is shifting to the direct-drive PMSG technology.

A DFIG wind turbine may suffer from severe electrical transients in a grid voltage drop, resulting in converter damage and mechanical oscillations and stress. Even in normal operation, the rotor-side converter (RSC) of a DFIG wind turbine is subject to greater thermal-mechanical stress than the grid-side converter (GSC) due to low frequency current variations, especially around the synchronous operating point. These problems reduce the wind turbine's reliability and grid support capability, and therefore should be properly addressed [6].

The research in this thesis is to mitigate the above problems through better control schemes. A comprehensive DFIG wind turbine model has been established in PSCAD/EMTDC which involves all relevant control systems. This model will be investigated extensively in an attempt to identify the correlations between different control loops as well as their impacts on the turbine's performance in both normal and fault conditions. The linearized models of the dc-link system and a 2-mass shaft system with the pitch controller are derived, providing an insight of their behaviours and the impacting factors; improved control strategies for the RSC current loop and GSC dc-link are evaluated; the implementation of crowbar protection, damping control and their coordination with the pitch control are discussed; an electro-thermal model of the converter is established and verified, which can predict semiconductor device junction

temperature variations under different loads and control schemes; based on this work, a new control strategy that produces reduced thermal stress around the synchronous operating point is proposed.

1.1. Project background

This PhD research is a small part of the SUPERGEN Wind Energy Technologies Consortium (SUPERGEN Wind) project [7] funded by the Engineering and Physical Sciences Research Council (EPSRC). This organization was established on 23rd March 2006. As a wind energy research consortium, it is part of Sustainable Power Generation and Supply (SUPERGEN) programme.

The consortium has the support of 18 industrial partners who are dedicated to wind farm operation, manufacturing and consulting. Seven university research partners with different expertise (including wind turbine technology, aerodynamics, hydrodynamics, materials, electrical machinery, control, reliability and condition monitoring) are involved in this programme. The second phase of this project starts from March 2010 till present, which is led by Strathclyde and Durham Universities, with the target of *achieving an integrated cost-effective, reliable and available offshore wind power station*. [7]

This PhD project, as part of the SUPERGEN Wind, also involves collaboration work between Durham University and Strathclyde University.

1.2. Research objectives

The main objective of this research is to help reduce the stresses exerted in a DFIG wind turbine system during operation by improved control strategies. A very common failure cause generally true for all assemblies is fatigue through long-time exposure to stress, where the stress can be constant reaction torque ripples for the shaft system, and intense thermal cycling or electric transients for the converter system, etc. Therefore, by reducing the stresses, the ultimate goal is to reduce the failure rates and improve the reliability for the overall wind turbine system.

The thesis has enclosed a broad literature study on the wind turbine power converter reliability, to reveal the most critical components and their failure mechanisms. This

background knowledge is essential for implementing condition monitoring. The key objectives of this thesis are summarised below:

- To establish a comprehensive DFIG wind turbine model in PSCAD/EMTDC, including the 2-mass shaft system and pitch control, as well as a set of mathematical transfer functions for system dynamics investigation and controller tuning. Based on this, to achieve enhanced design of the pitch control as well as dc-link voltage control through their small signal model analysis.
- To investigate the DFIG behaviour during a grid fault condition and identify the problems (such as electric transients and mechanical oscillations) induced by the fault.
- To find mitigating strategies that can improve the DFIG wind turbine fault-ride through capability and reliability. This involves improved RSC current loop control, dc-link voltage control, the coordination of the protection schemes with the damping control and pitch control.
- To propose a bandwidth segmentation method for different control loops in order to reduce the interference between the sub-system controllers and thus to reduce the resonance caused by electrical and mechanical interactions.
- To develop an electro-thermal model of the power converters. This is to be implemented together with the DFIG wind turbine model to predict the instantaneous temperature variation under different operating states and control schemes. To apply a modified control strategy to this joint model to demonstrate its effectiveness in reducing the deep thermal cycling around the synchronous operating point.

1.3. Thesis outline

The thesis consists of seven chapters. The remaining content is organized in the following way:

Chapter 2 provides an overview of power electronic converter reliability, focusing on a wind turbine application. The component failure mechanisms and state-of-art condition monitoring techniques are covered.

Chapter 3 introduces the principles of a DFIG wind turbine with relevant control systems. Both the steady state and dynamic machine equations are presented. The generic vector control method for the RSC and GSC, to achieve decoupled regulation of the active and reactive power, generic wind turbine control, including power maximization and pitch regulation are discussed.

Chapter 4 presents a detailed analysis of the DFIG wind turbine mechanical and electric systems by introducing mathematical models. The dynamics of the dc-link system and wind turbine mechanical system are explored using their linearized small signal models. The mathematical transfer functions are verified with the PSCAD model, thus it is shown that they can be used to determine the controller parameters analytically. The criterion for pitch controller design is proposed. Based on this, three pitch controllers (P, PI and PID) with a gain scheduling technique have been evaluated, which are tested in PSCAD/EMTDC with satisfactory responses.

Chapter 5 investigates the DFIG wind turbine grid fault behaviours. The strategies that can reduce the electrical and mechanical stresses during a grid voltage drop have been evaluated. These strategies also improve the system's fault ride-through capability. For the RSC current-loop control, use of demagnetizing current injection to help fast reduction of the electric transients is implemented; the effect of controller tuning has been analysed, from which the controller bandwidths resulting in unstable fault responses are determined and an improved tuning method is proposed. For the GSC dc-link control, the feed-forward compensator method is employed together with proper bandwidth coordination in order to reduce the dc-link voltage fluctuations. The coordination of protection schemes (crowbar and dc-chopper) and the RSC control are presented. Design of the damping control in coordination with the pitch control is explained in detail. In the end, an overall bandwidth segmentation method for different control-loops is proposed, and a coordinated method to implement the above strategies to reduce the mechanical oscillations is recommended.

Chapter 6 presents an electro-thermal model of the three-phase back-to-back converter, which is integrated with the DFIG wind turbine model in PSCAD/EMTDC. With this joint model, operating point analysis, overload analysis, simulations around synchronous speed with variable winds are under taken to observe the power device thermal cycling.

Moreover, an improved controller is implemented that significantly minimizes the amount of deep temperature cycling.

Chapter 7 summarises the main findings of this research with corresponding activities undertaken. Suggestions for the future work are given in the end.

Chapter 2. Literature Review

2.1. Introduction

Power electronics is making an important contribution in modern wind energy. Wind turbines equipped with power converters such as doubly-fed induction generator (DFIG) wind turbines and permanent magnet synchronous generator (PMSG) wind turbines, have increased the flexibility of turbine control. This gives them the possibility to be inherently more grid-friendly than the conventional fixed-speed concepts and potentially increases market penetration.

In the recent years, this technology has undergone a fast evolution due to the development of high switching frequency semiconductors and real-time computer controllers [8]. As a result, many advanced control techniques can be implemented to regulate mega-watt scale power. Component ratings are getting higher but the price per kVA is going down [9]. However, the power converter as a subassembly of the wind turbine is subject to high failure rates, which makes them a major concern in the overall reliability of future offshore wind farm developments[10]. Due to the limited accessibility of the offshore environment, the failure rates of wind turbine systems need to be minimized in order to improve the availability. As a result, the power converter becomes particularly crucial to improve the wind turbine performance.

This chapter reviews the state of art power electronic converters used in wind turbines. The relevant reliability research, including failure mechanisms and condition monitoring techniques, is discussed in order to get a starting-point for system enhancement.

2.2. Reliability of power electronic converter in wind turbines – an overview

It is very common that reliability studies are based on field data. Due to the commercial sensitivity of wind turbine systems, the available data source pool used to study reliability of wind turbine technology often is restricted to a few databases[11], not all of which are publicly accessible. Among these, the most famous one is German programme WMEP due to the long period and large population of WTs involved. Some other publicly available failure statistics such as LWK, Windstats, EPRI also contribute to reliability

research. A brief introduction on each of these data sources is given in [12]. These surveys are based on wind turbines with different configurations and sizes (from 200kW to 2MW). The data are collected without defining a consistent taxonomy for the wind turbine, and hence only the failure rates of the assembly are available. More detailed information related to the component or failure modes is not obtained. This makes it difficult for manufactures to identify high-risk components and take effective mitigating measurements.

The Relia-wind project, funded by European Union has been carried out in attempt to fill in this gap. This three-year project has the target to identify critical failures and their mechanisms through quantitative studies of field data recorded at modern wind farms [13]. The failures and downtime shown in Figure 2.1 and Figure 2.2 are classified based on standard turbine taxonomy to the best extent that the data permits. The results show that 50% of the total failure rate comes from power and rotor modules, with most significant contributions from the frequency converter, generator and pitch system.

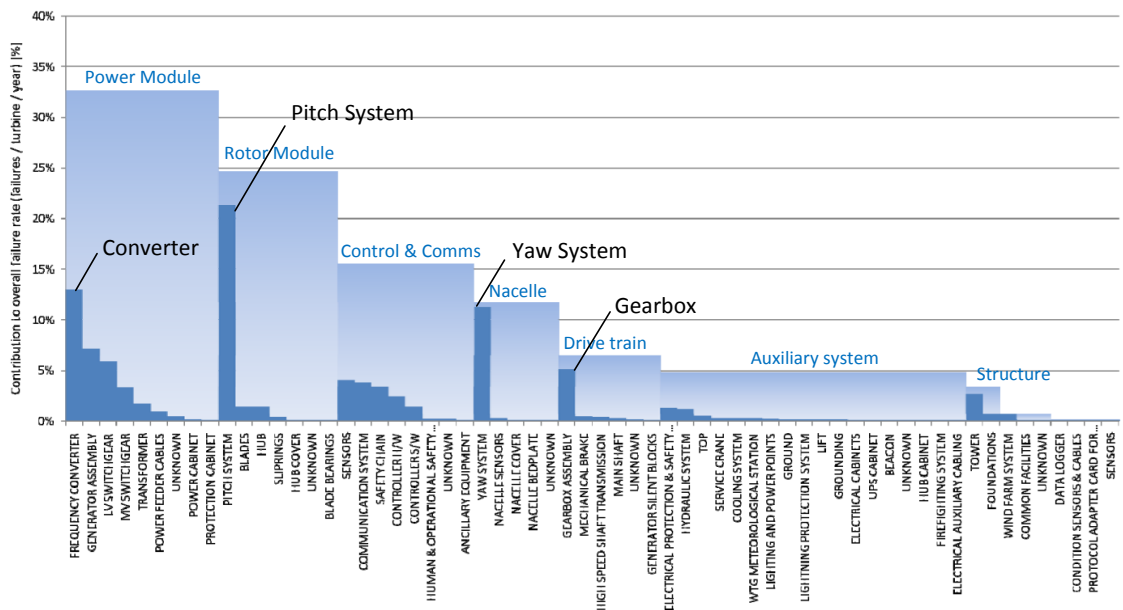


Figure 2.1 Normalised failure rate of subsystems and assemblies in variable speed wind turbines from multiple manufacturers [14]

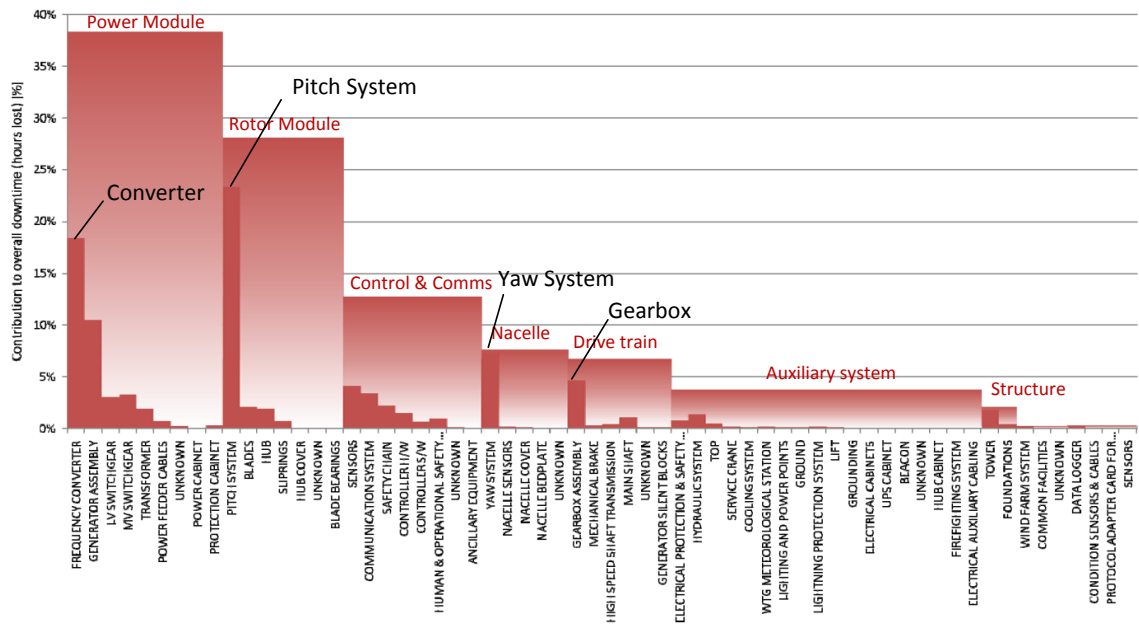


Figure 2.2 Normalised hours lost per turbine per year due to faults in subsystems and assemblies in variable speed wind turbines [14]

2.3. Development and challenge

Power electronics was at first employed in wind turbines as soft starters in the 1980's. With thyristors as the fundamental components, it was used to limit the high-inrush current during connection and smooth the transients, but then would be by-passed by a contactor. Later on, in the 1990's, power electronics was commonly seen in the fixed-speed wind turbines for controlling the rotor resistance with a diode bridge and a switch, giving an operating range of 10% above its synchronous speed. Today, different frequency converter topologies have emerged in variable speed wind turbines, with the 2-level back-to-back power converter as the most commonly adopted concept [9, 15]. The evolution of the wind turbine as well as power electronics in the last 30 years is shown in Figure 2.3, where the inner circle highlights the corresponding converter capacity.

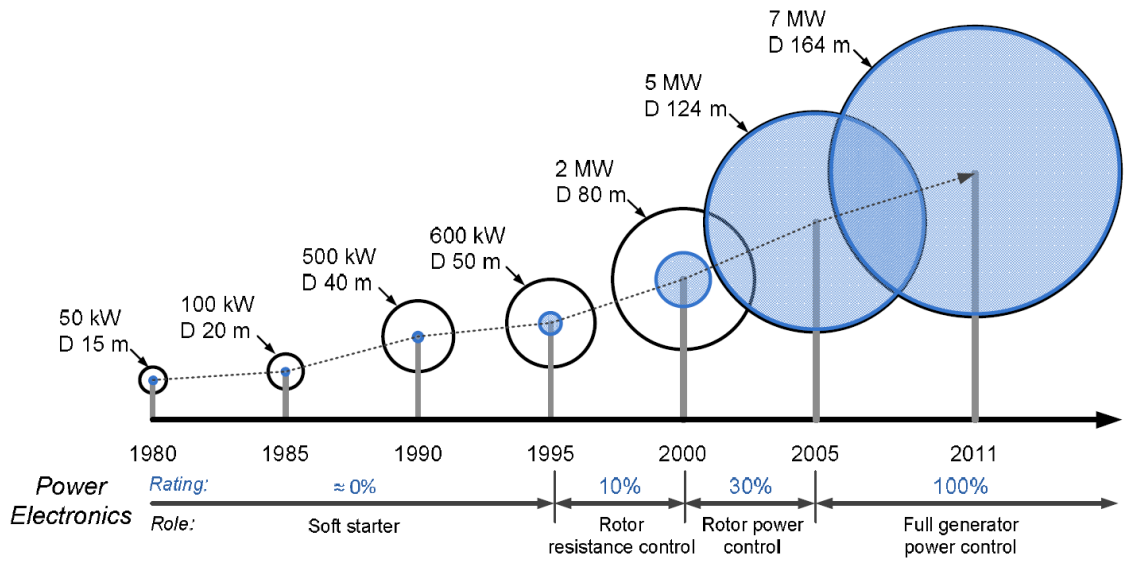


Figure 2.3 Trends of WTs with power electronics in the last 30 years [16]

The power electronics used inside a wind turbine today is a frequency converter with either partial scale or full scale power capacity. This type of converter was first introduced to DFIG wind turbines (Figure 2.4.a), which is the dominant concept in the market considering all turbine sizes. However, its fraction of market share is much smaller in multi-megawatt turbines, see Figure 2.4.c [16].

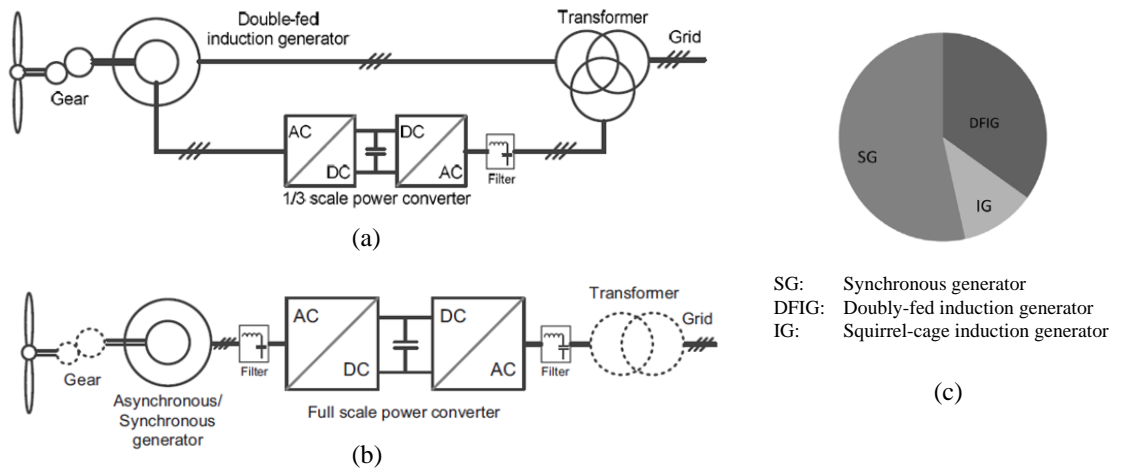


Figure 2.4 Dominant wind turbine concepts with power converter. (a) DFIG Wind turbine with partial-scale power converter; (b) Wind turbine with full-scale power converter; (c) Market share of the WTs in 1.5-3 MW [16]

Full-power converters are now implemented with synchronous generators, or squirrel-cage induction generators to transfer the total generated power to the grid (Figure 2.4. b). Synchronous generators, including the conventional rotor-excited generators and

PMSGs, are considered to be the most-promising technologies [4, 9, 16] for future large offshore installations. A PMSG equipped with a back-to-back power converter seems to be very attractive for wind turbines larger than 3MW, which may become the dominant concept instead of the DFIG wind turbine [2, 16].

The desired performance of the future power converter is listed in the following from the aspects of both generator side and grid side [16]:

Generator side performance:

- Adjust rotating speed by controlling generator rotor currents
- Control of the reactive power Q

Grid side performance:

- Respond fast to the change of transferred (active) power
- Control of the reactive power Q when the rotor converter blocks
- Maintain a constant frequency and voltage at the grid terminal
- Reduce the total harmonic distortion (THD) of the current

For the converter itself:

- Achieve (active) power balance at the two terminals
- High reliability, easy maintenance and cost effective
- High power density, modularity of the overall system

The state of the art converter topology so far in the best-seller wind turbine power range (1.5-3MW) is the pulse width modulation-voltage source converter with two-level output voltage in a back-to-back configuration (2L-BTB-VSC) [2]. It is a mature technology with proven, reliable performance and is relatively simple. This type of converter is based on IGBTs (typically 1700-V devices for a 690-V rated voltage). It has been adopted by DFIG wind turbines up to 6MW in the market [2].

Multi-level converter topologies, with higher power density, have become an attractive alternative especially in the 3 MW to 7 MW power range of wind turbines [8, 16, 17]. Most of these converters used today are implemented with neutral-point-clamped (NPC)

topologies with nominal voltages up to 5 kV, and are connected directly to a medium-voltage grid [2, 18, 19].

The configurations with two NPC inverters connected back-to-back are now commercially available, e.g. the high efficiency PCS6000 converter by ABB and the MV7000 converter by Convertteam with power-pack IGBTs. Both of these are designed for a power range up to 8MW. A newer technology now under development is the Britannia 10-MW wind energy converter system [19], which employs a rectifier on the machine side and a four-quadrant inverter at the grid side.

2.4. Components and properties

Power converters generally consist of semiconductor devices, driving circuits, protection, and control circuits which are used to implement voltage control or frequency conversion[20]. So far, this technology is still undergoing fast evolution. Some on-going research is to use different material for the components to increase the power density (from silicon to silicon carbide for semiconductors) or reliability (using film capacitors instead of electrolytic dielectric capacitors). As mentioned previously, various topologies have been designed for different purposes, among which, the 2L-BTB-VSC is mostly adopted for today's wind turbine technology. As shown in Figure 2.5, the back-to-back converter is constituted of two three phase voltage source inverters connected through a dc-link. The L-C filters are usually connected at the output of the grid-side inverters to remove the harmonics due to the switching circuit; a chopper circuit is connected in parallel with the dc-link to protect it from over voltage. In a large wind turbine for offshore applications (>3MW), several converter modules are often used in parallel, e.g. Repower 5M DFIG WT with 4 modules in parallel and the Gamesa 4.5MW PMSG WT with 6 parallelized converter modules [2, 21].

The basic elements of a power converter include semiconductor switches, diodes, capacitors and inductors. Since the electronic switches and capacitors are reported to have high failure rates in a power converter [22], these two elements will be further discussed in the following sections.

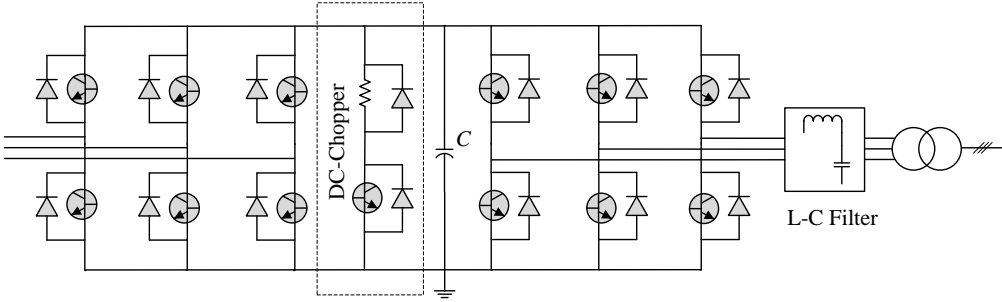
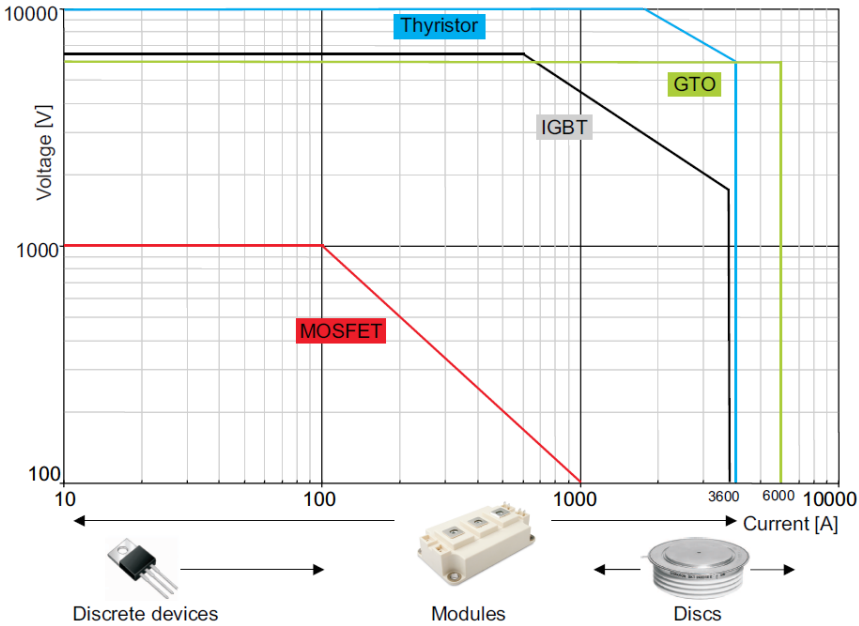
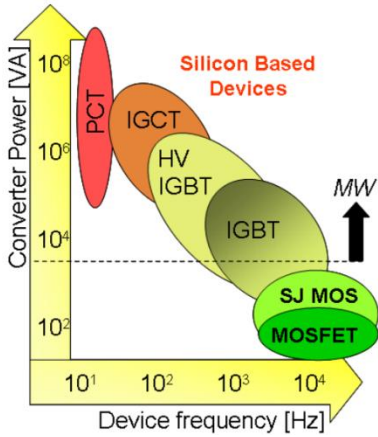


Figure 2.5 General circuit construction of a 2L-BTB-VSC

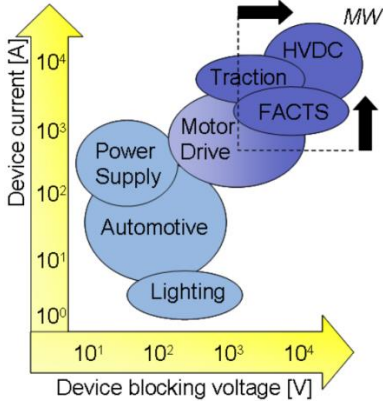
2.4.1. Semiconductor switches



(a)



(b)



(c)

Figure 2.6 Current and voltage limits for commonly used semiconductor switches (a) [23] with (b) switching frequencies and (c) application area [24]

Several technologies used for semiconductor switches on today's market are illustrated in Figure 2.6, where the operating voltage and current limits, switching frequency ranges and general application fields are presented.

Three types of the semiconductor switches, namely the Phase Controlled Thyristor (PCT), the Integrated Gate Commutated Thyristor (IGCT) and the Insulated Gate Bipolar Transistor (IGBT) are commonly used for the megawatt range. Among these, the symmetric PCT with low on-state losses and high rating (up to 8.5kV and 4kA) is adopted for High-Voltage-Direct-Current (HVDC) systems [24]. So far the IGBT is the mainly used product and also a mature technology in power electronic applications such as traction and wind energy, with blocking voltages and current ratings now up to 6.5 kV and 3.6 kA respectively [23, 25]. For higher power applications, they are challenged by the Gate Turn Off- (GTO) thyristors and IGCTs. Recently, hybrid converter topologies have been proposed in the literature [26, 27], which were designed for multi-level converters to provide better performance. The typical life expectancy requirement for a power device is 30 years or 100,000 hours operating time in vehicle equipment [28, 29]. This is similar to the life expectancy of wind turbines.

Two industrial standard packaging technologies exist for the semiconductor devices, the module technology with wire-bonded IGBTs (WBI) and press-pack IGBTs (PPI). Their structural layouts are shown in Figure 2.7.

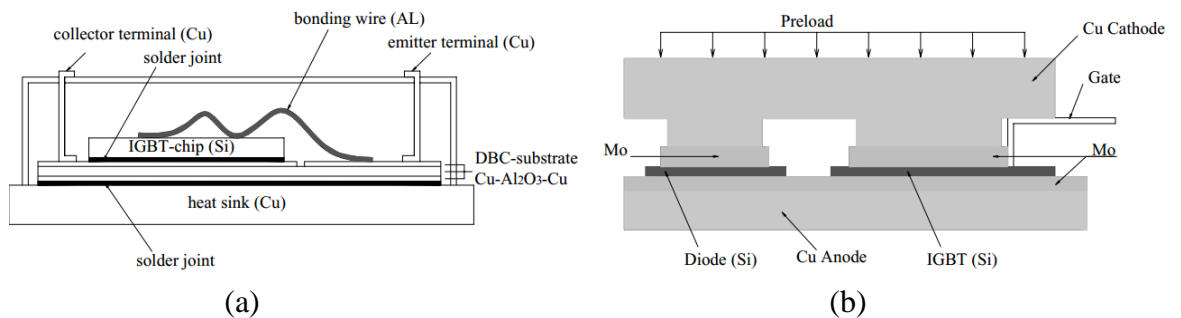


Figure 2.7 IGBT packaging structures. (a) WBI module; (b) PPI module [30]

The WBI package is the common technology used in contemporary wind turbines. It has a sandwiched structure where the chips (IGBT and diode) are bonded to the copper substrate (DBC), which is used to isolate the chips from the base-plate and is also used to conduct the heat. The entire assembly is surrounded by dielectric gel and is encapsulated

with a polymer housing [28]. The copper base plate can also pass the heat to the external heat sink. The IGBT/diode chips inside the module need numerous of wire bonds and solder joints, which are considered to be a critical reliability issue.

The press pack structure was originally designed for thyristors or diodes and now it has been widely used for manufacturing more advanced high power devices such as injection enhanced gate transistors (IEGTs) [31, 32]. In the PPI package, the device chips are clamped between the collector and emitter electrodes under pressure. Improved electrical/thermal contacts and uniform pressure distribution are achieved by inserting molybdenum (Mo) plates on top of the chips. This has many advantages compared with the WBI. The most significant ones are wire-bondless contacts and double-sided cooling which make them more tolerant to thermal cycling and thus more reliable [33]. Besides, higher power density and higher switching frequency can be achieved by this technology [33, 34]. A matter of concern is that the cooling of a PPI relies on deionised liquid such as oil, which is prone to contamination and may results in performance degradation [35].

2.4.2. Capacitors

The capacitors used in power converters are primarily for inverter ac filtering and dc-links [36]. The latter serves as energy storage to balance the power between the source side and the load side. For many years, the aluminium electrolytic capacitor has been preferred by engineers due to their large capacitance per volume and low cost per Farad [37, 38].

Generally, a capacitor can be characterized by an equivalent circuit constituted with capacitance (C), series inductance (ESL) and series resistance (ESR). ESL is often neglected in power converters. ESR reflects the total resistance of the electrolyte, paper, oxide layers, foils, leads, and connector [38]. The electrolytic capacitor has high ESR and ESL values and the ripple current withstanding capability is low. Inherently it has a limited lifetime [39]. Therefore, many power electronics applications such as electric vehicles and renewable energy, with high demand on converter performance, are now turning to film capacitors [39, 40]. For wind power, the system voltage is continuing to increase and now dc-link voltages over 1kV are very common. In this case, the film capacitors can offer both performance and cost advantages compared to the aluminium electrolytic capacitors [39, 40].

A film capacitor has a piece of plastic film (typically polypropylene) as the dielectric medium, and can have self-healing ability [40]. Besides, it also has many other performance benefits compared with an electrolytic capacitor [39]:

- Superior life expectancy due to self-healing
- Higher ripple current capability/less dissipation
- Higher operating voltages with less components
- Better capacitance stability vs. time and lower ESR
- Better conversion efficiency
- Better environmental performance

2.5. Reliability of converter - past survey results

A limited amount of good data on power electronics reliability exists. In the MIL-HDBK 217F standard [22], the failure rates of the components in two circuit topologies of a dc/dc forward-type power supply (PC1 and PC2) were obtained at the ambient temperature $T_a = 25^\circ$ [41]. This is shown in Figure 2.8, where Co is the aluminium electrolytic capacitor and Cr is the polypropylene capacitor. It can be seen that the component causing the most failures in a converter is the electrolytic capacitor, followed by the semiconductor switches (MOSFET in this case). The likelihood of inductors, diodes and polypropylene capacitor failures is very low.

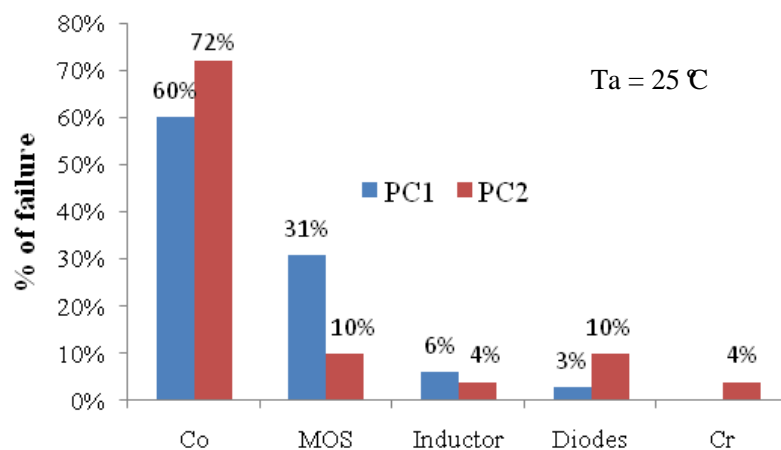


Figure 2.8 Failure distribution of each component in a power converter [41].

The MIL standard has received many criticisms due to the faults and limitations [39]. Other approaches should be developed to investigate the component failures more accurately.

Figure 13 shows two more recent surveys that approach the reliability analysis of converter components. The main root cause failures and the corresponding risk-priorities shown in Figure 2.9 (a) are based on more than 200 products from 80 companies [42]. Industry survey response in respect to fragile components is shown in Figure 2.9 (b). In both the figures, capacitors and semiconductors are found to be critical components of failure.

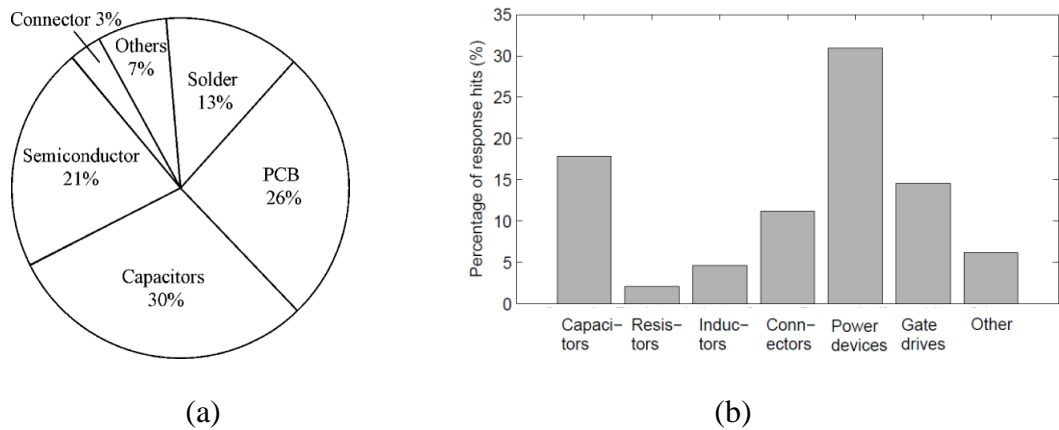


Figure 2.9 Component failures in power converters, (a) Failure distribution [42], (b) Fragile components claimed in an industrial survey [43]

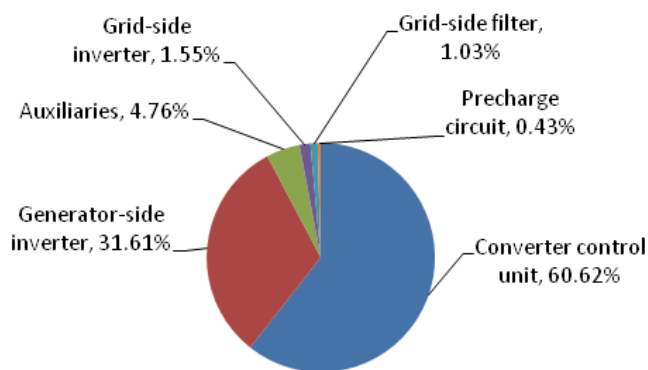


Figure 2.10 Converter components failure prediction from Relia-Wind FMEA [44]

Figure 2.10 shows the failure contributions from the main components in a back-to-back converter used in wind turbines. The data source is based on Failure Mode and Effect Analysis (FMEA) obtained from Relia-Wind project [44], which was then sorted out by

the author together with Professor Tavner at Durham University. It can be noticed that the control unit accounts for more than 60% of converter total failures. The generator-side inverter has a larger share in the total failures compared with GSC. This may result from the low frequency current cycling experienced by the semiconductors, as well as the more severe transients the RSC encountered during grid fault.

2.6. Failure causes and mechanisms

With higher standards imposed on the wind turbine power electronics, the conventional statistically-based studies cannot satisfactorily be used to enhance the design because the field data is limited and generally not applicable for component-level analysis. An understanding of every failure mechanism and root-cause is required in order to identify the critical components and provide a more sensible technical solution [16]. In this section, a summary of the failure mechanisms associated with the critical components mentioned in Chapter 2.5 will be provided based on an extensive literature research.

2.6.1. Possible failures in a voltage source converter

Before approaching the component level failures, the dominant faults that may trip or damage the converter should be considered [45-47]:

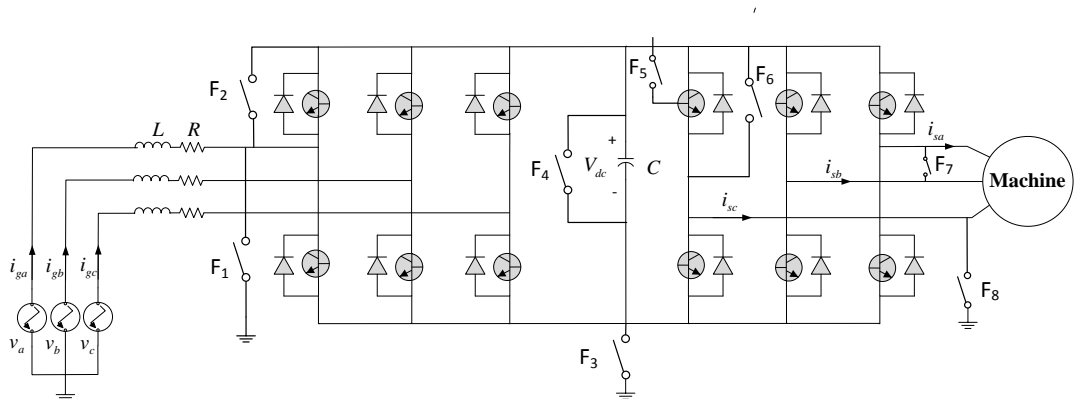


Figure 2.11 Possible fault locations in a back-to-back converter

- Control unit malfunctions
- dc-link failures (earth or short circuit fault, e.g. F3, F4)
- Power semiconductor failures (short/open/gate-misfiring faults, e.g. F2, F5, F6)
- Line fault (ground, line to line e.g. F1, F7, F8)

2.7. Control unit failures

The control system faults can be divided as hardware and software-related faults [48]. The former may attributed to the failure of sensor, signal processor and actuators, while the later may be due to internal problems or interaction with its external environment, as shown in Figure 2.12.

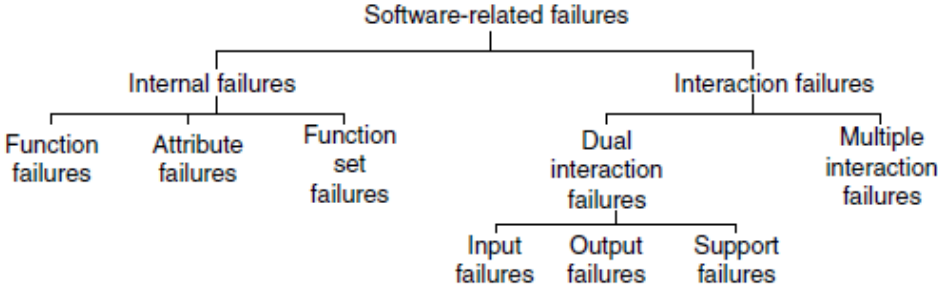


Figure 2.12 Software-related failure mode hierarchy [49]

2.7.1. Capacitor failures

Aluminium electrolytic capacitors are frequently used as dc-link and output smoothing capacitors. However, this capacitor has been reported as being the most fragile component in a converter system [38]. This section focuses on the most common failure modes of the electrolytic capacitor, for which the corresponding root causes and the identified failure mechanisms are illustrated in Figure 2.13

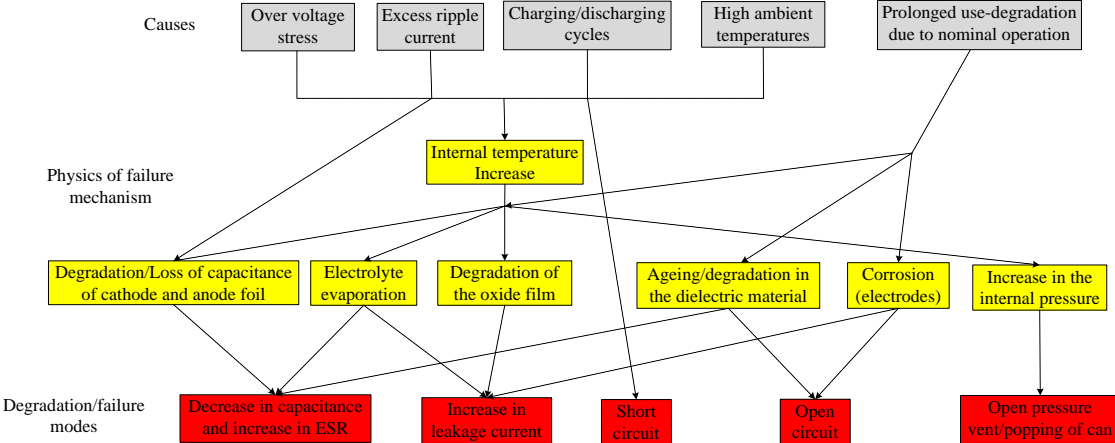


Figure 2.13 Links of causes, failure mechanisms and failure modes in aluminium electrolytic capacitor [50]

From the figure, it can be summarized that the capacitor failure can be in the form of gradually degradation of the function (wear out/aging) or a complete loss of function (catastrophic failure). For the latter, there are two classic failure modes, i.e. shorts and open circuits [50].

Wear out/ Aging

Capacitor wear-out (aging) is often affected by thermal, electromechanical and environmental stresses. It is known that the characteristics of aluminium electrolytic capacitors such as their capacitance and ESR are easily affected by temperature and frequency variations [51]. An important factor that contributes to the aging process is the evaporation of the electrolyte solution, which results in an increase in ESR and decrease in capacitance [38, 52]. Eventually this may drift the capacitor characteristics out of its required specification and cause damage in the converter [52]. Another reason responsible for aging failure is the partial discharge at the foil edge. This accounts for 90% of total capacitor failures [53].

Shorts of capacitor (dielectric breakdown)

Dielectric breakdown may be caused by inappropriate operation which produces high transients or electric surges in the circuit, resulting in deformation and fracture of the dielectric material. This process is often developed gradually after a long time of satisfactory operation and can be accelerated at higher temperature.

Open circuiting capacitors

Open-circuiting of a capacitor occurs if the connecting points inside a capacitor are separated from the external circuit due to mechanical overstress on the leads or capacitors in application. Besides, the capacitor can subject to rupture or explosion if the working voltage largely exceeds its rating; for PCB mounted capacitors, failures can also be caused by corrosion of the leads [38].

Film capacitors, on the other hand, with self-healing capability, may sustain the whole operating lifetime of an installed wind power system [40]. It has been claimed by AVX [40] that no catastrophic failure occurs even when they are used in rigorous applications. As the film capacitors gradually replace electrolytic capacitors for the dc-links in wind turbine applications, this part will be no longer a major concern in the converter reliability.

Most of recent work for converter reliability study have been focus on IGBT power modules [32].

2.7.2. Power semiconductor failures

In general, IGBT failure may result in three types of faults: short-circuit, open-circuit and intermittent gate-misfiring. A majority of diagnosis/protection methods for these faults are summarized in [54]. IGBT failures may originate from either an auxiliary circuit fault or damage in the device itself. In this section, only device intrinsic failure mechanisms will be discussed.

Generally, there are two main root causes responsible for power device failures: over-temperature and power (or thermal) cycling [55]. The power device may be subjected to the over-temperature failure when it is continuously operated until the junction temperature exceeds the safe operating temperature [56, 57]. Power cycling is induced by variable loads and it can impose mechanical stress cycles in the device, which gradually fatigues and damages it over long term operation. This effect is more significantly presented in WBIs due to their sandwiched structure.

The failure mechanisms of power devices have been discussed thoroughly in the literature [32] and [31]. Therefore this section will only to give a brief summary so that the reader can have a general idea of the failure mechanism. The reader is referred to the references for a more extensive coverage. The same order of mechanisms as in [32] will be presented to aid for referencing. The progressive failure mechanisms can be related to chips or the packaging. Although the former is the fatal reason, most of the time they can jointly result in a device failure.

2.7.2.1. Chip-related failure mechanisms

Electrical overstress (EOS)

The EOS can be expressed in the form of overvoltage or over-current, which generates significant heat and can result in secondary breakdown. Therefore the safe operating area (SOA) of a power device should be always checked to match with the specific application and heat sinking requirement.

Electrostatic Discharge (ESD)

The failure modes caused by ESD are similar to that caused by EOS [58]. A device suffering from ESD can present a satisfactory operating condition at the beginning of their life. However, the gate oxide may have been partially punctured and this gradually leads to a device failure [59].

Latch-Up

This is caused by fast ramp down voltage when turning off the device. It triggers the parasitic thyristor in an IGBT. The circuit must be designed properly to ensure the ramp rate of voltage is within the reversed bias SOA in order to avoid latch-up [60].

Electro-migration

This may occur during the manufacturing process due to various factors, which are related to the metallization of the semiconductor devices.

Thermal activation

Thermal Activation can result in degradation and the process will be accelerated under high temperature, according to Arrhenius' law

$$\text{rate of activation} \propto \exp\left(-\frac{E_a}{RT}\right) [32]$$

where E_a is the activation energy, T is the temperature, and R is the gas constant.

2.7.2.2. Package-related failure mechanisms

The two packing technologies WBI and PPI have different failure mechanisms of their own:

WBI failures

The number of wire bonds and solder joints are the dominant weaknesses which have been eliminated in PPI technology [28, 31]. The weakest areas most susceptible to break down are around the connections between the chip, DBC substrate, and base plate [61], as shown in Figure 2.14.

In a WBI, all the layer interfaces can suffer a shear stress due to different coefficients of thermal expansion (CTE). If the power converter is working under cyclic load for long periods, the stress cycling will eventually crack the connections. This results in two failure modes: bond wire lift-off and solder fatigue.

Bond wire lift-off is considered to be the principal failure mechanism that affects both IGBTs and free-wheeling diodes [62]. During the process, the cracks will initiate from both the ends of Al wires and grow towards the centre as shown in Figure 2.15 (a). In long enough continuous power cycling process, the thermal stress may exceed a certain threshold, and the surviving bond wires could melt leading to the failure of device.

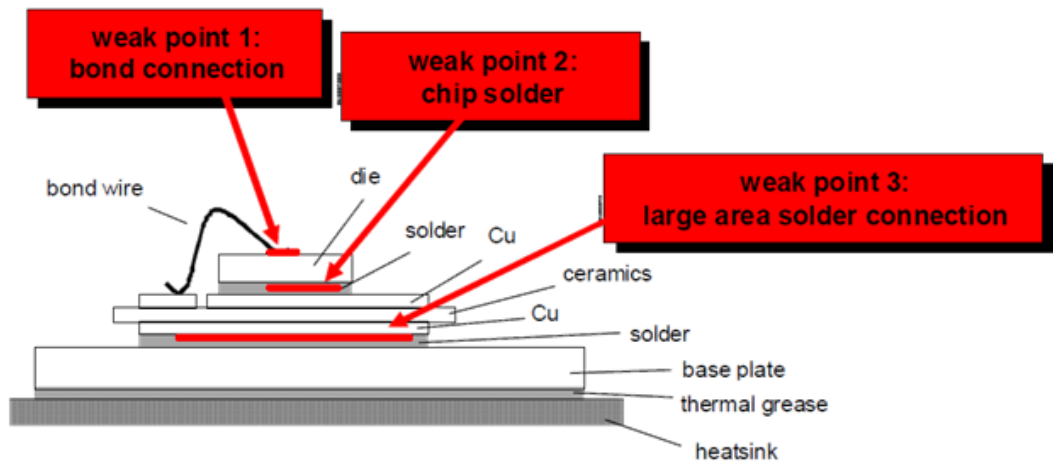


Figure 2.14 Weak points in WBI module regarding lifetime [61]

Solder fatigue is also an important failure mode for WBIs and is often accompanied by cracking and voids in the solder joint, as seen in Figure 2.15 (b). The voids result in an increased thermal resistance (effective conducting area decreased). As the length of crack grows with the number of cycles, the local heat increases to an unbearable level and finally damages the chip. For the two solder joints in Figure 2.14, the critical one is between the DCB substrate and base plate (weak point 3) as a larger CTE difference exists between the adjacent materials [62].

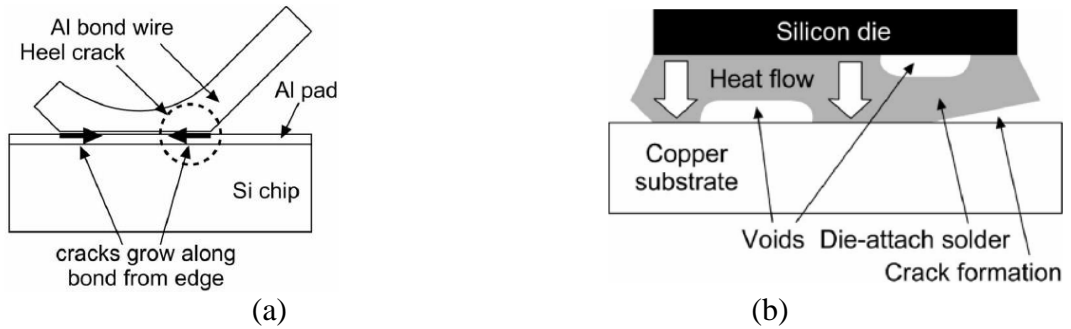


Figure 2.15 Common package-related failure mechanisms [32], (a) Bond wire lift-off propagation, (b) Solder fatigue - crack and void formation

PPI

The PPI has a unique feature – the device can become a conducting element when it fails. Therefore failing of PPI may not necessarily mean that the entire circuit fails. The most important failure mechanism for PPI is the fretting damage [31], which is driven by different CTEs of the internal components. As a result, relative moving between the components happens constantly under temperature variations. Fretting can lead to deterioration of the components' electrical and thermal properties. The gate-spring, on the other hand, is also a critical component as it is subjected to fatigue and stress relaxation. Some other failure mechanisms such as coolant contamination or base plate cracks can lead to thermal performance degradation as well.

2.8. Reliability prediction and condition monitoring technique for power converters

2.8.1. General concept

Reliability prediction of power electronics is conventionally based on handbooks, where the mean time between failures (MTBF) can be calculated by counting in each component's individual failure rates. These failure rates are mainly based on field data which proved to be unsatisfactory for more precise predictions. A physics of failure approach on the other hand, is required for higher-standard reliability prediction, as it enables the engineers to identify fragile components under particular operating conditions [37, 39, 54]. Besides, the information revealed by the physical reliability model, e.g. the precursors of failure, lifetime consuming status, can be used by a condition monitoring (CM) system, which is a cost effective way to improve reliability.

Condition monitoring is the real-time measurement method of a component's status, which can inform people to take action if any parameter deviates from the healthy condition [32]. This can help to schedule maintenance in order to extend a system's lifetime at a minimum cost. Usually, CM is implemented in the following ways [32, 54]:

- Device parameter-based methods: the parameters of device are monitored and a defined change from its normal state is used to signify the degradation.
- Sensor-based methods: dedicated sensors can be embedded into the device to detect the degree of damage.
- Model-based methods: this involves establishing reliability models to predict the stresses (temperature, strain) to which the power device or packaging is subjected to under operating conditions, instead of implementing costly tests.
- Fusion of techniques: The aforementioned methods can be integrated in order to achieve a more accurate, reliable and cost-effective prediction.

2.8.2. Parameter-based CM

Several parameters-based methods for condition monitoring power electronics have been reviewed in [32]. Here the three techniques for IGBTs are summarized, which capture the most common failure modes. Examples of the failure modes and the associated indicator parameters are presented.

2.8.2.1. Implementation on IGBT

On-state voltage/resistance – bond wire lift-off

The bond wire lift-off failure is accompanied by detectable changes in R_{on} or $V_{CE,sat}$. The end-of life criterion for an IGBT is defined by a 15% increment in $V_{CE,sat}$.

Thermal resistance – solder fatigue

As discussed in Chapter 2.7.2.2, thermal resistance R_{th} increase can result from the cracks and voids formed at the solder joint. Therefore this parameter can be used as an indicator of solder fatigue. The failure is said to occur when R_{th} is 1.2 times larger than the original value.

Gate signal – short circuit fault

A short-circuit of the IGBT can be signified by the gate signal variation during turn on. This can be noticed by comparing the gate voltage curves of a faulty case with the normal case.

2.8.2.2. Implementation on capacitors

For electrolytic capacitors, the ESR is an important indicator of deterioration as it determines the capacitor's thermal stability [37]. Different methods for predicting the ESR have been investigated [37, 38, 41, 52]. Besides direct use of ESR, using the output voltage ripple as an indicator is also feasible as it is directly related to ESR [41].

For the metalized polypropylene film (MPPF) capacitors, the ESR is very small ($10^{-2}m\ \Omega$), and this is not suitable to be used as a monitored parameter. Instead, the capacitance value is adopted as the indicator [63]. The curve of capacitance degradation at the end of life is given by manufacturers, as shown in Figure 2.16. It can be seen that after a certain operating time, the decrease of capacitance is much faster. A 2% capacitance loss can signify the end life in traction applications at 25 °C [63]. Sometimes 5% of capacitance loss can be used as in [64]

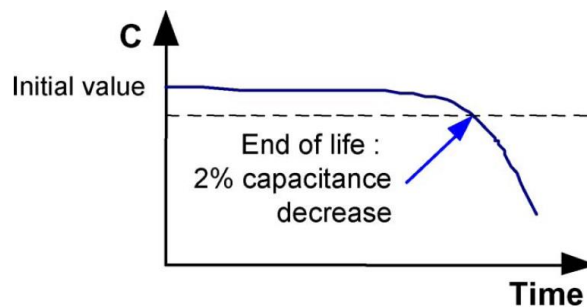


Figure 2.16 End-of-life behaviour of a MPPF capacitor [63].

2.8.3. Model-based CM

The model-based CM technique is very promising for power converters subjected to variable loads and external environments. The process generally includes three steps [32, 54]:

- Electro-thermal model: this is used to derive the temperature from the power dissipation on the device under a predefined load.

- Thermo-mechanical model: using the damage indicators that can be predicted (such as plastic strain ε_p).
- Lifetime model: this model allows the lifetime or accumulated damage to be estimated based on particular damaging factors which the device is subjected to.

In this approach, the reliability prediction technique - physics of failure model - is applied in CM to achieve the predictive CM, which is also known as the prognosis and health management (PHM) system [54]. Here precursory signals that cannot be monitored directly are obtained from the first two steps, and then used as inputs to the lifetime model. Instead of just sending a warning when a certain parameter drifts out of its normal state, this approach can predict the damage levels (health condition) and remaining lifetime, which will inform the engineers whether the converter should be replaced during a scheduled maintenance.

2.8.3.1. Implementation on an IGBT

For an IGBT, usually the junction temperature T_j is calculated with the thermo-electric model. Since the temperature is non-uniform, techniques such as the rainflow counting method [65] can be applied to extract the frequency of thermal cycles in different amplitude ranges. The temperatures at each interface in the power module can also be calculated in order to evaluate the stress at that position. In this thesis, a full thermo-electric model of the three – phase converter has been developed in PSCAD together with DFIG model, the details of which are presented in Chapter 6.

The thermo-mechanical models can predict mechanical stress factors. Parameters of the packaging materials and thermal cycling are required for analysis. Two common failure mechanisms of the WBI - bond wire lift-off and solder failure – are considered in this model [32]. The stress can otherwise be evaluated using finite element analysis (FEA). Equation (2.1) gives the dependence of strain ε_{tot} under a cycling load on temperature swing [66].

$$\varepsilon_{tot} = \frac{(\alpha_{Al} - \alpha_{Si}) \Delta T_j}{1 - \nu} \quad (2.1)$$

where α_{Al} and α_{Si} are the CTEs of Al and Si, ν is the Poisson ratio.

The lifetime of the device can be represented analytically by the number of thermal cycles to failure N_f [67]. A simple method to predict the lifetime of power device is the Coffin-Manson model (2.2). This model is applicable to a power device under uniform cycling load with peak temperature lower than 120 °C [32, 67]. Coffin-Manson models based on different number of parameters have been described in [67]. The basic Coffin – Manson is given by

$$N_f = a \cdot (\Delta T)^{-n} \quad (2.2)$$

Here only the device temperature swing ΔT is considered as a stress factor. Parameters 'a' and 'n' can be determined through experiment test or numerical simulations. An improved Coffin – Manson model is defined by Arrheniums relationship:

$$N_f = a \cdot (\Delta T)^{-n} \cdot e^{\frac{E_a}{k \cdot T_m}} \quad (2.3)$$

where T_m is the mean temperature of the thermal cycle, k is the Boltzmann constant (8.62e-5 eV/K) and E_a is the activation energy parameter measured by experiment. This model is capable of predicting the crack initiation of bond wire lift-off [32]. A unique form of equation exists for predicting the failure of a larger solder joint:

$$N_f = 0.5 \times \left[\frac{L \times \Delta\alpha \times \Delta T}{\gamma \times \chi} \right]^{\frac{1}{c}} \quad (2.4)$$

where L denotes the lateral size of the solder joint, $\Delta\alpha$ is the CTE mismatch of two adjacent layer materials, γ is the ductility factor of the solder, χ is the thickness of the solder layer and C is the fatigue exponent.

The lifetime prediction model can also be based on the energy, damage, stress or strain on the device, which is referred to as the physical model. The failure occurs if the monitored parameter exceeds a threshold value. The literature [32] presents several physical models, such as the Palmgren-Miner linear rule which can predict the damage accumulation of the packaging, and the Paris law which can be used to calculate crack propagation in the wire

bond as well as the solder joint. In [68], a stress model of the gate spring in a PPI is given as

$$100 \times (\sigma / \sigma_0) = A - B[\ln(t)]^2 \quad (2.5)$$

where σ is remaining stress in the gate spring material, σ_0 is the initial stress value, t (hours) is the time operated, A and B are constants related to the material and temperature.

2.8.3.2. Implementation on the capacitor

Similarly for capacitor lifetime prediction, a thermo-electrical model (2.6) is used to calculate the core temperature T_c based on the power dissipation [37, 69]. Then the vapor pressure of the electrolyte is obtained through the thermo-mechanical model (2.7).

$$T_c = T_a + I_r^2 R_c \times \theta \quad (2.6)$$

$$P = e^{\left(\frac{A}{T_c} + B\right)} \quad (2.7)$$

where I_r represents the ripple current (Arms), R_c is the equivalent series resistance (Ohm) and θ is the thermal resistance between core of capacitor and ambient ($^{\circ}\text{C}/\text{W}$), P is the vapor pressure of electrolyte (mmHg), A and B are liquid related constants

Finally, the life model is obtained which is expressed as the rate of electrolyte loss :

$$dV / dt = -kP \quad (2.8)$$

where k is the leak rate constant (units of the volume /mmHg/Hr), V is the remaining volume of the electrolyte. The end of life is defined as electrolyte loss of 40% of the initial volume [70]. Another lifetime model of the aluminium electrolytic capacitor is given by equation (2.9) from which, it is known that the life doubles with every 10°C temperature drop.

$$L_a = M_v 2^{(T_r - T_a)/10} \quad (2.9)[70]$$

Here, L_a is the predicted working life, M_v is dependent on the applied voltage, T_a and T_r is the actual and rated temperature

2.8.4. Model integration technique for CM

The research of condition monitoring techniques for the wind turbine power converter application is still at an embryonic stage. The conventional reliability prediction technique which is based on a known mission profile (temperature cycling) is not applicable to a wind turbine power converter due to the unpredictable load variations generated by the wind speeds [71]. Therefore the wind turbine model should be used in conjunction with the reliability model of the power device. The former will predict the electrical power or the current in the converter component, and pass them to the next stage, whilst the later undertakes the stress and lifetime prediction of the power device. In this way, a real-time CM with lifetime prediction function can be established. An example of such a model is shown in Figure 2.17.

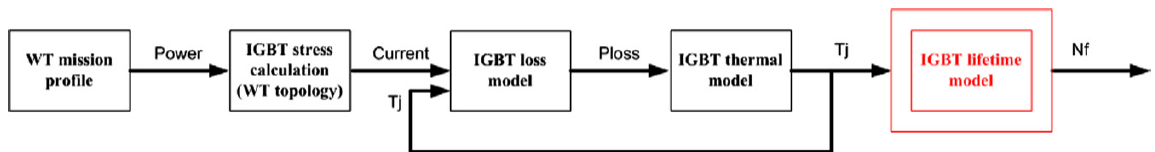


Figure 2.17 IGBT lifetime prediction in wind turbine applications [31]

2.9. Conclusions

This chapter first reviews the state of the art of power electronic circuits used in wind energy with the focus on frequency converters within the wind turbines. The 2L-BTB VSC is the dominant topology in the market at the moment. As the converter rating continuously increases, the multi-level converter is also becoming an attractive solution.

Historical field data and survey results can assist in identifying the critical components in a power converter. However, further investigation at the component level based on the statistical study is not implementable. The physics of failure study is more suitable for identifying failure mechanisms in this case. The main components – the semiconductor device and the capacitor - with large reliability concerns are discussed. Conventional WBIs and aluminium electrolyte capacitors are a less favourable choice compared with the newer PPI and MPPF capacitors in many applications due to lower reliability.

The failure mechanisms of converter sub-modules have been discussed. Bond-wire lift-off and solder joint crack are the main driving forces of WBI failure. For the electrolyte capacitor, aging is mainly due to the evaporation of the electrolyte. These factors have been eliminated in the newer technology (PPI or MPPF) and thus their reliability has been improved.

CM for power electronics is at an infant stage. Most of the research focuses on IGBT modules. Parameter-based and model-based CM techniques have been discussed for both the IGBT and capacitor. It has been suggested that an integration of the WT model and power converter reliability model can be implemented to achieve a real-time predictive CM method with which the system health and lifetime can also be predicted.

Chapter 3. Modelling and Control of DFIG Wind Turbine System

3.1. An overview of the DFIG wind turbine system

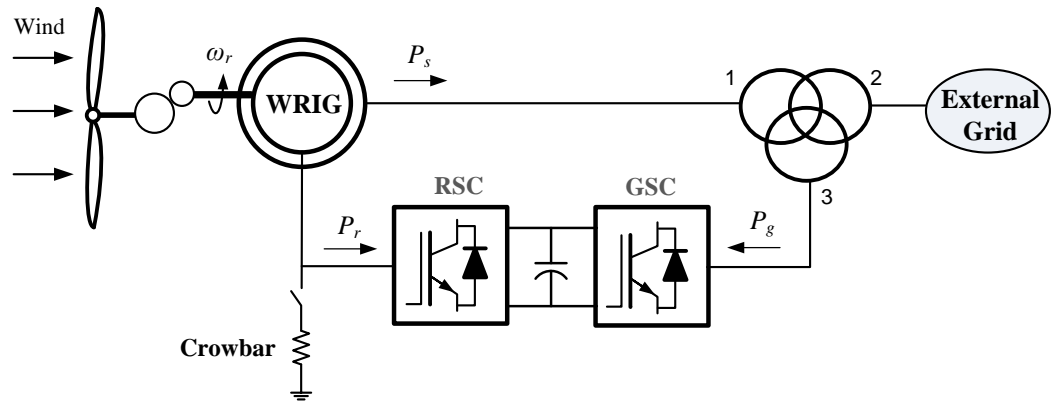


Figure 3.1 Schematic diagram of a typical DFIG wind turbine

3.1.1. Mechanical system

The mechanical system of the wind turbine includes the wind turbine blades, the shaft and the pitch control system [72]. The turbine blades produce aerodynamic torque from the wind and transfer it to the generator through the shaft system. Nowadays, the blades of MW wind turbines can usually be pitched to limit the mechanical power. In general, there are three strategies to limit the power using the blades, which are fixed stall, active stall, and pitching. Some wind turbines use a combination of the pitch and active stall control. Fixed stall control is the cheapest way since no moving parts are involved. It is commonly adopted by smaller wind turbines. Active stall control is similar to pitch control. The difference is that the blade angle is turned in the negative direction. Thus the angle of attack is increased, leading to a deeper stall [73]. Pitch control is the most expensive one of the three as it employs a hydraulic or electrical mechanism. However, this method produces the least mechanical stress on the drive-train system.

3.1.2. Generator

A typical DFIG wind turbine is shown in Figure 3.1. It has the stator connected to the grid and the rotor connected to a back-to-back power converter through separate slip rings for each winding. The converter only needs to handle a fraction of the stator power (up to 30%). A DFIG machine has the following characteristics [73]:

- The stator windings are supplied with three phase voltages of a constant frequency and magnitude, at the grid voltage. The induced magnetic field rotates at the synchronous speed in electric radians, i.e. 314.16rad/s. If divided by the pole pairs the spatial rotation speed is obtained.
- The rotor windings are supplied with three phase voltages of a variable frequency and magnitude, which are dependent on the rotor mechanical speed. The voltages are generated by the rotor-side converter (RSC). This results in a second magnetic field in the air gap, with the same spatial rotational speed as the stator flux.
- The two magnetic fields have a phase shift. Therefore, the machine's electro-magnetic torque is generated as the magnetic fields interact with each other.
- In normal operation, the stator will always supply the power from the DFIG to the grid. In the rotor circuit, the power flows to the grid at super-synchronous speed, and feeds back to the machine at sub-synchronous speed.

3.1.3. Converter

The DFIG rotor exchanges the power with the grid. This is achieved by the four-quadrant power converter that allows reversible power flow. Both of the voltage-source-inverters (VSI) are connected to a dc bus (or dc-link), which acts as an energy storage system and will smooth the power flow. So far, the two-level back-to-back (2L-BTB) converter with IGBTs is the most popular topology for medium size wind turbines in the range of 1.5 – 3MW. It is expected that three level converters may provide better performance for more powerful offshore wind turbines (3– 6MW) with fully rated power converter. In this document, only the 2L-BTB converter will be detailed.

For the voltage and current flowing in the RSC, the frequency equals to the slip frequency ω_{slip} , i.e. the difference between the stator electrical frequency ω_s and ω_m , i.e. the electrical equivalent of the rotor mechanical angular velocity. At the synchronous speed, the RSC has a dc current. The magnitude of the rotor voltage is proportional to the slip frequency.

The RSC is used for regulating the machine electric torque and reactive power produced from the generator, while the grid-side converter (GSC) is mainly used for exchanging

this power between the rotor circuit and the grid, by maintaining a constant dc-link voltage. The frequency of electric quantities of the GSC is roughly constant, which equals to the synchronous frequency. For a 2L-BTB converter, the switching frequency is commonly in the range of 2.5 to 5 kHz [73]. The dc-link voltage has a nominal value around 1kV.

3.1.4. Transformer

The wind turbine stator windings are commonly sized for low voltage levels (typically rated at 400V, 690V, 900V for a European 50Hz system) [73]. In order to connect with the distribution grids with a medium voltage level (10kV – 33kV), a transformer is necessary. One transformer connection type has been shown in Figure 3.1. Two other connections are depicted in Figure 3.2. In the upper configuration, the wind turbine stator and GSC terminal voltages are the same. In the lower configuration, the rating of transformer can be reduced to the same as the converter. However, the voltage rating for the stator needs to be as high as the grid. For small wind turbines, several units may share one transformer. This kind of transformer is usually separately installed beside the turbine, together with the breaker and protection systems. For large wind turbines, transformers can also be located in the tower base or even in the nacelle [73], though the former is more favourable for easy access.

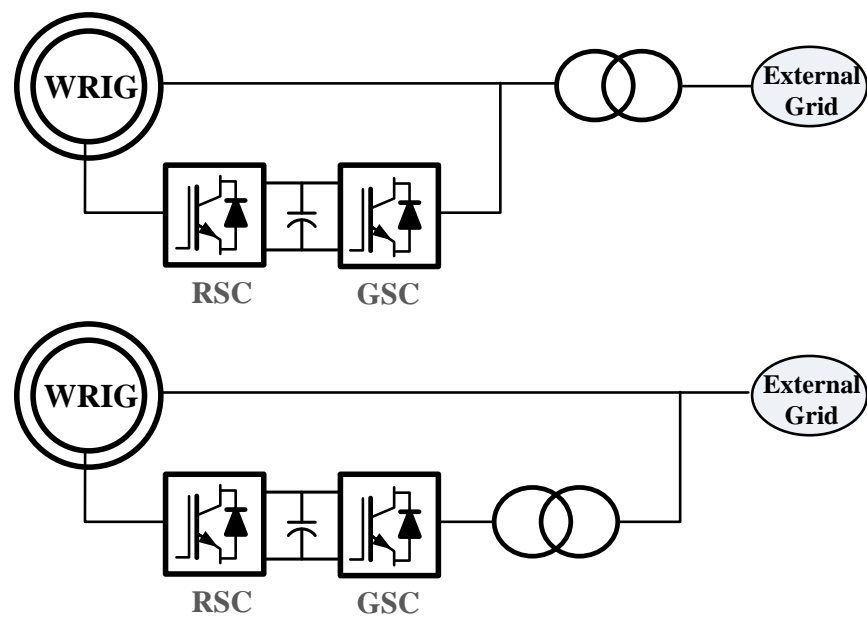


Figure 3.2 Two other transformer connection types [73]

3.1.5. Crowbar

A protective circuit is connected at the output of rotor windings as shown in Figure 3.3, which is referred to as the crowbar circuit. The crowbar configuration consists of a three-phase rectifier in connection with a resistor R_{CB} . In normal operation, the switch S_{CB} is open. When the monitor rotor current or dc-link voltage exceeds its respective limit, the switch closes to short-circuit the rotor, and results in no current flowing into the RSC. It is reported in [72] that the most common problem triggering the RSC protection is rotor over-current, since the maximum acceptable current is only slightly larger than the nominal rating. The purpose of using a crowbar is to protect the converter IGBT switches from electrical or thermal overloads, as well as to protect the dc-link from over-voltage.

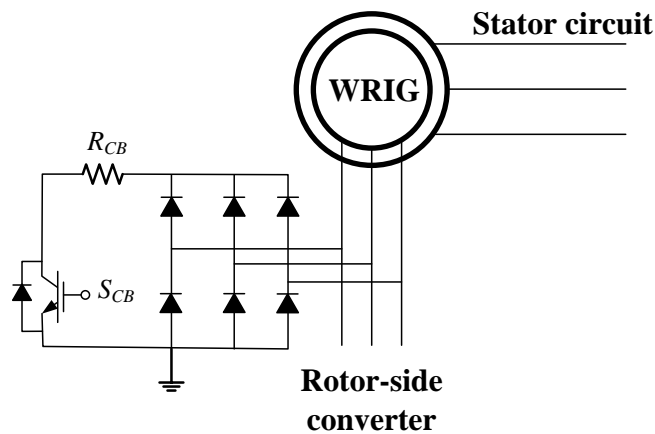


Figure 3.3 Schematic diagram of the crowbar circuit

3.1.6. Overall control systems

In the study of [74], two hierarchies of control systems have been identified. A superior control level is included by [73], as shown in Figure 3.4. From low to high, the three levels are respectively referred to as: (1) DFIG control, (2) Wind turbine control, (3) Grid integration and wind farm control. The functions of each control level are described below:

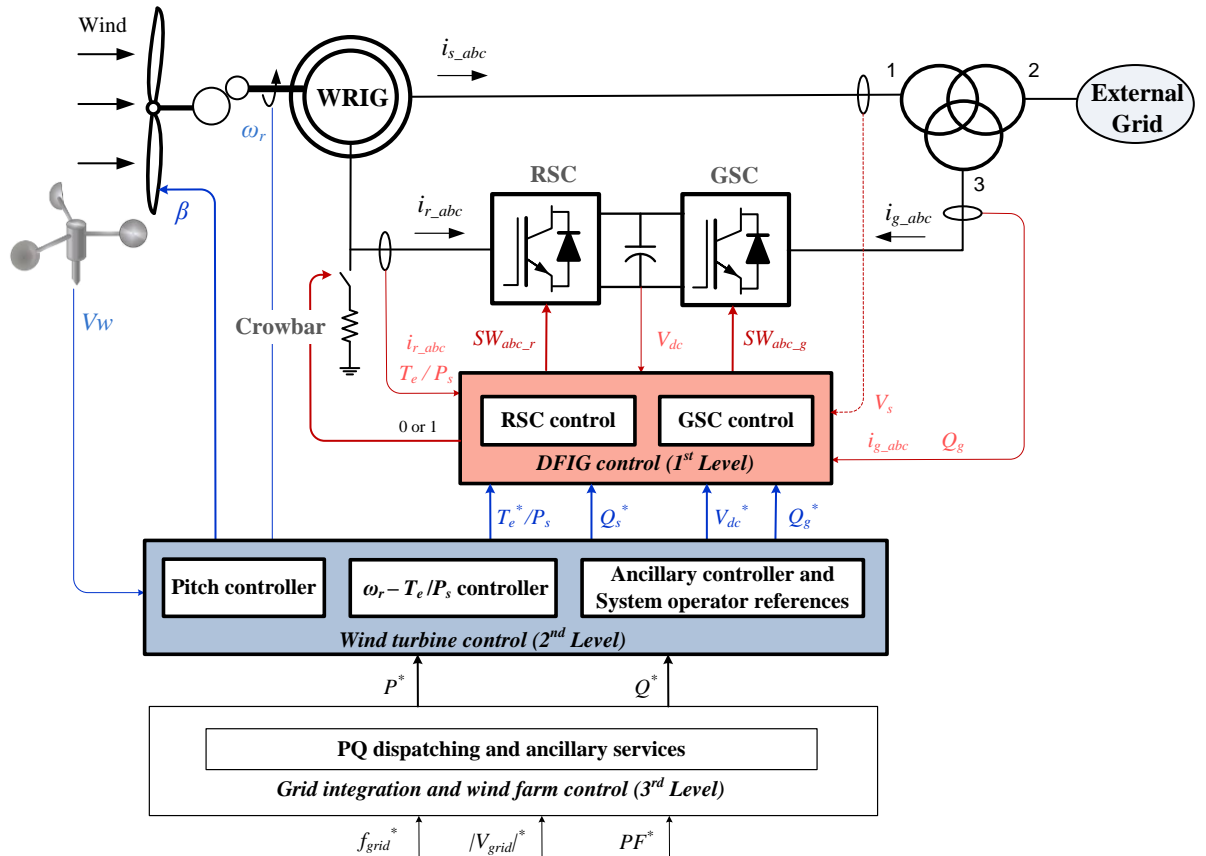


Figure 3.4 Overall control structure of the DFIG wind turbine [73, 74]

DFIG control

In this level, the wind turbine electrical control system (i.e. the rotor-side converter and grid-side converter) regulates the power flow between the generator and the grid. As shown in the figure, the control signals from this level are depicted by red lines. The converter receives reference signals from the superior control level, and measurements of the corresponding electrical quantities from the machine. The RSC controls the electric torque (stator power) and reactive power independently. The GSC mainly ensures good active power flow between the RSC and the grid by keeping a constant dc-link voltage. The nominal dc-voltage is related to the size of the converter. When the sensor detects an over current, a signal will be sent to activate the crowbar and protect the RSC from suffering any overloads.

The reactive power reference is usually set at zero for both the RSC and GSC, which implies neither the stator nor the rotor circuit will exchange reactive power with the grid, as in the case of a strong power system. However, in the circumstance of a weak power

system or voltage disturbances, the machine may be required to absorb or generate reactive power in order to support the grid voltage [73, 74]. The amount of reactive power is mainly determined by the RSC and is from the stator. The grid-side converter is set to be reactive neutral in order to maximize the active power transmission, until the RSC is short-circuited or blocked. In such a condition the GSC can take over to regulate the reactive power until the RSC resumes its normal operation [72].

Wind turbine control

In this level, the controller is mainly responsible for power maximization and limitation. In other words, it forces the wind turbine back to the balancing point between the aerodynamic torque and the electromagnetic torque by following the torque characteristics curves and pitch regulation. Compared with the 1st level electrical control, the bandwidths are much slower in this level. Generally, it involves the following tasks

- The electric torque (stator power) reference follows a predefined characteristic curve $\omega_r - T_e$. This curve can be modified according to different purposes. For example, for most regions of lower wind speeds, optimum torque reference is followed in order to extract maximum power from the wind. It can also be designed to improve power stability or to avoid critical operating points (e.g. synchronous point). At higher winds, the electric torque reference is often set at the nominal value. A higher reference can be demanded when necessary, as long as the converter limit is not exceeded.
- The pitch controller uses the rotor speed or electrical power (or both) to generate the pitch angle reference for the blades. At lower winds, the blade angle is generally set to be an optimum value, i.e. 0 degrees. At high winds, the pitch angle increases in order to shed off excessive mechanical power to restrict the rotor speed within the limit. Pitch control may also be activated in circumstances of a grid fault, turbine starting-up or shut down.
- This level supplies other reference signals to the 1st level, which is determined by the system operators. Besides, it also responds to the 3rd control level and coordinates the reactive power shared between the GSC and the stator.

Grid integration and wind farm control

This level is dedicated to dealing with the grid – integration issues. It receives the command from the wind farm central control system or directly from the grid operators. Then it can order the wind turbine to provide extra services such as inertial response or droop control based on specific voltage and frequency characteristic [73].

3.2. Mechanical system representation

As mentioned in section 3.1.1, the mechanical system model involves three parts, the aerodynamic model, the shaft system model and the pitch control system. This section only introduces the former two parts of the mechanical system. Pitch control will be discussed in section 3.7.

3.2.1. Aerodynamic model

The aerodynamic model (or wind turbine rotor model), gives a coupling effect between the incoming wind speed and the mechanical torque (power) produced by the turbine rotor. For wind turbines with variable-pitch, the aerodynamic model also gives a coupling between the blade angle and the torque [72]. The wind turbine aerodynamic model can be represented with the same equation for various generator configurations:

$$T_a = \frac{\rho}{2} \pi R^3 \frac{C_p(\lambda, \beta)}{\lambda} v_w^2 \quad (3.1)$$

The power extracted from the wind can be described as

$$P_a = \frac{1}{2} \rho \pi R^2 C_p(\lambda, \beta) v_w^3 \quad (3.2)$$

Where

ρ = Air density

R = Radius of the rotor

C_p = Performance coefficient or power coefficient

$\lambda = \frac{\omega_r R}{v_w}$ = Tip speed ratio, i.e. the ratio between blade tip speed and the effective wind speed upstream the rotor

β = Pitch angle of rotor blades, i.e. the angle between the plane of rotation and the blade cross-section chord.

v_w = Wind speed

The power coefficient C_p is a function of the tip speed ratio λ and the pitch angle β . Besides, the loads subjected by the wind turbine can be obtained from the Blade Element Momentum (BEM) method [75, 76]. As this method requires the knowledge of blade geometry, and the computation is very complicated, the numerical approximation is usually implemented [77-79]. Here the following approximation is adopted:

$$C_p(\lambda, \beta) = 0.22 \left(\frac{116}{\lambda_i} - 0.4\beta - 5 \right) e^{-\frac{12.5}{\lambda_i}} \quad (3.3)$$

$$\frac{1}{\lambda_i} = \frac{1}{\lambda + 0.08\beta} - \frac{0.035}{\beta^3 + 1} \quad (3.4)$$

Often it is modelled with use of the pre-calculated $C_p(\omega_m, V_w, \beta)$ surface. Any point on the surface is a static equilibrium point and corresponds to a certain wind speed and blade angle. In a real wind turbine, the blade angle has changes constantly due to wind variations in order to maintain an optimum angle. However, this deviation is very small. Therefore in simulations, zero degrees are sufficient to represent the optimum pitch angle for the lower wind speeds [72].

3.2.2. Shaft model

The shaft model is also known as the drive-train model. Four types of drive-train model exist in the literature [80], which are six-, three-, two- and one-mass drive train models. A basic six-mass drive-train model is constituted of six inertias, i.e. three for the blades and the rest are respectively for the hub, gearbox and generator. If the blades and the hub are combined as the wind turbine rotor, a three-mass drive-train model is derived. A two-mass model is obtained by integrating the gearbox inertia with either the turbine rotor or the generator rotor, as shown in Figure 3.5. The shaft with higher stiffness should be merged during the transformation leaving the other shaft to be considered for the two-mass model. The two inertias interact with the equivalent shaft stiffness K_s and the mutual damping D_s . If all the inertias in the drive-train system are taken as a single

rotation mass, the lumped model is obtained. Referring all the mechanical quantities to the turbine rotor, the equations for the lumped and two-mass shaft model are described as (3.5) and (3.6).

Equation of the lumped shaft model

$$J_r \frac{d\Omega_m}{dt} = T_a - T_e - D_r \Omega_m \quad (3.5)$$

Where

J_r = Total inertia of the rotational system

T_e = Electromagnetic torque of the generator

D_r = Damping coefficient of the rotational system

Ω_m = Mechanical speed of the rotor

Equation of the two-mass shaft model are described as

$$\begin{aligned} J_T \frac{d\Omega_T}{dt} &= T_a - T_s - D_T \Omega_T \\ J_G \frac{d\Omega_G}{dt} &= T_s - T_e - D_G \Omega_G \\ T_s &= K_s \theta_s + D_s (\Omega_T - \Omega_G) \\ \frac{d\theta_s}{dt} &= \Omega_T - \Omega_G \end{aligned} \quad (3.6)$$

Where

J_T, J_G =Inertias of the turbine rotor and the generator rotor

Ω_T, Ω_G =Mechanical speeds of the turbine rotor and generator rotor

D_T, D_G =Self damping of the turbine rotor and the generator rotor

T_s =Reaction torque from the low-speed shaft

D_s, K_s =Shaft mutual damping and stiffness (spring constant)

θ_s =Twisting angle between the generator rotor and the turbine rotor

The reaction torque T_s is induced in dynamic conditions due to the difference between Ω_T and Ω_G , and the resulting twisting angle θ_s . The total mechanical damping in the 2-mass model and lumped model is given by

$$D_r = D_T + D_G \quad (3.7)$$

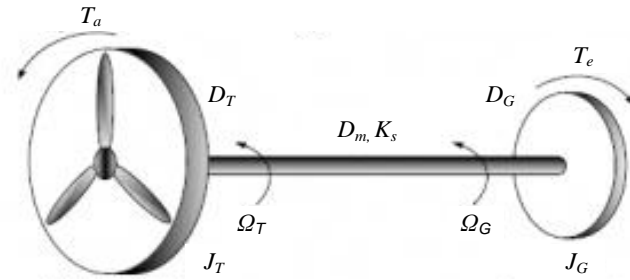


Figure 3.5 Two-mass wind turbine shaft system

The two-mass shaft model is mostly recommended in the study of transient stability analysis [72, 80] since it characterises the shaft torsional modes. This is implemented in the thesis for (a) detailed model analysis, (b) controller tuning and (c) controller coordination. No further simplification or complexity of the mechanical system is used due to the following reasons.

- 1) The complexity of the model must comply with the purpose of investigation. The focus of this work is on system stability and drive-train reliability and its correlations with various control-loops and control strategies. On one hand, the oscillations present during shaft relaxation (during grid fault) may destabilise the system. On the other hand, a very common reason leading to shaft fatigue is stresses exerted on the gearbox due to constant twisting. Therefore, oscillations and the twisting torque transmitted along the shaft must be shown by the model.
- 2) For a stiffness $K_s \cong 3pu/el.rad$, the magnitude of torsional oscillations will be very small and can be ignored [72]. However, for DFIG wind turbines, the shaft stiffness is very low ($0.7pu/el.rad$ in this thesis), and the induced resonance frequency (about 2.5 Hz) cannot be shown by the lumped model.

- 3) The twisting effect is mostly imposed by the low speed shaft, as the stiffness between the gear box and generator is very high [78]. Hence a three-mass system is not necessary.
- 4) Six-mass shaft model makes little difference in studying the transient stability of the wind turbine generator system [80]. It is useful in analyzing the torque sharing among the three blades. For the same reason, the tower effect can also be neglected. With a very high stiffness, it has almost no influence on the electro-magnetic interactions and thus the twisting torque [72].

3.3. Steady state DFIG model

The DFIG wind turbine is developed in PSCAD, where the standard library module for the wound-rotor induction machine can be used. Mathematical models are discussed in order to help understand the operating principles of the DFIG machine. The electric parameters of the stator and rotor are presented as phasors:

$\bar{V}_s, \bar{V}_r =$ Supplied stator and rotor voltages

$\bar{E}_s, \bar{E}_r =$ Induced stator and rotor emf

$\bar{I}_s, \bar{I}_r =$ Induced stator and rotor currents

$\bar{\psi}_s, \bar{\psi}_r =$ The stator and rotor fluxes

The machine parameters are given as

$R_s, R_r =$ Stator and rotor resistances [Ω]

$L_{\sigma s}, L_{\sigma r}, L_m =$ Stator and rotor leakage inductances, magnetic inductance [H]

$N_s, N_r =$ Number of turns in stator and rotor windings

$\omega_s, \omega_r =$ Angular frequencies of the electric quantities in stator and rotor windings [rad/s]

$\omega_m =$ Rotational speed of the rotor windings in electric unit [rad/s]

$\omega_r = \omega_s - \omega_m =$ Slip frequency or angular frequency of the voltages and currents in the rotor windings [rad/s]

The slip is defined as

$$s = \frac{\omega_s - \omega_m}{\omega_s} \quad (3.8)$$

Therefore, slip frequency is given by

$$\omega_r = s\omega_s \quad (3.9)$$

3.3.1. Steady state equivalent circuit

Assuming that the magnetic resistance is very large and thus it can be neglected, the equivalent circuit of the machine is represented in Figure 3.6.

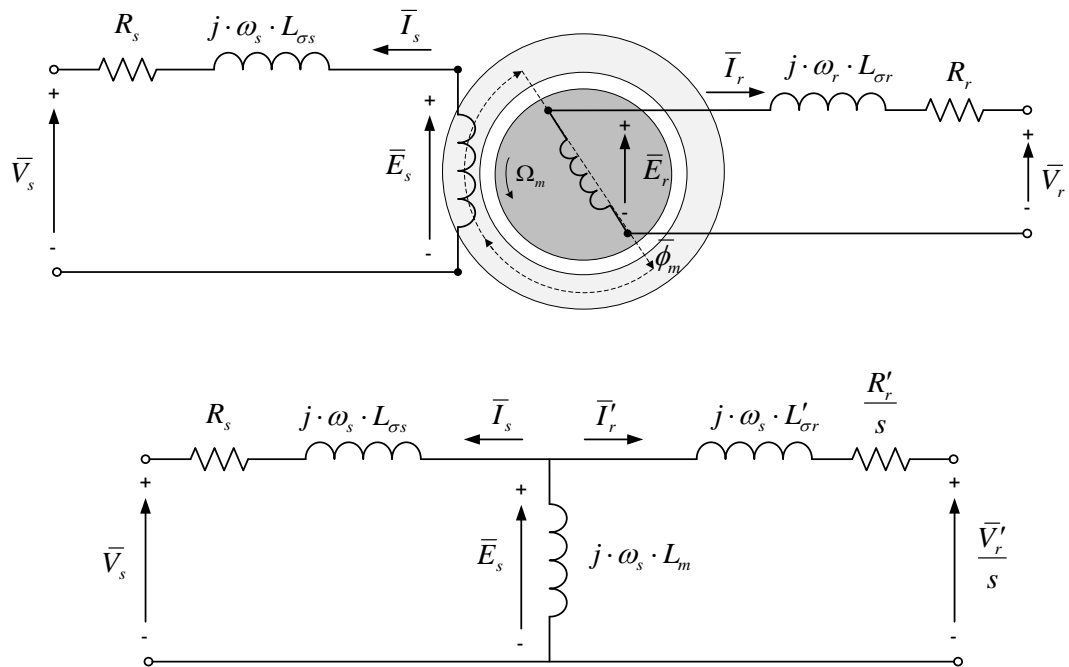


Figure 3.6 Steady state equivalent circuit of the DFIG – one phase representation [73]

The induced voltage in the stator and rotor winding are described as

$$\bar{E}_s = \sqrt{2} \pi \kappa_s N_s f_s \bar{\phi}_m \quad (\text{V}_{\text{rms}}) \quad (3.10)$$

$$\bar{E}_r = \sqrt{2} \pi \kappa_r N_r f_r \bar{\phi}_m \quad (\text{V}_{\text{rms}}) \quad (3.11)$$

Where

f_s, f_r = Stator and rotor electric frequencies [Hz]

$\bar{\phi}_m$ = Magnetizing flux [Wb]

κ_s, κ_r = Winding factors of the stator and rotor

The rotor and stator induced voltages are related by a factor n . In general case, it can be approximated that $\kappa_s \approx \kappa_r$. At standstill condition, i.e. $s = 1$ we have

$$n = \frac{\bar{E}_r}{\bar{E}_s} = \frac{N_r}{N_s} \quad (3.12)$$

The rotor electric quantities referred to the stator windings, can be derived as

$$\begin{aligned} \bar{E}'_r &= \bar{E}_s = \bar{E}_r / n \\ \bar{V}'_r &= \bar{V}_r / n \\ \bar{I}'_r &= n \cdot \bar{I}_r \end{aligned} \quad (3.13)$$

Similarly, the machine parameters referred to the stator are

$$\begin{aligned} R'_r &= R_r / n^2 \\ L' &= L / n^2 \end{aligned} \quad (3.14)$$

From now on, if not specified, all the quantities in the equations are referred to in the stator windings. However, the superscript is eliminated for simplification.

3.3.2. Steady state power flow

The positive directions of power flow for each circuit branch are shown in Figure 3.7, where the generator convention is used.

$$P_{mech} = T_e \Omega_m = T_e \frac{\omega_m}{pp} \quad (3.15)$$

Ω_m = Mechanical speed at the high speed shaft [rad/s]

pp = Number of pole pairs

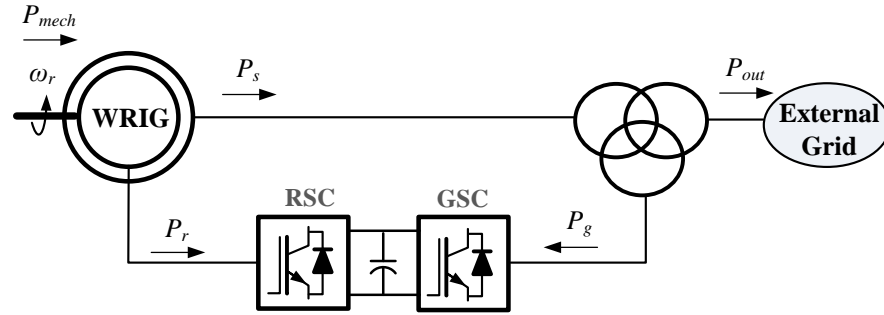


Figure 3.7 Directions of the power flow in the DFIG model

If the power loss in the machine windings is neglected, the power in stator and rotor has the following relationship:

$$P_{mec} \cong P_s + P_r \quad (3.16)$$

$$P_r \cong -sP_s \quad (3.17)$$

Combining equations (3.15) and (3.17), the stator and rotor power can be represented as

$$\begin{aligned} P_s &\cong T_e \frac{\omega_s}{pp} \\ P_r &= -sT_e \frac{\omega_s}{pp} \end{aligned} \quad (3.18)$$

Note that the rated power of a DFIG is defined as the stator rated power, i.e. the power generated when it is operating at the synchronous speed [73].

3.4. Dynamic DFIG model

3.4.1. Space vector representation

The space vector theory states that the three phase time-varying magnitudes can be presented in a compact form, i.e. a single rotating space vector [73]. Figure 3.8 shows a full schematic diagram of the reference frames of the DFIG. The three phase winding distributions of the stator and rotor are shown assuming one pole pair. In the figure, there are three reference frames, and each has two orthogonal axes:

- The stationary reference frame $\alpha - \beta$, where the α -axis is fixed to the stator winding A.
- The rotor reference frame $d^r - q^r$, where the d^r -axis is fixed to the rotor winding A and it spins in an anti-clockwise direction at the speed ω_m .
- The excitation frame $d - q$. This is the synchronous rotation frame. It rotates with the same speed as the voltages, currents and flux vectors.

The relative positions with respect to stationary frame are represented by different angles:

μ = Angle of the excitation frame with respect to the stationary frame

θ_r = Angle of the rotor winding with respect to the stationary frame

$\gamma = \mu - \theta_r$ = Angle of the excitation frame with respect to the rotor frame

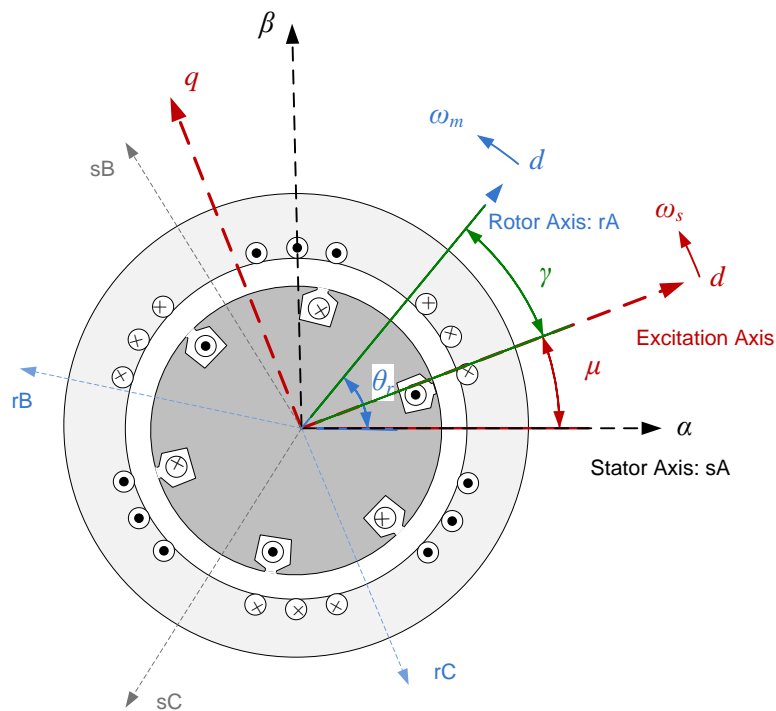


Figure 3.8 Reference frames with transformation angles of DFIG [73, 81]

Usually, the three phase sinusoidal electrical parameters are measured from the stator or rotor, and then the quantities should be converted to a common reference frame, for the purpose of implementing vector control.

The DFIG machine dynamic equations represented in the excitation reference frame can be described by (3.19) [79]. Generator convention is considered, i.e. positive current and power direction is from machine to grid.

$$\begin{aligned}
 \bar{V}_s^e &= -R_s \bar{I}_s^e + \frac{d\bar{\psi}_s^e}{dt} + j\omega_s \bar{\psi}_s^e \\
 \bar{V}_r^e &= -R_r \bar{I}_r^e + \frac{d\bar{\psi}_r^e}{dt} + j\omega_r \bar{\psi}_r^e \\
 \bar{\psi}_s^e &= -L_s \bar{I}_s^e - L_m \bar{I}_r^e \\
 \bar{\psi}_r^e &= -L_r \bar{I}_r^e - L_m \bar{I}_s^e
 \end{aligned} \tag{3.19}$$

Here the transformer reactance $L_{tr,12}, L_{tr,13}$ and the rotor converter coupling inductance L_{rsc} need to be added in series with the generator and rotor leakage inductance respectively, and therefore the inductance values in equation (3.19) are actually:

$$L_s = L_{\sigma s} + L_m + L_{tr,12} + L_{tr,13} = \text{Stator self-inductance}$$

$$L_r = L_{\sigma r} + L_m + L_{rsc} = \text{Rotor self-inductance}$$

The superscripts 'e' denotes the excitation reference frame, 's' is for the stationary (stator) reference frame and 'r' is for the rotor reference frame.

3.4.2. Dq0 transformation

Stator-flux orientation is adopted [82], where the d-axis of the excitation frame is aligned with the stator flux.

$$\begin{bmatrix} X_d^e \\ X_q^e \\ X_0^e \end{bmatrix} = k \begin{bmatrix} \cos \theta & \cos(\theta - \frac{2\pi}{3}) & \cos(\theta + \frac{2\pi}{3}) \\ -\sin \theta & -\sin(\theta - \frac{2\pi}{3}) & -\cos(\theta + \frac{2\pi}{3}) \\ \frac{1}{2} & \frac{1}{2} & \frac{1}{2} \end{bmatrix} \cdot \begin{bmatrix} X_a^{s(r)} \\ X_b^{s(r)} \\ X_c^{s(r)} \end{bmatrix} \tag{3.20}$$

X = Electric variables of the stator or rotor

θ = Transformation angle, the angle that the original reference frame where the electrical quantities are measured (stator or rotor frame)

Usually in a real controller, this transformation is carried out in two steps, which are known as the Clark transformation (3.21) and the Park transformation (3.22). The former is used to convert the three phase magnitudes into two phase magnitudes and is performed in the stationary frame, i.e. $\bar{X}^s = X_\alpha + jX_\beta$. The latter is for representing the quantity in another reference frame, by projecting the vector on the two orthogonal axes of the new frame, e.g. $\bar{X}^e = X_d + jX_q$.

$$\begin{bmatrix} X_\alpha^s \\ X_\beta^s \\ X_0^s \end{bmatrix} = k \begin{bmatrix} 1 & -1/2 & -1/2 \\ 0 & \sqrt{3}/2 & -\sqrt{3}/2 \\ 1 & 1/2 & 1/2 \end{bmatrix} \cdot \begin{bmatrix} X_a^s \\ X_b^s \\ X_c^s \end{bmatrix} \quad (3.21)$$

$$\begin{bmatrix} X_d^e \\ X_q^e \\ X_0^e \end{bmatrix} = \begin{bmatrix} \cos \theta & \sin \theta & 0 \\ -\sin \theta & \cos \theta & 0 \\ 0 & 0 & 1 \end{bmatrix} \cdot \begin{bmatrix} X_\alpha^s \\ X_\beta^s \\ X_0^s \end{bmatrix} \quad (3.22)$$

The coefficient k is the scaling factor which can either be $\sqrt{2/3}$ for power invariant transformation or $2/3$ for magnitude invariant transformation. The latter is adopted in this thesis so that the modulus of the d-q quantities is consistent with the peak phase value. The transformation angle θ for stator and rotor quantities are different. For stator quantities, $\theta = \mu$, while for the rotor quantities $\theta = \gamma$.

In order to derive the angle μ , the relationship between the stator flux and the stator voltage should be known, from:

$$\bar{\psi}_s = \frac{(\hat{V}_s + R_s \hat{I}_s)}{j\omega_s} \cdot e^{j\omega_s t} \quad (3.23)$$

where \hat{V}_s and \hat{I}_s are the stator voltage and current in peak values. As the stator resistance is much smaller compared with the impedance ($R_s \ll \omega_s L_s$), the associated voltage drop can be ignored. This approximation is especially true for larger machines. Therefore the magnitude of stator flux is:

$$|\psi_s| \approx \frac{\sqrt{2}V_s}{\omega_s} \quad (3.24)$$

with V_s the stator phase rms voltage. The stator voltage vector leads the stator flux vector by $\pi/2$ and therefore it is aligned with the q-axis. The angle of the stator voltage is measured by a Phase Locked Loop (PLL) in the stationary reference frame. $\pi/2$ is then subtracted to derive the angle μ .

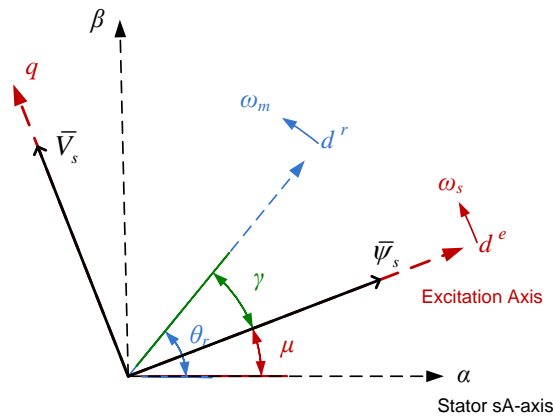


Figure 3.9 Stator flux orientation

Therefore, the vectors satisfy the following relationship

$$X_\alpha^s = X_\alpha, \quad v_{s-d}^e = 0, \quad v_{s-q}^e = \hat{V}_s, \quad \psi_{s-d}^e = \psi_s, \quad \psi_{s-q}^e = 0$$

where ' $\hat{\cdot}$ ' denotes the peak values

3.5. Implementation of the vector control

3.5.1. Rotor-side converter control

Independent control of electric torque and reactive power control is performed. This is achieved by regulating the rotor d-q current separately according to equation (3.25). The components used here are referred to the excitation frame [82, 83].

$$\begin{aligned} T_e &= \frac{3}{2} p p \frac{L_m}{L_s} \psi_s i_{r-q} \\ Q_s &= -\frac{3}{2} \frac{\sqrt{2}V_s L_m}{L_s} i_{r-d} - \frac{3}{2} \frac{\sqrt{2}V_s}{L_s} \psi_s \end{aligned} \quad (3.25)$$

There is a linear-dependency between the electric torque and q-component rotor current, and between the reactive power and the d-component rotor current. The second term in the reactive power equation is due to the effects of the stator flux induced emf. Substituting this term by the voltage in equation (3.24), the reactive power equation can be represented as

$$Q_s = -\frac{3}{2} \frac{\sqrt{2} L_m}{L_s} V_s \cdot \left(i_{r-d} + \frac{\psi_s}{L_m} \right) \quad (3.26)$$

$$\Rightarrow i_{r-d} = -K \cdot Q_s - \frac{\psi_s}{L_m}$$

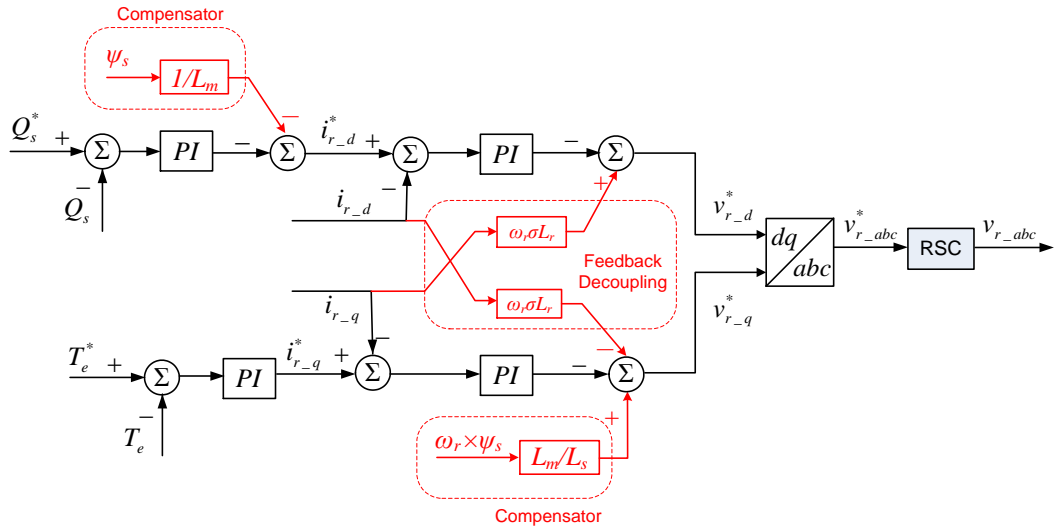


Figure 3.10 Generic control of the rotor-side converter

The rotor currents injected by the RSC are regulated by controlling the magnitude and phase of the output voltage, which is based on equation (3.27). Stator flux transients are neglected here ($d\psi_s/dt = 0$), then

$$v_{r-d}^* = -R_r i_{r-d} - \sigma L_r \frac{di_{r-d}}{dt} + \omega_r \sigma L_r i_{r-q}$$

$$v_{r-q}^* = -R_r i_{r-q} - \sigma L_r \frac{di_{r-q}}{dt} - \omega_r \sigma L_r i_{r-d} + \omega_r \frac{L_m}{L_s} \psi_s \quad (3.27)$$

where $\sigma = 1 - \frac{L_m^2}{L_s L_r}$ is the leakage coefficient. The first two terms are related to the control signal. The third terms are associated with the cross-coupling effect from the

orthogonal axis. The fourth term can be added at the controller to compensate the effect of the stator flux disturbances. However, the PI controllers can also eliminate this coupling effect.

3.5.2. Grid-side converter control

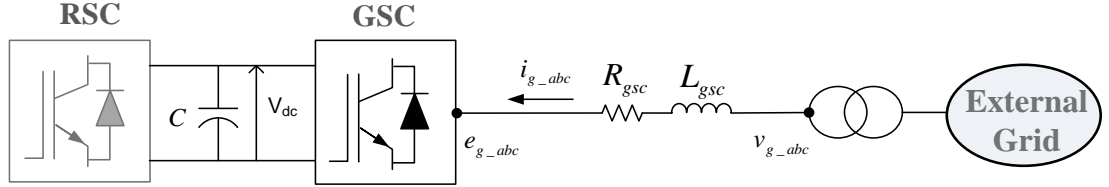


Figure 3.11 Circuit construction of the grid-side converter

The three phase equations of the grid-side circuit can be found as

$$\begin{aligned}
 v_{g-a} &= R_{gsc} i_{g-a} + L_{gsc} \frac{di_{g-a}}{dt} + e_{g-a} \\
 v_{g-b} &= R_{gsc} i_{g-b} + L_{gsc} \frac{di_{g-b}}{dt} + e_{g-b} \\
 v_{g-c} &= R_{gsc} i_{g-c} + L_{gsc} \frac{di_{g-c}}{dt} + e_{g-c}
 \end{aligned} \tag{3.28}$$

Transforming the equation (3.28) to the synchronous rotating frame, the d-q representation can be derived as

$$\begin{aligned}
 e_{g-d} &= -R_{gsc} i_{g-d} - L_{gsc} \frac{di_{g-d}}{dt} + \omega_s L_{gsc} i_{g-q} + v_{g-d} \\
 e_{g-q} &= -R_{gsc} i_{g-q} - L_{gsc} \frac{di_{g-q}}{dt} - \omega_s L_{gsc} i_{g-d} + v_{g-q}
 \end{aligned} \tag{3.29}$$

This is similar to the RSC control, equation (3.29) includes the controlled terms, cross-coupling terms and the grid voltage coupling terms.

The voltage vector is aligned with the q-axis of the synchronous rotating frame, as depicted in Figure 3.12. Hence, the d-q voltage components are

$$v_{g-d} = 0, \quad v_{g-q} = \hat{V}_g.$$

The grid voltage angle can be measured by PLL, then $\pi/2$ is subtracted to find the transformation angle ε (the angle of the d-axis with respect to the α axis).

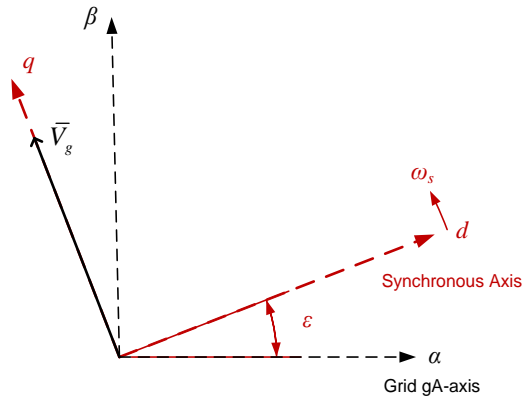


Figure 3.12 Reference frames with grid voltage orientation

The active power in the converter can be represented as

$$P_{conv} = \frac{3}{2} v_{g-q} i_{g-q} = V_{dc} i_{dc} \quad (3.30)$$

As can be seen, the dc-link voltage is regulated by the q-current component. A general GSC control structure is shown in Figure 3.13.

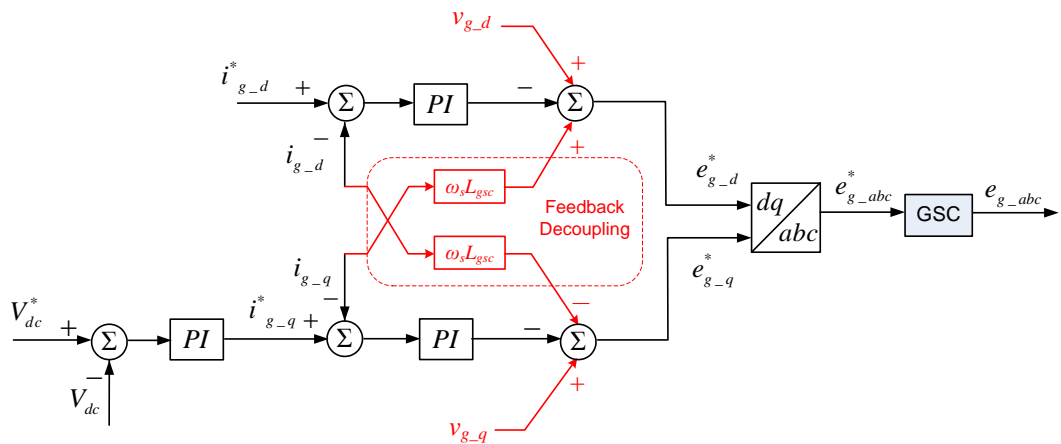


Figure 3.13 Generic control of the grid-side converter

3.6. Converter and dc-link model

Two converter models are developed, which are depicted in Figure 3.14. The upper one is the full switched model (FSM), in which all the IGBT switches are modelled with a PWM

frequency of 4.5 kHz. This model can provide a deeper insight of the converter dynamics over a short time scale. The lower graph shows the switch-averaged model (SAM), where the converter is presented as two voltage sources coupled through a dc-link. The coupling is based on the power flow between the RSC and GSC. The current disturbances from the voltage source inverters will charge or discharge the dc-capacitor. The SAM is suitable for inspecting the electrical or mechanical dynamics over a longer time scale without the disturbance from the switching noise.

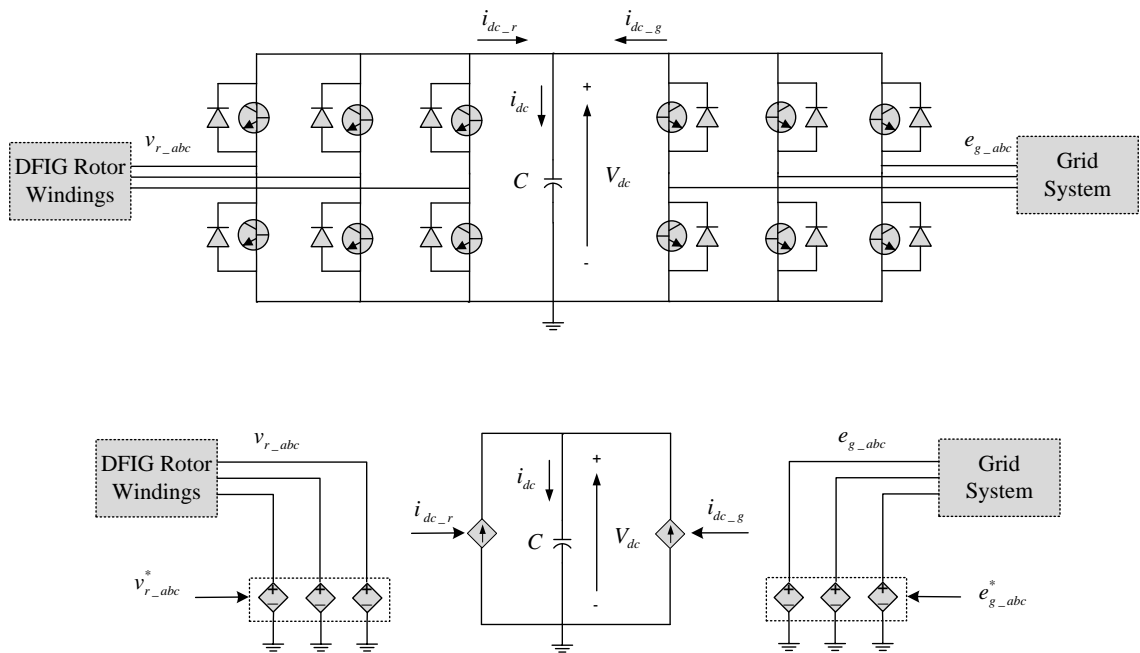


Figure 3.14 Schematic diagram of the full-switched and switch-averaged converter models

3.7. Wind turbine control

3.7.1. Operating curve description

In normal operation, the wind turbine control level mainly has two tasks: providing the reference signal (electric torque, or current demand) for the DFIG control level and modifying the blade pitch angle to retain the speed or power within their limits. For the lower wind speed region the pitch controller is saturated at 0 degrees. An optimum torque-speed curve is followed. There are several important operating points (refer to Figure 3.15):

- Minimum operating speed $\Omega_{m,min} = 7.7rpm$ –This is the minimum speed for the normal operation of the wind turbine. For a DFIG wind turbine, this speed is restricted to 25% below the synchronous speed in order to avoid the RSC voltage saturation.
- Synchronous operating speed $\Omega_{m,min} = 10.3rpm$ – The rotor circuit delivers nearly no power at this speed as the induced rotor voltages are closed to zero.
- Nominal operating speed $\Omega_{m,nom} = 12.1rpm$ – Rated power is generated at this point. This speed is generally half-way from the synchronous speed to the maximum speed.
- Maximum operating speed $\Omega_{m,max} = (1 + 15\%)\Omega_{T,nom} = 13.9rpm$ –This should be no larger than 30% above the synchronous speed, as illustrated in Table 3.1.This limit is designed due to noise restriction or mechanical stress limit of the wind turbine [72].

Parameter	Value	Unit
Nominal turbine power P_{nom}	5	MW
Turbine rotor radius R	63	m
Nominal wind speed V_w	12	m/s
Cut-in wind speed	4	m/s
Variable speed range $\Omega_{T,min} - \Omega_{T,nom}$	7.7– 12.1 (+15%)	rpm
Optimum tip-speed ratio λ_{opt}	6.3	-
Maximum power coefficient $C_{p,max}$	0.44	-
Air density ρ	1.1225	kg/m ³

Table 3.1 Aerodynamic parameters of 5MW wind turbine (data based on Repower 5MW wind turbine [84])

The wind turbine will be halted if the rotor is below the minimum speed or above the maximum speed. The turbine extracts maximum power from the wind when it is working between the minimum and the nominal speed. In normal operation, the pitch control will be engaged when the rotor speed reaches the nominal value in order to restrict it from increasing further as the wind increasing. The region between the nominal and maximum speed is left for safety reasons. This provides the controller some flexibility to counteract load fluctuations.

It should be noted that the nominal (or rated) power of the wind turbine is different from that of the DFIG machine. As mentioned before, the nominal power of the doubly-fed induction generator is the power produced solely by the stator at the synchronous speed. However, when it comes to the wind turbine based on a DFIG, the nominal power is referred to as the power produced by both the stator and rotor when it is working with the nominal rotor speed.

For a 4.5 MW DFIG machine, the theoretical rated power of the wind turbine should include the rotor generated power when working at the nominal speed

$$P_{WT, rated} = P_s \cdot (1 + s) = 4.5MW \times (1 + 0.17) \approx 5.27MW \quad (3.31)$$

Therefore it allows a total loss due to the electrical system up to 5%, in order to achieve an actual wind turbine output power of approximately 5MW².

The torque equation (3.1) is re-arranged as a function of the rotor speed:

$$T_{a, opt} = \frac{\rho}{2} \pi R^5 \frac{C_{p, opt}}{\lambda_{opt}^3} \Omega_m^2 \quad (3.32)$$

Here the tip-speed ratio is fixed at the optimum value λ_{opt} . The mechanical speed Ω_m is adopted here to represent the rotating speed of the lumped shaft model i.e. $\Omega_m = \Omega_T = \Omega_G$. The torque coefficient referred to the turbine rotor is expressed as

$$k_{opt} = \frac{\rho}{2} \pi R^5 \frac{C_{p, opt}}{\lambda_{opt}^3} \quad (3.33)$$

The operating curve is depicted in Figure 3.15. The blue solid curve (T_{m1}) is mechanical torque referred to the generator rotor. In a real wind turbine, the actual mechanical torque produced at the same rotor speed is smaller due to mechanical damping. Therefore, the torque demand should be adjusted as:

$$T_e^* = k_{opt} \Omega_m^2 - D_r \Omega_m \quad (3.34)$$

² Total electrical system losses obtained from personal correspondence with the Wind Energy Research Group at Strathclyde.

The corrected operating curve T_{m3} is depicted in a green dash-dot-line.

The generic strategy curve has some drawbacks when the turbine is working near the edge of its optimum region. Large torque transients may occur constantly due to the deep slope. In practical conditions, a modified torque – speed curve (T_{m2}) is usually implemented as depicted with the red dashed line. Two ramp sections are inserted instead of vertical lines. The sacrifice is that the maximum power region is reduced.

Another way to solve this difficulty is discussed in [74]. The controller is illustrated in Figure 3.16, where a speed reference is generated from the optimum power-speed characteristic curve with the power measured from the grid. A PI controller is used to generate the reference power to the DFIG level from the rotor speed error. Whenever the rotor speed changes, the DFIG will modify the generator power to eliminate the error. In this way, it keeps the turbine tracking the characteristic curve. Since no steep slope exists in the strategy curve, transients can be avoided. The control parameters should be adjusted for different operating regions in order to achieve a good performance for all working regions.

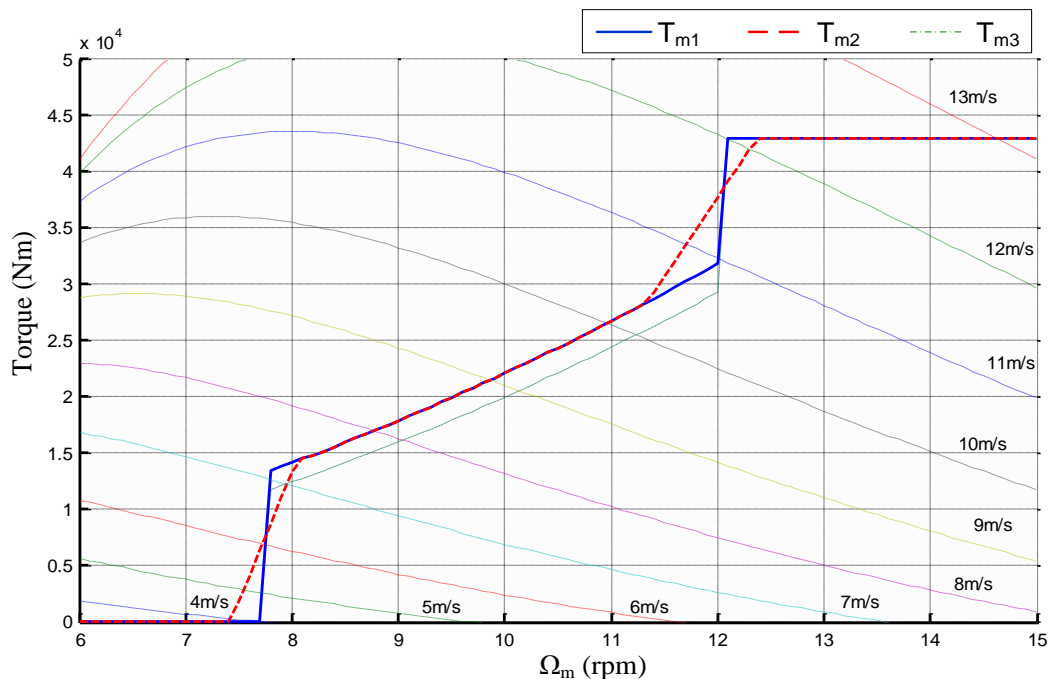


Figure 3.15 Operational strategies of a 5 MW wind turbine.

All the control methods discussed above do not need wind speed measurement. The drawback of the last method is relatively slow response. As the reference rotor speed is obtained from the measured power, both of the reference and feedback signals are varying. Thus the power cannot reach the desired value immediately as the wind speed changes.

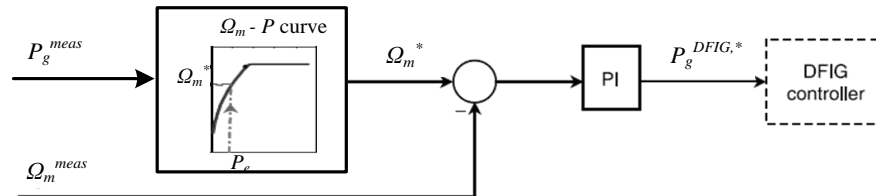


Figure 3.16 Alternative control method for the tracking the characteristic curve [74]

The key factor for tracking the maximum power is to find the optimum rotor speed. In other words, an optimum tip-speed ratio is required to get maximum power coefficient C_p . Therefore, instead of using the torque – speed curve, one can measure the effective wind speed and send an optimum rotor speed reference to the DFIG control level. In this case the rotor speed is directly regulated by the current of the rotor-side converter. The challenge for this method is measuring the effective wind speed. Accuracy of the sensor will significantly affect the turbine's output efficiency.

3.7.2. Per unit transformation of the mechanical parameters

In PSCAD v4.2.1, the DFIG wind turbine model adopts different units for the component parameters and state variables. For example, most of the machine parameters are set in per unit, while some of the outputs such as the current, voltage and power are in real values. Some internal output signals such as torque and rotor speed are in per unit. One should be very cautious about these differences when evaluating the system and controller performances. Especially before tuning the controller, it is necessary to do the unit transformation first in order to make all the parameters consistent. This section provides the per unit transformation for the mechanical system. The electric parameter transformations are given in the Appendix A.

The per-unit values of the wind turbine mechanical parameters are listed in Table 3.2. The mechanical damping values are adopted from [80]. The optimum torque coefficient used

in the characteristic curve is the same as Strathclyde University's 5-MW wind turbine model.

The following base values are referred to the generator rotor (high-speed shaft).

$$\Omega'_{m,base} = \frac{\omega_s}{pp} = \frac{314.6rad / s}{3} = 104.72rad / s$$

$$T'_{m,base} = \frac{P_{base}}{\Omega'_{m,base}} = \frac{4.5MW}{104.72rad / s} = 42971.8Nm$$

$$J'_{base} = \frac{P}{\frac{1}{2}\Omega_m^2} = 820.70 [Nm / (rad / sec)]$$

$$K'_{s,base} = D'_{base} = \frac{T'_{m,base}}{\Omega'_{m,base}} = \frac{42971.8Nm}{104.7rad / s} = 410.35$$

$$k'_{opt,base} = \frac{T'_{m,base}}{\Omega'^2_{m,base}} = \frac{P_{base}}{\Omega'^3_{m,base}} = \frac{4.5MW}{(2\pi \times 50 / 3)^3} = 3.92$$

Parameter	Value	Unit
Turbine rotor inertia H_T	3	s
Generator rotor inertia H_G	0.5	s
Spring constant K_S	0.7	p.u./el·rad
Turbine rotor self-damping D_T	0.02	p.u.
Generator rotor self-damping D_G	0.031	p.u.
Mutual damping between two mass D_S	3	p.u.
Optimum torque coefficient k_{opt}	0.55	p.u.

Table 3.2 Turbine mechanical parameters

The base values referred to the turbine rotor (low speed shaft) are related to the generator rotor base quantities by a gearbox ratio G :

$$\begin{aligned} \Omega_{m,base} &= \Omega'_{m,base} / G & D_{base} &= G^2 \cdot D'_{base} \\ T_{m,base} &= G \cdot T'_{m,base} & K_{s,base} &= G^2 \cdot K'_{s,base} \\ J_{base} &= G^2 \cdot J'_{base} & k_{opt,base} &= G^3 \cdot k'_{opt,base} \end{aligned}$$

All the real values are calculated in Appendix A. Several important operating points on the wind turbine strategy curve, with the per-unit values, are listed in Table 3.3.

Operating points	Mechanical speed	Rotor speed	Torque
	Ω_m [rpm]	[pu]	T_m [pu]
Minimum	7.7	0.75	0.309
Synchronous	10.3	1	0.55
Nominal	12.1	1.17	0.753 - 1
Maximum	13.9	1.35	1

Table 3.3 Important operating points on the strategy curve

3.7.3. Pitch control strategies

This section reviews the most common pitch control strategies mentioned in the literature. Figure 3.17 shows the structure of a general pitch controller. The controller input signal X can be a mechanical value ω_r [85, 86], electric value P_e [74], or a combination of both [77, 87]. For a fixed-speed wind turbine, total generated power P_e will be used and for variable speed wind turbines, the rotor speed Ω_m is used. It is suggested that the torque and rotor speed errors could be combined as the input of the pitch controller, which allows the pitch to vary quickly when the wind speed rises rapidly towards the rated value [87].

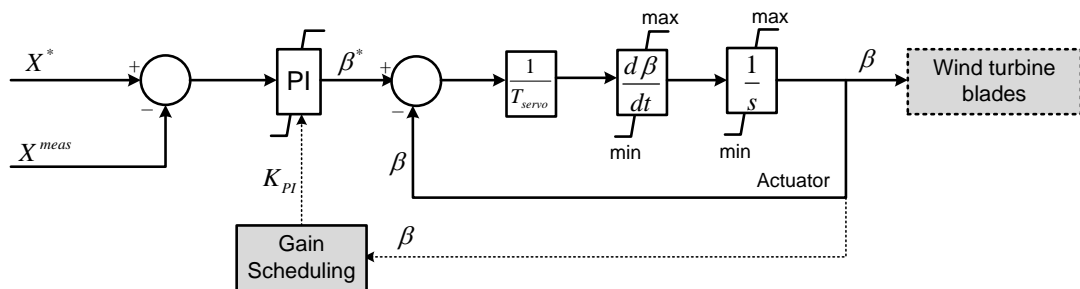


Figure 3.17 Pitch controller with actuator and gain scheduling

The common pitch controllers used by industry today are PI or PID. The PID controller with an derivative term can improve the system's error sensitivity [72, 88]. This method has been adopted by the U.S. industry as a standard pitch control strategy. Some authors think that it is sufficient to use proportional-only (P) controller as fully eliminating the error is not practical due to the constantly varying wind speed [79]. The performances of all the three controllers are evaluated in Chapter 4.4.

The bandwidth of pitch control should be selected carefully. Although higher bandwidths can provide a faster response, there is a risk of exciting various turbine modes and destabilizing the system. NREL [89] estimates the pitch controller loop bandwidth should be in the range of 2rad/s (0.32Hz) and 0.2 rad/s (0.032Hz). This bandwidth has been adopted by them for experimental testing. Riso [86] suggests a controller setting of 0.1Hz frequency and 0.6 damping. In [79], a sampling frequency of 2Hz is used for the pitch controller, indicating a control bandwidth lower than 1Hz. Therefore, the general pitch controller bandwidths are in magnitudes of 0.01Hz to 1Hz. For a specific design, one should take other factors into consideration, such as the turbine operation modes, and the coupling with other control loops. A detailed analysis will be presented in Chapter 5.

The effect of an actuator is to introduce a lag between the commanded pitch from the PI controller and the actual pitch angle. Like a low-pass filter, it can also remove the frequencies that destabilise the system [89]. A 0.2s time constant is suggested for a general actuator in this kind of application [86, 89]. Limitation of the pitch rate should also be considered due to design restriction and actuator fatigue. The maximum pitch rate is within 3 %s – 10 %s depending on the turbine size [79]. However, this limit is designed for extreme conditions and is not suitable for normal operation.

3.8. Conclusions

In this Chapter, the general structure of the DFIG wind turbine has been briefly introduced with the overall control systems. Three control levels are distinguished with the highest level interacting with the wind farm, and the most inner level implementing converter control. General models for mechanical and electrical sub-assemblies are given. It has been discussed that the 2-mass shaft system is appropriate to be implemented in this work for investigating stability problems and controller correlations. The steady state DFIG model has been presented with an equivalent circuit. The dynamic model with

different reference frames is introduced, based on which the stator flux orientation method is implemented for the rotor-side converter control, while the grid-voltage orientation is implemented for the grid-side converter control. A full switched and a simplified back-to-back converter model are presented. The former is better used for detailed analysis of fast electric transients, while the latter is suitable for investigating slower system dynamics. Several control strategies of the wind turbine are explained using the operation curves. A general pitch controller is discussed with respect to different reference quantities, as well as to the settings of actuator, general bandwidths and rate limitation.

Chapter 4. Mathematical Modelling for Detailed Analysis of the Control Systems

The general control structure of the DFIG converter and the wind turbine has been introduced in Chapter 3. Considering the controllers' bandwidth, this can be separated into the electric inner control loops (d-q current control), the electric outer control loops (active, reactive power control and the dc-link control), and the mechanical control loop (pitch or rotor speed control). In this Chapter, detailed analysis for each control system will be presented. Mathematical models are investigated using transfer functions and using control block diagrams. The dc-link and the mechanical control loops are more complex than the current and power control loops due to the non-linearity of their plant models. One contribution of this thesis over the state of art when this research was started is that detailed presentation and analysis for the dc-link and mechanical control system are provided. Using the transfer functions of these loops, the controllers are tuned to satisfy desired system specifications.

4.1. Power and current control loops

4.1.1. Mathematical model of the RSC current loops

The rotor-side converter power and voltage equations in the synchronous reference frame (3.25) and (3.27) are re-written here:

$$\begin{aligned} T_e &= \frac{3}{2} pp \frac{L_m}{L_s} \psi_s i_{r-q} \\ Q_s &= -\frac{3}{2} \frac{\sqrt{2} V_s L_m}{L_s} i_{r-d} - \frac{3}{2} \frac{\sqrt{2} V_s}{L_s} \psi_s \end{aligned} \quad (4.1)$$

$$\begin{aligned} v_{r-d}^* &= -R_r i_{r-d} - \sigma L_r \frac{di_{r-d}}{dt} + \omega_r \sigma L_r i_{r-q} \\ v_{r-q}^* &= -R_r i_{r-q} - \sigma L_r \frac{di_{r-q}}{dt} - \omega_r \sigma L_r i_{r-d} + \omega_r \frac{L_m}{L_s} \psi_s \end{aligned} \quad (4.2)$$

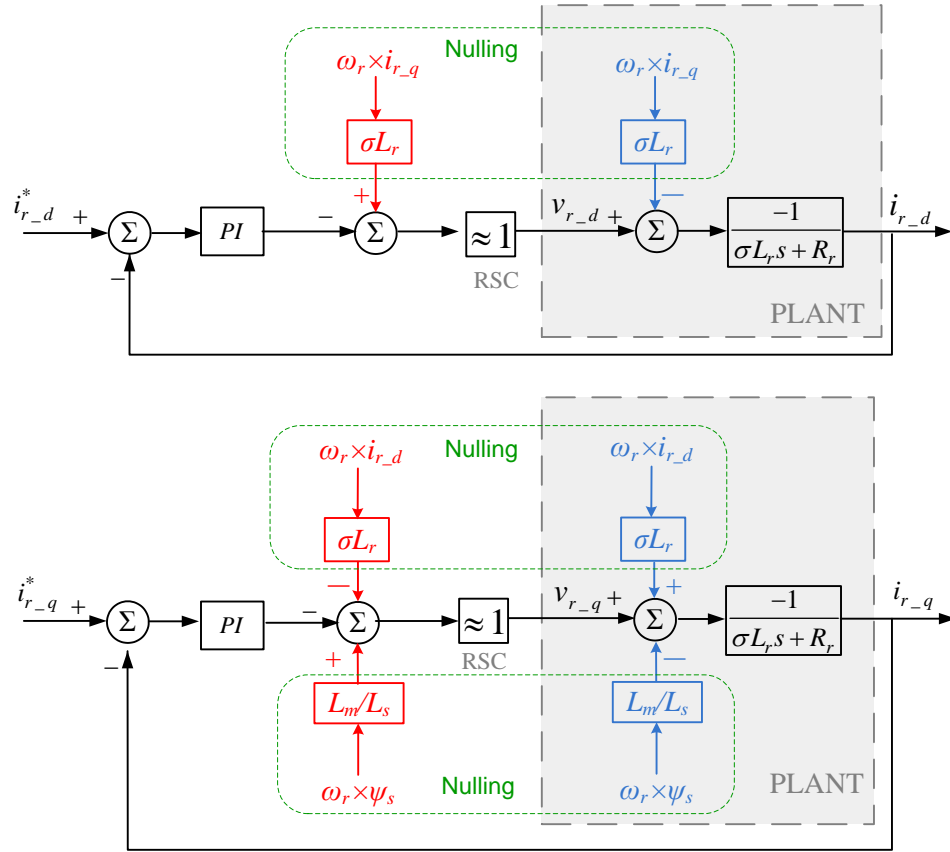


Figure 4.1 Current control loops of the rotor-side converter

From Figure 4.1 and equation (4.2), the plant model includes the voltage drop in the transitory inductance σL_r (cross-coupling from the orthogonal loop) and the emf induced by the stator flux. These couplings are nulled at the controller output by the compensating terms. This results in the same closed-loop transfer function for the two current control loops:

$$\frac{i_{r-dq}}{i_{r-dq}^*} = \frac{\frac{k_p}{\sigma L_r} s + \frac{k_i}{\sigma L_r}}{s^2 + \frac{R_r + k_p}{\sigma L_r} s + \frac{k_i}{\sigma L_r}} \quad (4.3)$$

Assuming $K_p \ll K_i$, then (4.3) can be approximated as a second-order transfer function:

$$\frac{i_{r-dq}}{i_{r-dq}^*} \approx \frac{\frac{k_i}{\sigma L_r}}{s^2 + \frac{R_r + k_p}{\sigma L_r} s + \frac{k_i}{\sigma L_r}} = \frac{\omega_n^2}{s^2 + 2\xi \cdot \omega_n s + \omega_n^2} \quad (4.4)$$

Here ξ is defined as the damping ratio. It influences the maximum overshoot and response speed. In classical second-order system design, an optimum damping ratio is considered as 0.707, which gives a very small overshoot (less than 5%) with reasonable settling time [90]. ω_n is the undamped natural frequency that affects the response speed. Theoretically, a larger ω_n is desired to achieve fast response. However, this requires a high controller gain, which is often not very practical due to stability problems. The overshoot is only determined by the damping, and it can be improved by increasing k_p . In contrast, k_i only influences the natural frequency.

Attention should be paid to the PI output signal $v_{r_dq}^*$ (also known as the manipulated input signal) when tuning the controller. A large peak of this quantity may stress the converter since it can cause spikes in the dc-voltage and also on the grid-side electric quantities. It has the following relationship with the current reference:

$$\frac{v_{r_dq}}{i_{r_dq}^*} = - \frac{k_p s^2 + \left(\frac{R_r}{\sigma L_r} k_p + k_i\right) s + \frac{R_r}{\sigma L_r} k_i}{s^2 + \frac{R_r + k_p}{\sigma L_r} s + \frac{1}{\sigma L_r} k_i} \quad (4.5)$$

Different damping ratios are tested for the full-closed-loop transfer function (see Appendix B.1). Compared with the simplified 2nd-order transfer-function with $\varepsilon = 0.7$ (referred to as 'TF_sim'), a significant overshoot is present due to the derivative term in the numerator. This is not desirable as it may cause damage to the converter. Therefore, a larger damping is required, which is achieved by increasing k_p . Meanwhile, the peak v_{r_dq} and the settling time are also increased with k_p . For damping from 0.7 to 2.5, the settling time has no significant increase (0.1s - 0.15s). Balancing the three factors, an proper damping is chosen as $\xi = 1.2$, which gives an overshoot lower than 10% and peak voltage transient smaller than 5%.

4.1.2. Mathematical model of the RSC power loops

The feed-forward control method may not give the exact power demand due to the uncertainty of machine parameters. Therefore, another PI controller is often cascaded with the current controller to compensate these uncertainties. The bandwidths of the outer

loop are set at least four times slower than the inner loop, thus dynamics of the inner loop can be ignored (assumed as a constant gain) as shown in Figure 4.2.

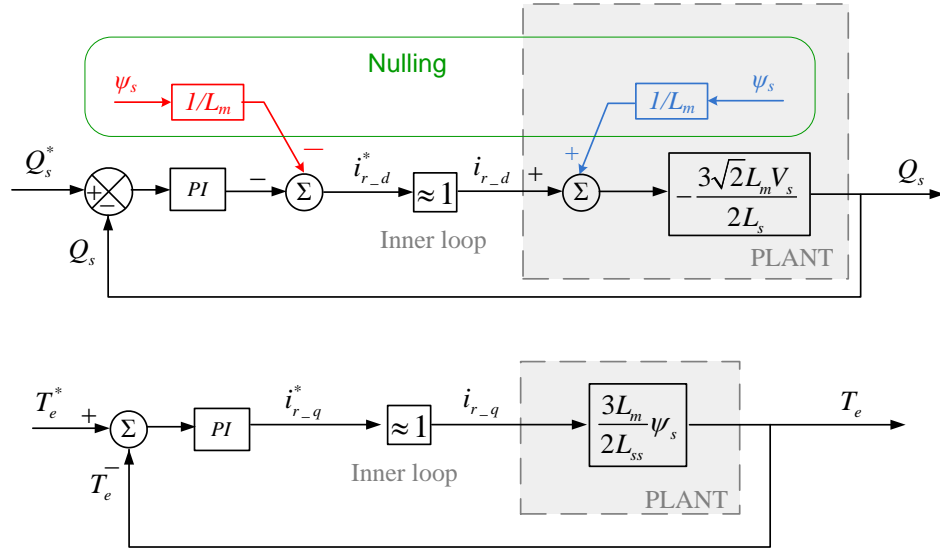


Figure 4.2 Power control loops of the rotor-side converter

The transfer functions of the reactive power and electric torque are derived as

$$\frac{Q_s}{Q_s^*} = \frac{X_{pi1} \cdot s + 1}{\left(\frac{1}{m_1 k_i} + X_{pi1}\right)s + 1} \approx \frac{1}{\tau \cdot s + 1}$$

$$\frac{T_e}{T_e^*} = \frac{X_{pi2} \cdot s + 1}{\left(\frac{1}{m_2 k_i} + X_{pi1}\right)s + 1} \approx \frac{1}{\tau \cdot s + 1} \quad (4.6)$$

$$\text{Here } m_1 = \frac{3\sqrt{2}}{2} \times \frac{L_m}{L_s} \times V_s = 1.173, \quad m_2 = \frac{3}{2} \times \frac{L_m}{L_s} \times \psi_s = 3.735, \quad X_{pi} = \frac{k_p}{k_i}$$

Note that if X_p is the dominant term in the denominator, then the transfer function is close to a unity gain with a poor noise rejection property. Thus X_p should be very small so that the transfer function can be approximated as a 1st order transfer function. In fact, with k_p set to be 0, very similar responses are obtained. The time constant is mainly dependent on k_i . Therefore, a pure integral controller could be adequate for the outer loop of RSC control.

4.1.3. Mathematical model of the GSC current loops

The grid-side converter current control loop (Figure 4.3) has the following transfer function

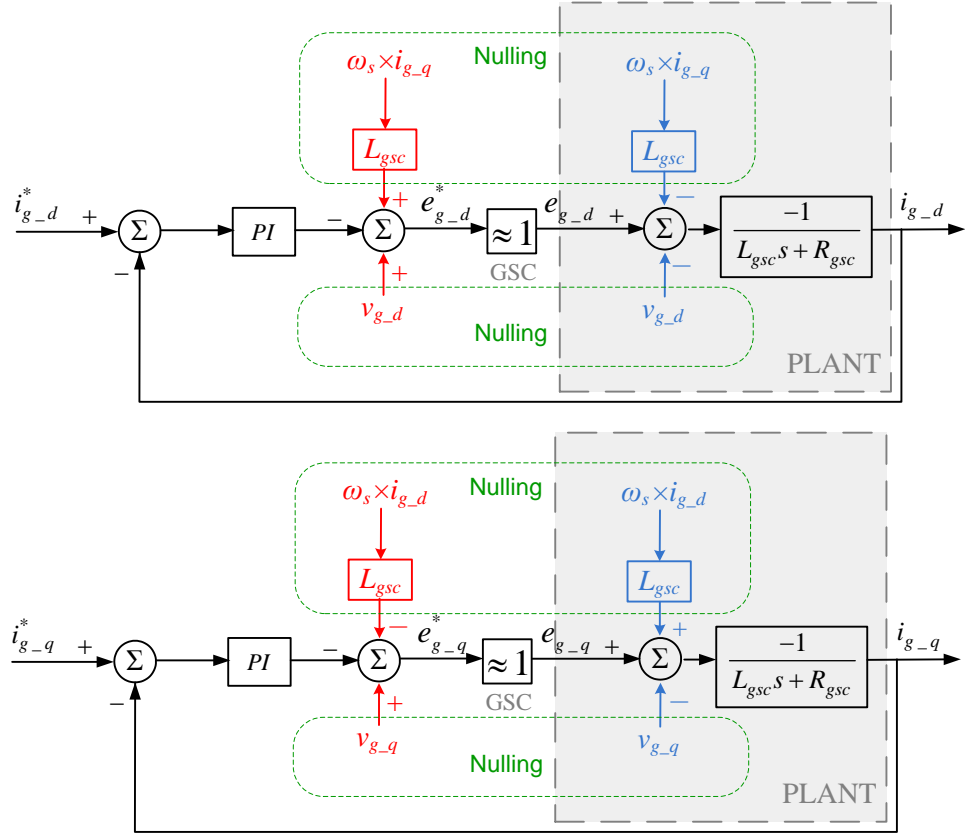


Figure 4.3 Current control loops of the grid-side converter

$$\frac{i_g}{i_g^*} = \frac{\frac{k_p}{L_{gsc}}s + \frac{k_i}{L_{gsc}}}{s^2 + \frac{(R_{gsc} + k_p)}{L_{gsc}}s + \frac{k_i}{L_{gsc}}} \approx \frac{\omega_n^2}{s^2 + 2\xi\omega_n s + \omega_n^2} \quad (4.7)$$

As the transfer function for the two orthogonal control loops d and q are the same, they are not separately represented here. The transfer function to manipulated input e_{g-dq}^* is

$$\frac{e_g^*}{i_g^*} = -\frac{k_p s^2 + \left(\frac{R_{gsc}}{L_{gsc}}k_p + k_i\right)s + \frac{R_{gsc}}{L_{gsc}}k_i}{s^2 + \frac{(R_{gsc} + k_p)}{L_{gsc}}s + \frac{1}{L_{gsc}}k_i} \quad (4.8)$$

Impacts of varying the damping on the control current overshoot and transient GSC voltage have been obtained in Appendix B.3. The damping ratio that gives a similar overshoot with 'TF_sim' is found to be $\xi = 1.6$. This damping still keeps the peak transient of GSC voltage lower than 2.5%.

All the mathematical models presented previously in this section have been verified with PSCAD model (Appendix B). The verification is done with each control loop independently without considering interference with the cascaded control loop. All controllers are set to be at 10Hz. Step signals for different quantities are applied. The responses from the two models match very well, indicating the transfer functions fully characterise the PSCAD model, and thus are accurate for tuning the controller by analysing the Mathematical model.

4.2. Small signal analysis of the dc-link control

4.2.1. State feed-back model derivation

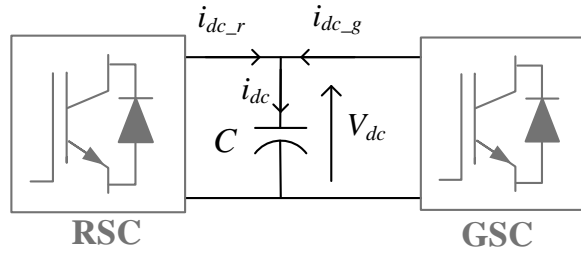


Figure 4.4 Configuration of the current flow in the dc-link system

As shown in Figure 4.4, the power flowing through the dc-link can be represented by:

$$P_{conv} = V_{dc} i_{dc_r} = -V_{dc} i_{dc_g} = -\frac{3}{2} v_{g-q} i_{g-q} \quad (4.9)$$

$$C \frac{dV_{dc}}{dt} = i_{dc_g} + i_{dc_r} \quad (4.10)$$

Substituting the term i_{dc_g} in (4.10) with i_{g-q} , the relationship between the dc-voltage and q-component current can be found as

$$C \frac{dV_{dc}}{dt} = \frac{3}{2} \frac{v_{g-q} i_{g-q}}{V_{dc}} + i_{dc_r} \quad (4.11)$$

The first term in (4.11) is associated with the grid quantities, and the second term is the RSC injecting currents, which can be viewed as an input disturbance as in Figure 4.5. This current perturbation is caused by power change. Therefore, equation (4.11) can be represented as

$$C \frac{dV_{dc}}{dt} = \frac{3}{2} \frac{v_{g-q} i_{g-q}}{V_{dc}} + \frac{P_{conv}}{V_{dc}} = f \quad (4.12)$$

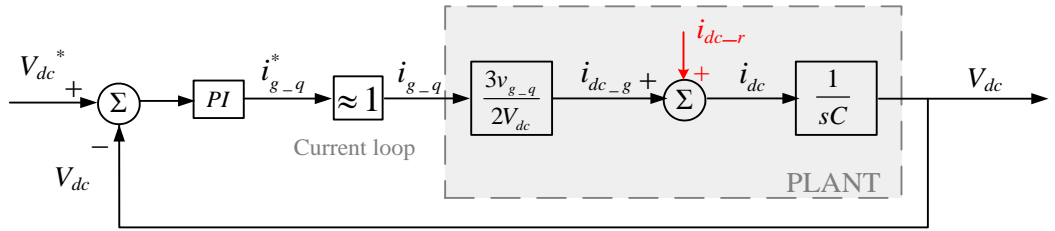


Figure 4.5 Non-linear block diagram of the dc-link control system

Differentiating equation (4.9) with respect to all variables at a particular operating point $v_{g-q0}, i_{g-q0}, V_{dc0}$:

$$\begin{aligned} C \Delta \dot{V}_{dc} &= \frac{\partial f}{\partial i_{g-q}} \Delta i_{g-q} + \frac{\partial f}{\partial v_{g-q}} \Delta v_{g-q} + \frac{\partial f}{\partial V_{dc}} \Delta V_{dc} + \frac{\partial f}{\partial i_{dc-r}} \Delta i_{dc-r} \Rightarrow \\ \Delta P_{conv} &= V_{dc0} \Delta i_{dc-r} \\ sC \Delta V_{dc} &= \frac{3}{2} \frac{v_{g-q0}}{V_{dc0}} \Delta i_{g-q} + \frac{3}{2} \frac{i_{g-q0}}{V_{dc0}} \Delta v_{g-q} - \frac{3}{2} \frac{v_{g-q0} i_{g-q0}}{V_{dc0}^2} \Delta V_{dc} + \frac{\Delta P_{conv}}{V_{dc0}} \\ &= \frac{3}{2} K_V \Delta i_{g-q} + \frac{3}{2} K_G \Delta v_{g-q} + \frac{1}{V_{dc0}} \Delta P_{conv} - \frac{3}{2} K_V K_G \Delta V_{dc} \end{aligned} \quad (4.13)$$

Here $K_V = \frac{v_{g-q0}}{V_{dc0}}$ and $K_G = \frac{i_{g-q0}}{V_{dc0}}$

The first term of equation (4.13) is related to the control signal i_{g-q} ; the second and third terms are disturbances respectively related to the grid-side quantity Δv_{g-q} and the rotor-side quantity ΔP_{conv} ; the last term is related to the feed-back signal from dc-voltage perturbations.

Using the above values, step responses are obtained with varying damping ratios, as is shown in Figure 4.7. This is not like the current loops, where a large transient of manipulated input can be induced by fast changes of the set point, as the function of dc-link control is mainly disturbance rejection or smoothing. Therefore, increasing the damping reduces both the current overshoot and peak dc-ripples, as observed in the two upper graphs. The lower graphs are magnified views of the circled area in the upper graphs. The lower graphs are magnified views of the circled area in the upper graphs. TF_sim indicates the optimum response from the simplified standard 2nd order transfer function ($\xi=0.7$). As seen in the left bottom graph, the overshoot is comparable with 'TF_sim' when the damping approaches to 3.5. However, this significantly increases the settling time (from 1.5s to 5s), as observed in the right bottom graph. Here $\xi=2.5$ is chosen which gives an overshoot lower than 7%.

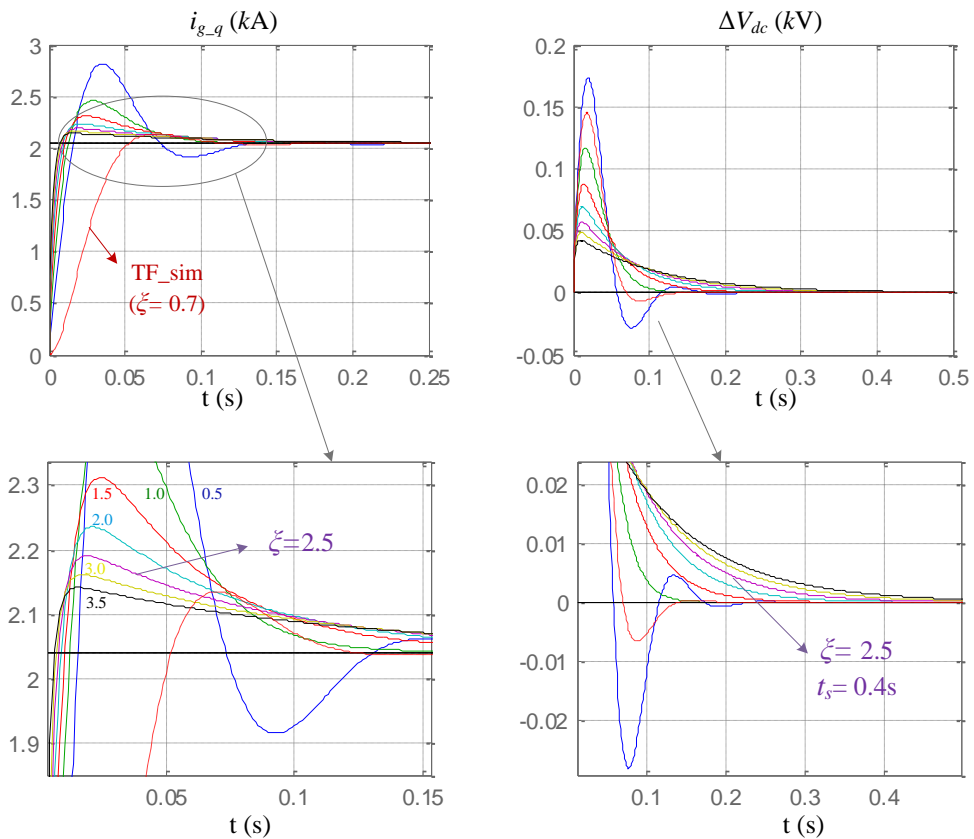


Figure 4.7 Dc-link responses to a 1 pu torque step from the nominal operating point, with different damping values ($f_n = 10\text{Hz}$)

To test the model further, the controller bandwidth was set at 10Hz and all the parameters described were substituted into the transfer functions (4.14) and (4.15). A 0.2 per unit ΔP was introduced at the input, the responses are verified by PSCAD simulations (denoted as 'model') in Figure 4.8 with the same controller setting. For the current and dc-voltage,

there are two spikes present at each transition. The slower transient is the dynamic of the dc-link control. The model and transfer functions have very good correspondence for this transient, which proves the accuracy of dc-link mathematical model. The faster transient is caused by the set point step in the RSC current control.

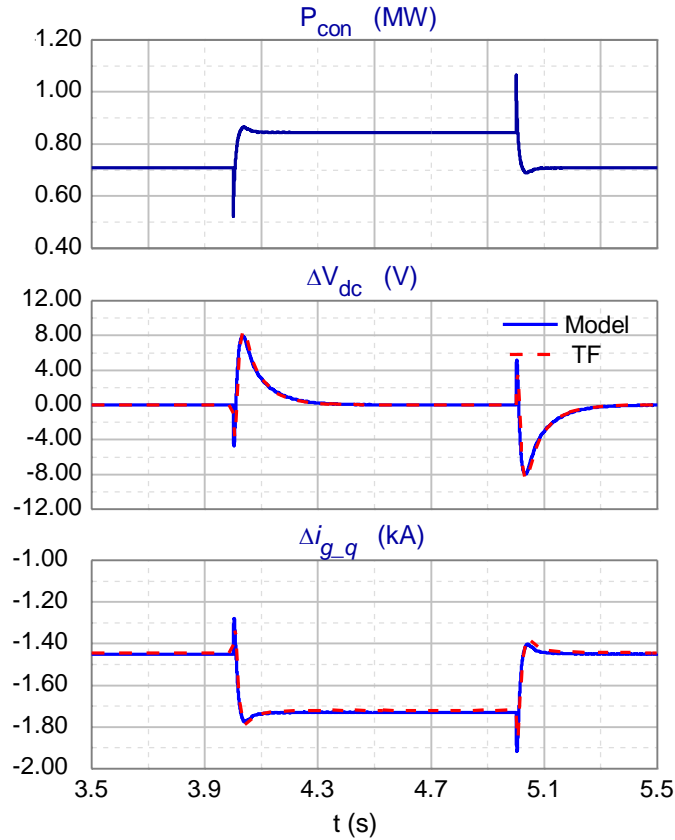


Figure 4.8 Verification of the dc-link model

4.2.2. Dynamic stiffness analysis at different operating points

Disturbances will cause voltage ripples on the dc-link. The magnitude of the ripples may vary with the grid voltage, dc-link voltage, rotor speed and electric torque. In this section, dynamic stiffness (DS) [91] of the dc-link will be investigated for different operating points. This quantity reveals the resistance of the system to a certain disturbance. Here, the dc-link DS is given as the inverse of power perturbation function (4.15):

$$\begin{aligned}
 DS_p &= CV_{dc0}s + 1.5K_vV_{dc0}(K_G + k_p) + \frac{1.5K_vk_iV_{dc0}}{s} \\
 &= CV_{dc0}s + 1.5v_{g-q0}\left(\frac{i_{g-q0}}{V_{dc0}} + k_p\right) + \frac{1.5v_{g-q0}k_i}{s}
 \end{aligned} \tag{4.16}$$

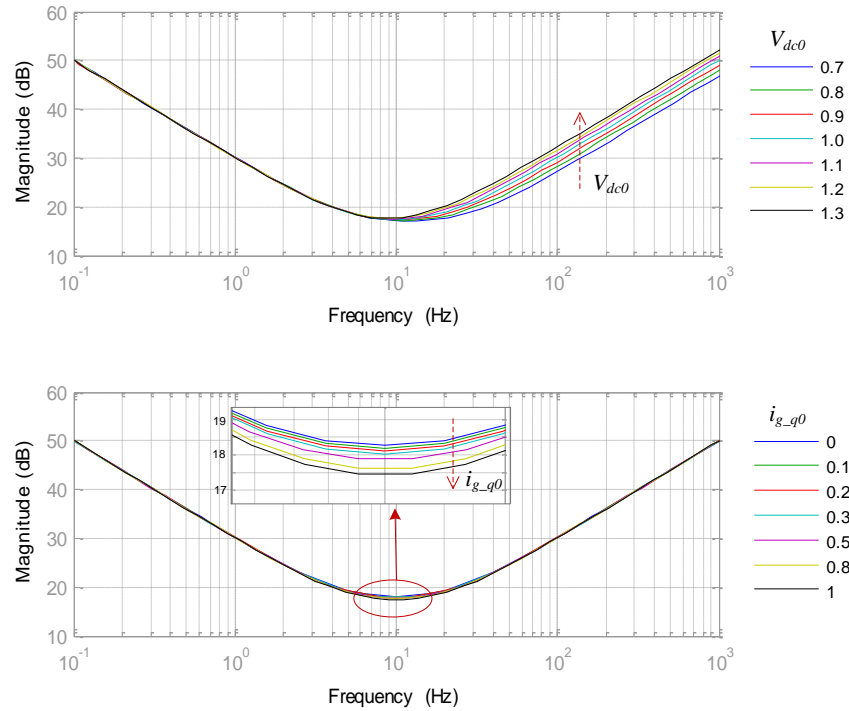


Figure 4.9 Dc-link dynamic stiffness to power disturbance at varying V_{dc0} and i_{g_q0}

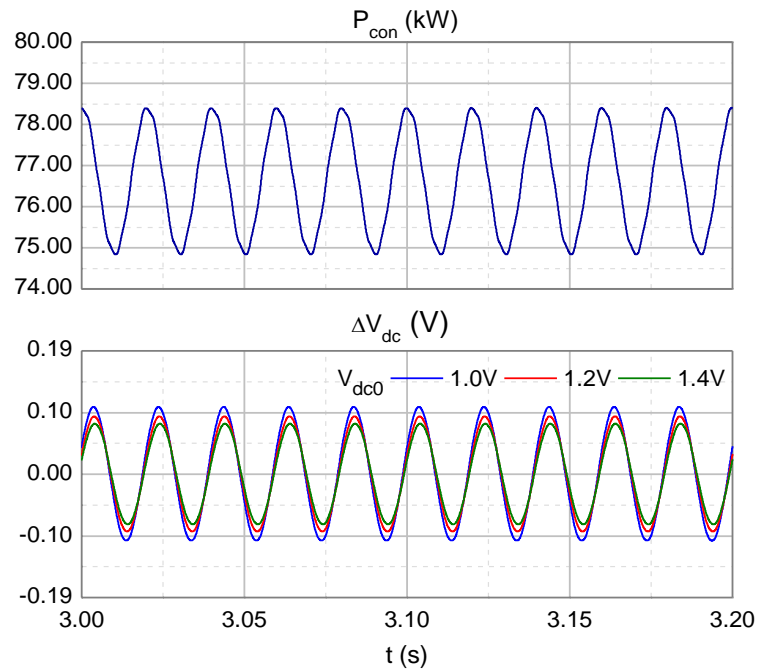


Figure 4.10 Dc-link ripples at 50Hz power oscillation

The frequency response is plotted in Figure 4.9. From (4.16), it is known that the system's DS is proportional to the dc set point for high frequencies ($f > 10\text{Hz}$ as seen in the figure). In the middle frequency range (around 10Hz), system DS depends on both i_{g_q0} and V_{dc0} , where i_{g_q0} is dependent on the rotor speed and electric torque and may vary from 0.7kA

to 1.56kA. It can be seen from the lower graph that both of the two quantities have a very slight effect on DS. As no or negligible grid voltage change is considered in normal operations, only the dc-ripples caused by power perturbations are investigated for different V_{dc0} . In Figure 4.10, 50Hz torque ripple is applied. A reduction of 25% on the dc-ripples is obtained as V_{dc0} increases from 1kV to 1.4kV.

4.3. Small signal analysis of the pitch control system

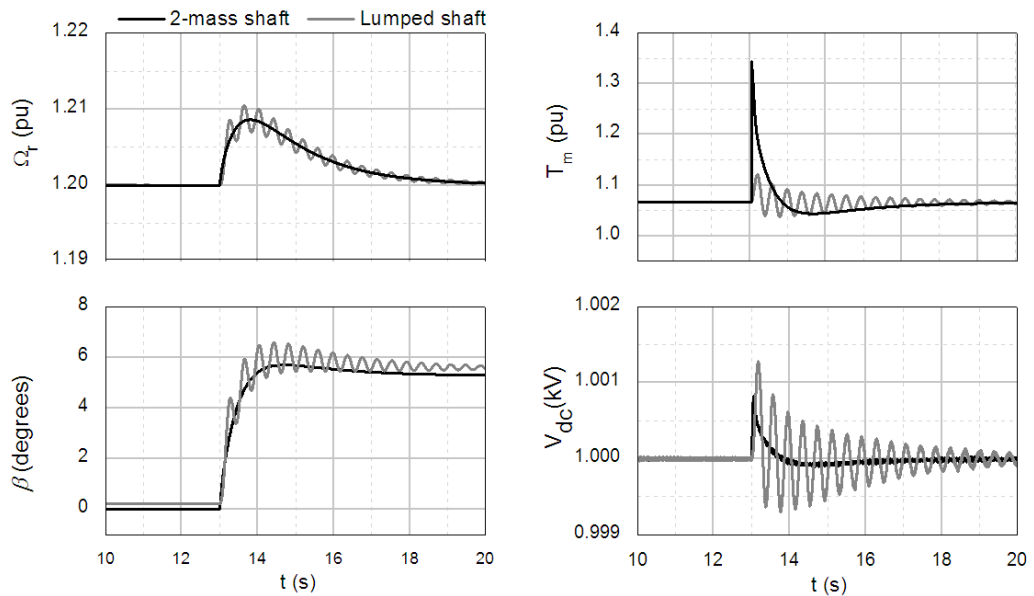


Figure 4.11 Simulation of the lumped and 2-mass shaft systems

Using a lumped or two-mass model to represent the shaft system has been discussed in Chapter 3.2. The simplified model is not sufficient to be used for controller design since the shaft torsional mode is eliminated, which is critical since it may destabilize the system if the controller is not properly tuned. The transient responses of the two models with a same controller setting are shown in Figure 4.11. A wind step from 12m/s to 13m/s is imposed. It can be seen that a controller that works well on the lumped-shaft model may induce significant oscillations on a 2-mass-shaft model. The frequency of this oscillations is in the range of a few Hz and is given by

$$f_{shaft} = \frac{1}{2\pi} \sqrt{\frac{K_s \omega_s (H_T + H_G)}{2H_T H_G}} = \frac{1}{2\pi} \sqrt{\frac{0.7 \times 2\pi \times 50 \times (3 + 0.5)}{2 \times 3 \times 0.5}} = 2.55 \text{ Hz} (16 \text{ rad} / \text{s}) \quad (4.17)$$

Therefore, in this chapter, the system dynamic analysis and controller design are implemented based on the 2-shaft model.

Since the system is highly non-linear, its dynamic behaviour changes with operating point. A common method for investigating this kind of system is to derive a linear model at a particular operating point and do small signal analysis. The frequency domain analysis can then be done with transfer functions, just like the procedures for the other control loops. The following briefly introduces the linearization process[89].

4.3.1. State feed-back model derivation

The turbine aerodynamic model has already given in (3.1) as:

$$T_a = \frac{\rho}{2} \pi R^3 \frac{C_p(\lambda, \beta)}{\lambda} v_w^2 \quad (4.18)$$

Differentiating the aerodynamic torque function with respect to the operating point $\Omega_{T0}, \beta_0, V_{w0}$:

$$\begin{aligned} T_a \Big|_{\Omega_{T0}, \beta_0, V_{w0}} &= T_{a_0}(\Omega_{T0}, \beta_0, V_{w0}) + \Delta T_a \\ &= T_{a_0}(\Omega_{T0}, \beta_0, V_{w0}) + \frac{\partial T_a}{\partial \Omega_T} \Big|_{\Omega_{T0}} \Delta \Omega_T + \frac{\partial T_a}{\partial \beta} \Big|_{\beta_0} \Delta \beta + \frac{\partial T_a}{\partial V_w} \Big|_{V_{w0}} \Delta V_w \end{aligned}$$

Here $\Delta \Omega_T, \Delta \beta, \Delta V_w$ are small deviations from their respective operating points. Let

$$\frac{\partial T_a}{\partial \Omega_T} = \gamma, \quad \frac{\partial T_a}{\partial \beta} = \zeta, \quad \frac{\partial T_a}{\partial V_w} = \eta$$

The small deviation of the aerodynamic torque is expressed as

$$\Delta T_a = \gamma \cdot \Delta \Omega_T + \zeta \cdot \Delta \beta + \eta \cdot \Delta V_w \quad (4.19)$$

Considering the 2-mass shaft model (3.6), the dynamics of the turbine rotor and the generator rotor are re-presented with their deviations:

$$\begin{aligned}
 J_T \Delta \dot{\Omega}_T &= T_{a_0} + \Delta T_a - T_{s_0} - \Delta T_s - D_T \Omega_{T_0} - D_T \Delta \Omega_T \\
 J_G \Delta \dot{\Omega}_G &= T_{s_0} + \Delta T_s - T_{e_0} - \Delta T_e - D_G \Omega_{G_0} - D_G \Delta \Omega_G \\
 \Delta \dot{\theta}_s &= \Omega_{T_0} + \Delta \Omega_T - \Omega_{G_0} - \Delta \Omega_G
 \end{aligned} \tag{4.20}$$

In steady state operation, the balance point exists

$$\begin{aligned}
 T_{a_0} &= T_{s_0} + D_T \Omega_{T_0} = T_{e_0} + D_G \Omega_{G_0} + D_T \Omega_{T_0} \\
 \Omega_{T_0} &= \Omega_{G_0}
 \end{aligned} \tag{4.21}$$

Then equation(4.20) can be simplified as

$$\begin{aligned}
 J_T \Delta \dot{\Omega}_T &= \Delta T_a - \Delta T_s - D_T \Delta \Omega_T \\
 J_G \Delta \dot{\Omega}_G &= \Delta T_s - \Delta T_e - D_G \Delta \Omega_G \\
 \Delta \dot{\theta}_s &= \Delta \Omega_T - \Delta \Omega_G
 \end{aligned} \tag{4.22}$$

On the other hand, the reaction torque is given by

$$\Delta T_s = K_s \Delta \theta_s + D_s (\Delta \Omega_T - \Delta \Omega_G) \tag{4.23}$$

Substituting equations (4.19) and (4.23) into (4.22), and representing it in state-space model:

$$\begin{bmatrix} \Delta \dot{\Omega}_T \\ \Delta \dot{\theta}_s \\ \Delta \dot{\Omega}_G \end{bmatrix} = A \cdot \begin{bmatrix} \Delta \Omega_T \\ \Delta \theta_s \\ \Delta \Omega_G \end{bmatrix} + B \cdot \Delta \beta + B_{d1} \cdot \Delta W + B_{d2} \cdot \Delta T_e \tag{4.24}$$

where the coefficients are $A = \begin{bmatrix} \frac{\gamma - D_s - D_T}{J_T} & -\frac{K_s}{J_T} & \frac{D_s}{J_T} \\ 1 & 0 & -1 \\ \frac{D_s}{J_G} & \frac{K_s}{J_G} & -\frac{D_s + D_G}{J_G} \end{bmatrix}$, $B = \begin{bmatrix} \frac{\zeta}{J_T} \\ 0 \\ 0 \end{bmatrix}$,

$B_{d1} = \begin{bmatrix} \frac{\eta}{J_T} \\ 0 \\ 0 \end{bmatrix}$, $B_{d2} = \begin{bmatrix} 0 \\ 0 \\ -\frac{1}{J_G} \end{bmatrix}$. The output is given by $y = C \cdot \begin{bmatrix} \Delta\Omega_T \\ \Delta\theta_s \\ \Delta\Omega_G \end{bmatrix}$. Let $C = [0 \ 0 \ 1]$, then

the open-loop transfer function from the disturbance ΔV_w to the rotor perturbations $\Delta\Omega_G$ can be found as

$$\left. \frac{\Delta\Omega_G(s)}{\Delta V_w(s)} \right|_{op} = C \cdot (sI - A)^{-1} \cdot B_{d1} \quad (4.25)$$

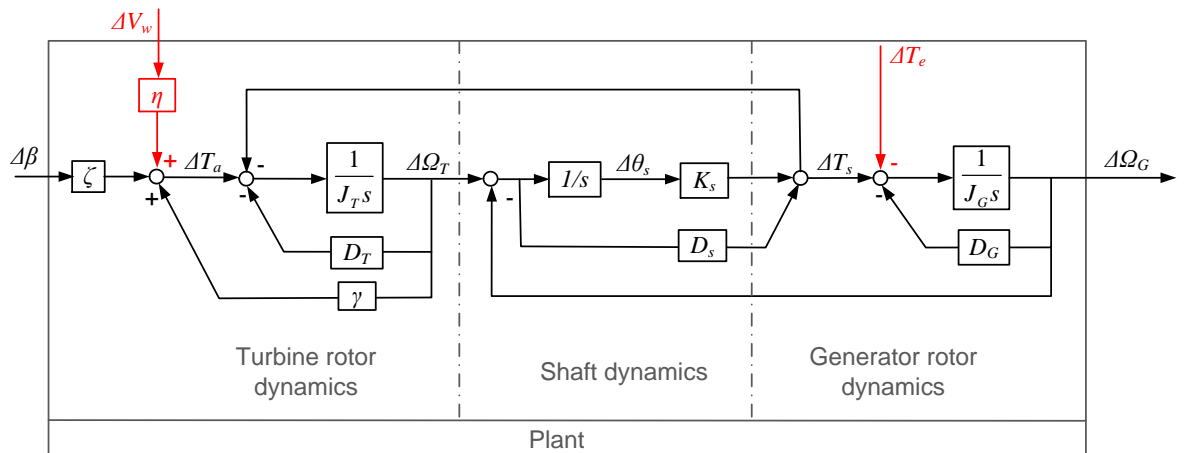


Figure 4.12 Small signal model of the 2-mass shaft wind turbine mechanical system

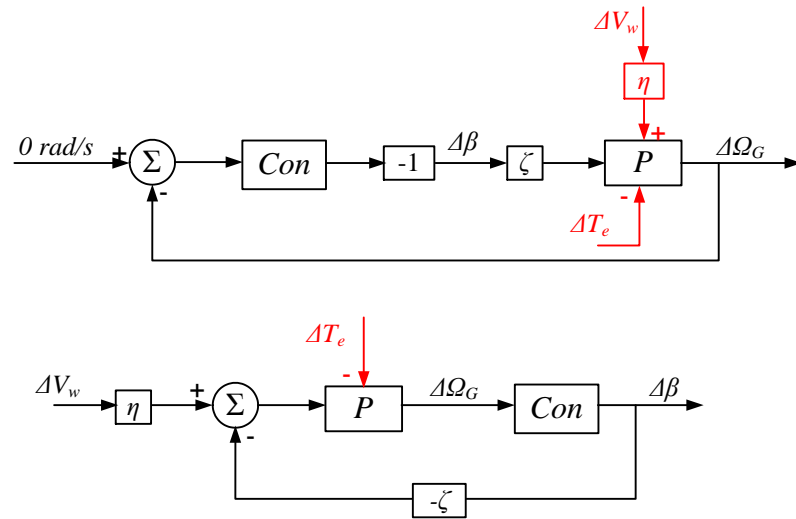


Figure 4.13 Block diagram of closed loop pitch control system

Now a controller is added which relates the pitch angle to the rotor speed variation, as shown in the closed-loop diagram (Figure 4.13). The top one is the original form in which the rotor speed perturbation is considered as the input signal. The reference is set to be 0 rad/s as desired in steady state. The wind speed and electric torque perturbations are considered as external disturbances. The system can be represented in the bottom diagram, in which the system transforms the mechanical torque perturbations caused by the wind variation to the pitch angle deviations.

The transfer function of the plant is known from equation(4.25):

$$P(s) = \frac{C \cdot (sI - A)^{-1} \cdot B_{d1}}{\eta} \quad (4.26)$$

The open loop gain without the controller is

$$G(s) = -\zeta \cdot P(s) \quad (4.27)$$

Then closed-loop transfer functions from wind to the blade angle and from the wind to the rotor speed are presented as

$$\left. \frac{\Delta\beta}{\Delta V_w} \right|_{cl} = \frac{\eta \cdot P \cdot Con}{1 + (-\zeta) \cdot P \cdot Con} \quad (4.28)$$

$$\left. \frac{\Delta\Omega_G}{\Delta Vw} \right|_{cl} = \frac{\eta \cdot P}{1 + (-\zeta) \cdot P \cdot Con} \quad (4.29)$$

4.3.2. Open-loop response verification

The derived linear model will be implemented later for tuning controller of the PSCAD non-linear model. Before this, it is necessary to verify the open-loop linear model with the PSCAD non-linear model. The operating point is chosen as: $Vw = 13m/s$, $\Omega_{T0} = 1.17 pu$, $\beta_0 = 0.73^\circ$. Using Matlab to calculate the transfer functions, the open-loop plant is then obtained from (4.25):

$$\left. \frac{\Delta\Omega_G(s)}{\Delta Vw(s)} \right|_{op} = \frac{0.141 \times (s + 73.314)}{(s + 0.1213) \times (s^2 + 3.546s + 256.571)} \quad (4.30)$$

Wind steps of $\Delta Vw = 0.5m/s$ and $1m/s$ are imposed at $t=60s$, the variations of rotor speed $\Delta\Omega_G$ of the non-linear and linear models are compared in Figure 4.14. It can be seen that the two curves have very good correspondence at the initial transient. However, the difference becomes larger as the rotor speed deviates from the original operating point. The maximum errors reached for $0.5m/s$ and $1m/s$ wind step are approximately 6% and 10%. Thus it can be considered that the linear model dynamics can accurately characterize the full model for with a wind change smaller than $1m/s$.

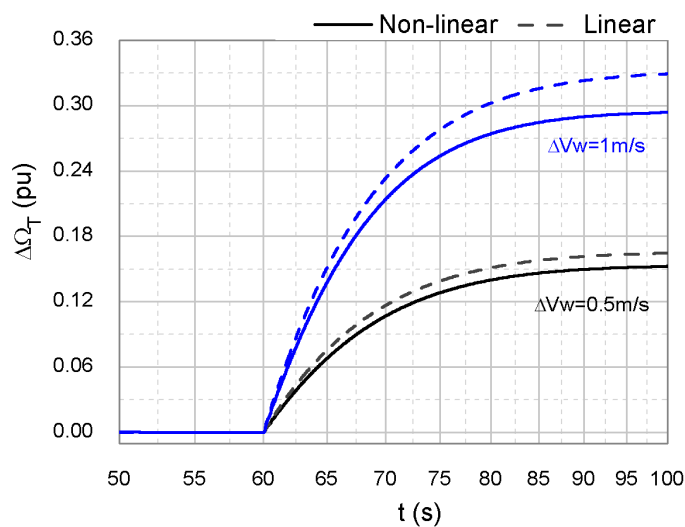


Figure 4.14 Open-loop plant model verification

4.4. Pitch controller design based on linear model

Adding the shaft torsional mode makes the plant model more complex as the system order is increased. The conventional controller design method by observing the characteristic function is not applicable. Unlike the 2nd order system, where the damping ratio and natural frequency are determined by the only pole pairs, other poles in a higher order system may modify the system's transient characteristics. Therefore, in this section, the root-locus and frequency responses of the system are used to help analyse and improve the system responses.

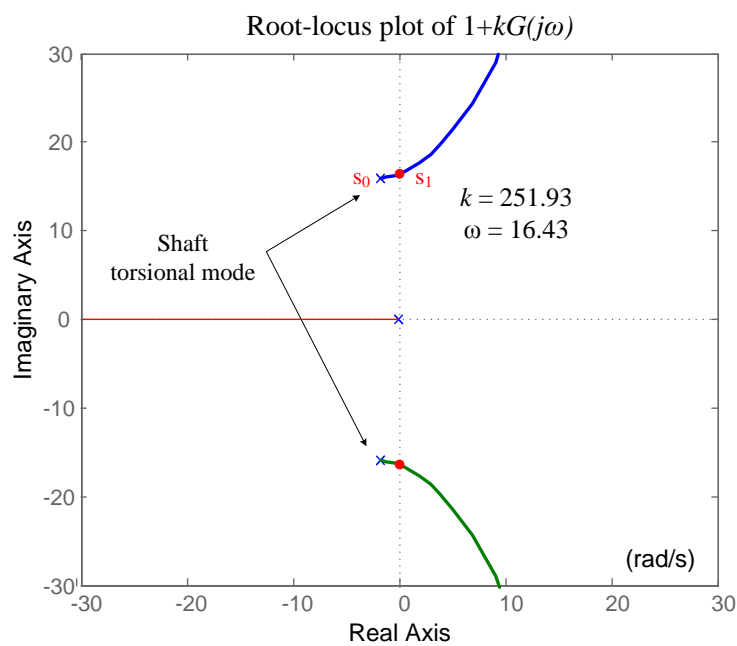


Figure 4.15 Root-locus plot of the characteristic function $1+kG(j\omega)_{op}$ with marginally stable points

The root-locus plot shows the locations of closed loop poles with variations of one system parameter [92]. In Figure 4.15, the root-locus for the characteristic equation $1+k \times G(s)$ has been plotted with k varying from 0 to infinity. There are three branches which start from the open-loop poles and end at the open loop zeroes. The complex root s_0 characterizes the shaft torsional modes as it has a natural frequency of $\omega_n = |s_0(j\omega)| \approx 16 \text{ rad/s}$, which is the same as calculated in (4.17). The transient behaviour of the closed-loop system is reflected by the dominant pair of complex-conjugate roots on the locus. For instance, as k increases, the system becomes less stable as the closed loop poles move to the right-half of the s plane. Meanwhile, the

damping decreases, the natural frequency and overshoot all increase. This will become evident later in the closed-loop step response. The marginally stable gain corresponds to the roots on the imaginary axis: $k=250$ (251.93). When designing the controller, it is appreciated that the root locus can be shifted to the left using various techniques so that the system stability can be improved.

The frequency response of a system can be presented by a Bode diagram, where one graph shows the magnitude versus frequency and the other shows the phase versus frequency. The root-locus provides the information on the closed-loop system's transient response, while the frequency response shows steady-state or low-frequency performances and stability margins.

Figure 4.16 presents the frequency response of $G(s)_{op}$. Here the spike on the magnitude diagram indicates the shaft torsional frequency. Several parameters need to be considered in designing the pitch controllers [92]:

- Dc gain $Con(0)G(0)$: this term determines the final steady state error. The higher the dc gain is, the smaller the output error will be.
- High frequency gain $Con(j\omega)G(j\omega)$: -it can be seen in the figure that the system loop gain decreases with the frequency which indicates good noise rejection ability at higher frequencies.
- Phase margin (PM): in the Bode diagram it is defined as the phase above -180° at the cross-over frequency (0dB).
- Gain margin (GM): the magnitude below 0 dB when the phase passing across -180° . A good phase margin combined with a good gain margin is vital to insure adequate system stability.

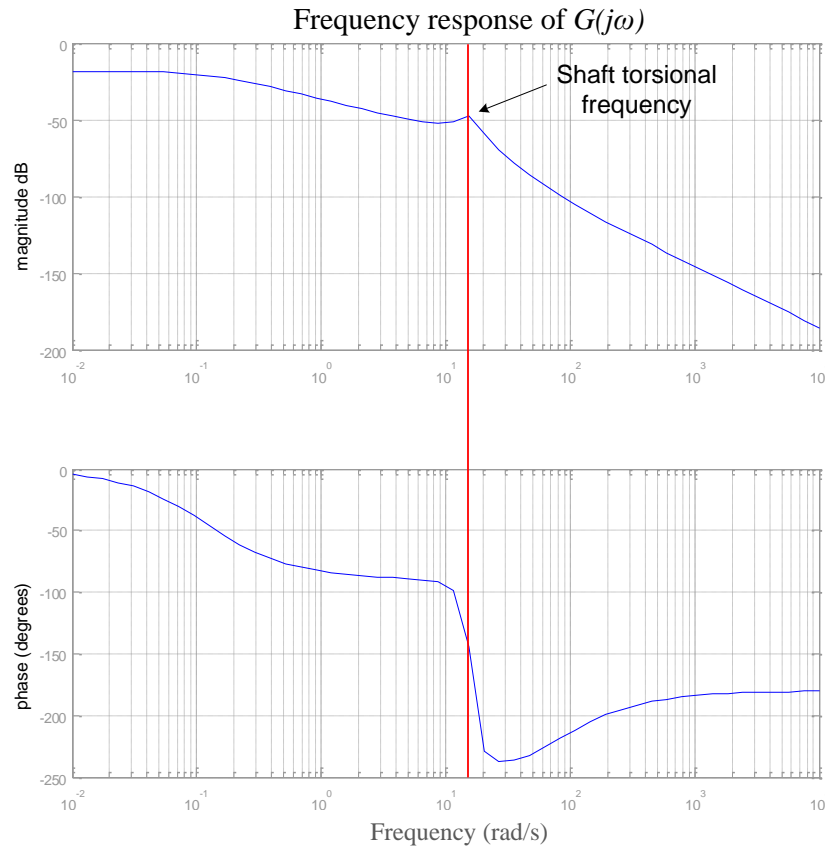


Figure 4.16 Bode diagram of the open-loop transfer function $G(s)$

From Figure 4.16, the stability margin of the open loop plant without controller is $PM = \infty$ and $GM = 2.52$, which indicates the chosen operating point is stable. Including all the compensators, a stability margin adopted by [93] is $GM > 10dB$ and $PM \approx 60degrees$ for the wind turbine open loop transfer function. This is used in this thesis as a baseline reference for tuning the controller. The rest of this chapter evaluates the influence of three commonly used controllers in industry, which are the proportional-only controller, proportional-integral controller (PI), and the proportional-integral-derivative (PID) controller. A better stability margin is suggested that can improve the system dynamic response. Optimum controller parameters are proposed for each of the controllers.

4.4.1. Proportional – only (P) controller

Using a proportional-only controller is proposed in [79]. Although this method will not entirely remove the rotor speed error, it is still a practical strategy since the incoming wind varies constantly. In this case, the controller is simply a constant gain:

$$Con = k_p$$

The performance of this controller can be described by the steady state error, as shown in (4.31). This expression is used when the input is constant and is also known as the position error

$$E_{ssp} = \frac{1}{1 + \lim_{s \rightarrow 0} k_p G(s)} = \frac{1}{1 + k_p G(0)} \quad (4.31)$$

The dc gain of the plant is a constant value $G(0) = 0.12$. In order to reduce the error, a larger k_p is desired. However, from the root-locus analysis there is a gain limit $k_p < 250$, beyond which the system will go unstable. The step responses for the rotor speed (4.28) and the blade angle (4.29) are simulated as k_p increases from 60 to 200, as seen in Figure 4.17.

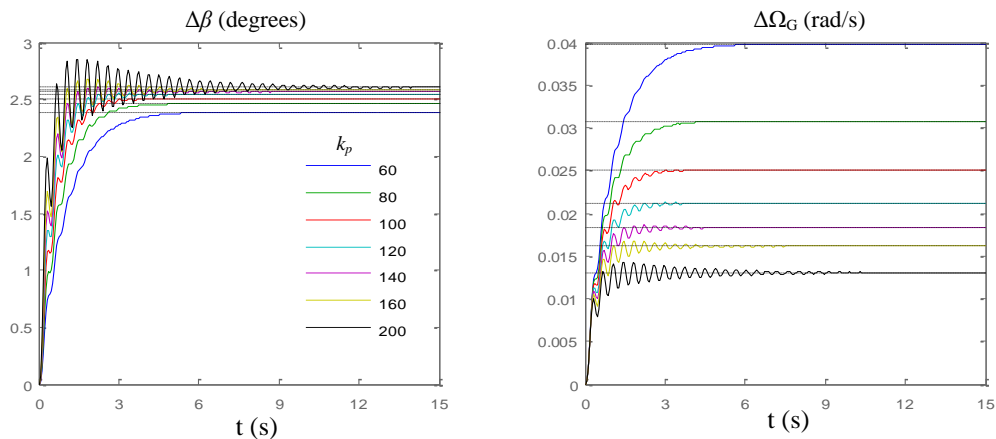
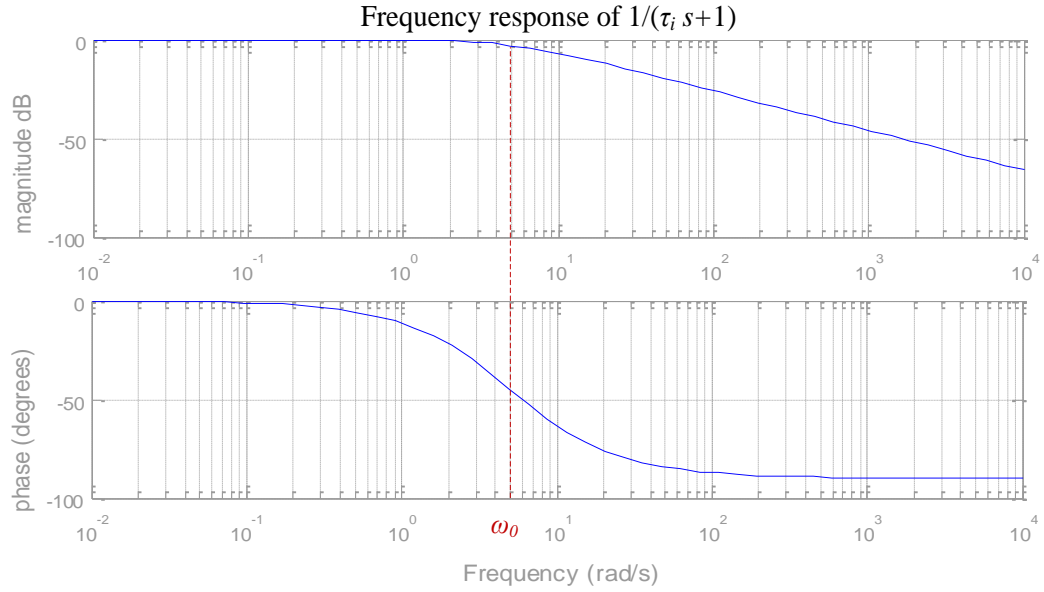


Figure 4.17 Step responses to a 1 m/s wind speed step from nominal point ($V_w=13\text{m/s}$, $\Delta\Omega_G=122.5\text{ rad/s}$), with different controller gains

As can be seen from the step response, rotor speed error is not eliminated, but is reduced with the increasing of k_p . Meanwhile, from the pitch response of Figure 4.17, the overshoot increases and the damping decreases, leading to larger oscillations. The GM drops below 10dB when $k_p > 79.5$.


 Figure 4.18 Frequency response of the actuator for $\tau_i=0.2s$

In a real wind turbine, an actuator is added after the pitch controller, which will receive the demanded signal and generate the real pitch angle. As shown in Figure 4.18, an actuator acts as a phase lag compensator (45° phase lag is introduced at its cut-off frequency $\omega_0=1/\tau_i$). On one hand, this results in a smaller phase margin, on the other hand, the system's GM is increased thus it allows a larger k_p . Also, like a low pass filter, the actuator further decreases high frequency gain. Different combinations of gain value and actuator time constant were simulated, which can be found in Appendix C.1. In general, a large actuator time constant will increase the GM and better restrain shaft oscillations. However, the actuator time constant should be smaller than 3s, or else the cut-off frequency ω_0 would be too close to the system cross-over frequency ω_c . This will cause significant reduction on the PM, and hence induce large overshoot, as the damping ratio ξ proportionally decreases with PM Φ_m :

$$\xi = \frac{\phi_m}{100} \quad (4.32)$$

From the test, the PM without the actuator is approximately 90° . With an actuator, a PM no less than 75° is needed in order to produce over-damped responses. This determines that $\tau_i = 0.15s$, and the maximum controller gain to satisfy the gain margin is $k_p=150$. The resulted stability margin is GM=13.0dB, PM=75.3°. The closed loop response's time

constant is determined from the real-part of the dominated complex root $\tau_{cl} \approx 0.64s$. The settling time is approximately $t_{ss} = 4\tau_{cl} = 2.6s$. The steady state error is

$$E_{ssp} = \frac{1}{1 + k_p G(0)} = 5.2\% \quad (4.33)$$

Please note that design specifications used for the proportional controller and actuator can be extended and applied to the more complex PI and PID controllers, which will be discussed in next two sections.

4.4.2. Proportional and integral (PI) controller

A PI (or PID) controller is the most common control method adopted by industry. Here the controller is constituted of a proportional term plus an integral term:

$$Con(s) = \frac{k_p s + k_i}{s} \quad (4.34)$$

It can be observed from the frequency response of the PI controller (Figure 4.19) that it improves the open-loop low frequency gain without significant change of the high frequency gain. However, as a phase-lag compensator, a smaller phase at low frequencies is obtained. Thus it needs to be cautiously implemented to maintain a required PM.

The PI controller makes the system type increased by 1 (one pure derivative term added in the denominator). For this type of system the steady state position error is always zero. Another quantity is adopted here, i.e. the steady state velocity error, given by equation (4.35). This quantity describes the system's tracking performance when the input is a ramp [92].

$$E_{ssv} = \lim_{s \rightarrow 0} \left(\frac{1}{s} \cdot \frac{1}{1 + Con(s)G(s)} \right) = \frac{1}{k_i \cdot G(0)} \quad (4.35)$$

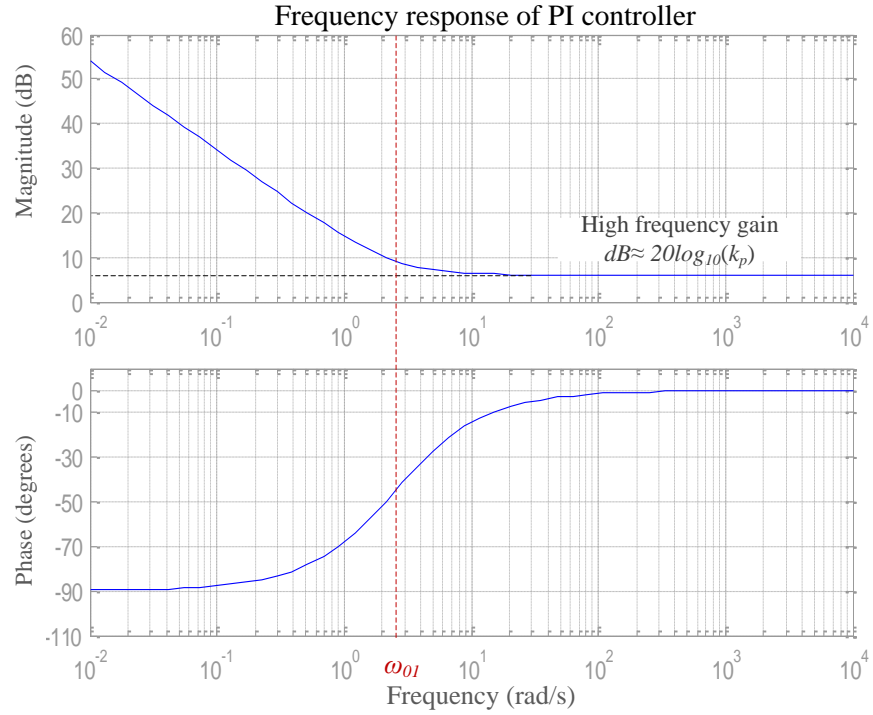


Figure 4.19 Frequency response of the PI controller with $k_p=2$, $k_i=5$

The velocity error is mainly dependent on term k_i . Assuming that the compensated system satisfies the required phase margin without the actuator ϕ_m at a cross-over frequency ω_c , then the following relationship exists[92]:

$$\text{Con}(j\omega_c) \cdot G(j\omega_c) = 1\angle(-180^\circ + \phi_m) \quad (4.36)$$

The controller phase angle at the cross-over frequency is determined as

$$\theta_c = \angle \text{Con}(j\omega_c) = -180 + \phi_m - \angle G(j\omega_c) \quad (4.37)$$

The controller gain values can be derived by equating the real parts and imaginary parts in (4.36) respectively:

$$\begin{aligned} k_p &= \frac{\cos \theta_c}{|G(j\omega_c)|} \\ k_i &= \frac{-\omega_c \sin \theta_c}{|G(j\omega_c)|} \end{aligned} \quad (4.38)$$

From previous analysis and Appendix C.2, an appropriate phase margin before adding the actuator should be about the same with that of P controller, i.e. $\phi_m = 90^\circ$, and the set cross-over frequency and actuator time constant are chosen as $\omega_c = 2 \text{ rad/s}$, $\tau_i = 0.15 \text{ s}$. Then the PI controller parameters can be determined as $k_p = 132.7$, $k_i = 15.88$. This provides a satisfactory stability margin of GM=14dB, PM=74° and reasonable response speed. The closed loop response's time constant is $\tau_{cl} \approx 0.63 \text{ s}$, with corresponding settling time $t_{ss} = 4\tau_{cl} = 2.5 \text{ s}$. Note that the selected proportional gain, actuator time constant, stability margins and time constant are similar to that of the P-only controller. The steady state velocity error is

$$E_{ssv} = \lim_{s \rightarrow 0} \left(\frac{1}{s} \cdot \frac{1}{1 + \text{Con}(s)G(s)} \right) = \frac{1}{k_i \cdot G(0)} = 51.5\% \quad (4.39)$$

4.4.3. Proportional integral and derivative (PID) controller

The frequency response of the PID controller is given in Figure 4.20, which shows it will increase both the low frequency and high frequency gains. The low frequency gain is mainly determined by k_i , which should be large for the purpose of a smaller the velocity error; the high frequency gain is dependent on k_d , which should be relatively small so that high frequency noise cannot easily pass. On the other hand, the PID controller introduces a 90° phase lag at low frequencies, and 90° phase lead at high frequencies, with two cut-off frequencies at $\omega_a = \frac{k_i}{k_p}$, and $\omega_b = \frac{k_p}{k_d}$. The positions of both cut-off frequencies may impose modifications on the system stability margins.

The system specifications can set the same as those used for the PI controller ($\phi_m = 90^\circ$, $\omega_c = 2 \text{ rad/s}$ and $\tau_i = 1.5 \text{ s}$), then

$$k_p = \frac{\cos \theta_c}{|G(j\omega_c)|} \quad (4.40)$$

$$k_i = \left(k_d \cdot \omega_c^2 - \frac{\omega_c \cdot \sin \theta_c}{|G(j\omega_c)|} \right)$$

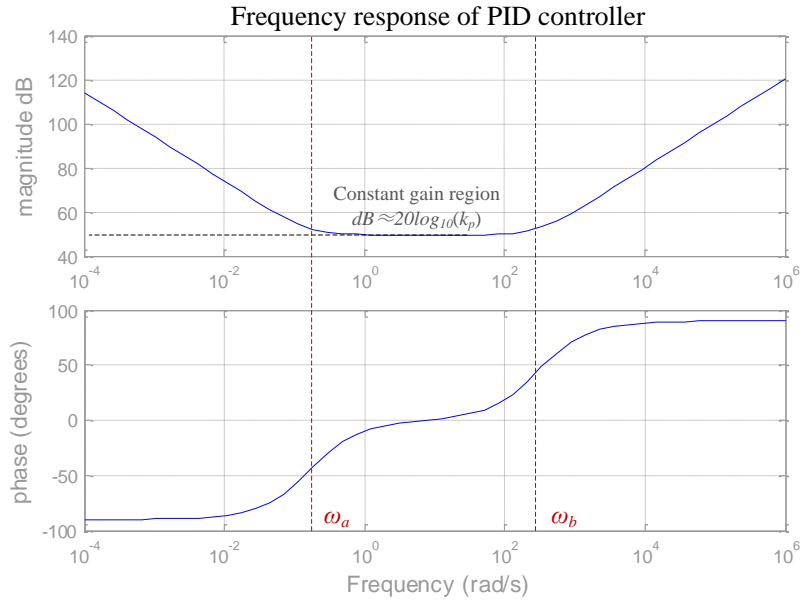


Figure 4.20 Frequency response of the PID controller with $k_p=315$, $k_i=56$, $k_d=1$

From equations (4.40) and (4.38), the expressions of proportional gain k_p are the same. In PID controller, there is an extra flexibility of determining the error sensitivity by k_d . Step responses are simulated as shown in Figure 4.21, where the controller gains are obtained by (4.40) with the derivative gain increased from 0.03 to 8.5. A larger k_d indicates higher error sensitivity, as shown in the right graph, the time needed to arrive zero error is reduced from more than 30s to 10s. This higher error rejection is achieved by over pitching the blade and slowly returning it to the demanded value, as is seen in the left graph.

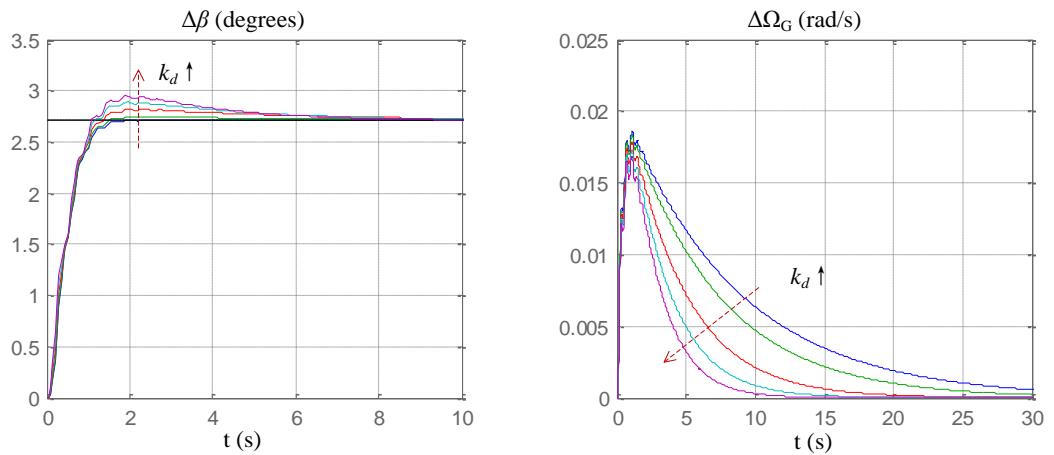


Figure 4.21 Step responses of PID controller with increasing k_d

The frequency responses of the open loop system with previous controllers and an actuator are shown in Figure 4.22. It can be seen that PI and PID controllers have similar low frequency characteristics. They have better steady state performance than the P controller. P and PI controllers have similar high frequency characteristics. Their noise rejection property is better than the PID controller. In the medium range around the cross-over frequency, the three controllers have similar performances, as they are designed to have similar stability margins.

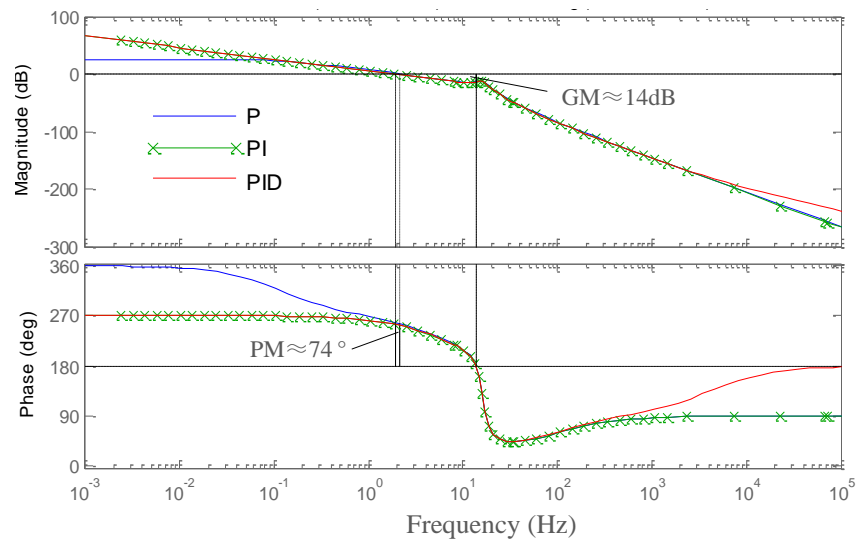


Figure 4.22 Frequency responses of the open-loop system with the three controllers

4.4.4. Model verification

The model is linearized at five different operating points, as illustrated in Table 4.1. The PID controller is designed for each operating point. Here the derivative gain is fixed, and the other gains are derived from the procedure discussed in section 4.4.3. Then a wind step of $\Delta V_w = 0.5\text{m/s}$ is imposed for both PSCAD non-linear model and the transfer function of the linear model (this step value is chosen since the non-linearity effect can be ignored for such a small deviation, as has been illustrated in Figure 4.4), and the results are compared in Figure 4.24.

It is shown that the two curves have very good correspondence at all the examined operating points, which cover the entire turbine operating range. Therefore the linear model is accurate and that the transfer functions are faithful to be employed for designing the controller.

V_w (m/s)	β (degrees)	k_p	k_i	k_d
13	0.73	132.2	16	0.033
16	15.0	183.8	37.6	0.033
19	23.3	96.4	34.07	0.033
22	28.5	59.62	30.6	0.033
25	32	40.5	27.67	0.033

Table 4.1 Controller parameters at different operating points derived from linear model

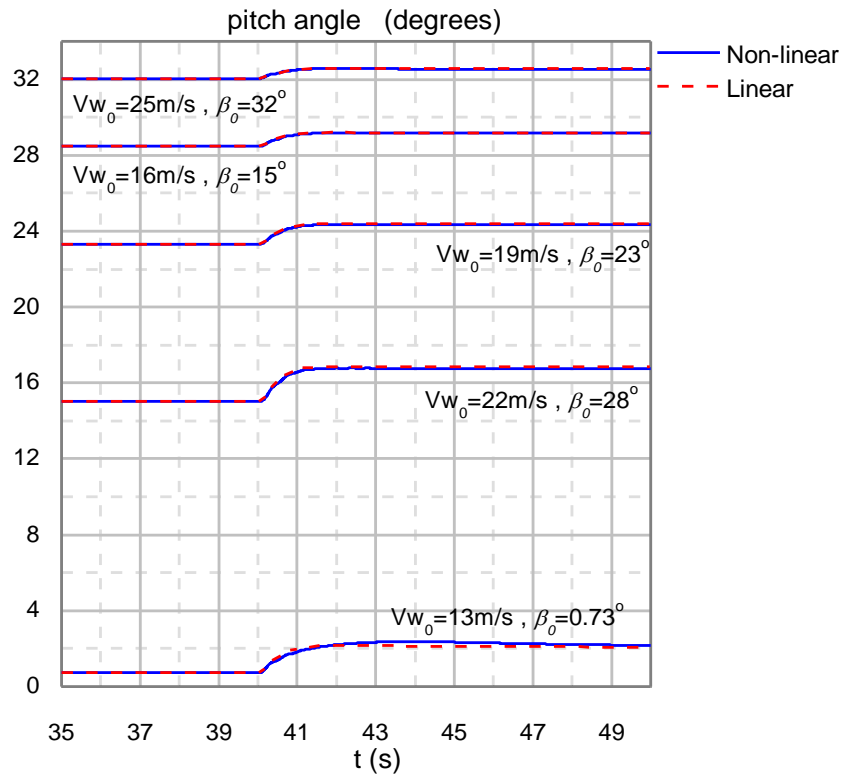


Figure 4.23 Verification between linear model and the PSCAD non-linear model at five operating points

4.4.5. Gain scheduling

The controller parameters (Table 4.1) vary with operating points. Due to the non-linearity of the wind turbine system, a constant controller setting will result in varying performances at different operating points. The gain values determined for one operating point may cause instability for another operating point. In Figure 4.24, the parameters are determined at the rated operating point, which is then tested under wind steps at four points. The pitch angle shows over-damped behaviour at a lower wind speed. This becomes under-damped at a higher wind speed and oscillations present. The peak rotor speed error is decreasing for higher wind.

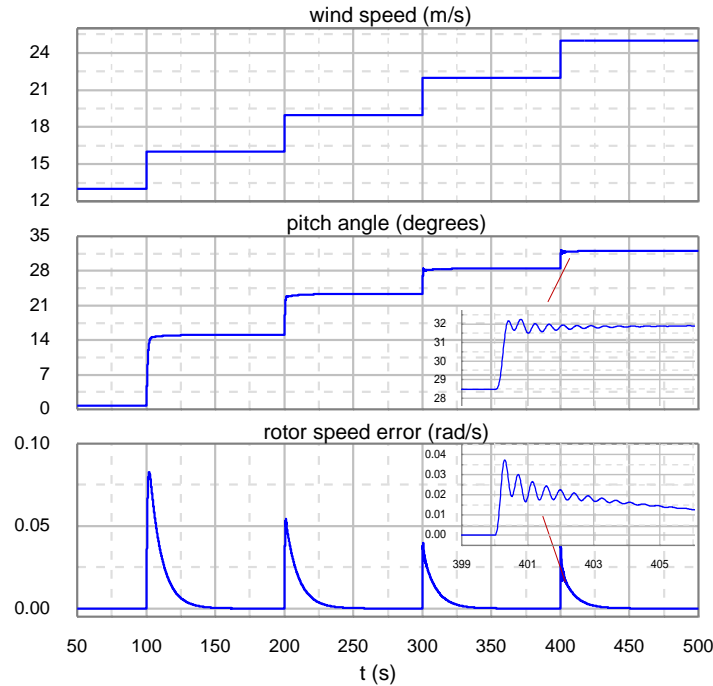


Figure 4.24 Step responses at different operating points without gain scheduling

Usually, a gain scheduling technique is implemented to counteract the non-linearity problem and maintain a consistent performance for the entire operating range of wind turbine. It is known that the system performance is dependent on the characteristic function, which is the denominator of the closed-loop transfer function (4.28). The total gain of pitch control system is the combination of the pitch sensitivity and the controller gain:

$$k_{pitch} = (-\zeta) \cdot k_{con} \quad (4.41)$$

The pitch sensitivity $|\zeta|$ is also known as the aerodynamic sensitivity with respect to pitch angle. The curve is depicted in Figure 4.25. The sensitivity increases with the pitch angle but it is not an exact linear relationship. In a real wind turbine controller, the pitch sensitivity is assumed to be linear and the controller gains can be set as a function of the pitch angle [74]. In this way, the total gain k_{pitch} is maintained at constant. In Appendix C.3, all the sensitivities and PID controller parameters are determined from the rated wind speed 13/m to the cut-off wind speed 25m/s. The product of pitch sensitivity (ζ) and proportional gain (k_p) is almost constant. The integral gain (k_i) reduces with the increase of pitch angle. Here the controller gains at each wind speed are loaded in PSCAD as look-up table.

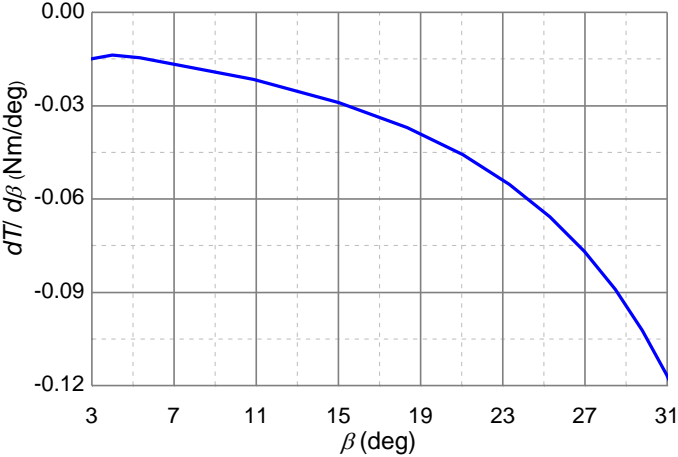


Figure 4.25 Sensitivity of the turbine aerodynamic torque versus pitch angle

Now, with a gain scheduled controller the PSCAD model is simulated for different operating points (Figure 4.26), for which similar damping, response speeds and peak errors are produced. No oscillations are present for higher wind speeds.

The three controllers with gain scheduling are tested with variable wind speeds. Wind turbulences of 10% and 20% are simulated respectively, as shown in Figure 4.27 and Figure 4.28. The P-controller shows a large discrepancy of the rotor speed from the reference point, with maximum value approaching 1.3 pu. The responses by PI and PID controllers are very similar. Visible difference only occurs at deep rotor speed ramps. The maximum transient rotor speed is below 1.19 pu, which indicates an error smaller than 1.71% of the reference value.

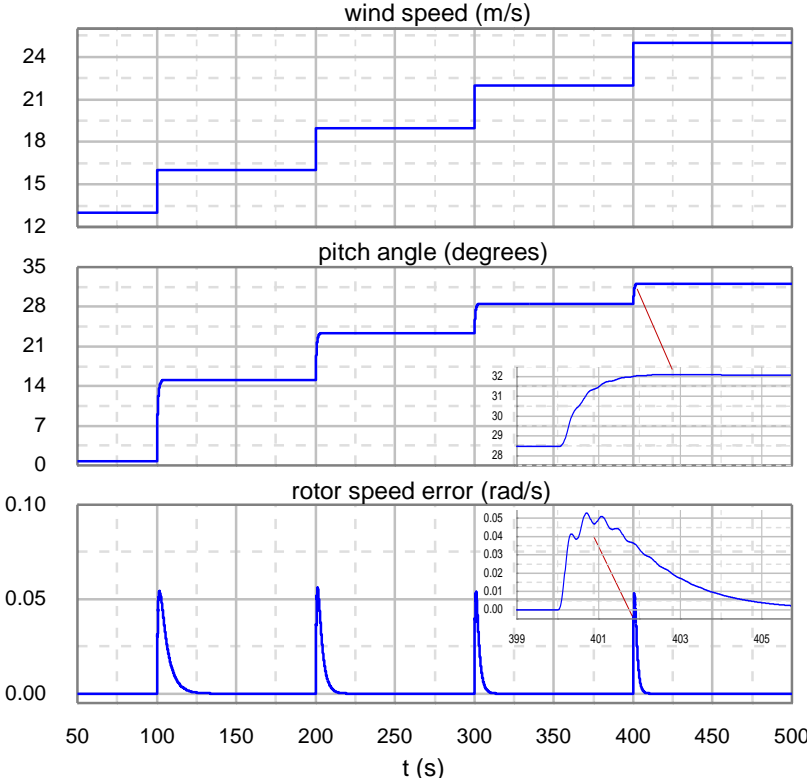


Figure 4.26 Step responses at different operating points with gain scheduling

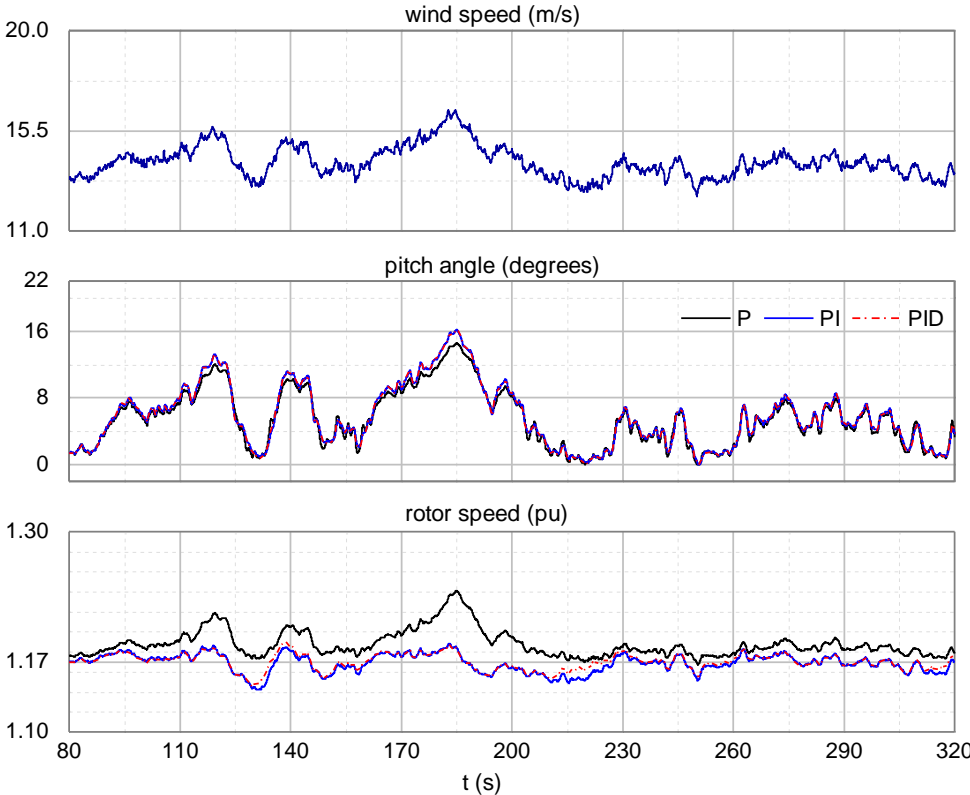


Figure 4.27 Comparison of the three pitch controllers under 10% wind turbulence

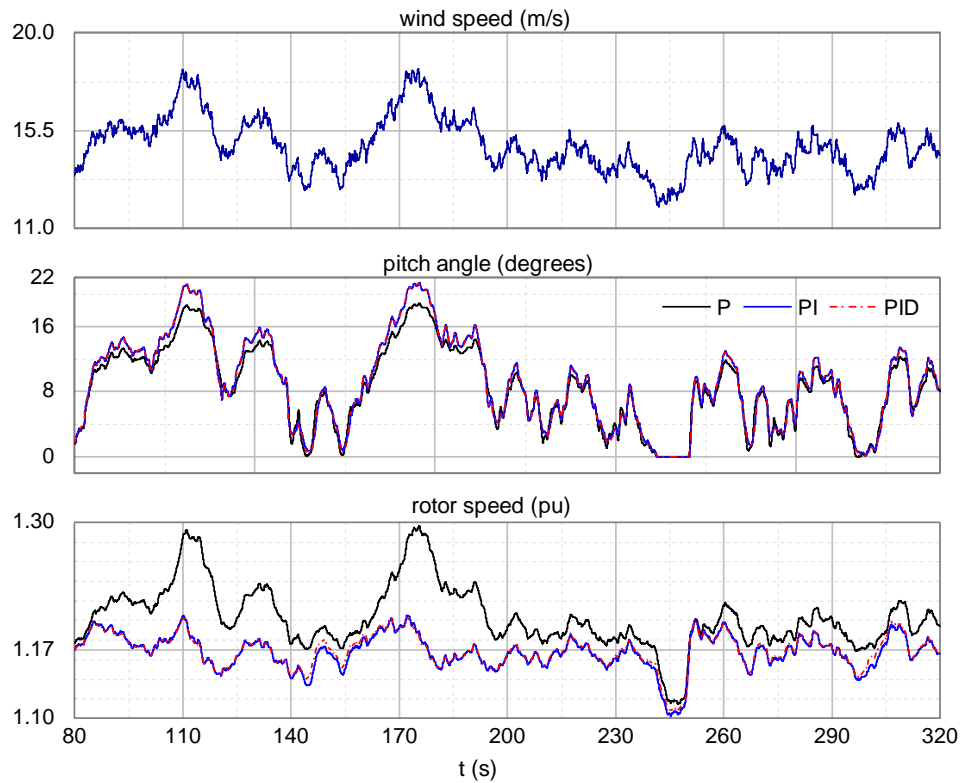


Figure 4.28 Comparison of the three pitch controllers under 20% wind turbulence

4.5. Conclusions

In this chapter, the mathematical models for DFIG electric control loops and the wind turbine mechanical loops are derived in the form of transfer functions. They are all verified by the PSCAD/EMTDC model and present a good coincidence. Optimum damping ratios are determined for the current and dc-link control loops. It is found that the damping of RSC current loop has a larger impact on the manipulated input compared with the GSC current loop. Hence for the latter, a larger damping can be set to give a smaller overshoot and response time without inducing significant transients on the GSC voltage. The dc-link dynamic is mainly investigated from the responses to power disturbances. Increasing the damping value will not increase the peak value of the manipulated input but reduce the dc-ripples and current overshoot. However, the damping should not be too large as there is a trade-off between a smaller overshoot and a larger settling time.

For pitch controller, the three most commonly used controllers (P, PI and PID) are evaluated with respect to the system margin stabilities. For the open-loop system including the controller and actuator, a phase margin of approximately 75° and a gain

margin larger than 10 dB is recommended, as it gives reasonable speed with no overshoot in the pitching action. The P controller leaves an error on the rotor speed. PID controller with a larger derivative term has better error sensitivity in step response. However, in practical variable wind speeds, its response is similar with PI controller. Gain scheduling is implemented, where the optimum controller parameters for each operating point are obtained as a look-up table. It is tested for various operating points and all of which show satisfactory performance.

With a clear understanding of different control loops' dynamics and the mathematical models well designed, the author is ready to present the interactions of these control loops and the strategy of the controller bandwidths coordination. System behaviours during a grid voltage drop are investigated in next chapter. Controller coordination scheme is used to enhance the wind turbine's fault ride through capability.

Chapter 5. Controller Coordination to Improve Fault Ride-through Capability

5.1. Introduction

This chapter mainly focuses on control strategies that can improve the wind turbine system performance during a grid fault. Firstly, the DFIG wind turbine behaviour during a grid voltage drop will be analysed. In this case, two common problems that need to be dealt with are the electrical transients and mechanical oscillations. The former can cause severe stresses in the converter and destabilize the DFIG control system, while the latter may stress the shaft system and trip the wind turbine. Two control strategies for the RSC current loops are investigated: demagnetizing current injection and a modified control tuning. The purpose is to reduce the duration of electric transients after a grid voltage change. Meanwhile, an improved tuning method and adding compensating terms for the GSC dc-link control are investigated to reduce dc-link voltage fluctuations. Besides, the implementation of crowbar protection, as well as its coordination with the pitch control, damping control and the RSC electric torque control are discussed that will mitigate the torsional oscillations caused by a grid fault. All the above strategies have been implemented in PSCAD. The main contribution made from this work is to provide a proper system integration and bandwidth allocation for the overall DFIG wind turbine control system.

5.2. RSC current control strategy for improving stability in small dips

In this section, we consider a small voltage dip, where the converter current and dc-link voltage are within their maximum limits, and also the converter is not saturated by over voltage. This means the controller can work effectively.

5.2.1. DFIG behaviour under voltage dips

A detailed study of DFIG fault behaviour has been shown in [73]. This chapter briefly describes theoretical principles. Consider a balanced three phase voltage dip: here it is assumed that the voltage drops to a fault value \hat{V}_{fault} from \hat{V}_{pre} abruptly at time t_0 . From equation (3.23), the steady state flux before and during the dip are expressed as

$$\bar{\psi}_{sf} = \begin{cases} \frac{\hat{V}_{pre}}{j\omega_s} \cdot e^{j\omega_s t} & \text{for } t < t_0 \\ \frac{\hat{V}_{fault}}{j\omega_s} \cdot e^{j\omega_s t} & \text{for } t \geq t_0 \end{cases} \quad (5.1)$$

where the voltage drop on the stator resistance is neglected. \hat{V}_{pre} is the peak the stator voltage in the normal operating condition. The peak fault voltage is $\hat{V}_{fault} = (1 - p)\hat{V}_{pre}$, p is the fault depth.

An important feature of the voltage drop is that the stator flux cannot change suddenly from $\bar{\psi}_s$ to $\bar{\psi}_{sf}$. Instead, as well as the steady state (or forced) flux component $\bar{\psi}_{sf}$, another flux component is generated in order to compensate for the reduced voltage. This is called natural flux $\bar{\psi}_{sn}$. It is fixed to the stator reference frame and decays exponentially to zero. For the open rotor circuit condition where no rotor current is considered, the natural flux can be expressed as

$$\bar{\psi}_{sn} = \bar{\psi}_{sn0} \cdot e^{-t/\tau_s} \quad (5.2)$$

It decays with a stator time constant $\tau_i = L_s/R_s$ (about 0.8s – 1.5s for MW level generators), which is very long compared to the average fault time. The initial value is determined by the fault depth $\bar{\psi}_{sn0} = p\hat{V}_{pre}/j\omega_s$.

Seen from the rotor reference frame, the forced flux rotates at the slip frequency $\omega_r = s\omega_s$, inducing an steady state emf just as in normal operation. However, the natural flux rotates in the inverse direction to the rotor speed $\omega_m = (1 - s)\omega_s$. Then the total emf is the sum of the two components [94]:

$$e_r(t = t_0) = \frac{L_m}{L_s} \left(\underbrace{(1 - p) \cdot V_{pre} \cdot s}_{\psi_{sf}} - \underbrace{p \cdot V_{pre} (1 - s)}_{\psi_{sn0}} \right) \quad (5.3)$$

As a result, the originated rotor current also involves two components: the steady state current component \bar{I}_{rf} and the natural current component \bar{I}_{rn} . In the RSC current control, the feedback terms are constituted by the addition of these two components. The former rotates at synchronous speed and is viewed as a constant in the vector control

reference frame. The latter is seen by the control reference frame as a sinusoidal component at the grid frequency. Hence, it is not as easy to compensate for as the steady state term. As a consequence, this perturbation further causes electric transients in electric torque rotor power and dc-link voltage.

From equation (5.3), in a severe voltage dip, the natural flux induced emf is higher than the steady-state emf, causing the saturation of the converter and hence a loss of control. For this case, a hardware protection technique must be implemented, which will be discussed in Chapter 5.4. For a shallower voltage dip, other strategies can be implemented in order to reduce the electric transients. The rest of Chapter 5.2 describes mitigating strategies, for dealing with electric transients caused by a grid fault, using the rotor current control. The first method involves injecting a demagnetizing current at the controller input. This technique is developed recently by other authors [95] and is improved by Lopez [94]. The limitations are discussed. Then the influence of varying the controller bandwidths on the system robustness to grid disturbances is discussed. In the end, a new strategy to reduce electric transients is proposed. This method is easier to implement and has the potential for cost savings since no extra compensator is needed.

5.2.2. Demagnetizing current injection [94]

The machine equations represented in the stator reference frame (or stationary frame) are given in (5.4) [73]:

$$\begin{aligned}\bar{V}_s^s &= -R_s \bar{I}_s^s + \frac{d\bar{\psi}_s^s}{dt} \\ \bar{\psi}_s^s &= -L_s \bar{I}_s^s - L_m \bar{I}_r^s\end{aligned}\quad (5.4)$$

In this thesis generator convention is used for the machine equations where the positive stator and rotor currents are flowing from the machine to the grid. Then the changing of the stator flux can be expressed by the rotor current:

$$\frac{d\bar{\psi}_s^s}{dt} = \bar{V}_s^s - \frac{R_s}{L_s} \bar{\psi}_s^s - \frac{R_s L_m}{L_s} \bar{I}_r^s \quad (5.5)$$

In the case of a grid fault, the first term is the remaining voltage that produces a synchronously rotating flux; the second term represents the natural flux decay; the third

term reveals the effects of rotor current. This can either accelerate the flux decay if this current component is in phase with the natural flux, or decelerate this process when it is in anti-phase with the natural flux. The rotor current term may completely cancel the effect of second term, and make the flux derivative positive. In that case, the natural flux will not be reduced and may even increase and the control will go unstable [96]. The magnitude and phase of this current is closely related to the controller gains, which will be discussed later. A well-known method to counteract the natural flux is thus to introduce a current in phase with the natural flux. By doing this, it is also possible to reduce the induced rotor voltage.

Machine equations in the rotor reference frame are given as:

$$\begin{aligned}\bar{V}_r^r &= -R_r \bar{I}_r^r + \frac{d\bar{\psi}_r^r}{dt} \\ \bar{\psi}_s^r &= -L_m \bar{I}_r^r - L_s \bar{I}_s^r \\ \bar{\psi}_r^r &= -L_m \bar{I}_s^r - L_r \bar{I}_r^r\end{aligned}\quad (5.6)$$

The induced rotor voltage is expressed by the natural flux as

$$\bar{V}_m^r = \frac{L_m}{L_s} \frac{d\bar{\psi}_{sn}^r}{dt} - R_r \bar{I}_m^r - \sigma L_r \frac{d\bar{I}_m^r}{dt}\quad (5.7)$$

Seen from the rotor frame, the natural flux and the corresponding current rotate in opposite direction with respect to the synchronous reference frame, i.e. $\bar{\psi}_{sn}^r = |\bar{\psi}_{sn}| \cdot e^{-j\omega_m t}$, $\bar{I}_m^r = |\bar{I}_m| \cdot e^{-j\omega_m t}$, hence equation (5.7) can be represented as

$$\bar{V}_m^r = \frac{L_m}{L_s} (-j\omega_m \bar{\psi}_{sn}^r) - R_r \bar{I}_m^r + j\omega_m \sigma L_r \bar{I}_m^r\quad (5.8)$$

Neglecting the voltage drop on the rotor resistance, in order to completely eliminate the emf, a demagnetising current should be set as

$$\bar{I}_m^r \approx c_d \cdot \bar{\psi}_{sn}^r\quad (5.9)$$

where $c_d = \frac{L_m}{L_s \sigma L_r}$. It can be noticed that the coefficient is independent of the rotating speed of the space vectors.

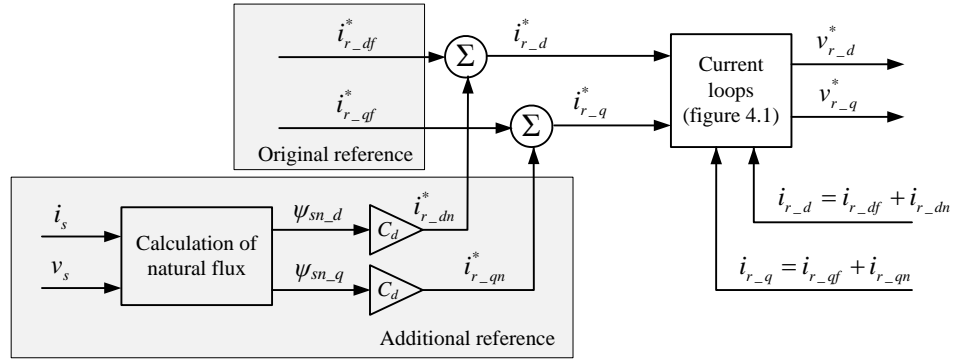


Figure 5.1 Demagnetizing current injection [73]

The control scheme with demagnetizing current injection is shown in Figure 5.1. The subscript 'f' denotes the quantities induced by the forced flux. As the control is implemented in the excitation (synchronous) reference, the computed demagnetizing currents are sinusoidal. Correctly implementing this method is substantially dependent on accurate identification of the natural flux. The method to calculate the natural flux is shown in Figure 5.2, where the total flux is obtained from (5.4) and the forced flux is obtained according to (5.1).

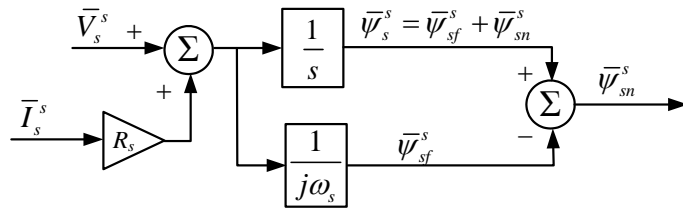


Figure 5.2 Calculation of the natural flux [73]

The total flux is obtained by an integration of the stator voltage. If an error is accumulated, dc offset will present in the natural flux which will cause additional oscillations in the control loop during normal operation. More importantly, setting a proper initial value for the integrator is necessary to remove most of the dc component.

Simulations were undertaken in PSCAD. The DFIG initially operates at 17% above the synchronous speed with a full load. At $t = 2s$, the grid voltage drops to 50% of its rated

value. The space vectors of the stator total and natural flux are shown in Figure 5.3. The natural flux reaches the peak value immediately when the fault occurs, and decays to zero. The centre of the blue circle moves along with the evolution of natural flux.

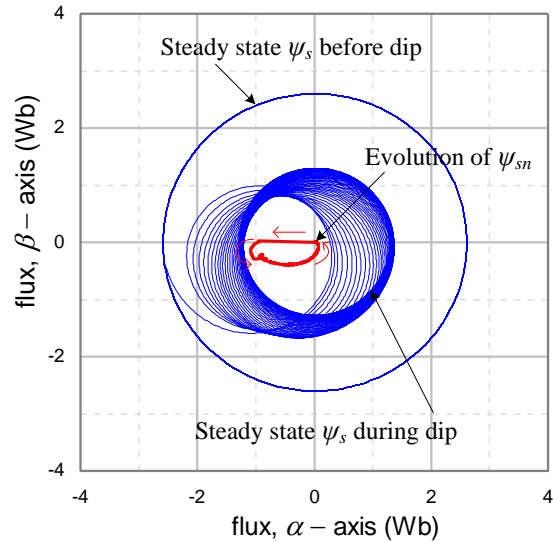


Figure 5.3 Variation of the total flux and natural flux in a voltage dip

The necessary demagnetizing current in the synchronous reference frame is compared with the measured rotor current in Figure 5.4. At this point, this demagnetizing current has not yet been applied. With the coefficient $C_d \approx 3.0$, the rotor current and the injected demagnetizing current are in-phase and have almost the same oscillation amplitude. Hence, the natural flux induced component could be compensated at the controller input and will not circulate within the loop.

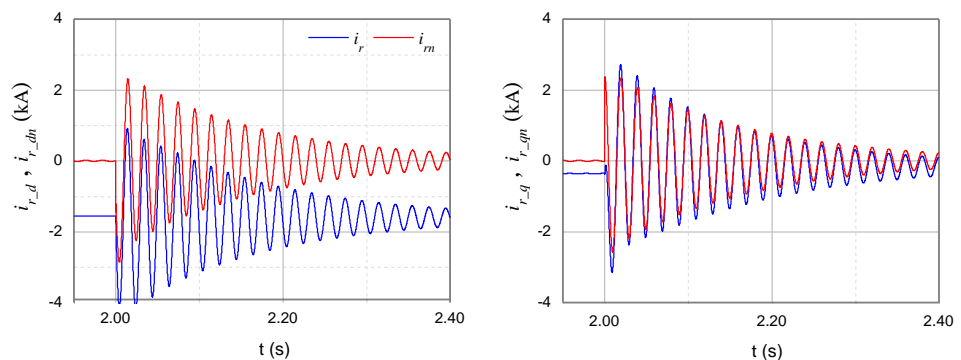


Figure 5.4 Original rotor current without compensation and the calculated demagnetizing current in d-q reference frame (50% voltage drop at full speed)

Simulation results of the conventional control scheme without demagnetizing current injection are compared with the improved strategy (Figure 5.5). Both the controller bandwidths are set to be at 30Hz for now. The rotor voltage, current, natural flux, rotor power, electric torque and dc-link voltage are all illustrated. With the improved strategy, the high frequency oscillations decrease quickly (approximately 0.6s) due to the fast decay of the natural flux. Significant improvements are seen in the rotor voltage, power, electric torque and the dc-link voltage, as their peak transients are all reduced within their operating limits.

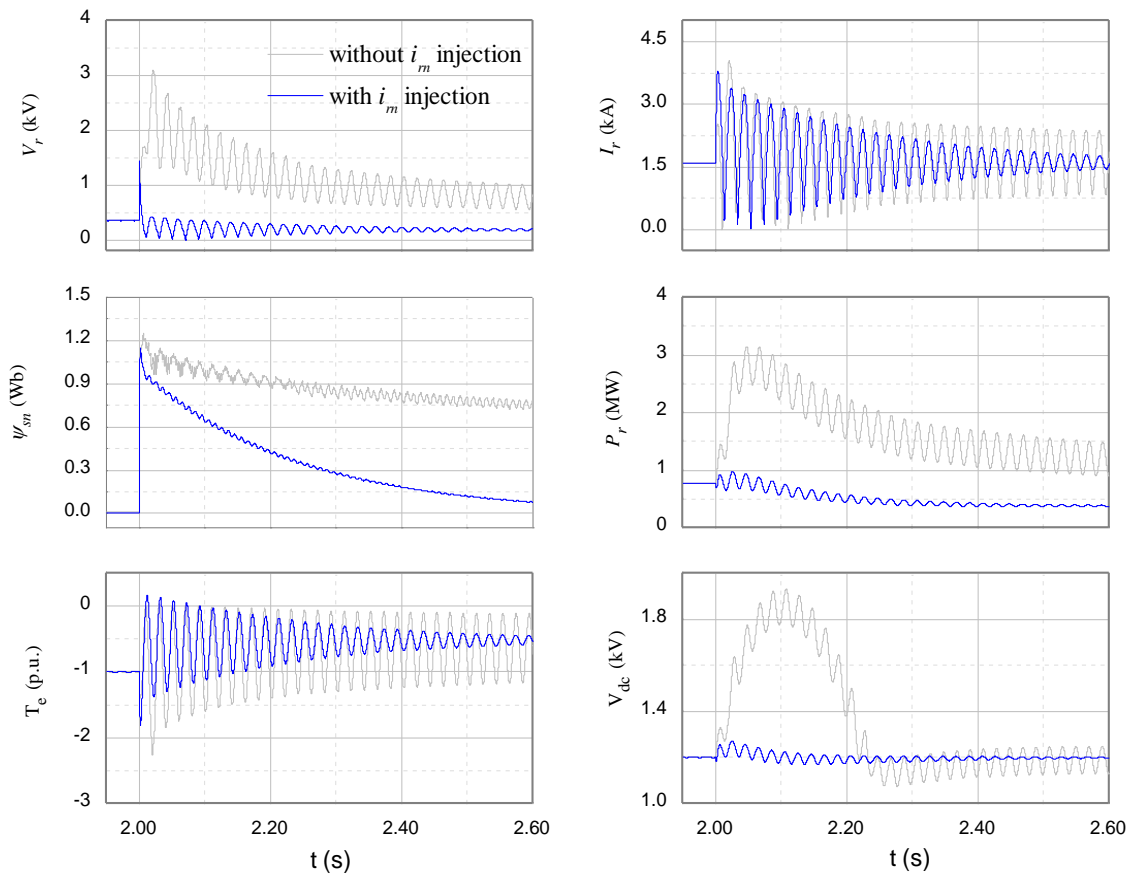


Figure 5.5 Improvement by injecting demagnetizing current at 30Hz controller bandwidth

5.2.3. Influence of controller tuning

The natural current can be modified by the controller gains. Neglecting the voltage drop due to the resistance, equation (5.8) is represented as

$$\bar{V}_m = \bar{E}_m + jX_r \bar{I}_m \quad (5.10)$$

where

$$X_r = \omega_m \sigma L_r$$

$$\bar{E}_m = \frac{L_m}{L_s} (-j\omega_m \bar{\psi}_{sn}) = \text{emf induced by the natural flux at the rotor windings}$$

\bar{V}_m = Voltage generated at the converter due to the natural flux

From the RSC control block diagram (Figure 4.1), the relationship of the converter voltage and rotor current is [73]

$$\bar{V}_m = -\bar{k}_{PI}(-\bar{I}_m) = k_p \bar{I}_m - j \frac{k_i}{\omega_s} \bar{I}_m \quad (5.11)$$

The phasors are depicted in Figure 5.6. If the integral function dominates, the resulting phasor diagram is similar to the left one. The rotor current tends to be in anti-phase with the natural flux. According to (5.5), this configuration can slow down the damping effect and may even result in negative damping. In contrast, if the proportional effect dominates, as shown in the right diagram, the rotor current has positive projection on the natural flux vector (or in-phase), which assists in the damping effect [73].

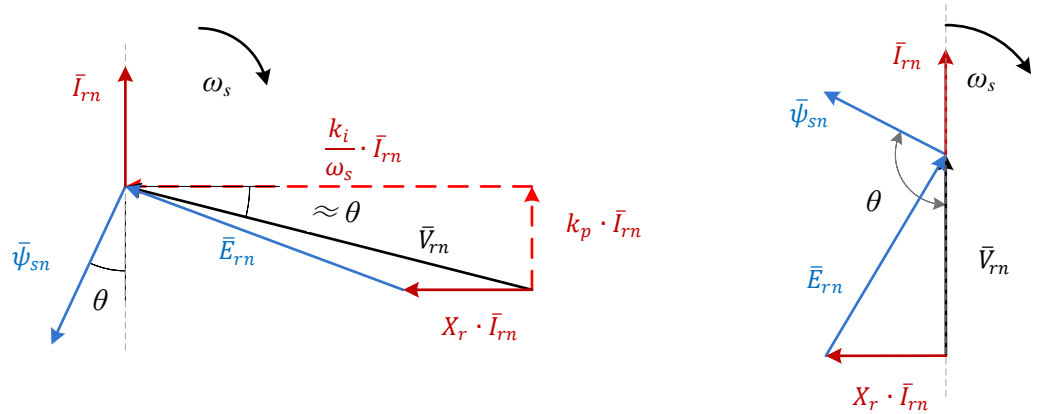


Figure 5.6 Phasor diagram using PI controller. Left: predominant integral action, Right: predominant proportional action [96]

Both of the controller gains increase with the loop bandwidth as depicted in Figure 5.7. The proportional term needs to be significantly larger than the integral action to make the current in phase with the flux and accelerate its decay (see Figure 5.7). This is only possible at very low frequencies (around 10Hz). It is more evident when looking at the

responses of natural flux in Figure 5.5 and Figure 5.8. Here the grey curves represent responses without demagnetizing current injection. At 50Hz bandwidth, the natural flux does not decay at all since the damping has been completely cancelled by the anti-phase rotor current.

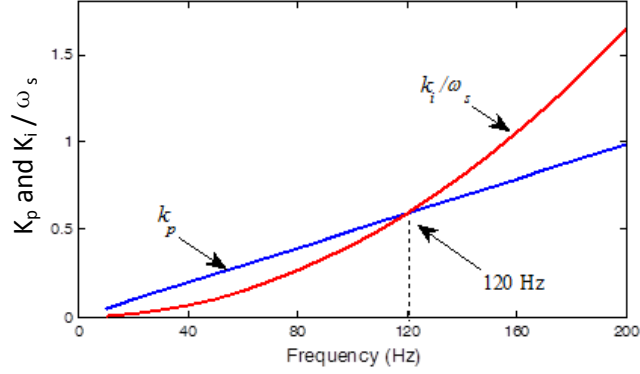


Figure 5.7 Changing of the dominant control action with the increase of bandwidth

Since the controller's noise rejection ability improves with higher bandwidths (gains), a smaller i_{rm} is produced. Although the integral action becomes more significant, the damping of ψ_{sn} may still be positive. As seen in the 150Hz and 200Hz simulations in Figure 5.8, the natural flux decaying becomes faster at a higher bandwidths. Note that it requires a very large converter voltage in order to compensate for the current disturbance, which is not feasible in practical design.

In the following, the control bandwidths at which the flux damping is small or negative (system becomes unstable) will be evaluated. Since the stator voltage only has the forced component, i.e. $\bar{V}_{sn}^s = 0$, equation (5.5) can be restated in scalar form as (refer to Figure 5.6):

$$\frac{d\bar{\psi}_{sn}}{dt} = -\frac{R_s}{L_s}\bar{\psi}_{sn} + \frac{R_s L_m}{L_s}\bar{I}_r \cos \theta \quad (5.12)$$

The following relationship should be satisfied for a system to remain stable during a fault

$$\begin{aligned} \frac{d\bar{\psi}_{sn}}{dt} &< 0 \\ \Rightarrow L_m \bar{I}_r \cos \theta &< \bar{\psi}_{sn} \end{aligned} \quad (5.13)$$

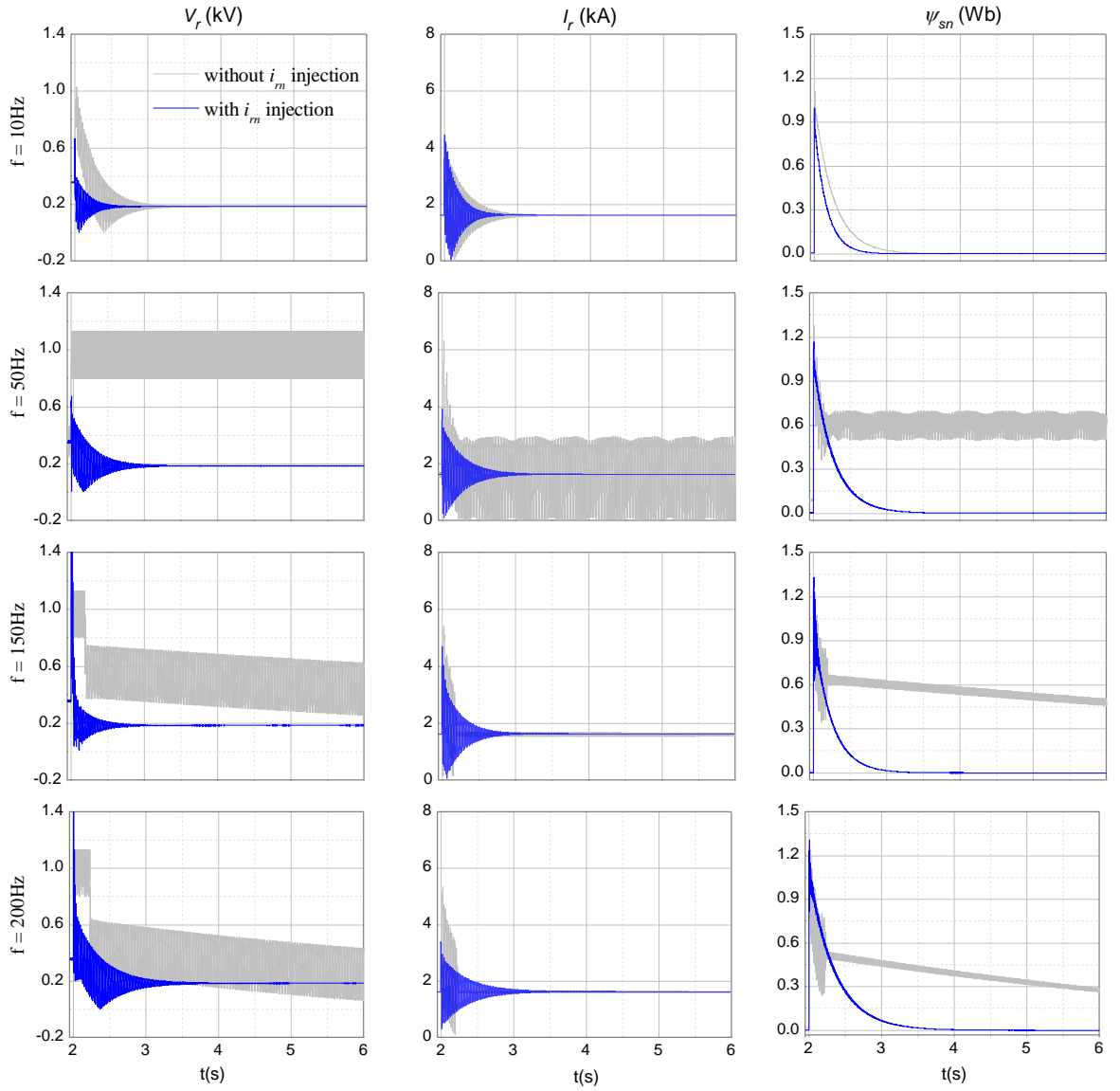


Figure 5.8 Comparison of different controller bandwidths in a 50% voltage dip

Introducing the expressions (5.10), (5.11) into the stability condition (5.13), the following relationship can be derived [73]:

$$y = \frac{(L_m^2 / L_s) \omega_m \cos \theta}{\sqrt{k_p^2 + (k_i / \omega_s)^2 + \sigma L_r \omega_m}} < 1 \quad (5.14)$$

$$\tan \theta = \frac{k_p}{k_i / \omega_s}$$

Equation (5.14) is a necessary condition for stability. In fact, from the simulations, absolute stability is achieved when $y < 0.7$. Figure 5.9 presents the curves of y versus controller bandwidth. The effects of changing the damping ratio and rotor speeds are also

plotted for comparison. It can be concluded that the bandwidths for which the lowest stability presents are around 50Hz. The unstable region is not symmetrical about 50Hz, as can be seen the stability is resumed at around 130Hz for 1.2 damping and 1.17pu rotor speed. Using a larger damping improves the stability for the medium control bandwidths, while increasing the rotor speed will reduce the stability for both the medium and higher bandwidths.

Using the demagnetizing current can improve the stability for all the controller bandwidths of interest. As shown in the blue curves in Figure 5.8, the natural flux is damped after about one second. When using this method, the damping ratio (k_p) needs to be reduced with the increase of frequency to maintain stability. As a consequence, the controller can be no faster than 200 Hz due to insufficient damping for higher bandwidths.

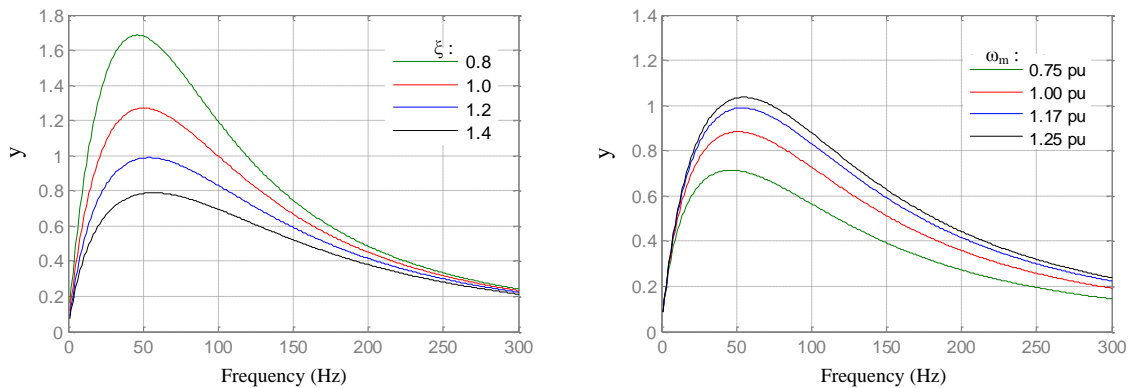


Figure 5.9 Plots of the stability function versus controller bandwidths with different damping ratios with $\omega_m=1.17$ pu (left) and rotor speeds with $\xi=1.2$ (right)

5.2.4. Stability improvement by coordinated dq-controller tuning

Since the demagnetizing current injection method has its limitations and requires extra computation efforts in order to obtain the natural flux, an alternative strategy is proposed here. If the need to fit with other cascaded control-loops is not considered, the RSC current control can be set at 10Hz, which has shown good stability during faults, as is seen Figure 5.8. However, for practical wind turbines, the q-loop is usually cascaded with a damping controller [72, 97] in order to reduce the torsional oscillations, which will be investigated later. Hence the inner-loop should not be set too low or else there is no much head room left for the outer loop to perform its function effectively. Nevertheless, it has

been shown that at higher bandwidth, large electrical oscillations will exist for a long time after the fault. This is because the controller is dominated by the integral action and sets i_{rn} in anti-phase with the natural flux (see the left graphs of Figure 5.10 or $\bar{\psi}_{sn}$ and \bar{I}_{rn} in Figure 5.11).

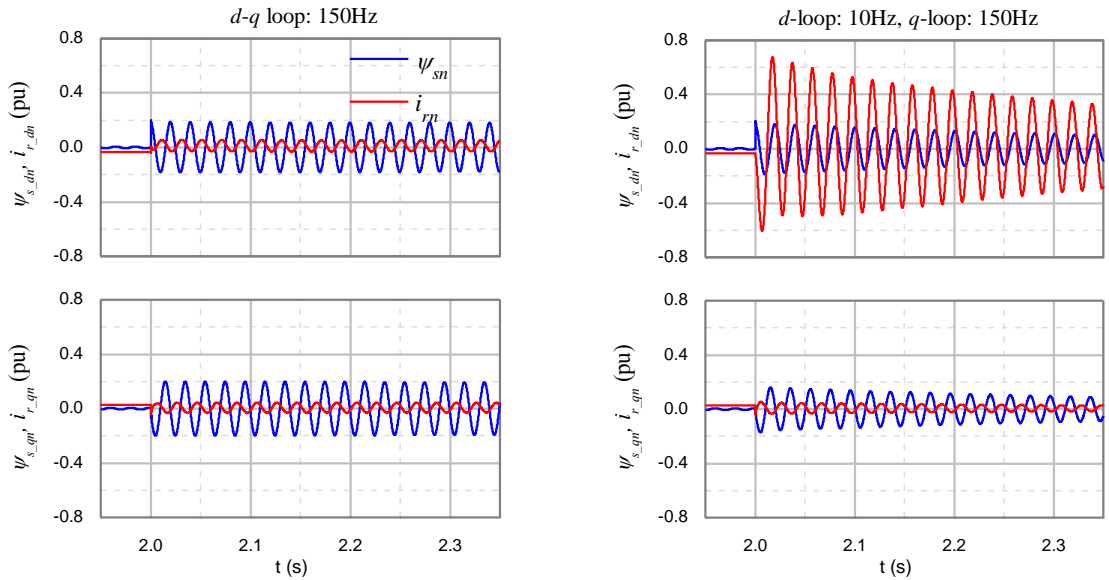


Figure 5.10 Natural flux and the induced rotor current result from the two controller settings

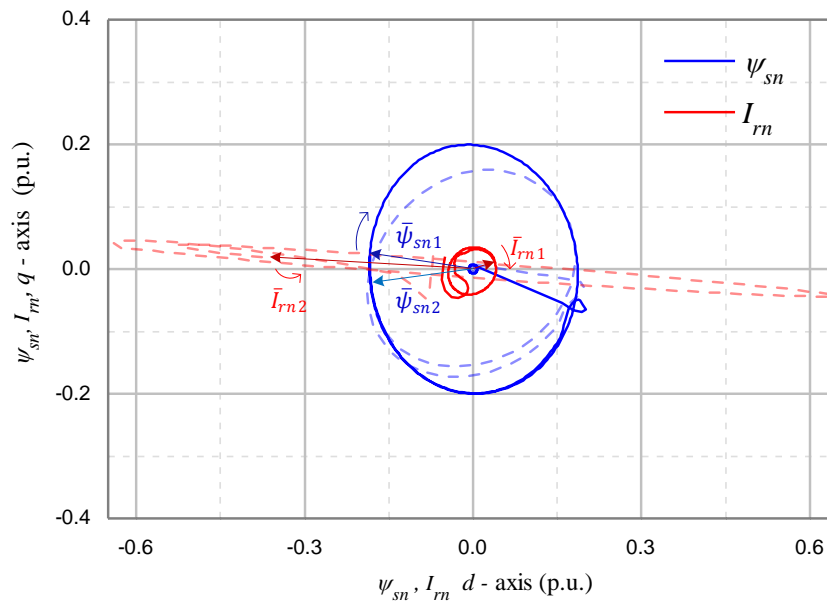


Figure 5.11 Relative positions of the natural flux and the induced rotor current in d-q reference frame for the two controller settings

The alternative way proposed here is to set one of the orthogonal control loops to a higher bandwidth and keep the other bandwidth low (no larger than 10Hz). In this thesis, the q-loop is set at higher speed (150Hz) for purposes of reducing the transients in electric torque and designing the damping controller. The modifications made to the natural flux and the rotor current can be viewed from the right graphs in Figure 5.10. As the forced current component appears as a dc component in the d-q reference frame, this has been removed from the rotor current here for simplicity and only the induced current i_{rn} is presented. In Figure 5.11, the flux (blue) and current (red) trajectories from the modified controller are depicted in dashed lines. It can be seen that $\bar{\psi}_{sn2}$ and \bar{I}_{rn2} arrive at the d -axis simultaneously. As the d-controller has smaller gains and is proportional-dominant, the current has larger magnitude and is nearly in phase with the natural flux. On the other hand, as the current phasor (\bar{I}_{rn2}) passes through the q-axis, its magnitude is decreased and it turns in anti-phase with the natural flux. The performances of three different controller settings (Table 5.1) during a 20% voltage dip are compared in Figure 5.12.

The total effect is that the modified controller C has the both the advantages of A and B. Compared with controller B, the natural flux is damped faster due to the contribution of large demagnetizing current generated from the d-loop. On the other hand, the peak transients of the rotor current, electric torque and dc-voltage are reduced compared with controller A due to contribution of high controller gain values in the q-loop.

Controller setting	A	B	C
d-loop	10 Hz	150 Hz	10 Hz
q-loop	10 Hz	150 Hz	150 Hz

Table 5.1 Three controller settings of the RSC current loops

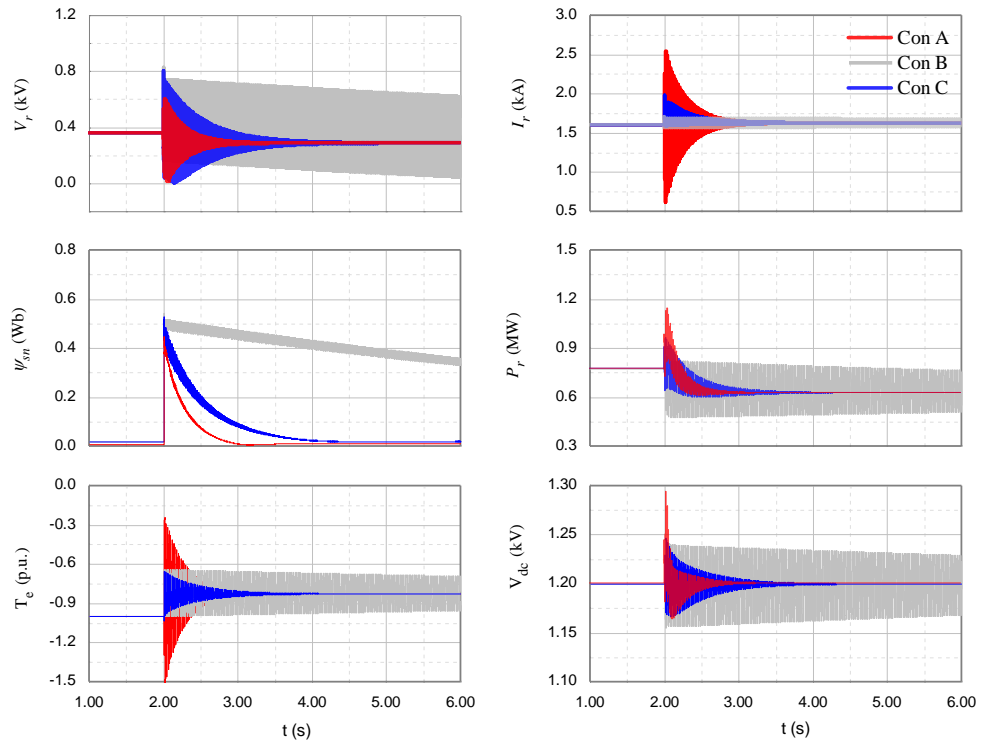


Figure 5.12 Response comparison of the three controllers

5.3. Improvement of dc-link control for limiting the voltage fluctuations

The mathematical model of dc-link control has been described in Chapter 4. From the small signal block diagram (Figure 4.6), the dc-link voltage fluctuations are mainly affected by two factors: the perturbations of injected power from the RSC and the grid voltage disturbances. The latter usually occurs during grid faults and the former can be as a result of either grid voltage dips or the change of torque demand. In this section, an investigation is carried out from the above two aspects. The simulations show that dc-link fluctuations can be reduced through proper tuning and feed-forward compensation.

5.3.1. Bandwidth coordination

Generally, dc-link voltage ripples are caused by an unbalance of power flow between the injected RSC power and the GSC power absorption at the dc-link capacitor. Considering the case of changing the torque demand, the amount of power increased at the machine-side of the capacitor, ΔP_{RSC} , is affected by the torque-loop control. How fast this power is removed is determined by the dc-link control (for the GSC) and will affect the peak ripple on the capacitor. From Chapter 4.1.2, the transfer function of electric torque can be represented by a first order system. Assuming the time constant is

$\tau_i = 0.1s$, this is equivalent with a dc-link control frequency of $\omega_n = 1/(\xi \cdot \tau_i) = 4rad/s(0.64Hz)$. However, the dc-link control bandwidth should be set higher than this value in order to transfer the power immediately to the grid. In Figure 5.13, the response to a 1 p.u. torque step is obtained from MATLAB, with the controller bandwidth increasing from 1Hz to 12Hz. It can be seen that higher bandwidths give smaller peak dc-ripples. For $f_{DC} > 6Hz$, the ripple has been reduced to below 0.05 p.u. The drawback of using a higher bandwidth for dc-link control is that the power and grid current can be very high during grid fault and may saturate the converter, as seen in Figure 5.14.

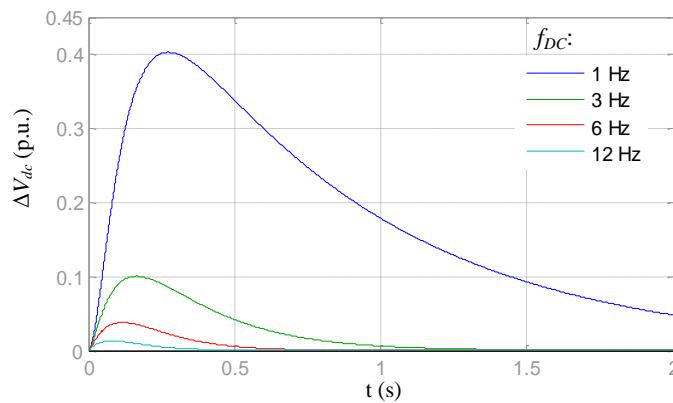


Figure 5.13 Dc-voltage responses to a torque step under different controller bandwidths

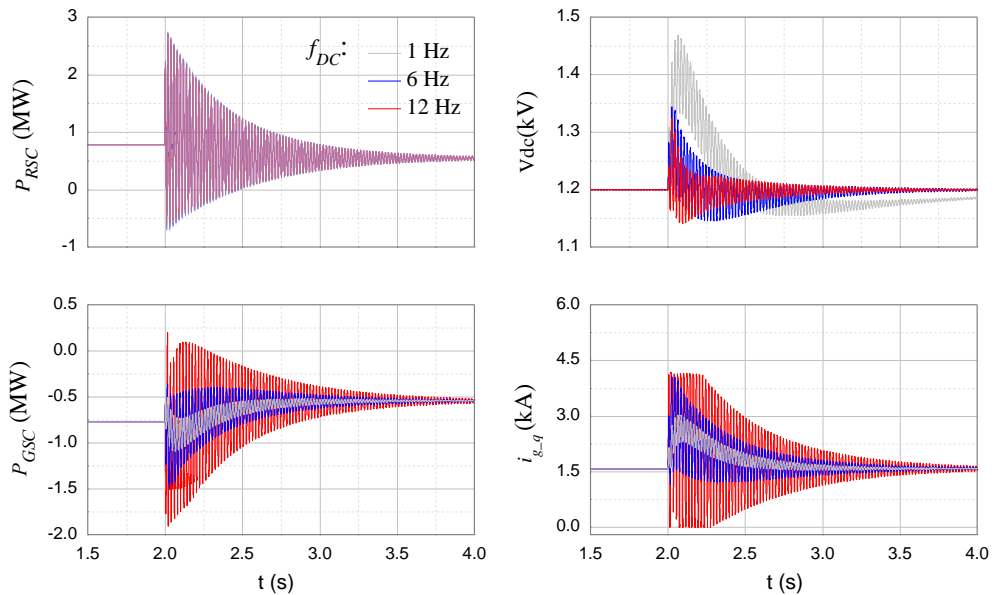


Figure 5.14 Responses of the dc-link control under 30% voltage dip for three different bandwidths

5.3.2. Feed-forward compensation

In the case of a grid voltage dip, the main reason causing the dc-link voltage to increase beyond the point where control can cope normally is the transient rotor voltage induced by the natural flux. The high transients are also present in the power injected at the dc-link, which are difficult to remove due to the potential saturation of the control current. The extra power can be removed from the rotor current control, with demagnetizing current injection, as shown in Figure 5.5. Despite the effort it takes to obtain the natural flux, this is an effective way to reduce dc-fluctuations. If no compensation is added on the RSC, it can be done conveniently by feed-forward compensation in the dc-link control, as shown in Figure 5.15. Similar strategies have been adopted by other authors [98, 99].

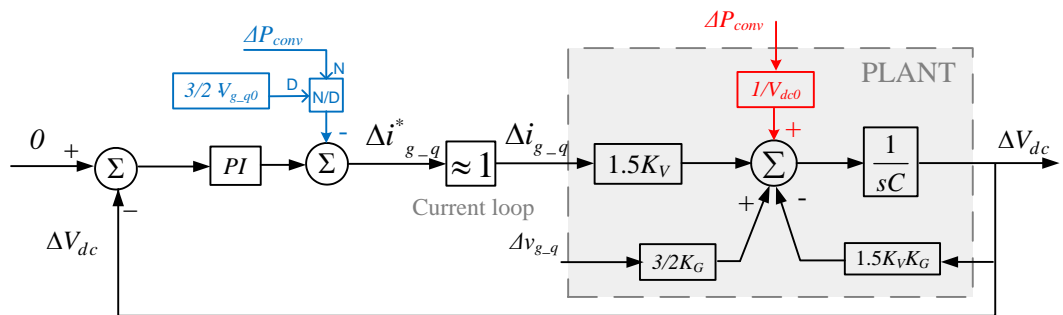


Figure 5.15 Control strategy of the dc-link using feed-forward compensation

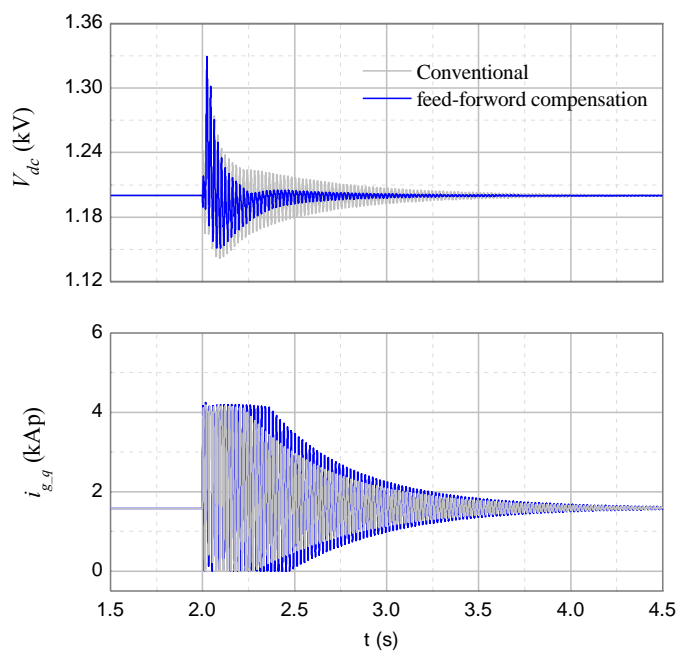


Figure 5.16 Impact of feed-forward compensation on dc-link control

The simulations with and without feed-forward compensation have been compared in Figure 5.16. The improvement in dc-dynamics is at the expense of the increased length of current oscillations. Besides, the effectiveness is often limited by the GSC current rating.

5.4. Active crowbar protection for severe voltage dip

The strategies of either an improved controller tuning or adding extra compensation in principle work in similar ways. That is, they reduce the transients of some parameters while keeping others high. This can be implemented without problems for a shallow voltage dip. However, for a severe voltage dip, where the converter may be saturated by over-voltage or current, a hardware protection is necessary. Most of the DFIG wind turbines are equipped with an active crowbar protection circuit. The general layout has been presented in Chapter 3.1.5. In this section, the active crowbar protection is implemented in PSCAD for different depths of faults.

5.4.1. Crowbar activating strategy

The block diagram used to generate a crowbar switching signal is constructed as in Figure 5.17. When any of the monitored parameters (rotor current, voltage or dc-link voltage) exceed their upper limit, the switch will be on ('1') and the crowbar is engaged. If all of the monitored parameters drop below their lower limits, the switch will be off to release the crowbar. The upper and lower limits of different parameters are given in Table 5.2. An S – R flip flop block is adopted here. The output state Q may be modified on the triggering of the clock signal C (rising or falling edge). If S and R are in the same state (both are 0 or 1), Q remains at its previous state. Otherwise, it will duplicate the state of S. A delay block is added after the flip-flop to give a delay time when switching off the crowbar. Note this should be set in coordination with the clock frequency C. If f_c is too low, the converter may be subjected to excessive transient rotor voltage or current before the crowbar is activated. On the other hand, a short off-delay time may lead to frequent cycles of the crowbar triggering, being turned off and re-triggering even after the fault is cleared. Here f_c is set at ten times the grid frequency (500Hz), in combination with an off-delay time 0.4s.

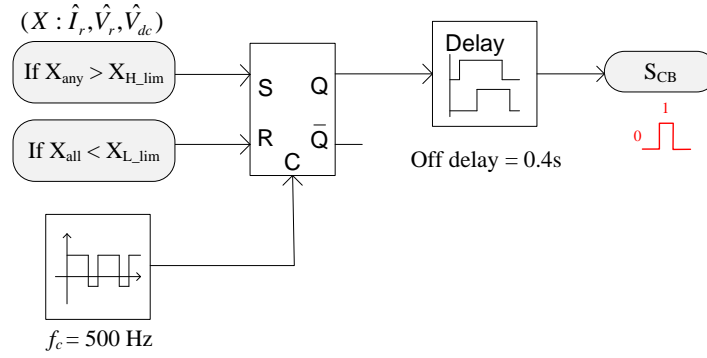


Figure 5.17 PSCAD circuit construction for crowbar activation

	\hat{I}_r	\hat{V}_r	V_{dc}
Upper limit	$1.5\hat{I}_{r,rated}$	$1.5\hat{V}_{r,rated}$	$1.3V_{dc,rated}$
Lower limit	$1.2\hat{I}_{r,rated}$	$1.2\hat{V}_{r,rated}$	$1.1V_{dc,rated}$

Table 5.2 Threshold values of crowbar activation

The external resistor is set to be $R_{CB} = 2$ p.u. when transformed to the rotor circuit it is

$$R_{CB} = n^2 R'_{CB} = 2\text{pu} \times 0.22\Omega \times 2.5^2 = 2.75\Omega \quad (5.15)$$

where n is the rotor/stator turns ratio

5.4.2. Setting of the RSC control during crowbar activation

When the crowbar is engaged, the RSC switches are disabled, which can be represented as an open circuit in PSCAD. The controllers of both the inner and outer loops are 'frozen'. As shown in Figure 5.18, the inputs of the PI controllers are switched to zero by 'S_{CB}'. At the time of crowbar switching off, the controllers are switched back to their normal states with an initial value the same as they had before the fault. In this way, significant transients can be avoided when the controller resumes normal operation. The GSC can be set in either normal operation or reactive power compensation mode, depending on the grid's requirement. This is out of the scope of this thesis though and will not be discussed further.

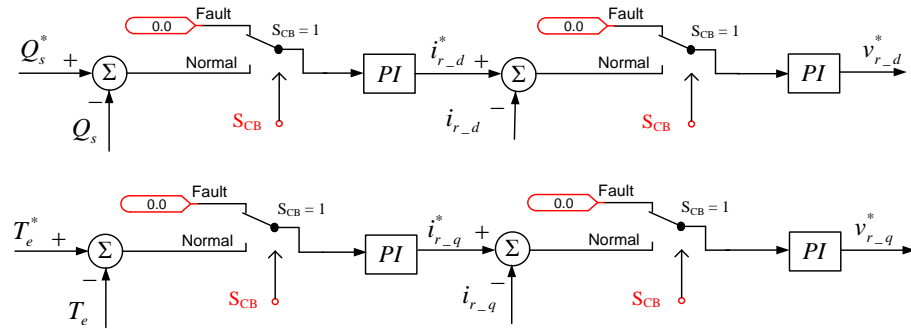


Figure 5.18 Control scheme of the RSC during crowbar activation

5.4.3. Simulation results

The grid code has included a fault ride-through requirement for wind turbines, where a voltage profile of the voltage depth and clearance time is specified, which the wind turbine must withstand without tripping [100]. The UK grid code is adopted here as the reference to simulate the voltage sag. Two different levels of voltage sag are simulated. Figure 5.19 shows a full voltage sag lasting 0.15s, and Figure 5.20 shows a 50% voltage sag lasting 0.7s. Three events happened as have been marked in the figures: 1. A fault is initiated and the crowbar activates, 2. The fault is cleared, 3. The crowbar is released. The rotor power P_r indicates the power flowing in the converter. The transients of both the rotor current and voltage at the fault starts are within their allowable limits. In the case of a full voltage sag, if no other protection scheme is used, the dc-link voltage can increase to a very high value after the fault (as shown in the blue curve). This is because the RSC control is still frozen and thus cannot handle the disturbances from the GSC. A chopper circuit is often used along with the crowbar for fault ride-through. It can discharge the capacitor when the dc-link voltage exceeds a limit. The improvement of the dc-link performance with chopper circuit protection is shown in the red curve in Figure 5.19. In the case of a 50% voltage sag, a chopper circuit is not necessary, as the dc-transients can be well controlled.

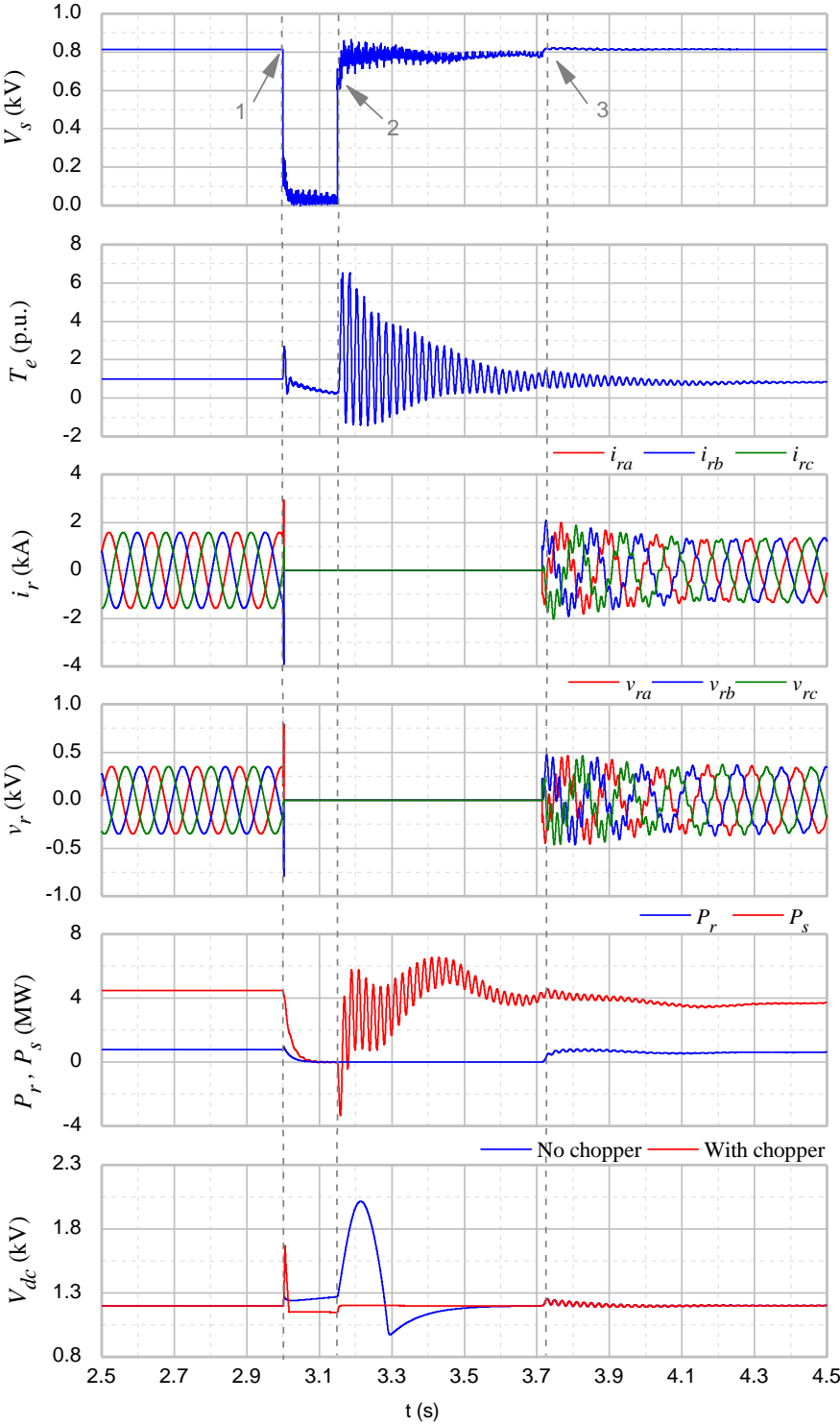


Figure 5.19 Simulation of active crowbar protection under a full voltage dip

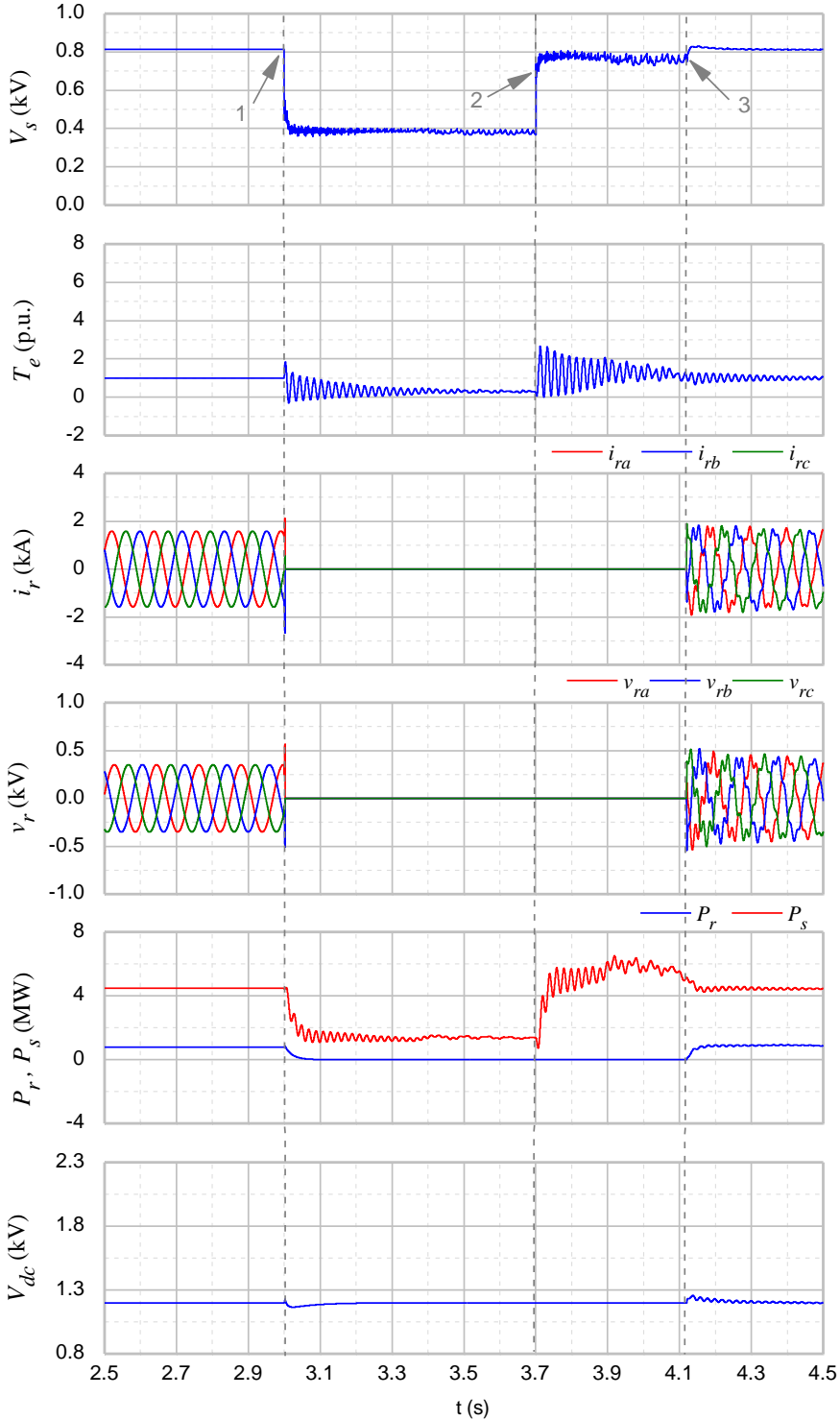


Figure 5.20 Simulation of active crowbar protection under 50% voltage dip

5.5. Controller coordination to reduce shaft oscillations

In the case of grid disturbances, there will be an abrupt change in the electric torque, resulting the twisting of the motor shaft. This excites significant oscillations known as shaft or torsional oscillations. The controllers should also be tuned properly to minimize

this where possible, and if necessary, adding a damping controller also helps to minimize these oscillations and reduce the risk of tripping. Implementation of such a control scheme should be coordinated with the crowbar protection.

5.5.1. RSC outer loop controller tuning – generic control strategy

The dynamic equations describing the mechanical shaft system (4.24) are:

$$\begin{bmatrix} \Delta \dot{\Omega}_T \\ \Delta \dot{\theta}_s \\ \Delta \dot{\Omega}_G \end{bmatrix} = A \cdot \begin{bmatrix} \Delta \Omega_T \\ \Delta \theta_s \\ \Delta \Omega_G \end{bmatrix} + B \cdot \Delta \beta + B_{d1} \cdot \Delta V_w + B_{d2} \cdot \Delta T_e \quad (5.16)$$

The full plant transfer function (4.26) is re-written here

$$P(s) = \frac{C \cdot (sI - A)^{-1} \cdot B_{d1}}{\eta} \quad (5.17)$$

Let $C_1 = [0 \ 0 \ 1]$, the transfer function from the electric torque to the generator speed is given as

$$P_2(s) = \left. \frac{\Delta \Omega_G(s)}{-\Delta T_e(s)} \right|_{op} = -C_1 \cdot (sI - A)^{-1} \cdot B_{d2} \quad (5.18)$$

Let $C_2 = [0 \ 1 \ 0]$, the reaction torque is related to the electric torque disturbances by

$$\begin{aligned} \left. \frac{\Delta \theta_s(s)}{\Delta T_e(s)} \right|_{op} &= C_2 \cdot (sI - A)^{-1} \cdot B_{d2} \\ \Rightarrow P_0(s) = \left. \frac{\Delta T_s(s)}{\Delta T_e(s)} \right|_{op} &= C_2 \cdot (K_s + sD_s) \cdot (sI - A)^{-1} \cdot B_{d2} \end{aligned} \quad (5.19)$$

Considering the generic control strategy in Chapter 4.1.2, the RSC outer loop transfer function is:

$$P_{ro}(s) = \frac{T_e}{T_e^*} \approx \frac{1}{\tau_i \cdot s + 1} \quad (5.20)$$

From equations (5.18) to (5.20), a change in the commanded torque reference will lead to perturbations in the rotor speed and reaction torque

$$\left. \frac{\Delta\Omega_G(s)}{\Delta T_e^*(s)} \right|_{op} = -P_{ro}(s) \cdot P_2(s) \quad (5.21)$$

$$\left. \frac{\Delta T_s(s)}{\Delta T_e^*(s)} \right|_{op} = P_{ro}(s) \cdot P_0(s)$$

The responses using different time constants to a 1 Nm torque step are simulated with MATLAB, as seen in Figure 5.21. The torsional oscillations are mainly present in the reaction torque when the time constant is smaller than 0.3s. This disturbance only affects the initial rotor speed transient, and most oscillations have been smoothed by the large system inertia. Since these ripples in the reaction torque indicate stress in the shaft and may result in failure by fatigue, the control-loop should best be used in this case with $\tau_i > 0.3s$ (0.53Hz).

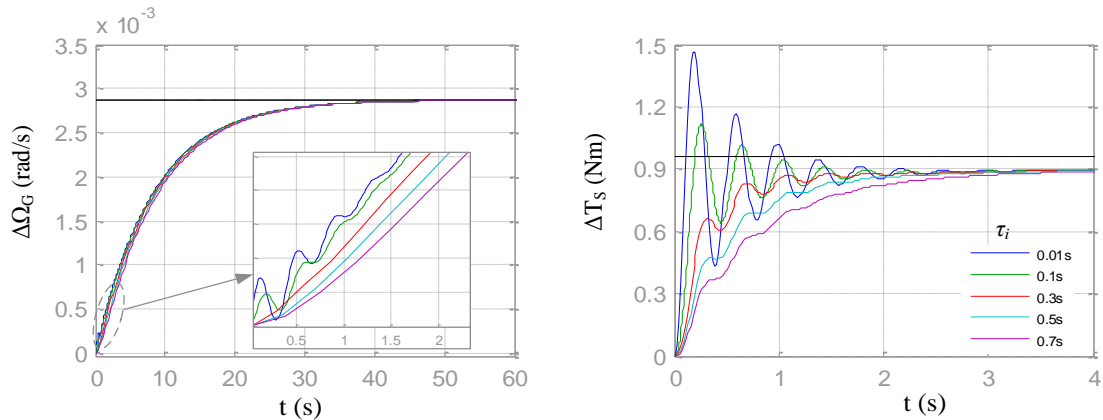


Figure 5.21 Mechanical oscillations using different time constants for T_e – loop response to 1 Nm torque step

5.5.2. RSC outer loop controller tuning – additional damping control

During a grid fault, the high transients in electric torque may also excite low frequency mechanical oscillations (torsional oscillations). This oscillation not only exists in the mechanical parameters such as the rotor speed and pitch angle, but also in the electric parameters such as the power and current. If not properly damped, there may be a risk of tripping the wind turbine in a severe voltage dip. Therefore, a damping control is often

added, which is used to produce the torque reference for the RSC control, based on the rotor speed error [72].

The feed-back block diagram of the mechanical control system has been depicted in Figure 5.22. This involves three cascaded control-layers with the pitch control as the outer most (slowest) loop, damping control in the middle, and the RSC torque-control the inner most (fastest) loop, where

$$P_1(s) = \frac{P(s)}{P_2(s)} \quad (5.22)$$

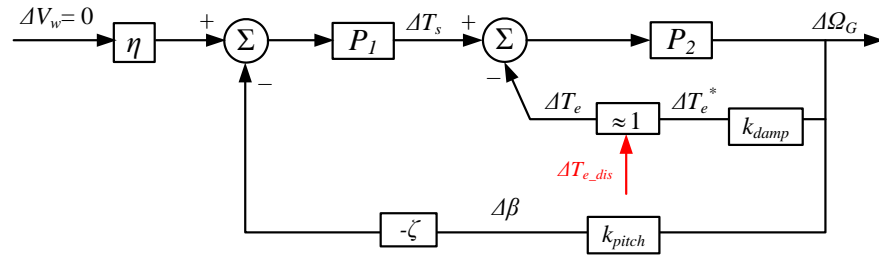


Figure 5.22 Three-layer cascaded wind turbine mechanical control system

It is assumed that the bandwidths of the three control layers are segregated perfectly, so that from the perspective of the damping control, the torque control is very fast and can be seen as a constant unity gain, while the pitch control is very slow and its effect can be ignored. Here a PI controller is used:

$$k_{damp} = \frac{k_p s + k_i}{s} = k_p \left(\frac{s + m}{s} \right) = k_p \cdot C(s)_d \quad (5.23)$$

Then the loop-gain of damping control system is given by:

$$G_d(s) = k_p \cdot C(s)_d \cdot P_2(s) \quad (5.24)$$

The closed-loop transfer function of the damping control is

$$\frac{\Delta\Omega_G}{\Delta T_{e_dis}} = \frac{-P_2(s)}{1 + G_d(s)} \quad (5.25)$$

The root loci of the characteristic function $G_d(s)$ with different controller settings (A, B, C and D) are shown in Figure 5.23. There are four branches corresponding to the increase of k_p : the red and green branches (r_1, r_2) originate from the shaft modes; the other two branches (r_3, r_4) are the results of the compensator and the rotor dynamics. The rotor speed responses from the four controllers are illustrated in Figure 5.24, where two types of dynamics (one faster and one slower) can be observed. In general, according to the relationship of PI gains, there are three forms of loci:

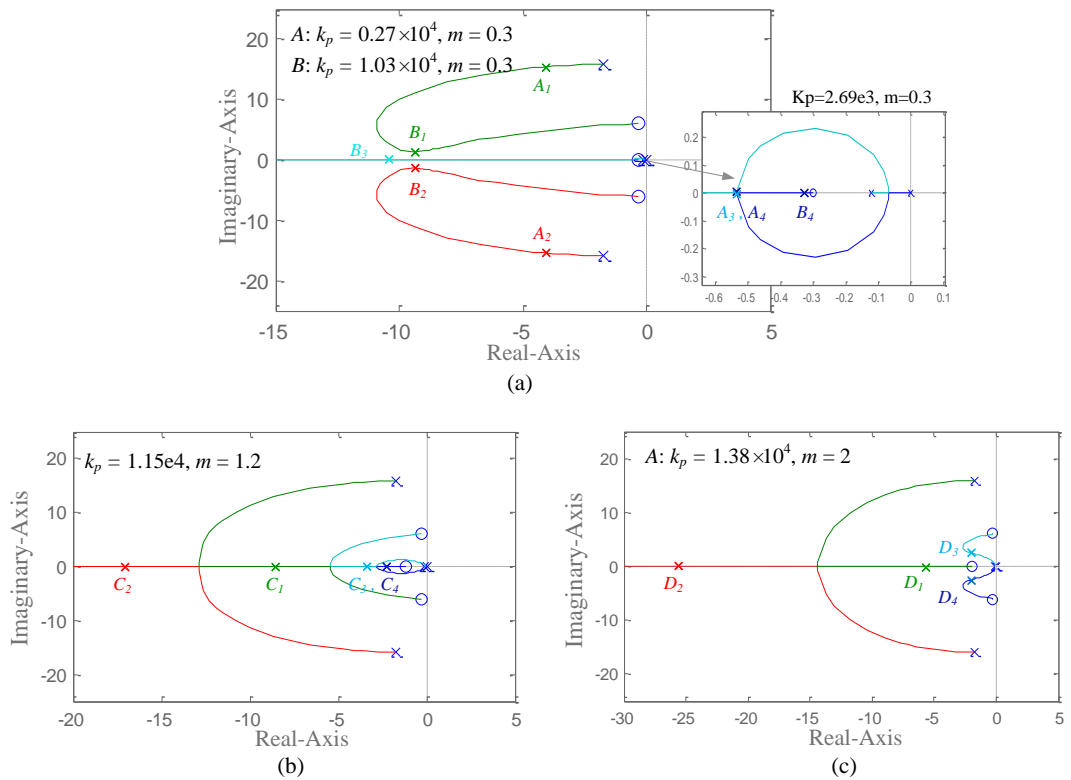


Figure 5.23 Root-loci of the system characteristic function with damping control

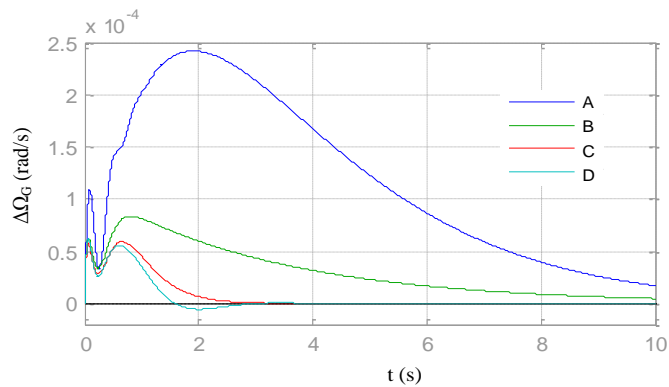


Figure 5.24 Responses to a 1m/s step in wind speed with different controller gains for the damping control

- When $k_p \gg k_i$ ($m \ll 1$), there always exists one pair of complex conjugate roots, which implies the faster dynamic (4.58rad/s for controller A) is under damped. The response also includes a slow dynamic (0.53rad/s) due to the root (or roots) very close to the origin (A_3, A_4). Controller B with a larger gain has more damping (smaller peak value), but it still takes a long time to remove the error due to the slower transient (0.32rad/s).
- When $k_p \approx k_i$ ($m \approx 1$), the controller C sets all the roots critically damped (on the real-axis). The rotor speed is influenced by both the faster dynamic of 8.86rad/s (C_1) and the slower dynamic of 2.60rad/s (C_3, C_4)
- When $k_p \ll k_i$ ($m \gg 1$), the slow dynamic will be under damped as branches r_3, r_4 are complex conjugate roots. This can be observed from Figure 5.24, the rotor response of D controller.

According to the above analysis, controller C will be adopted here for the damping control. This provides sufficient damping and relatively fast response (0.41-1.41 Hz). Based on this, the inner Te-loop can be set to be 5-10 times faster than the damping control (7-14Hz). Note this is faster than the generic control scheme.

5.5.3. Coordination with the pitch control

The loop gain of the pitch control system is given by (5.26). If a PI controller is used (Chapter 4.4.2), the root-locus can be depicted as in Figure 5.25.

$$G_p = k_{pitch}(s) \cdot (-\zeta) \cdot P(s) \quad (5.26)$$

The responses of generator rotor speed and blade angle to a wind step are illustrated here (Figure 5.26), in order to explain the dynamics of pitch control system. From the figure, the pitch control loop also involves two dominant kinds of dynamics: the slower rotor dynamics determined by r_5 and the faster pitch dynamics determined by r_4 . It is coordinated with the damping control in this way: the pitch control regulates low frequency rotor speed oscillations in a slow and delayed manner while the damping control can react quickly to high frequency perturbations. As can be seen from their respective rotor responses, the dominant (slower) rotor dynamic in the damping control-loop is still much faster than that of the pitch control-loop. On the other hand, the

pitch dynamic should be slower than this dynamic in order to reduce the pitch activity, thus reducing the stress on the pitch system. In this thesis, referring to table C.7 in the appendix, the controller is set with a pitching speed of 2.16rad/s (0.35Hz).

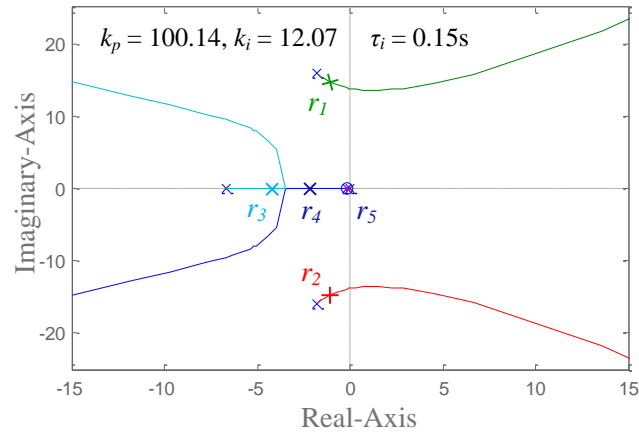


Figure 5.25 Root-locus of the pitch control system

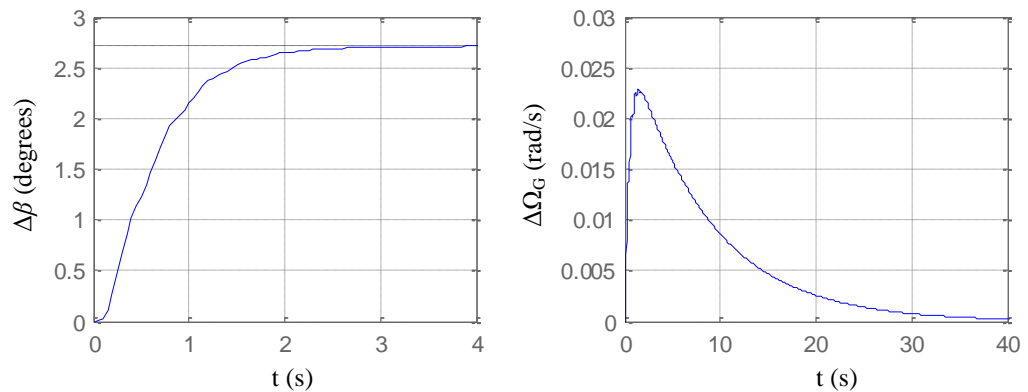


Figure 5.26 Responses of pitch controller to a 1m/s step in wind speed

5.5.4. Proposed control strategy for fault ride-through

From previous analysis in Chapter 4 and 5, the bandwidths of the main control-loops in a DFIG wind turbine system can be allocated as in Figure 5.27, where the respective damping ratio is illustrated as well.

With the control bandwidths determined, this chapter focuses on a coordinated strategy of implementing the damping control and crowbar protection to reduce oscillations during grid fault. Using a damping control all the time may not be necessary, as in normal operations the wind turbine generic control has already shown good performance. Besides, this requires the knowledge of wind speed in order to give a rotor speed reference [97].

The proposed strategy in this thesis eliminates the trouble of using an anemometer. The damping control is only engaged during grid fault and a short time after. What is more, since the RSC control will be disabled when the crowbar is engaged, the damping control should not be used for this circumstance.

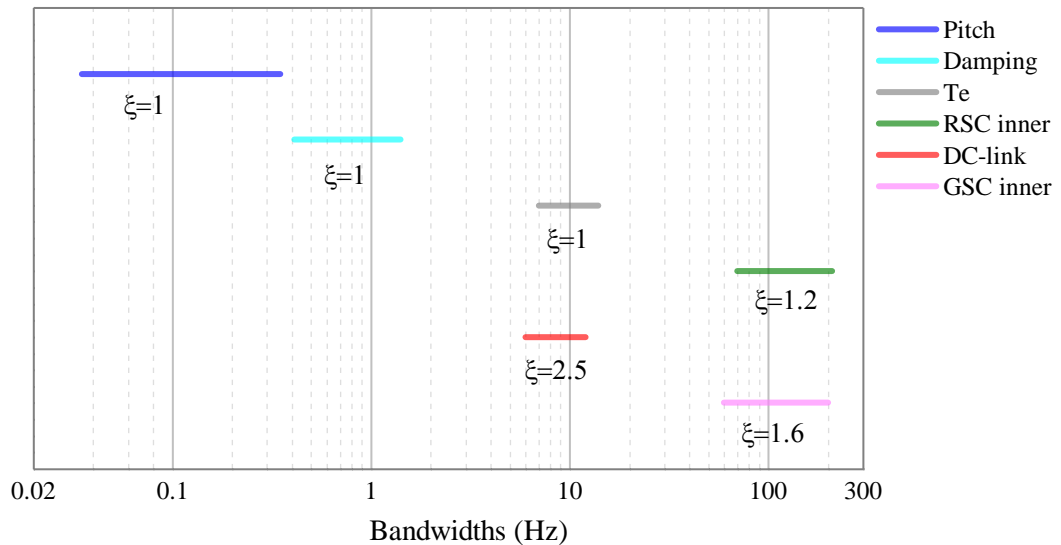


Figure 5.27 Bandwidth allocations for several main control-loops in DFIG wind turbine system

The strategy is illustrated in Figure 5.28. In a normal condition, the generic control of optimum torque tracking is used. The damping mode S_{damp} will be on when a fault is detected ($<95\%V_{s,\text{rated}}$) and the crowbar is off ($S_{\text{CB}} = 0$). It will last until 2s after the fault is cleared. A 'sampled and hold (S/H)' block is used to generate the reference input of the damping controller. When S_{damp} is off, the S/H output duplicates the input, setting the PI input to be 0. Therefore the damping controller is frozen. When the damping mode is enabled, the S/H holds the output at the last sampled value before S_{damp} is on. In this way, the reference rotor speed is set to be the last measured value before the fault. This is reasonable as the fault duration is very short, and thus constant rotor speed can be considered. Every time the damping control is triggered, the PI controller will re-initiate with T_{e1}^* in order to ensure a smooth transition.

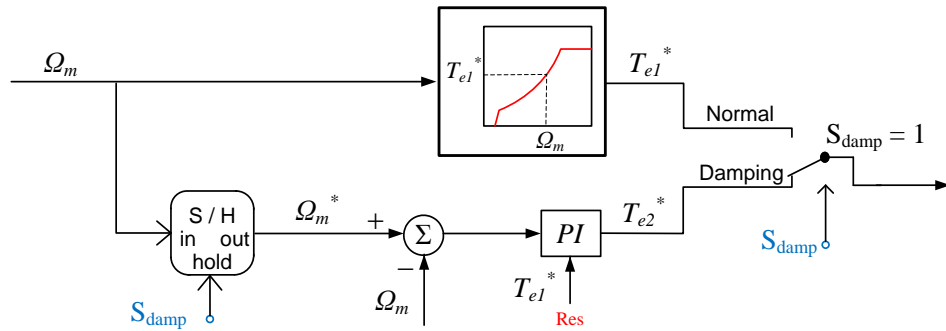


Figure 5.28 Strategy of the damping control

In the previous discussion, the control speed of T_e – loop should be different in the generic control scheme and in the damping mode. A further improvement can be achieved by varying the torque controller parameters when it switches between different modes. In the following, a 40% voltage sag is simulated. The wind turbine is operating with nominal speed (1.17 pu) at 13m/s wind. The mechanical responses with and without crowbar protection are presented in Figure 5.29 and Figure 5.30. The control schemes used for comparison are:

Scheme A: Generic control strategy used all the time

Scheme B: Generic control strategy in normal operating, damping mode activated during fault, where the T_e -loop controller parameters are fixed

Scheme C: Generic control strategy in normal operating, damping mode activated during fault, where the T_e -loop controller parameters vary according to the activated mode

The events illustrated in the figure are:

1. Fault initiates (damping enabled or crowbar engaged)
2. Fault clears
3. Crowbar released (and damping mode enabled)
4. Damping mode disabled and resuming generic control strategy

In Figure 5.29, the use of damping control substantially reduces the oscillations in the rotor speed and reaction torque. It also reduces the pitch action. As a result, this strategy mitigates the stresses in both the shaft and the pitch systems and improves the reliability.

In Figure 5.30, the three schemes actually function in the same way during crowbar protection. After the crowbar is switched off, Scheme B and C damp the post-fault oscillations immediately. At t_4 , Scheme B presents small perturbations following the controller transition when it resumes normal operations. Scheme C damps the oscillations effectively after the crowbar is released. A slower response is observed compared with B, this is due to larger time constant set for the torque controller when resuming the generic control mode.

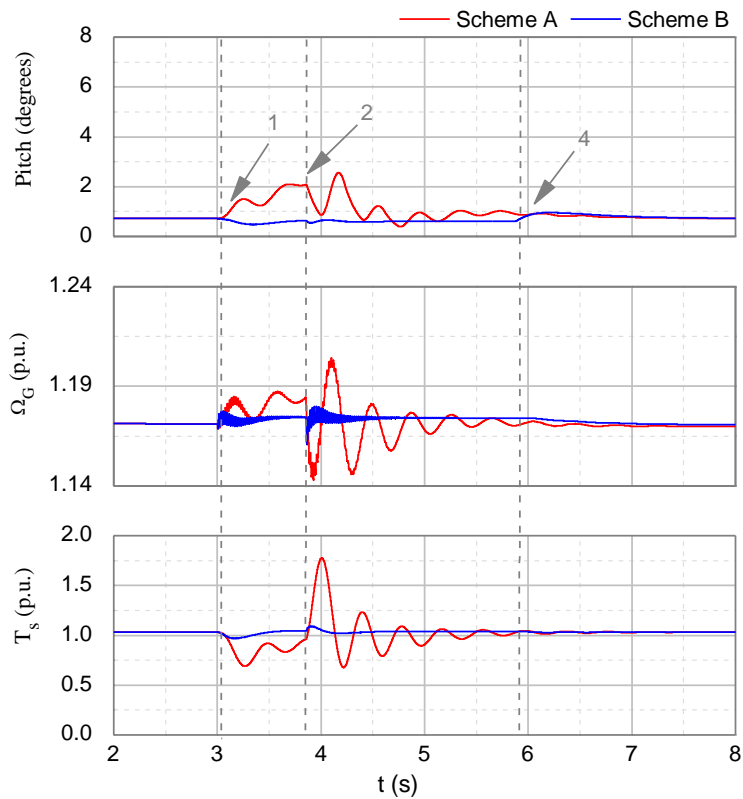


Figure 5.29 Improvement through damping control without crowbar engagement under 40% voltage dip

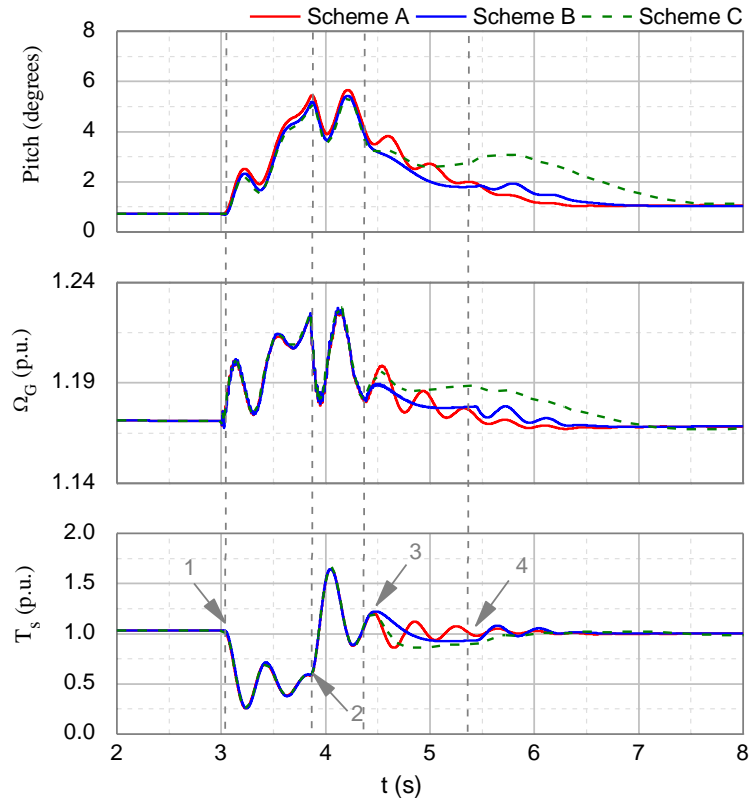


Figure 5.30 Improvement through damping and crowbar coordinated control

5.6. Conclusions

In a balanced three-phase voltage sag, significant oscillations are induced by the transient stator flux. This imposes several undesired fault behaviours on the DFIG wind turbine: high frequency oscillations in the electric parameters lasting for seconds, dc-link fluctuations, mechanical oscillations that last until several seconds after the fault. The former two phenomena may lead to instability or converter over-loading; the last one will result in drive-train system fatigue. Based on the above problems, several strategies to improve the system response during grid faults have been investigated.

From the aspect of increasing stability and reducing the electric transients, the RSC inner-loop can either be compensated with a demagnetizing current or use a coordinated bandwidth setting. Similar to the dc-link control, the voltage fluctuations can be reduced by increasing controller bandwidth or adding a feed-forward compensator associated with the power disturbance. For a severe voltage dip, where converter may be saturated and possibly damaged, a crowbar should be implemented. The crowbar protection has been implemented in PSCAD under different level of faults. In terms of counteracting torsional oscillations, the RSC outer-loop control, damping control and pitch control need to be

tuned carefully in order to reduce the interference with one another. Both of the damping and pitch controllers influence the rotor speed. However, the pitch control is mainly used for counteracting the perturbations caused by wind change, while the damping control is more effective in reducing the high frequency oscillations caused by a grid fault. In the end, a successful implementation of the damping control in PSCAD has been presented with the scenario of crowbar protection and pitch action (higher wind speed).

Chapter 6. Using Improved Power Electronics Modelling and Turbine Control to Improve Asset Management

A comprehensive literature review on the components' failure mechanisms and root causes has been given in Chapter 2, where the semiconductor switches are considered as the component of most interest in a power converter. This component is frequently stressed by thermal cycling at its internal layers which have different coefficients of thermal expansion (CTE). This can result in failure by either bond-wire lift-off or solder fatigue.

In contrast to other applications such as traction, the stress imposed on the wind turbine power converter (WTPC) can be affected by a stochastic event such as wind speed, as well as by operating conditions of the wind turbine itself. It is important to establish an adequate model that integrates a clear mission profile and a reliability model [16, 31]. Recent research in this area will be discussed. This chapter describes a thermal-electric model of the three-phase back-to-back converter developed in PSCAD/EMTDC, which takes the electric signal from the DFIG machine as the input. The interfacing block diagram has been depicted in Figure 6.1. The modelling of DFIG wind turbine and converter control system has been presented in Chapter 3 and 4. This chapter mainly focuses on the following tasks:

- a). Full detailed thermal models for both the rotor-side and grid-side three-phase are developed in PSCAD, which are verified against the manufacturer software 'SemiSel';
- b). Implementing operating point analysis by getting the temperature swing from the joint model;
- c). Performing overload analysis to observe the converter thermal capability under over-rated electric torque and grid fault condition;
- d). Simulating electrical and thermal variations under variable wind speed, enhancing performances around the synchronous operating point through improved control

strategy. As collaboration with Strathclyde University, the last task employs the simulated outputs from a 5 MW wind turbine ³.

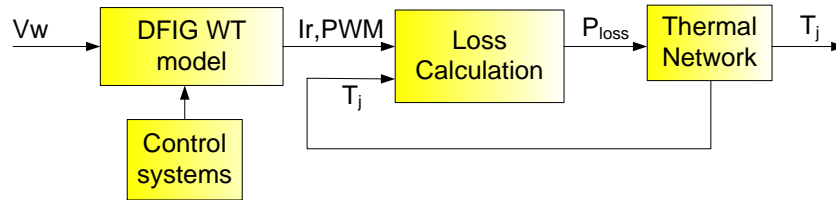


Figure 6.1 Interactions within the joint model for stress analysis

6.1. Review of the recent reliability studies for the wind turbine power converter

Reliability studies of the WTPC based on joint modelling of the wind turbine and electro-thermal circuit has been carried out in recent years, from the impacts of different operating points [6, 21, 101], control strategies [71, 102] to wind speed variations[48, 103]. This section provides a brief review of these studies.

6.1.1. Thermal cycling affected by operating point

The two most critical operating points for the semiconductor reliability have been identified, which are respectively the synchronous point and the rated point [6, 21, 101]. For a DFIG wind turbine, working at the synchronous speed is an undesirable condition [6, 101], since in this case the rotor three phases are energized by almost dc currents with different magnitudes. Thus there is unequal power loss distribution among the semiconductors, which will result in overheating of a single switch. In fact, working at small slip (rotor current oscillates at a few Hertz) is also considered to be the most thermal stressing zone and should be avoided. Due to the low frequency of rotor current, the long rise period of junction temperature leads to very large temperature swings (variations). In order to reduce this hazard, the literature [101] suggests that rotor speed should be set at a safer slip. The value of this depends on the thermal-time constant of the power device. On the other hand, the rated operating point is sometimes considered to be the most lifetime consuming point [21] due to the high mean junction temperature

³ Here Strathclyde’s input was the controller modification suggestion (Figure 6.33), as well as the series data of the rotor speed and torque demand used both with the conventional and modified (speed exclusion) turbine control (Figure 6.34).

suffered by the power device. However, the amplitude of temperature swings around this is smaller, so that the lifetime may not be impacted as much as by the synchronous operating point. Slightly over-dimensioning the power module is an effective way to improve system reliability.

6.1.2. Impact of different control strategies

Concerning the aspect of control strategies, past investigations have looked at mainly two levels. From the DFIG control level, there are three control schemes for the RSC: minimal rotor loss control, minimal stator loss control, and minimal overall loss control [102]. It is considered that the minimal rotor loss control leads to longer mean time to failures (MTTF) due to lower output current. However, an increased stress in the GSC may result due to higher reactive power demand.

From the wind turbine control level, the curve of torque demand versus rotor speed can be designed in different ways. From the literature [71, 104], the main schemes are Maximum Power Tracking (MPT), Constant Power Mode (CPM) and Constant Torque Mode (CTM). The merits and drawbacks of the three strategies are illustrated in Table 6.1.

Control strategies	Productivity	Power smoothing	Power module degradation effect
MPT	Highest	Poor	Large
CPM	Depend on average wind	Good	Medium
CTM	Lower	Medium	Small

Table 6.1 Performances evaluation of the three control strategies [71, 104]

6.1.3. Impact from other factors

Besides the operating point and control strategy, the variation of system output states (voltage, current, frequency) owing to the random wind speeds, has a direct impact on the WTPC thermal cycling. The power converter reliability level may vary with season, air temperature and wind sites. Higher failure rates are expected for wind turbines with a lower rated wind speed. Increasing the wind roughness will reduce the converter lifetime since the temperature excursions will be larger. For a three-level neutral-point-clamped

(3L-NPC) converter, the uneven thermal distribution among different devices is a problem, which can be improved by properly controlling the reactive current [105].

6.2. Modelling considerations

Temperature variation is an important factor that results in thermal-mechanical fatigue, which especially affects conventional IGBT modules with solder and bond wires. Evaluating the stress with FEM has been adopted for both WBI and PPI devices [106-108]. This provides accurate results but requires considerable computation time. In order to reduce the computation time, a thermal equivalent circuit (thermal network model) is sometimes used in combination with FEM to generate the temperature variations [109, 110]. The thermal network is especially useful when the interaction with external circuits or the impact from a variable load is to be considered, e.g. the impact from an electric machine and control system. Such a thermal model is used in this thesis.

6.2.1. Power modules in wind energy

This section gives a brief introduction on the typical IGBT power modules designed for wind energy applications. In today's market, IGBT modules with a current rating up to 3600A and 1700V blocking voltage are available [111]. Some leading manufacturers already provide solutions specifically for wind turbines. Two types of high power wind turbine converter, Semikron's SEMISTACK and Infineon's ModSTACKTMHD, are listed as examples in Table 6.2. These power converter cells are arranged in a cabinet and optimized for different wind turbine sizes. They can work as stand-alone or parallel in order to adapt to a broad power range. Each converter includes a three phase inverter with six switches (B6CI) or a four quadrant back-to-back converter (B6CI+B6CI). Both of the converter systems are constituted of powerful IGBT modules (SKiiP intelligent power module (IPM) by Semikron and PrimePACK by Infineon). Such an IGBT module includes a half bridge (GB) or two switches. The SKiiP IPM covers a variety of ratings, depending on the number of folds in the module. The PrimePACK, in contrary, is designed with a single fold in each module. When used in a ModSTACKTMHD, several modules (up to three times) may be connected in parallel. Understanding this construction is important to correctly calculate the loss dissipation and develop the thermal model


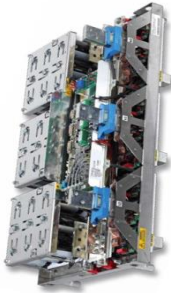


Manufacturer		Semikron	Infineon	
Example		SEMISTACK	ModSTACK™HD	
Stack	Layout			
	Sub-modules (Number/ phase)	SKiiP (single module)	PrimePACK™ (1 –3in parallel)	
	Typical output	RMS current	900 – 1400 A	600 – 2000 A
		RMS L-L voltage	690V	690V
		dc – Link	1100 – 1250 V	1100V
		Max blocking voltage	1700V	1700V
	Dimension (mm) width × depth × height	600 × 600 × 2000	Typical 596 × 342 × 1090	
Circuit topology	B6CI① or B6CI+B6CI②			
Example		SKiiP	PrimePACK	
IGBT module	Layout			
	Component	Switches, heat sink Gate driver unit, protection & monitoring circuit	Switches, thermistor (NTC)	
	Mounting technology	Pressure contact (Sinter technology)	Soldered	
	Nominal current	500 – 3000 A	450 – 1400 A	
	Max blocking voltage	1200V, 1700V	1200V, 1700V	
	Maximum junction temperature	$T_{j,max} \leq 170 \text{ }^\circ\text{C}$	$T_{j,max} \leq 150 \text{ }^\circ\text{C}$	
	Devices/ phase leg	2 - 4 folds	1	
	Circuit topology	GB③, GD④, GL⑤	GB	

Table 6.2 IGBT modules for wind turbines from two manufacturers

① Three phase inverter

② Four quadrant converter

③ Half bridge

④ 3-phase bridge

⑤ 3-phase bridge + brake chopper

In a SKiiP IPM, the switches are included together with the heat sink, control unit, protection and monitoring circuit, whilst the PrimePACK IGBT module includes only the switches and thermistor (NTC). Other components are all assembled in the ModSTACK converter cell. Another two features that distinguish Semikron's SKiiP IPM are the use of sintered technology and pressure contact structure, which largely increases the maximum junction temperature (up to 175 °C compared with the conventional 125-150 °C) and improves thermal cycling capability.

6.2.2. Power module selection

6.2.2.1. Rating of the rotor side converter

Modern wind turbine power device modules such as the SKiiP IPM and the PrimePACK are usually designed for two voltage levels, i.e. 1200V and 1700V IGBT. It is important that the electrical and thermal parameters are properly set, and the rating of the power converter is chosen as in the real industry. This is to ensure the predicted junction temperature and the cycling duration are sufficiently close to that of the actual power device.

The rated current is determined from the electric torque and reactive power at nominal conditions. Equation (3.25) is given below

$$\begin{aligned} T_e &= \frac{3}{2} pp \frac{L_m}{L_s} \psi_s i_{r-q} \\ Q_s &= -\frac{3}{2} \frac{\sqrt{2} V_s L_m}{L_s} i_{r-d} - \frac{3}{2} \frac{\sqrt{2} V_s}{L_s} \psi_s \end{aligned} \quad (6.1)$$

Here, the electric torque and the stator flux will be considered as 1 p.u., unity stator power factor is assumed, i.e. $Q_s = 0 pu$. Therefore, the rated rotor current in per unit is obtained as

$$I_r^{pu} = \frac{\sqrt{i_{r-q}^2 + i_{r-d}^2}}{\sqrt{2}} = 1.07 pu \quad (6.2)$$

The turns-ratio between the rotor and stator windings should be determined with care. A low turns-ratio results in higher rotor current and thus increases the converter size, while a high turns-ratio can make the rotor voltage exceeds the dc-bus capability and cause over modulation. Here this ratio is determined as $n = 2.5$, which is close to the typical range of 2.6-2.8 specified in [73]. When the induction machine reaches the maximum slip of the normal operating region (0.75 p.u. to 1.17 p.u.), i.e. $s_{\max} = 0.25$, the rotor voltage is

$$V_r = s \cdot n \cdot V_s = 0.25 \times 2.5 \times \frac{1kV}{\sqrt{3}} = 0.36kV \quad (6.3)$$

For 1.2 kV dc-link voltage, the maximum phase-rms voltage that can be handled by the rotor side converter is approximately

$$V_r^{\max} = \frac{1}{\sqrt{2}} \frac{V_{dc}}{\sqrt{3}} = 0.49kV \quad (6.4)$$

The selected turns-ratio leaves a safely margin of $(0.49 - 0.36) / 0.49 = 26.5\%$ below the maximum rotor voltage the dc-bus can handle. This is reasonable to allow for torque-speed corrections [112, 113]. The actual nominal rotor current is therefore derived as

$$I_{r_rms}^{rated} = I_r^{pu} \cdot \frac{I_{base}}{n} \approx 1.12kA \quad (6.5)$$

Usually in practical designs, the nominal current of the power device is chosen as twice of the rated rms value [112, 114, 115], i.e. $I_{c,nom} = 2I_{r_rms}^{rated}$. Three Semikron IGBT modules with a similar nominal current are compared in section 6.2.2.3.

6.2.2.2. Rating of the grid-side converter

For the normal working range 0.75 pu to 1.17 pu, the rotor power increases with the rotor speed. Thus the rated rotor power is achieved at the nominal rotor speed (1.17 p.u.). The corresponding rated rms current in the GSC is

$$I_{g_rms}^{rated} = \frac{-sP_s^{rated}}{\sqrt{3}V_{gsc_LL_rms}} = \frac{0.17 \times 4.5MW}{\sqrt{3} \times 0.4kV} = 1.104kA \quad (6.6)$$

It can be seen that the rating of GSC is comparable with that of RSC (6.5). In this thesis, the two thermal models are based on the same prototype.

6.2.2.3. Device temperature comparison with SemiSel

The average temperatures under two load conditions are generated by 'SemiSel'. Three SKiiP products of different ratings are compared in Table 6.3. The 'over load' condition indicates 1.3 times the rated current. T_{hs} is the temperature of the heat-sink, T_{tr} is the transistor's (IGBT's) junction temperature, T_D is the diode's junction temperature. The maximum temperature the device can survive is assumed to be 150 °C. In normal working conditions, it is better to keep the temperature below 125 °C [23]. Among the three SKIIP modules, the one of 2 kA [116] is chosen as it can provide satisfactory performance for the given load with relatively low cost.

	SKiiP 2013 GB172-4DW		SKiiP 1803 GB172-3DFW		SKiiP 2414 GB17E4-4DUW	
I_{nom}	2 kA		1.8 kA		2.4 kA	
	Rated Current	Overload	Rated Current	Overload	Rated Current	Overload
T_{hs}	97	118	111	143	72	84
T_{tr}	108	132	125	163	77	92
T_D	104	129	120	155	77	91
	Fine		Overloaded		Too Powerful	

Table 6.3 Performance comparison of three SKIIP modules under various loads

6.3. Power loss calculation

Generally, there are two ways to perform device loss calculations. The first approach is to analytically characterize the electrical behaviour by modelling each type of loss [117-120]. This method at first involves very complex mathematical derivations [120], based on which a simplified representation is introduced. This method typically provides the average loss for one load cycle. An alternative method is numerical circuit simulation, where the device model is established and typically a series of pulse patterns will be generated based on the switching states [121, 122]. The accuracy of the predicted loss

depends on the level of modelling. Using this method can be very time consuming especially when longer time simulation is needed, as the instantaneous power loss is calculated at each switching cycle.

Considering the large time constant of the thermal model, a quasi-instantaneous loss method is proposed, where the average loss in a sampling time is calculated, which varies with the load current. In this section, the factors that affect power loss will be discussed with the extended loss equations. A fast numerical simulation method based on the manufacturers' datasheets will be employed on the PSCAD/EMTDC DFIG converter model to derive the instantaneous power loss. Finally, the simulation result will be verified against the calculations from manufacturer software.

6.3.1. Operating states of the three – phase inverter

The schematic diagram of a three phase inverter is shown in Figure 6.2. The dc-bus voltage is roughly constant and serves as the power input for the switches. Generally, a pulse-width modulation (PWM) technique is used for the switches to regulate the output ac voltage's magnitude and frequency. There are various PWM schemes to synthesize a sinusoidal output voltage [123]. Among these modulation schemes the two most popular ones are sinusoidal PWM and space-vector PWM. In this model, the sinusoidal PWM method is implemented for the three-phase inverter, as will be discussed in detail later. Commercially space-vector PWM would be used, however, the differences in dynamics made no difference in these simulations and sinusoidal PWM should simulate more quickly in PSCAD.

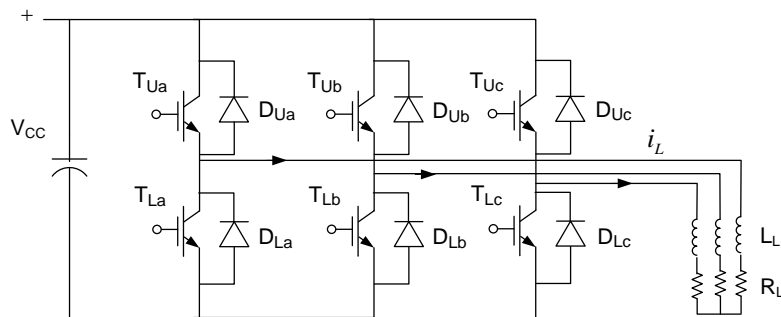


Figure 6.2 Diagram of a three phase inverter

In a three phase inverter with a sinusoidal PWM scheme, three sinusoidal control signals that are shifted with respect to each other by 120° will be compared with the same carrier signal (triangular waveform), as shown in Figure 6.3. The control signal v_{con} provides the desired fundamental frequency f_1 , for the synthesized output voltage. The triangular signal v_{tri} establishes the switching frequency of the semiconductors f_{sw} . The carrier signal is modulated by the control signal to produce different duty ratio $\delta \cdot \tau$. The amplitude modulation ratio m_a is defined as

$$m_a = \frac{\hat{v}_{con}}{\hat{v}_{tri}} \quad (6.7)$$

where the symbol \hat{v}_{con} and \hat{v}_{tri} denote the peak values. Then the duty cycle δ is given by

$$\delta = \frac{1}{2} [1 + m_a \cdot \sin(\omega t)] \quad (6.8)$$

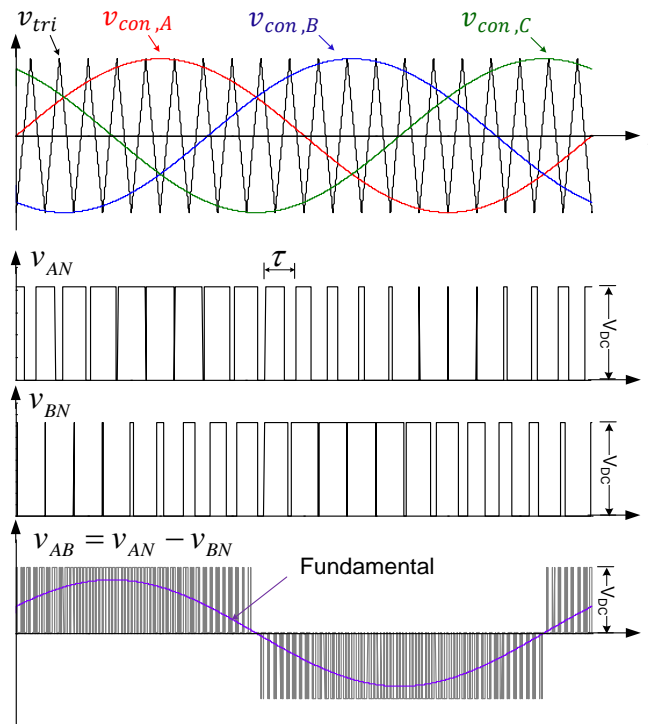


Figure 6.3 Waveforms in pulse-width-modulation

The output voltage at each inverter ac terminal depends on the dc-bus voltage V_{DC} and also the switching states. If only the fundamental component is considered here, the magnitude of the phase and line-to-line rms voltage can be represented as

$$v_{AN} = \frac{m_a}{\sqrt{2}} \frac{V_{DC}}{2} = 0.354m_a V_{DC} \quad (6.9)$$

$$V_{LL,rms} = \sqrt{3}v_{AN} = 0.612m_a V_{DC} \quad (6.10)$$

Each pair of IGBTs and the opposite diodes conduct interactively in a full switching cycle. In Figure 6.4, when the load current is positive (states a and b), the upper IGBT (T_U) will conduct the current for a time $\delta \cdot \tau$ and the opposite lower diode (D_L) will conduct the current for a time $(1-\delta) \cdot \tau$. During the current negative half cycle (states c and d), T_U and D_L are not conducting. The other pair of T_L and D_U will repeat this process. Mainly two kinds of power losses are generated from the above states, i.e. conduction loss and switching loss. Assuming the switching strategy is ideal by ignoring the blanking time and the minimum on-time constraints, the power dissipations generated at each switching state are illustrated in Table 6.4.

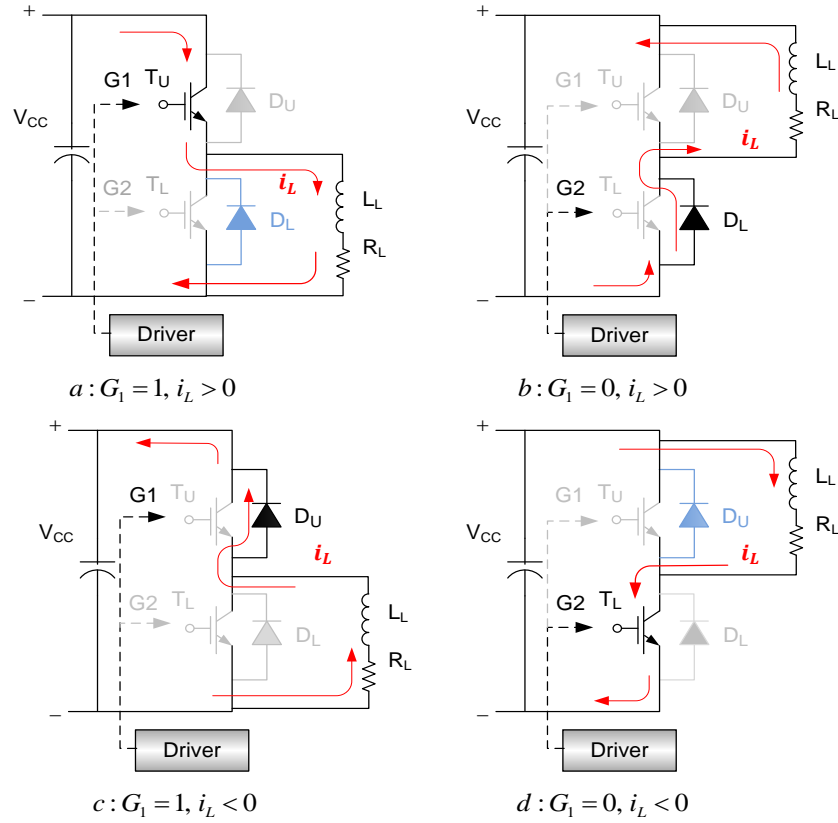


Figure 6.4 Four quadrant operating states for one leg

Losses Generated	Switching states			
	T _U	T _L	D _U	D _L
$P_{con} [W]$	a	d	c	b
$E_{on} [J]$	$b \rightarrow a$	$c \rightarrow d$	$d \rightarrow c$	$a \rightarrow b$
$E_{off(rr)} [J]$	$a \rightarrow b$	$d \rightarrow c$	$c \rightarrow d$	$b \rightarrow a$

Table 6.4 Power loss and device switching states

6.3.2. Conduction loss

The conduction loss of PWM IGBT-inverters is affected by the load current i_L , depth of modulation m_a and power factor $\cos\theta$ [120]. The effect of temperature is sometimes taken into account [124]. The universal representations for semiconductor conduction loss are given as below [23, 117].

Average conduction loss for an IGBT:

$$P_{Tr,con} = \left(\frac{1}{2\pi} + \frac{m_a \cdot \cos\theta}{8}\right) \cdot V_{CE0}(T_j) \cdot \hat{i}_L + \left(\frac{1}{8} + \frac{m_a \cdot \cos\theta}{3\pi}\right) \cdot r_{CE}(T_j) \cdot \hat{i}_L^2 \quad (6.11)$$

Average conduction loss for a Diode:

$$P_{D,con} = \left(\frac{1}{2\pi} - \frac{m_a \cdot \cos \theta}{8}\right) \cdot V_{F0}(T_j) \cdot \hat{i}_L + \left(\frac{1}{8} - \frac{m_a \cdot \cos \theta}{3\pi}\right) \cdot r_F(T_j) \cdot \hat{i}_L^2 \quad (6.12)$$

where

V_{CE0}, V_{F0} = Threshold voltages of the IGBT and the Diode respectively

r_{CE}, r_F = On-state slope resistances of the IGBT and diode forward characteristic respectively

\hat{i}_L = Peak output current of the inverter

The conduction losses calculated by equations (6.11) and (6.12) are averaged for one load current cycle. Instantaneous loss prediction is feasible based on numerical simulation. However, using a detailed power device model can be very time consuming and unnecessarily complex. Based on the dependency of the power loss on the passing current, a curve fitting method [124, 125] can give a fast solution. It does require laboratory test and measurement to obtain the data however. Instead, using the loss characteristic provided by the manufacturer's datasheet [121] can provide a sufficiently accurate result with less effort. Here this method will be adopted. The conduction power can be obtained directly by multiplying the voltage drop (V_{CE} or V_F) with the current (I_C or I_F) through the device (6.13). The 2nd order polynomial functions are derived to give the relationship between the on-state power loss and the current at two operating temperatures (T=25 °C and T=125 °C), as depicted in Figure 6.5.

$$P_{Tr,con} = V_{CE}(I_C) \cdot I_C = a \cdot I_C + b \cdot I_C^2 \quad (6.13)$$

Based on the two operating curves, coefficients a and b in (6.13) can be expressed as temperature-dependent:

$$\begin{aligned} a(T) &= a_0 + a_1 T \\ b(T) &= b_0 + b_1 T \end{aligned} \quad (6.14)$$

Therefore, the conduction loss can be described in terms of the load current and device temperature (6.15). The coefficients for diode conduction loss can be determined in the same way, as shown in Table 6.5.

$$P_{Tr,con}(I_C, T) = (a_0 + a_1 T)I_C + (b_0 + b_1 T)I_C^2 \quad (6.15)$$

	a_0	a_1	b_0	b_1
IGBT	1.0075	-0.0007	0.68	0.0032
Diode	1.19	-0.0028	0.7275	0.0005

Table 6.5 Coefficients for conduction loss characteristic

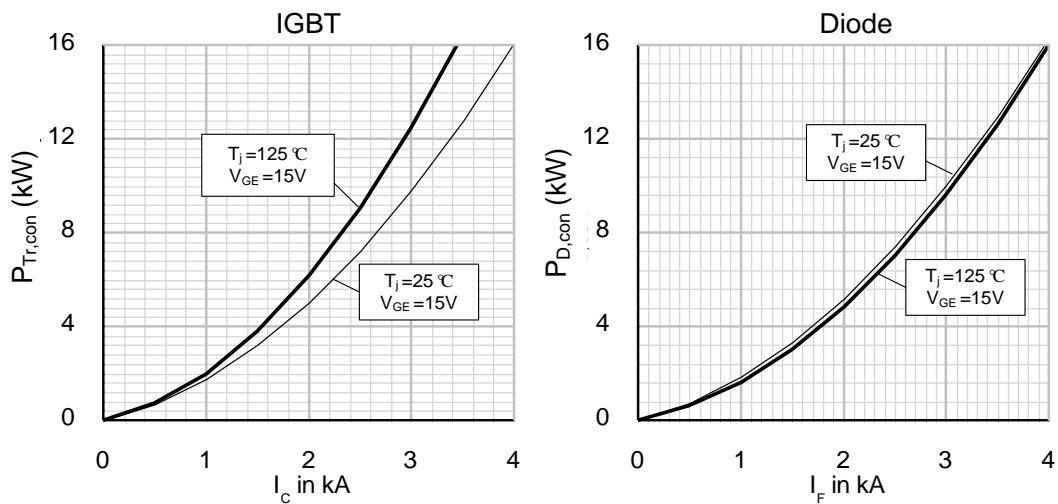


Figure 6.5 Conduction loss and current dependency obtained by curve fitting [116]

6.3.3. Switching/reverse recovery loss

The switching losses for the power devices include turn-on and turn-off losses. The turn-off loss for a diode is often referred to as reverse recovery loss and it accounts for almost the entire diode switching loss (more than 99%) [126]. The diode turn-on loss is often neglected. As shown in Figure 6.4, diode turn-off happens at the same time as IGBT turn-on (from state 'b' to 'a' or 'c' to 'd'). The typical waveforms characterizing this process are shown in Figure 6.6. This is divided as three phases:

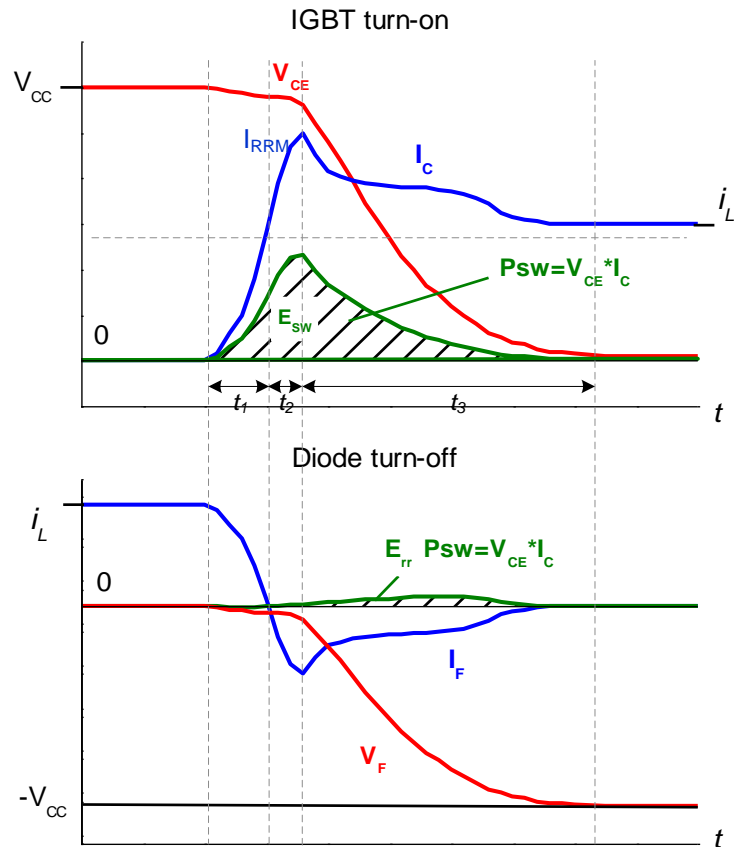


Figure 6.6 Typical waveforms of IGBT turn-on and Diode turn-off [23]

- In period t_1 , the forward current in the diode I_F decreases linearly and is gradually transferred to the IGBT;
- In period t_2 , negative current starts to increase in the diode due to the stored charge. A depletion region is formed at the end of this period with the peak reverse current I_{RRM} reached;
- In period t_3 , the stored charge in the diode is removed by recombination and the IGBT collector voltage drops as the load current returns to the rated value.

For all the three phases, the IGBT will generate loss while the diode mainly dissipates loss in t_2 and t_3 . The IGBT turn-off is the reverse of this process except there is no reverse-recovery diode current. In this case, the collector voltage will increase first. After reaching a threshold value V_{CE0} the current is then transferred gradually to the opposite diode. Several parameters that affect the switching loss are [23]:

- The rate of the current rise during the diode turn-off di / dt . This factor determines the amount of the stored charge recombined in the diode and it is related with the IGBT turn-on speed, gate resistance or the stray inductance [23, 119, 127].
- The blocking voltage V_{CC} or V_R for the diode (equals to the dc-link voltage)
- The current through the device, i.e. I_C or I_F
- The device junction temperature T_j

The first parameter depends on the device technology. The other three factors are related to the electrical system states, which are included in the switching loss model (6.16)-(6.17). The IGBT turn-on and turn-off are counted as one single event

$$E_{on+off} = E_{on+off}^{ref} \cdot \left(\frac{I_C}{I_C^{ref}}\right)^{Ki1} \left(\frac{V_{CC}}{V_{CC}^{ref}}\right)^{Kv1} (1 + TC_{Esw} \cdot (T_j - T_j^{ref})) \quad (6.16)$$

$$E_{rr} = E_{rr}^{ref} \cdot \left(\frac{I_F}{I_F^{ref}}\right)^{Ki2} \left(\frac{V_{CC}}{V_R^{ref}}\right)^{Kv2} (1 + TC_{Err} \cdot (T_j - T_j^{ref})) \quad (6.17)$$

where

$$E_{on+off}^{ref} = 1150mJ \text{ generated at } I_{ref} = 1200A, V_{CC}^{ref} = 1200V \text{ and } T_j^{ref} = 125^\circ C$$

$$E_{rr}^{ref} = 171mJ \text{ generated at } I_F^{ref} = 1200A, V_R^{ref} = 1200V \text{ and } T_j^{ref} = 125^\circ C$$

Ki = Current dependency exponent

Kv = Voltage dependency exponent

$TC_{Esw(Err)}$ = Temperature coefficient

The superscript 'ref' denotes the reference values for each quantity, which can be found in the manufacture's datasheets. The parameters used are given as in Table 6.6.

K_{i1}	K_{v1}	TC_{ESW}	K_{i2}	K_{v2}	TC_{Err}
1	1.3-1.4	0.003 1/K	0.6	0.6	0.006 1/K

Table 6.6 Parameters used for the switching energy equations

As the load current of the converter is sinusoidal, the average value (6.18) should be substituted into the switching loss equation. The switching power can be presented by (6.19)

$$I_C = I_F = \frac{1}{2\pi} \int_0^\pi \sqrt{2} I_{L,rms} \sin \alpha \cdot d\alpha = \frac{\sqrt{2}}{\pi} I_{L,rms} \quad (6.18)$$

$$\begin{aligned} P_{Tr,sw} &= f_{sw} E_{on+off} \\ P_{D,sw} &= f_{sw} E_{rr} \end{aligned} \quad (6.19)$$

In the manufacturer's datasheet, the characteristic curve of switching energy and current is only given for $T_j = 125^\circ C$. According to equations (6.16)-(6.19), the curves for other temperatures can be derived. In Figure 6.7, the switching energy curve of $T_j = 25^\circ C$ is presented as well.

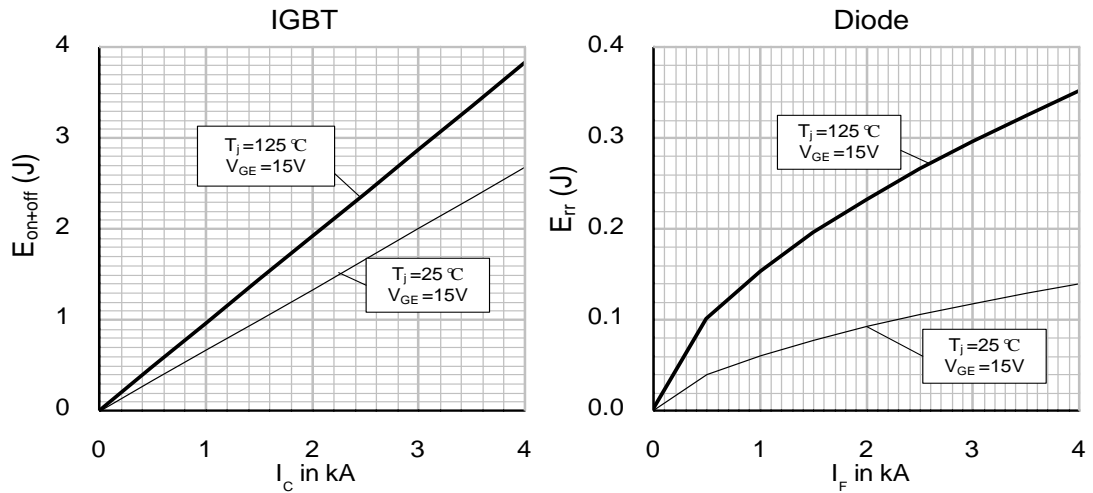


Figure 6.7 Characteristics of switching loss at two different temperatures [116]

6.3.4. Implementation – switched model

The application in a three phase inverter including PWM switching is depicted in Figure 6.8. The blue dotted box shows the detection of the switching-states which is based on Figure 6.4 and Table 6.4. The diode switching-on loss is neglected and IGBT turn-on and turn-off loss are added together for the switching-on event. The load current and temperature is used for loss prediction. The operating dc-link voltage equals the reference value given on the datasheet and is considered as constant, since the impact of its

variation on the predicted loss is little. The instantaneous switching power is generated in this way: when a positive transition of gate signal is detected, a pulse signal with width ΔT will be generated and scaled by $E_{sw}(I_L, T_j) / \Delta T$. Therefore the total switching energy remains the same. As the switching time constant is very small (μs) compared with device thermal constant or electric system time constant, this high frequency component will not be present in the junction temperature. Therefore, varying the pulse width ΔT makes no difference on the predicted temperature as long as it is smaller than the switching period, i.e. $\Delta T < 1 / f_{sw}$. In order to have a larger simulation step, the pulse width is set to be $\Delta T = 200 \mu s$ (for $f_{sw} = 4500 Hz$). The total loss produced $P_{Tu,tot}$ will be fed into the thermal network, from which it takes the junction temperature T_j for accurate loss prediction.

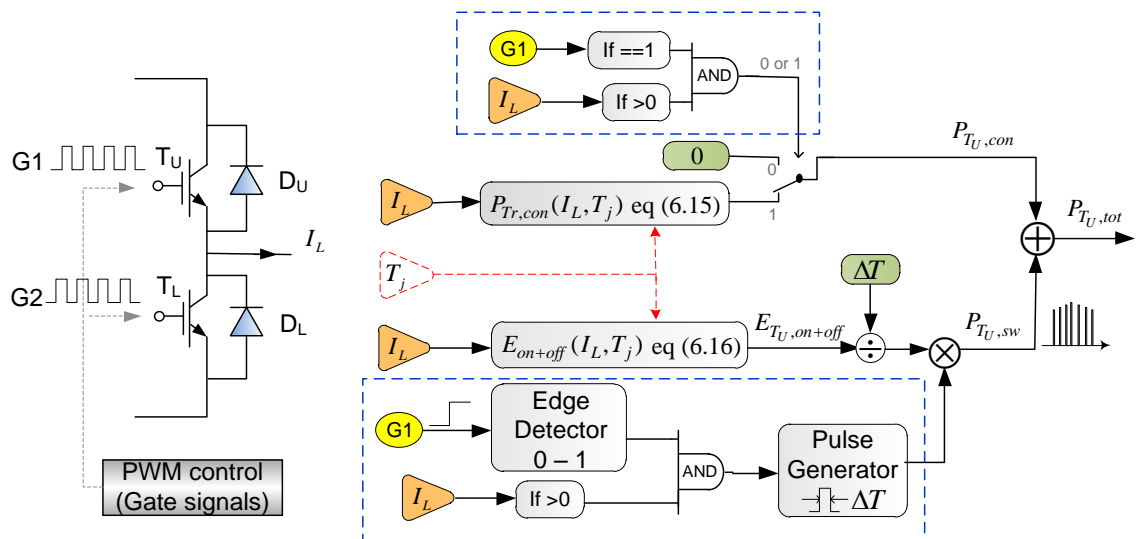


Figure 6.8 Schematic diagram of IGBT power loss prediction using PWM switched model

6.3.5. Implementation – switch averaged model

In the previous method, a small simulation step time ($10 \mu s$) is required due to the PWM signal. As a result, to run a 100-second simulation, it takes about one hour in real time, which is extremely time-consuming. A quasi-instantaneous loss prediction method can be implemented on the averaged three-phase inverter model, which eliminates the PWM switching signals.

Considering that the switching frequency is much faster than the control signal's frequency (50Hz for the GSC and slip frequency for the RSC), the current in each switching cycle is nearly constant. Then the conduction power averaged for one switching cycle is given by

$$\begin{aligned} P_{con} \cdot \delta \cdot \tau &= P_{con,av} \cdot \tau \\ \Rightarrow P_{con,av} &= P_{con} \cdot \delta \end{aligned} \quad (6.20)$$

From (6.7)-(6.8) the duty ratio can be expressed as a function of the dc-link voltage and the rotor voltage:

$$\delta = \frac{1}{2} \times \left(1 + \frac{v_{r,a}}{V_{dc}/2}\right) \quad (6.21)$$

The loss prediction method for IGBT and Diode are depicted in Figure 6.9, and the simulations are presented in Figure 6.10. It can be seen that the quasi-instantaneous loss is averaged for each sampling time (simulation time step) but it still varies with the load current. The time step can be set ten times larger than in the switched model, and thus the simulation speed is greatly increased.

$$I_p = \begin{cases} |I_L| & \text{if } I_L > 0 \\ 0 & \text{if } I_L < 0 \end{cases} \quad I_n = \begin{cases} 0 & \text{if } I_L > 0 \\ |I_L| & \text{if } I_L < 0 \end{cases} \quad (6.22)$$

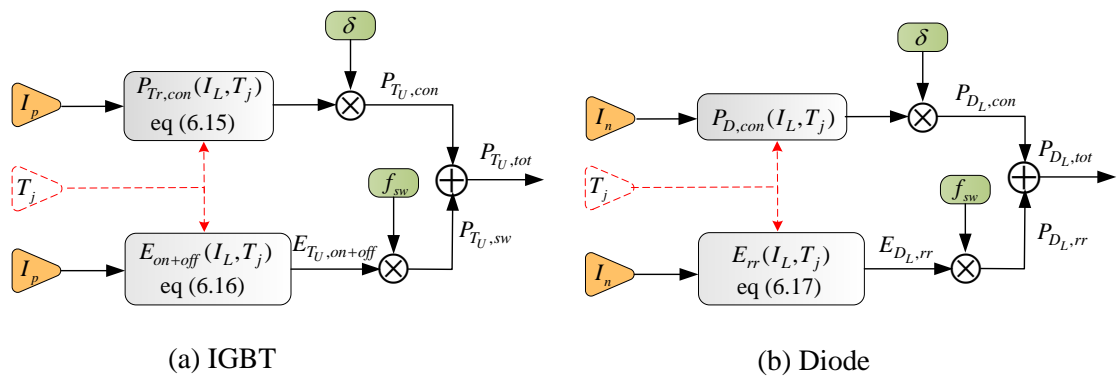


Figure 6.9 Schematic diagram of the loss prediction using the switch-averaged model

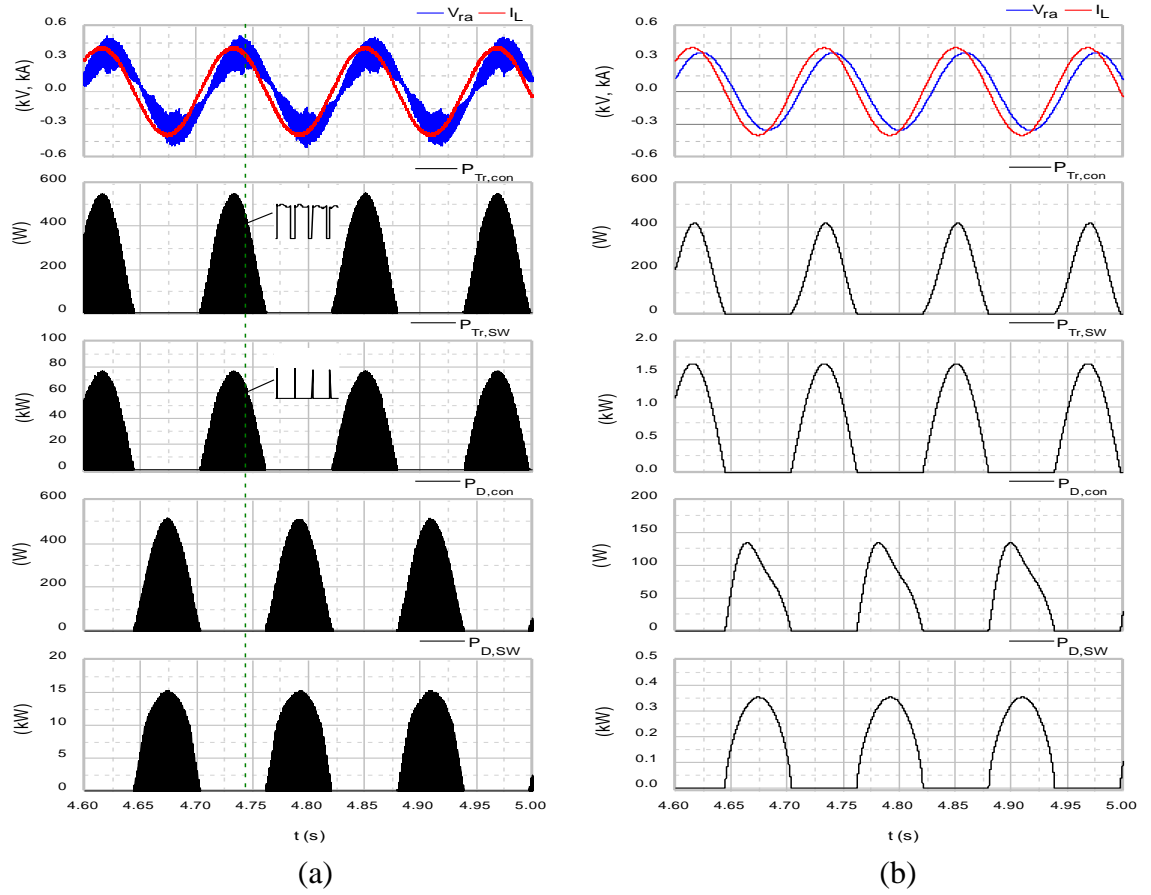


Figure 6.10 Device power losses obtained from (a) switched model and (b) switch-averaged model

By applying (6.23) to the instantaneous loss P_{ins} , the averaged loss are obtained, where T_C is one load cycle period. The averaged losses predicted with the above two methods are compared in Figure 6.11, where the wind turbine speed increasing from 0.75pu to 1.2pu. From the figure, the averaged model can give practically the same⁴ results as the PWM switched model. Hence it is implemented with the thermal model for fast simulation.

$$P_{mean} = \frac{1}{T_C} \int P_{ins} dt \quad (6.23)$$

⁴ Given that parameter variation and estimations add error bars of perhaps 10% on to these results, the differences in the model results are acceptable.

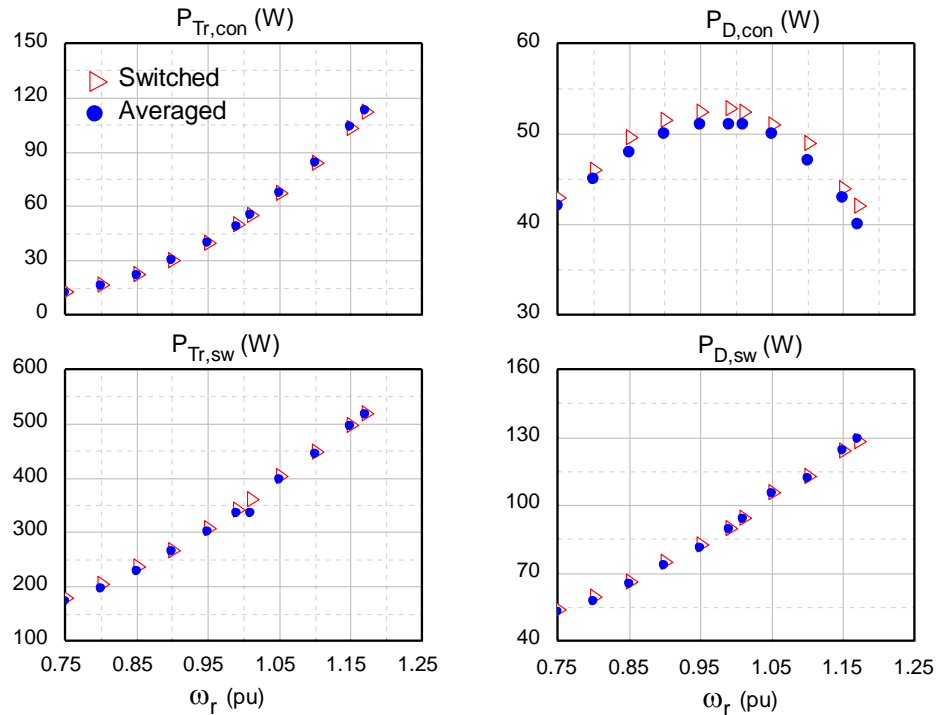


Figure 6.11 Comparison of the losses predicted by switched and averaged models at different turbine operating speeds

6.3.6. Verification with SemiSel

In this section, the power loss predicted in PSCAD/EMTDC will be verified with results from manufacturer's software, SemiSel. SemiSel is numerical simulation software provided by Semikron. The purpose is to aid their customers with device selection and comparison by performing power loss and temperature calculations. SemiSel will generate the mean loss values based on input information such as the transmitted power through the inverter, dc-bus voltage, load voltage and current in rms values. The algorithm is based on equations (6.11)-(6.12) and (6.16)-(6.17).

The model is tested for two operating regions. a). Below the nominal speed (ω_r : 0.75 p.u. - 1.17 p.u., optimum torque tracking region), where T_j or P_{loss} versus ω_r are obtained. b). over-load region (T_e demand increased from 1 p.u. to 2 p.u. at the nominal rotor speed), where T_j or P_{loss} versus T_e is obtained. In this way, the model is verified for a range of load frequencies, power dissipation levels and temperatures.

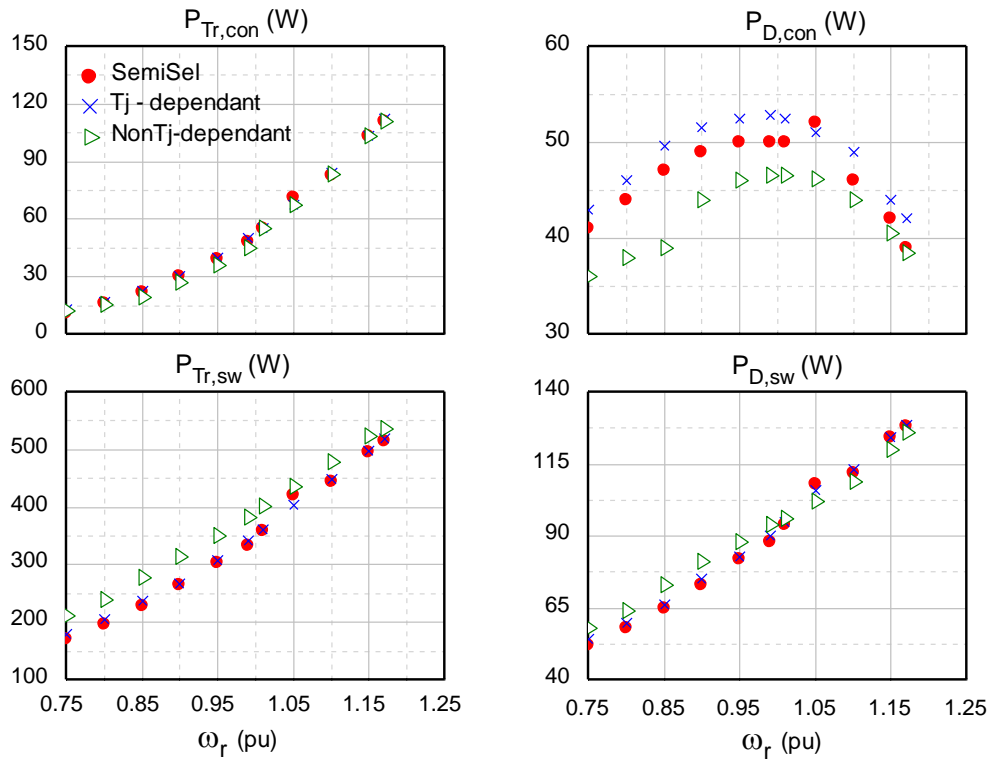


Figure 6.12 Verification of PSCAD/EMTDC models at different rotor speeds (below rated operating point)

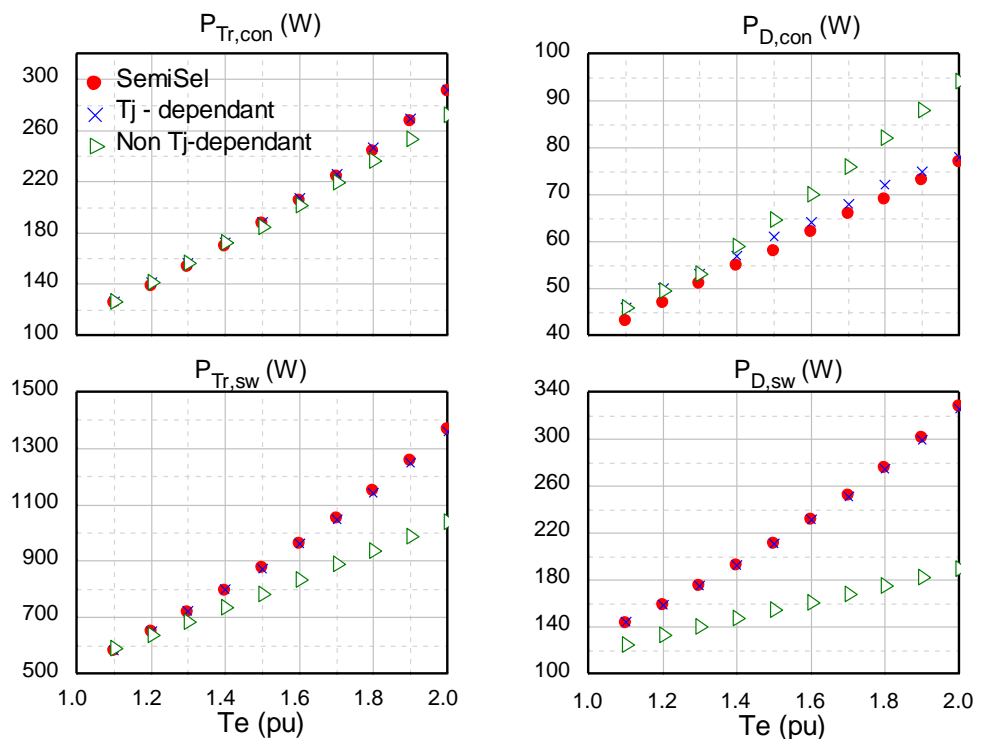


Figure 6.13 Verification of the PSCAD/EMTDC models at different torque demands (over-load condition)

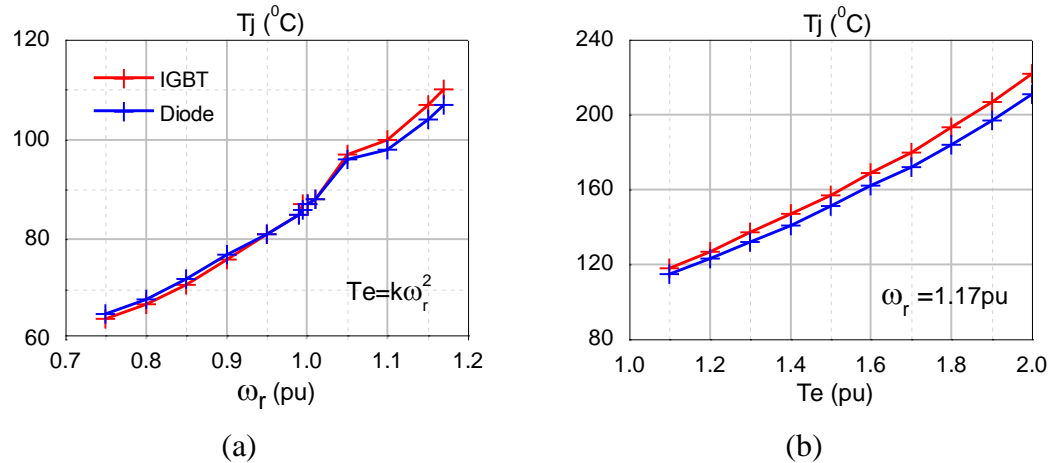


Figure 6.14 Mean device junction temperature obtained from SemiSel, (a) below the nominal operating point; (b) torque over-load conditions

In order to illustrate the temperature-dependency in the loss prediction, the switched averaged PSCAD model is simulated with and without the junction temperature effect, which are denoted in Figure 6.12 and Figure 6.13 as 'Tj-dependant' and 'non-Tj-dependant'. Below the nominal operating point, the junction temperature T_j is smaller than 120° as seen in Figure 6.14, and the power losses (Figure 6.12) produced by PSCAD and SemiSel have a good agreement. The temperature effect is more obvious for higher temperatures. As seen in Figure 6.13, the discrepancy between 'non-Tj-dependant' and 'SemiSel' becomes larger as the temperature increases. However, this effect is small for the IGBT conduction loss.

6.4. Thermal network

6.4.1. Concept of power device thermal model

Generally, from the thermal point of view, a solid system can be described by two alternative equivalent circuits composed of resistances and capacitances, as shown in Figure 6.15. In the circuit, the current source represents the power dissipation from the heat source, and the voltage source at the other end of the circuit indicates the heat sink with constant temperature. The electrical ground corresponds to the ambient temperature.

Each network represents transient thermal impedance characterized by the same set of thermal constants. The Foster network (also referred to as a 'chain' type model) is constructed from a mathematical point of view, where each RC cell corresponds to a

particular time constant of the transient; while the Cauer network (also referred to as a 'ladder' type model) is built from a physical point of view, where each time constant depends on all the RC elements and each node N indicates an actual physical position in the solid system. In this topology the RC cells have real physical meaning, i.e. R_{th} (thermal resistance) describes the material conductivity and dimensions while C_{th} (thermal capacitance) describes the heat storage capacity of a particular section [128].

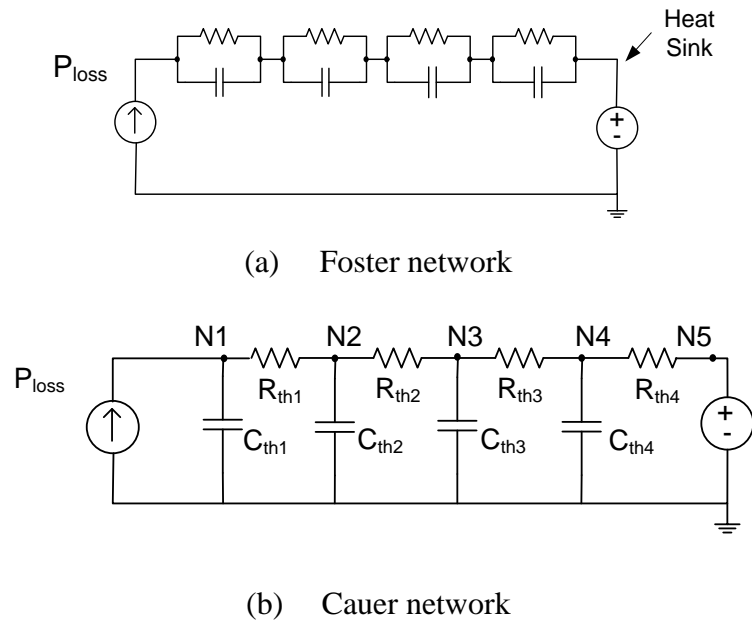


Figure 6.15 Two equivalent thermal networks

6.4.2. Thermal network development for SKiiP module

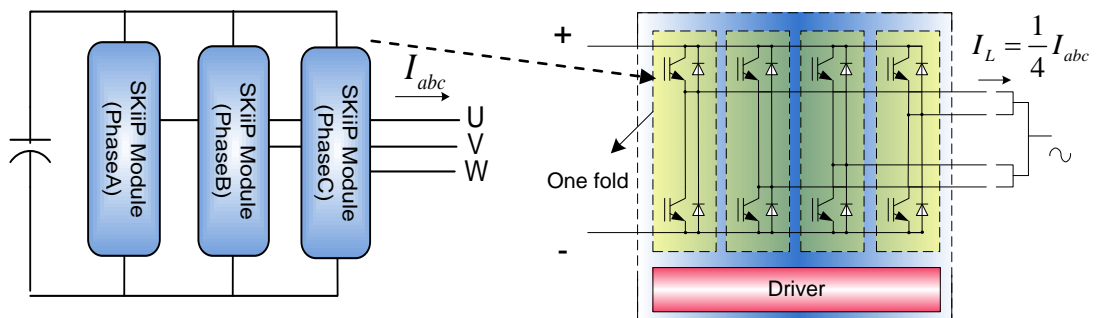


Figure 6.16 Three-phase inverter and the circuit construction in one SKiiP module

The prototype used for establishing the thermal network is the Semikron IGBT module SKiiP 2013 GB172-4DW, for which the circuit structure and loss dissipation has been depicted in Figure 6.16 and Figure 6.17. The half bridge SKiiP module constitutes

one-phase of the inverter switches, in which four IGBT folds are mounted on separate ceramic substrates, sharing a common heat-sink. Therefore the current passing through each device is a quarter of the load current.

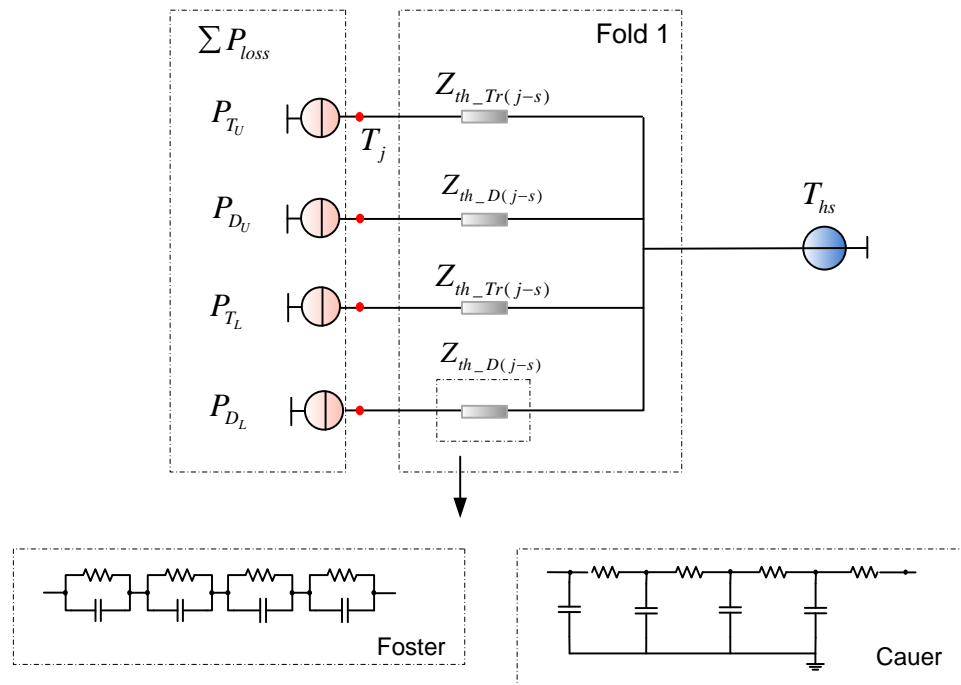


Figure 6.17 Device thermal network and power loss dissipation in one 'fold'

6.4.3. Circuit transformation from Foster to Cauer network

Most of the manufacturer datasheets only provide the Foster network data. However, this type of thermal model does not reveal the temperature variations at the inner layers of the device, which is important for identifying the high temperature point and improving the system design. On the other hand, the Foster network with no real physical meaning, cannot be cascaded directly to simulate the temperature variations. Therefore, it is necessary to perform a circuit transformation to obtain the equivalent Cauer circuit. This can be implemented in different ways. In [109], 3-D FEM together with time constant analysis is employed. A faster way has been introduced in [129]. The former can deliver a Cauer circuit with accurate physical correspondence. The latter method when used in combination with a spatial resolution analysis can provide a rough physical correspondence. This method will be adopted here for fast and convenient operation. Basic equations of the Cauer circuit are given by (6.24).

$$i = 1, \dots, n$$

$$\frac{1}{Z_{th_i}(s)} = s \cdot C_{th_i} + \frac{1}{R_{th_i} + Z_{th_i+1}(s)} \quad (6.24)$$

$$Z_{th_i+1}(s) \equiv 0$$

where Z_{th_i} denotes the impedance of the Cauer circuit seen from the i_{th} node. The transfer function of the Foster circuit will be decomposed in order to find the corresponding term with the (6.24). For the i th decomposition, the Foster impedance should be

$$\frac{1}{Z_{th_i}(s)} = \frac{D_i(s)}{N_i(s)} = a_i s + b_i + \frac{rem_i(s)}{D_i(s)} \quad (6.25)$$

Equating (6.24) with (6.25), and associating the corresponding terms

$$\Rightarrow \begin{cases} C_{th_i} = a_i \\ R_{th_i} + Z_{th_i+1} = \frac{D_i(s)}{b_i D_i(s) + rem_i(s)} \end{cases}$$

$$\Rightarrow \begin{cases} R_{th_i} = 1 / b_i \\ Z_{th_i+1} = -\frac{rem}{b_i^2 D_i(s) + b_i rem_i(s)} \end{cases}$$

This procedure must be follow for all $i = 1$ to n . In this way, an equivalent Cauer circuit can be found given the Foster thermal parameters. The transient thermal impedances of the IGBT (Z_{th_Tr}), Diode (Z_{th_D}), and heat-sink (Z_{th_hs}) are obtained by applying a step power at both of the equivalent circuits. As depicted in Figure 6.18, where the solid line indicates the Foster circuit and dashed line indicates the Cauer circuit, the derived Cauer circuit can accurately characterize the system's transient impedance.

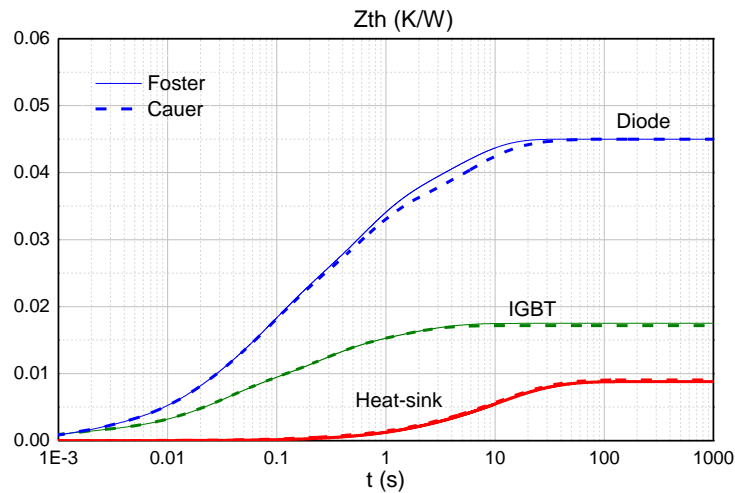


Figure 6.18 Transient characteristics obtained from the equivalent circuits

6.4.4. Spatial resolution analysis

In reality, to obtain a Cauer RC network with accurate physical correspondence is difficult without experimental measurement. The rapid circuit transformation method is easy to implement but provides ambiguous resolution. Finding this spatial resolution, however, will help to inspect the heat distributions at the internal layers. The layer construction of a power semiconductor with the corresponding section in a Cauer network is given in Figure 6.19. The thermal resistance share of the internal layers in a common module is given on the right, where TIM indicates the thermal compound (or thermal interface material).

Therefore, each node of the derived Cauer circuit corresponds to a unique location in the physical system as shown in Figure 6.20. The horizontal axis represents the thermal resistance measured from the top (Chip). Given a power P_0 , the steady-state temperature at each identified position is obtained. Here a fourth-order Cauer model is obtained. It is the layer interfaces that are considered to be critical points. A higher-order model can provide better resolution and thus will give the temperature for the point closed to the layer interfaces.

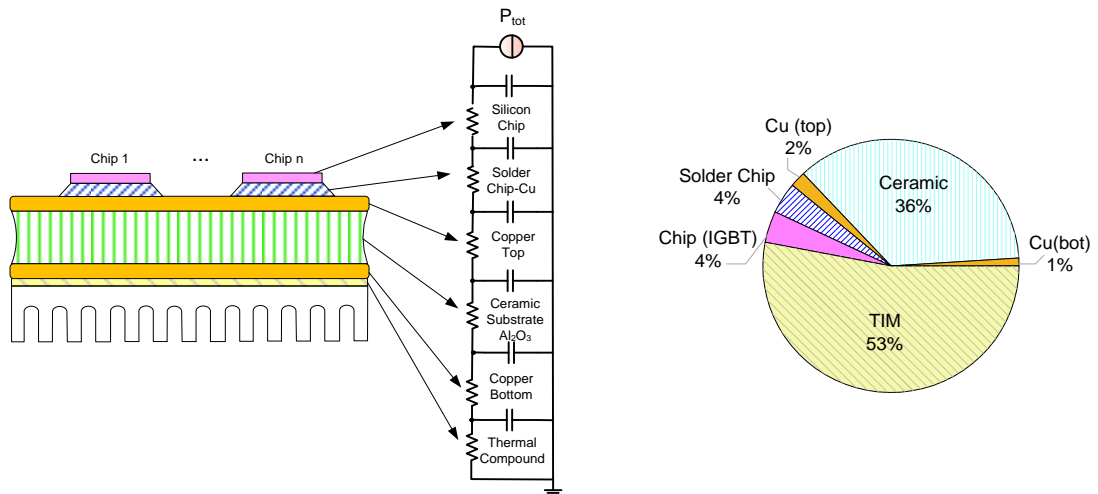


Figure 6.19 Basic structure with the thermal resistance share of each layer in a common power module [23]

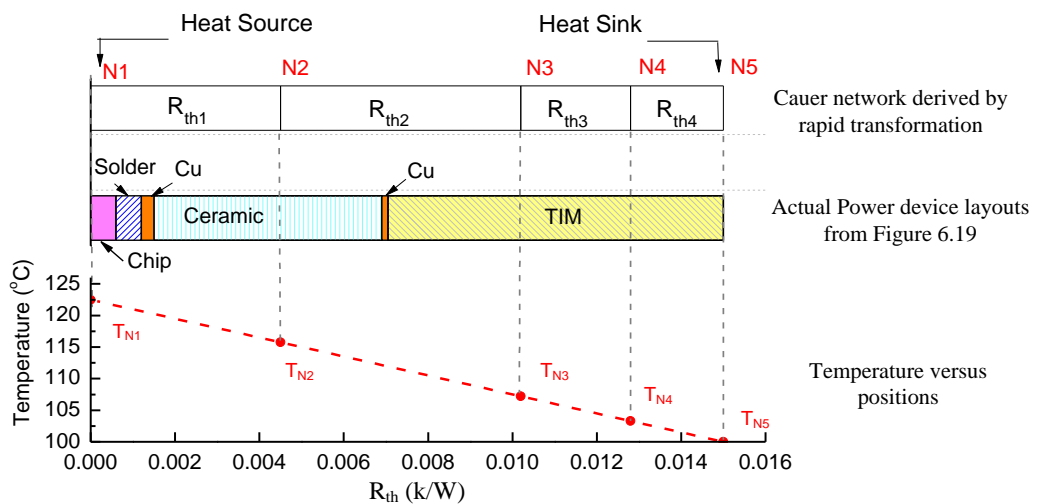


Figure 6.20 Spatial resolution of the derived Cauer network

6.4.5. Full thermal network

The main purpose of deriving the Cauer network by rapid circuit transformation is to establish the complete thermal network from junction to ambient. As depicted in Figure 6.21, the imposed losses $P_{Tr(D),tot}$ are constituted of both the power device's switching and conduction losses obtained from the switch-averaged model in Chapter 6.3.5. Neglecting the thermal loss via radiation or convection, the intermediate loss passing through the bottom of devices (P_{Tri}, P_{Di}), the TIM (P_{fold}) and the total loss transmitted to the heat sink P_{hs} has the following relationship:

$$\begin{aligned}
 P_{fold} &\approx 2 \times (P_{Tri} + P_{Di}) \\
 P_{hs} &\approx P_{fold1} + P_{fold2} + P_{fold3} + P_{fold4} \approx 4P_{fold1}
 \end{aligned}
 \tag{6.26}$$

The loss dissipations are measured from both the equivalent circuits at the same positions, and their time variations are depicted in Figure 6.22. For the Foster network, the instantaneous $P_{Tri(Di)}$ is equal to $P_{Tr(D),tot}$, and the heat distribution reaches the steady state in a short simulation time. In fact, in the Foster network, as RC cells are connected in series, the power flow at any point is the same as the source. That is, the heat transmission is instantaneous. In the Cauer network, the losses measured at the RC cells are different. Each thermal capacitance can store heat like a buffer, thus there is delay of heat transmission.

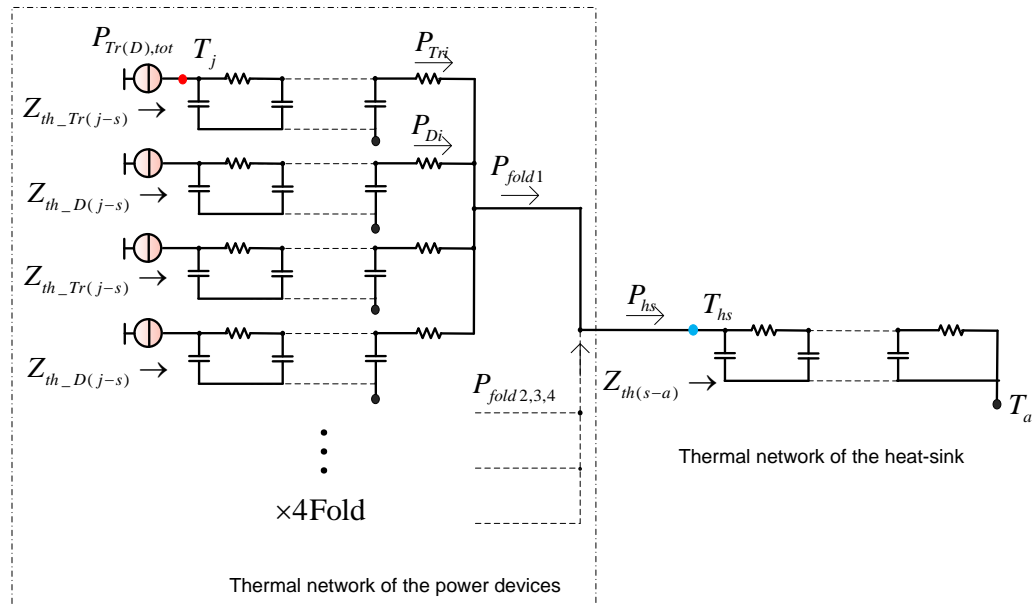


Figure 6.21 Full Cauer network including the power devices and the heat-sink

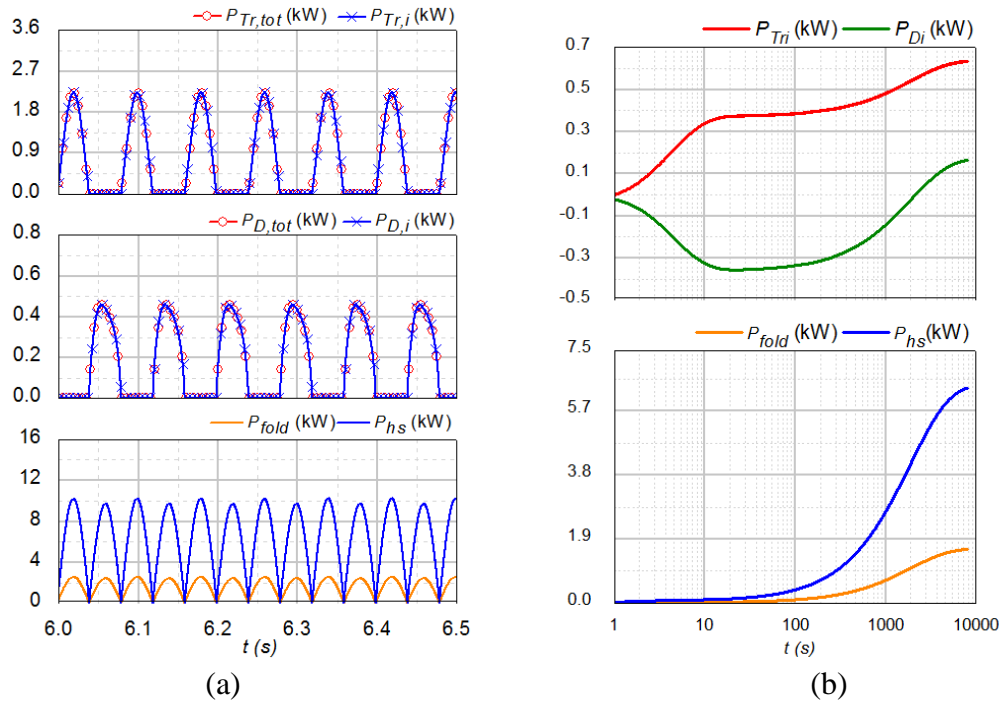


Figure 6.22 Loss distributions (a) instantaneous loss in the Foster network, (b) loss variations in the Cauer network during system start-up

It is found that for the diode, the heat transmission direction is at first from the heat-sink to the chip, and after approximately 2000s, heat starts to transfer from the chip to the heat-sink. This is because the diode's time constant is much larger than the IGBT's (refer to Figure 6.18). As shown in Figure 6.23, with the same loss input, it takes the Foster network approximately 100s to reach the steady state temperature, and about 6000s for the Cauer network. From the above results, only the Cauer network can properly represent the transient thermal behaviours of the whole system including the heat-sink. The combined Foster network can be used when only the steady state temperature is considered.

The temperatures at the nodes marked in Figure 6.20 are presented in Figure 6.24. It can be seen that N5 and N6 at the same layer (TIM) have very close temperature variation. Only the ceramic layer (N2) presents temperature swings at the load frequency.

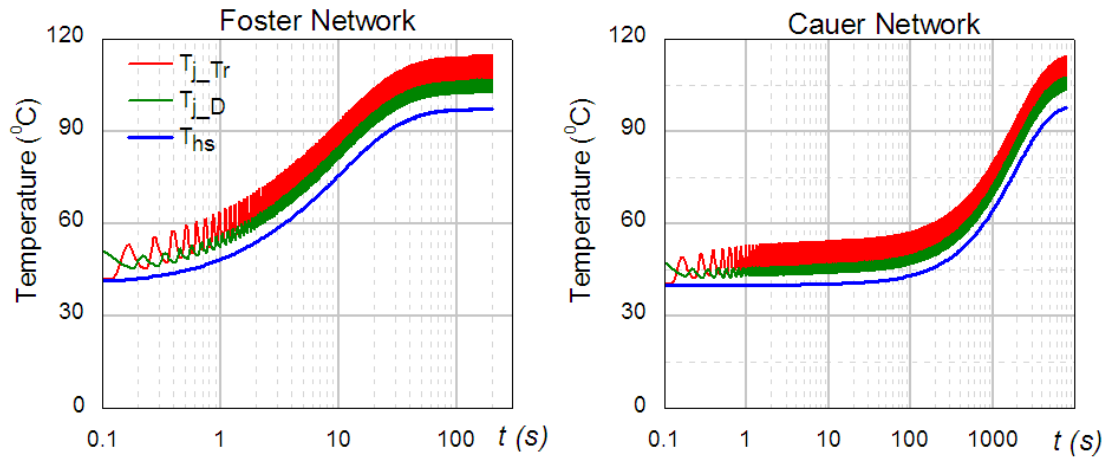


Figure 6.23 Transient temperature obtained from the two full thermal networks during system start-up

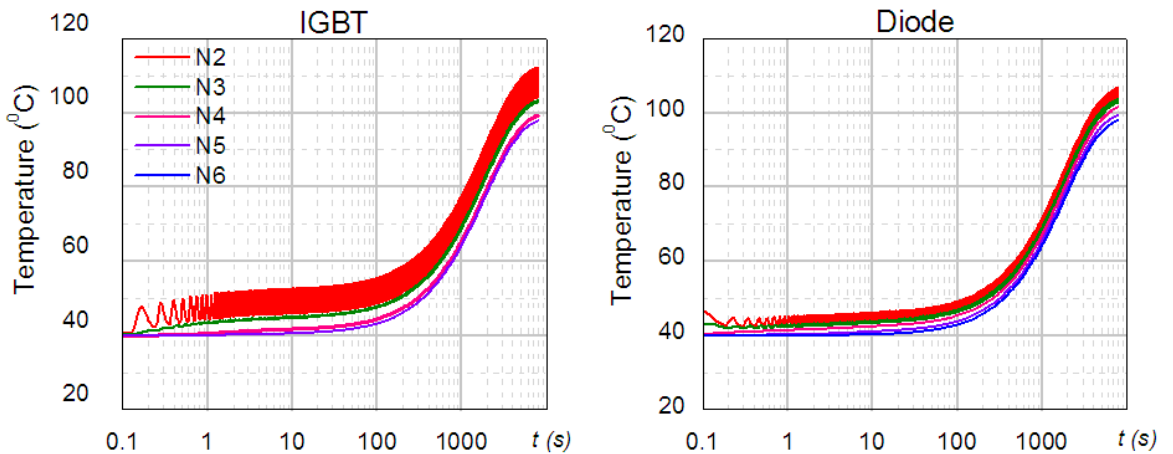


Figure 6.24 Transient temperatures at the internal nodes in the Cauer network

6.5. WTPC thermal capabilities under different conditions

6.5.1. Steady-state thermal cycling

The power losses predicted by PSCAD have been verified with the manufacturer's software, and the thermal model's transient characteristics agree very well with the datasheet. According to (6.27), the model can be used faithfully for temperature prediction.

$$T = P_{loss} \cdot Z_{th} \quad (6.27)$$

It is known that the thermal response of the power device determines the junction temperature variations during a load cycle. The temperature at the heat-sink has negligible changes during a load cycle due to the relatively high frequencies of the electrical system and the relatively large thermal constant of the heat-sink. However, the heat-sink significantly influences long term temperature change such as system start-up [130]. Therefore, to investigate device thermal cycling in steady-state, constant temperature can be assumed for the heat-sink.

The average temperature of the IGBT junction and heat-sink with corresponding variations ΔT_j are recorded for a range of operating points in Figure 6.25. It is observed that the mean temperature – speed curve takes a similar form as the wind turbine torque – speed curve. This is because that the power loss of the device has a linear dependency of the rotor current, which in turn is determined by the electric torque.

According to the Coffin-Manson-Law [32], the number of cycles to failure for a semiconductor is determined by both of the mean junction temperature and the temperature variations. For a typical DFIG wind turbine, the rotor current is at slip frequency, which is in the range of ± 0.3 p.u., or -15 Hz to +15 Hz. As the rotor speed approaches the synchronous point, the temperature variation increases, thus the possible number of cycles to failure reduces. However, the period for each cycle is longer. Therefore it is not necessary that the remaining life time reduces proportionally with the slip frequency. There is a threshold-slip frequency (0.2-0.4Hz) which is most lifetime consuming for this operating range [6].

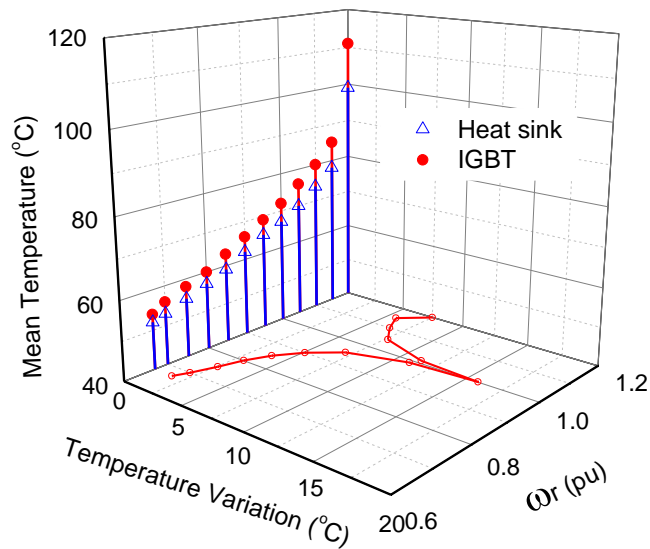


Figure 6.25 Average temperature and corresponding variations at different rotor speeds

6.5.2. Transient thermal response under electric torque over-load

The maximum temperature for the power device to survive is 150°C , which is reached at torque commands $T_e = 1.5$ pu (see Figure 6.26). However, it is recommended by Semisel that it is better to keep the device temperature less than 125°C (referred as the rated temperature) for normal operation. This implies that the RSC can work without significant degradation below 1.2 pu T_e . Above this point the power device is subjected to enormous stress and may wear out quickly.

ΔT_e	0.2	0.3	0.4	0.5	0.6	0.7	0.8	ΔT_e	0.2	0.3	0.4	0.5	0.6	0.7	0.8
t (min)	IGBT junction temperature ($^{\circ}\text{C}$)							t (min)	Diode junction temperature ($^{\circ}\text{C}$)						
5	120	123	126	129	132	135	138	5	111	113	115	116	118	120	122
10	122	126	130	133	138	142	146	10	113	116	118	121	124	127	130
15	123	128	133	138	143	148	153	15	114	118	122	125	129	133	137
20	125	130	136	141	148	153	159	20	116	120	124	129	134	138	143
25	126	132	138	145	151	158	165	25	117	122	127	132	137	143	149
30	127	134	140	147	155	162	170	30	118	124	129	135	141	148	154
35	128	136	142	150	157	166	175	35	119	126	132	137	144	152	159
40	129	138	144	152	160	170	179	40	120	128	135	139	147	156	164

Table 6.7 Device temperature evolution with time under different steps in torque demand from a nominal operating point ($T_e=1$ pu, $\omega_r=1.17$ pu)

Different electric torque steps were imposed at the nominal operating point ($\omega_r = 1.15 pu$, $T_e = 1 pu$), and the transient thermal responses are shown in Figure 6.26. The peak temperatures of both devices were recorded at every 5 minutes, as shown in Table 6.7. The temperatures over $125^\circ C$ and $150^\circ C$ are distinguished in orange and red respectively. From the table, for a 0.2 p.u. torque step, it takes the power module about 20 minutes to exceed the rated temperature ($125^\circ C$). On the other hand, for 0.5 p.u. torque step, the device will reach the critical point ($150^\circ C$) after 35 minutes. The result shows that the power module's capability of over-load duration is quite long. Considering the heat-sink is water-cooled and well designed, and it can take hours for the heat-sink to reach a steady state temperature at start-up {Bryant, 2008}, this result is not surprising. However, this does not take account of other abnormal conditions such as load disturbances or grid-faults, in which case the heat-up process may be accelerated and overload survival time for the power devices will be reduced.

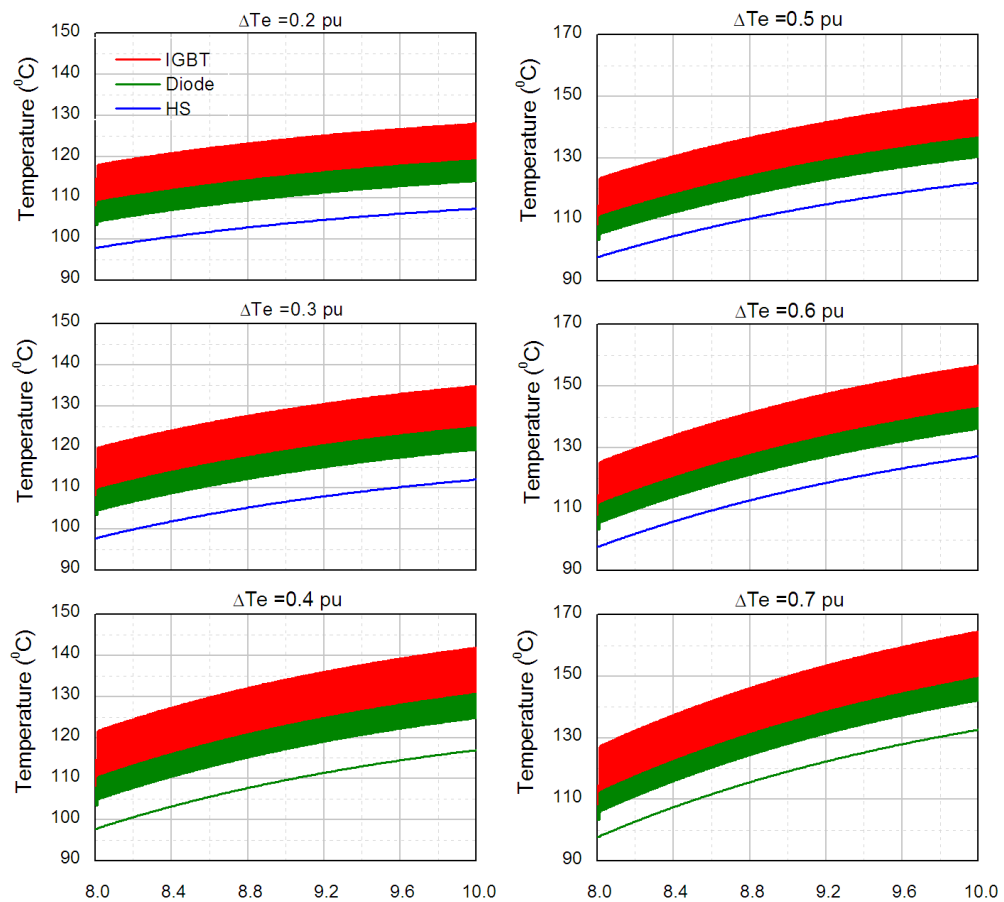


Figure 6.26 Transient thermal responses under different torque steps

6.5.3. System performance under grid voltage drop

The DFIG wind turbine model is initially working at its rated operating point. A 40% three-phase balanced voltage drop is introduced for 0.5s. Since the thermal constant of the heat-sink is much longer compared to the fault duration, constant temperature is considered. In Figure 6.27, the RSC d-q current-loops are both set at 10Hz. The three phase currents and voltages, the dc-voltage, and the junction temperatures of both the RSC and GSC are presented. A significant transient occurs when the fault starts and clears, and the device junction temperatures increases correspondingly. The diode's temperature swing is smaller than the IGBT due to a relatively larger thermal constant. Figure 6.28 is obtained by setting the RSC d-q current loop to be 10 Hz and 150 Hz respectively. The modified controller results in smaller current transients and thermal stress, especially for the GSC (from 150 °C peak temperature to 130 °C).

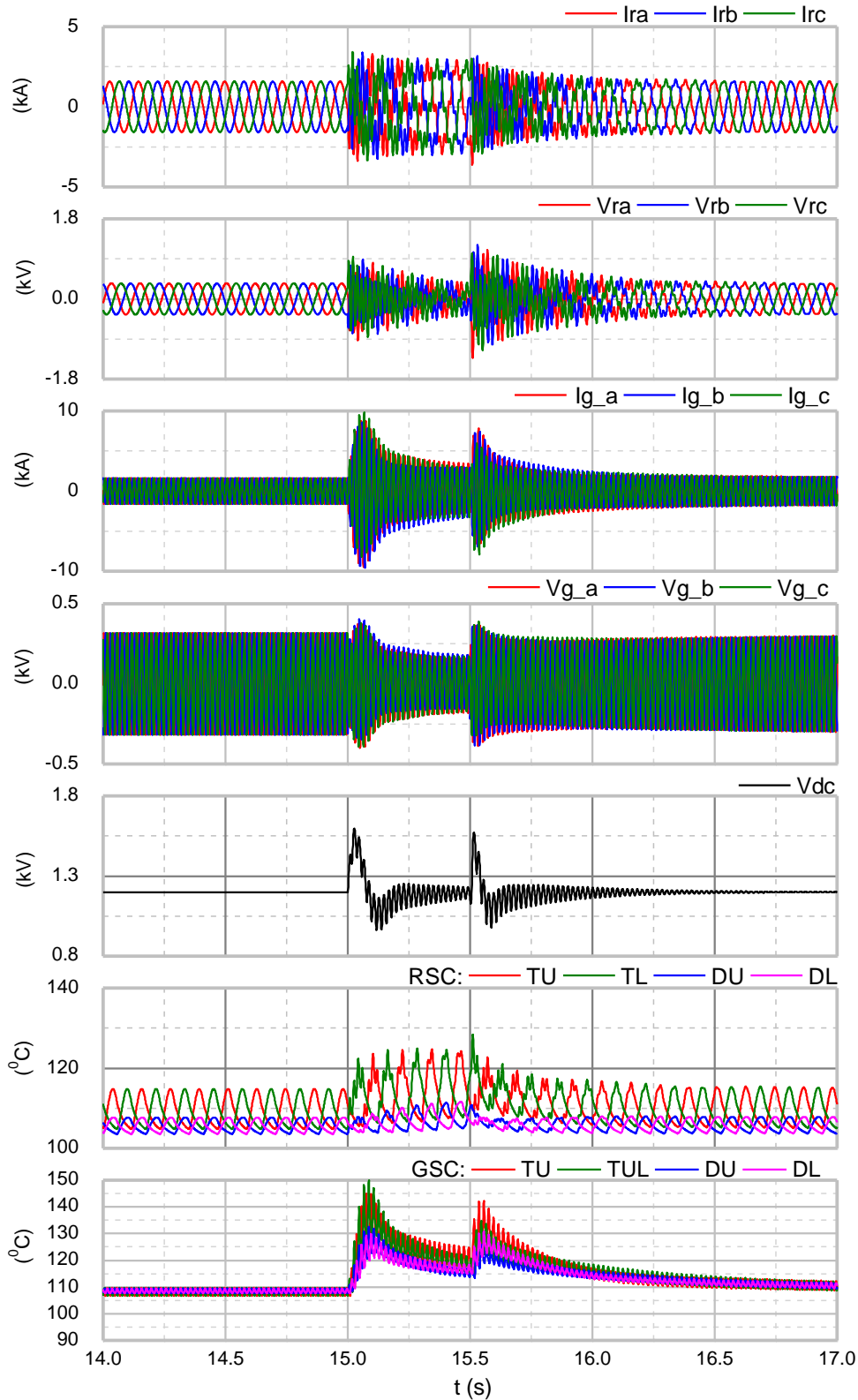


Figure 6.27 Converter electrical and thermal responses under 40% grid voltage drop with RSC d-q loop at 10Hz

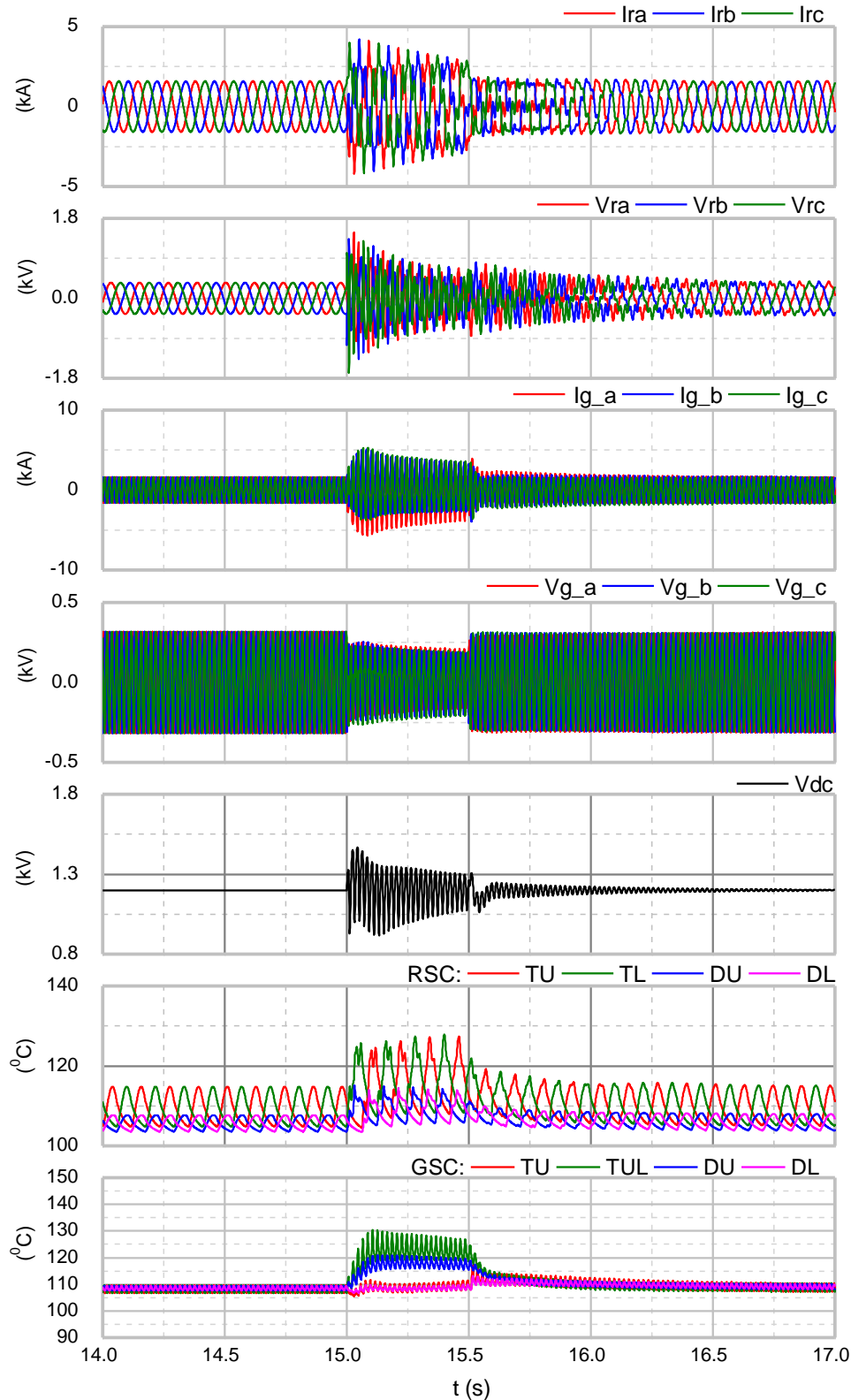


Figure 6.28 Converter electrical and thermal responses under 40% grid voltage drop with RSC d-loop 10Hz and q-loop 150Hz

6.5.4. System performance under variable wind speeds

The rest of the work presented in this chapter is based on the collaboration with Strathclyde University. The torque demand and rotor speed generated from the generic, and a modified, control strategy are obtained, given a wind profile as shown in Figure 6.29. Over 800s, the wind has an average speed of 8.5m/s and 10% turbulence. The optimum torque tracking strategy is implemented here as the generic control strategy. The RSC performances are presented in Figure 6.30. In this case, the Cauer network including the heat-sink is used. In order to reach a steady state, the model should be run at least 6000s with constant inputs (wind speed, torque demand and rotor speed). After then, the given wind profile is employed. As shown in Figure 6.30, the heat-sink temperature is not changed significantly (approximately 1.5 °C). Large junction temperature cycling (numbered 1 to 10) occurs frequently as the rotor speed passes across the synchronous point. Figure 6.31 shows a magnified view at point 6. Uneven heat distributions are observed among different devices. The cycling period lasts about 10s with a peak junction temperature rise of over 15 °C.

The responses of the GSC are shown in Figure 6.32, where the dc-voltage presents little disturbances. The three phase voltages remain almost constant. In this case, the GSC device temperatures are much lower due to smaller load currents. Two types of variations present in the device temperatures: the slow variation is introduced by the variable electric torque, and the high frequency (50Hz) variation is introduced by the load currents.

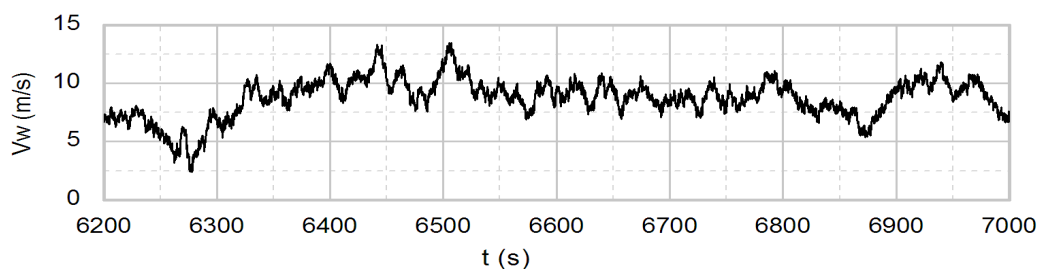


Figure 6.29 800s wind variations with 10% turbulence

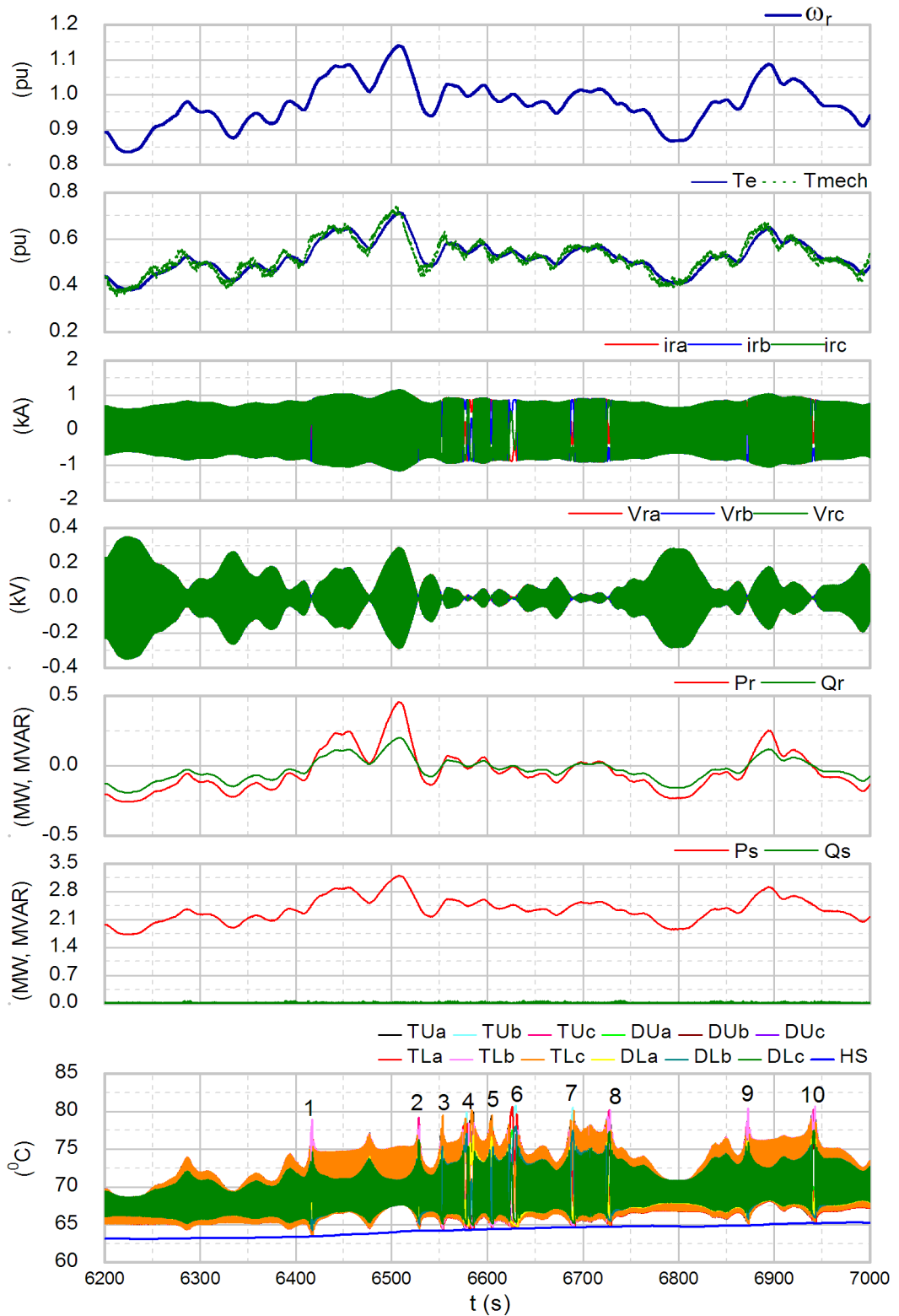


Figure 6.30 RSC electrical and thermal responses under 10% wind turbulences

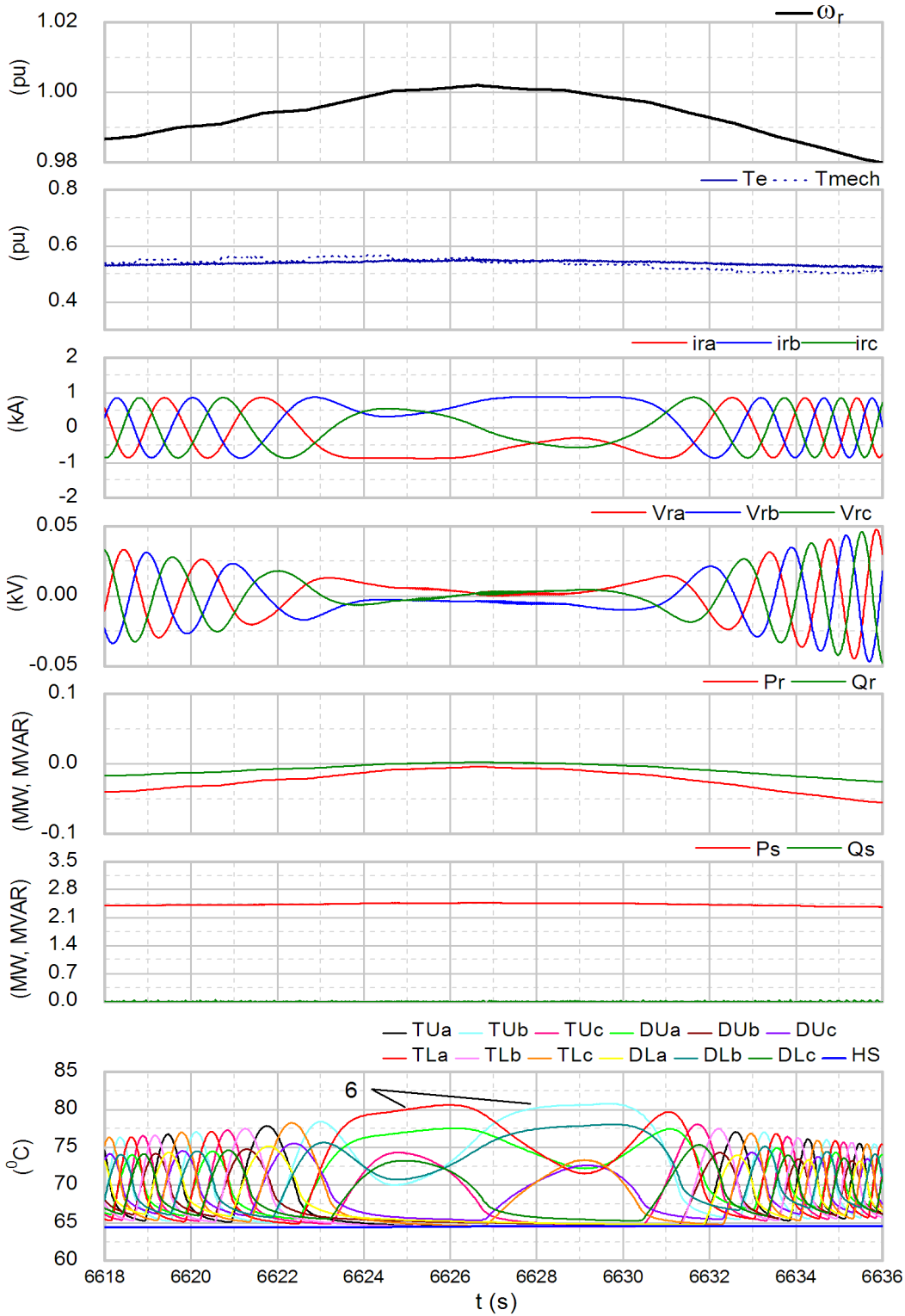


Figure 6.31 Magnified graph of the RSC electrical and thermal performances

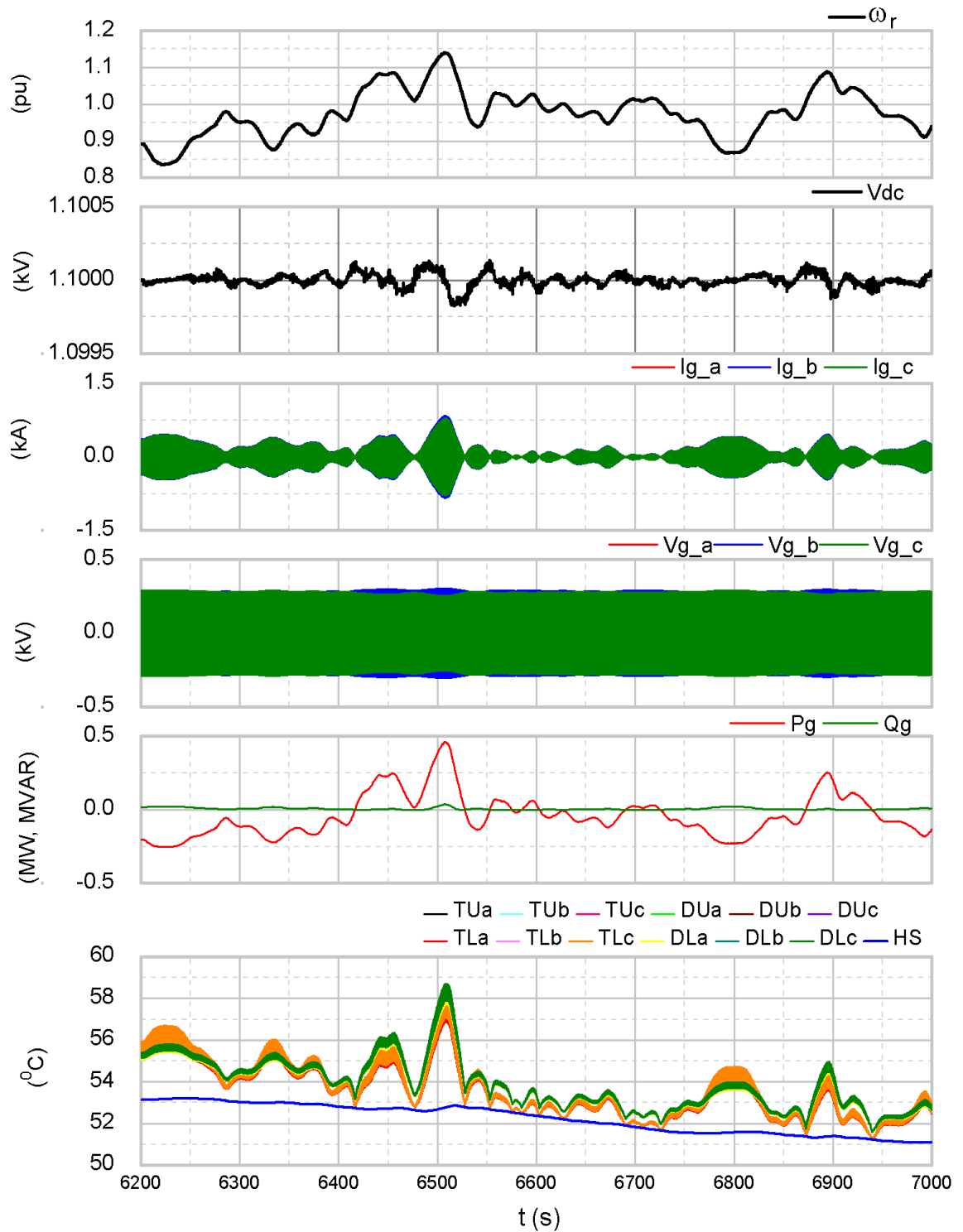


Figure 6.32 GSC electrical and thermal responses under 10% wind turbulences

6.6. Synchronous point enhancement through the modified controller

Finally, a modified controller that regulates the wind turbine to avoid long-period operation near the synchronous point is employed into this model. The method was

initially introduced in [131] to prevent the excitation of structural resonance. The strategy diagram is shown in Figure 6.33. Instead of following the original $C_{p_{max}}$ curve, the turbine tracks a discontinuous torque-speed curve. A bandwidth of 1 Hz around the synchronous point is set to be the critical region that the turbine should avoid. Based on this, two cut-off speeds are defined i.e. ω_{rA} and ω_{rB} . The electrical and mechanical outputs of both the generic and the modified controllers are compared in Figure 6.34. If the rotor speed is increasing from A to B, the controller will maintain the turbine speed at ω_{rA} for a while by increasing the torque demand ΔT_{e1} until the mechanical torque exceeds the threshold value $\Delta T_{eA} + \Delta T_{e1}$. The controller then switches to point B and follows a new reference $\Delta T_{eA} - \Delta T_{e2}$. The balance between mechanical and electric torque breaks, which forces the rotor speed to pass across the critical region quickly. This transition corresponds to point 1 in Figure 6.34. Similarly, the transition from B to A corresponds to point 2.

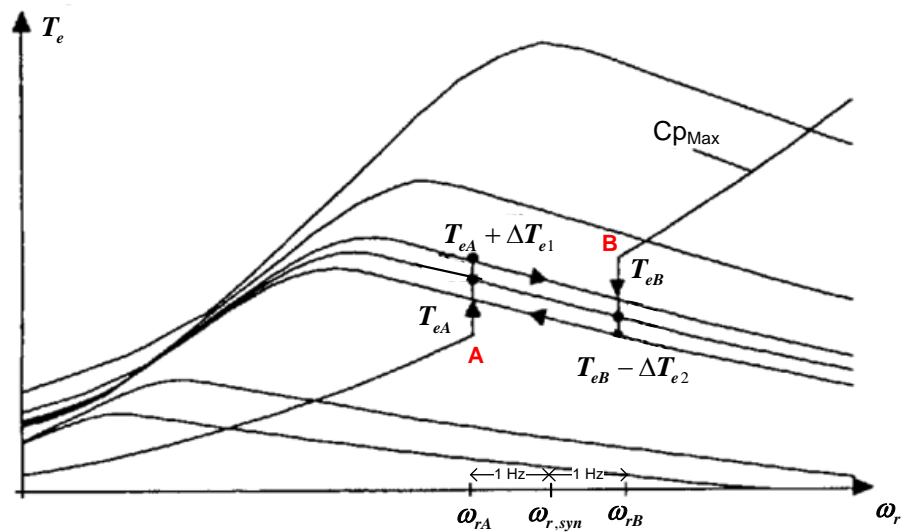


Figure 6.33 Modified controller avoiding synchronous operating point

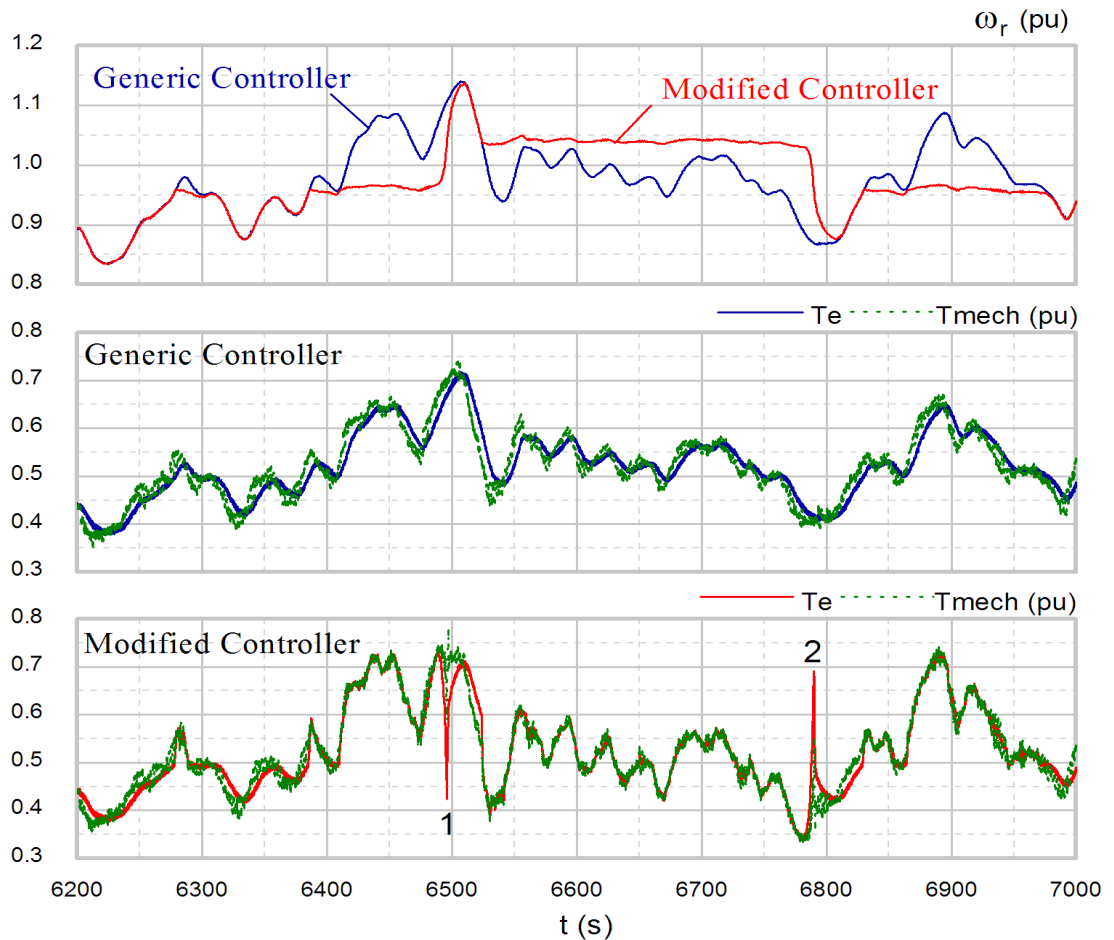


Figure 6.34 Rotor speed, electrical and mechanical torque from the generic and the modified controller

The RSC electrical and thermal performances produced from the modified controller are shown in Figure 6.35. Figure 6.36 and Figure 6.37 show the magnified views of the two transitions. The responses of GSC are presented in Figure 6.38. The controller transition causes electric transients in the rotor currents, stator power and the dc-link voltage. For the RSC device junction temperature, the number of pulsations reduces to 2 (Figure 6.35) from 10 (Figure 6.30). For the GSC, the fluctuations in the current, power and device temperatures are reduced.

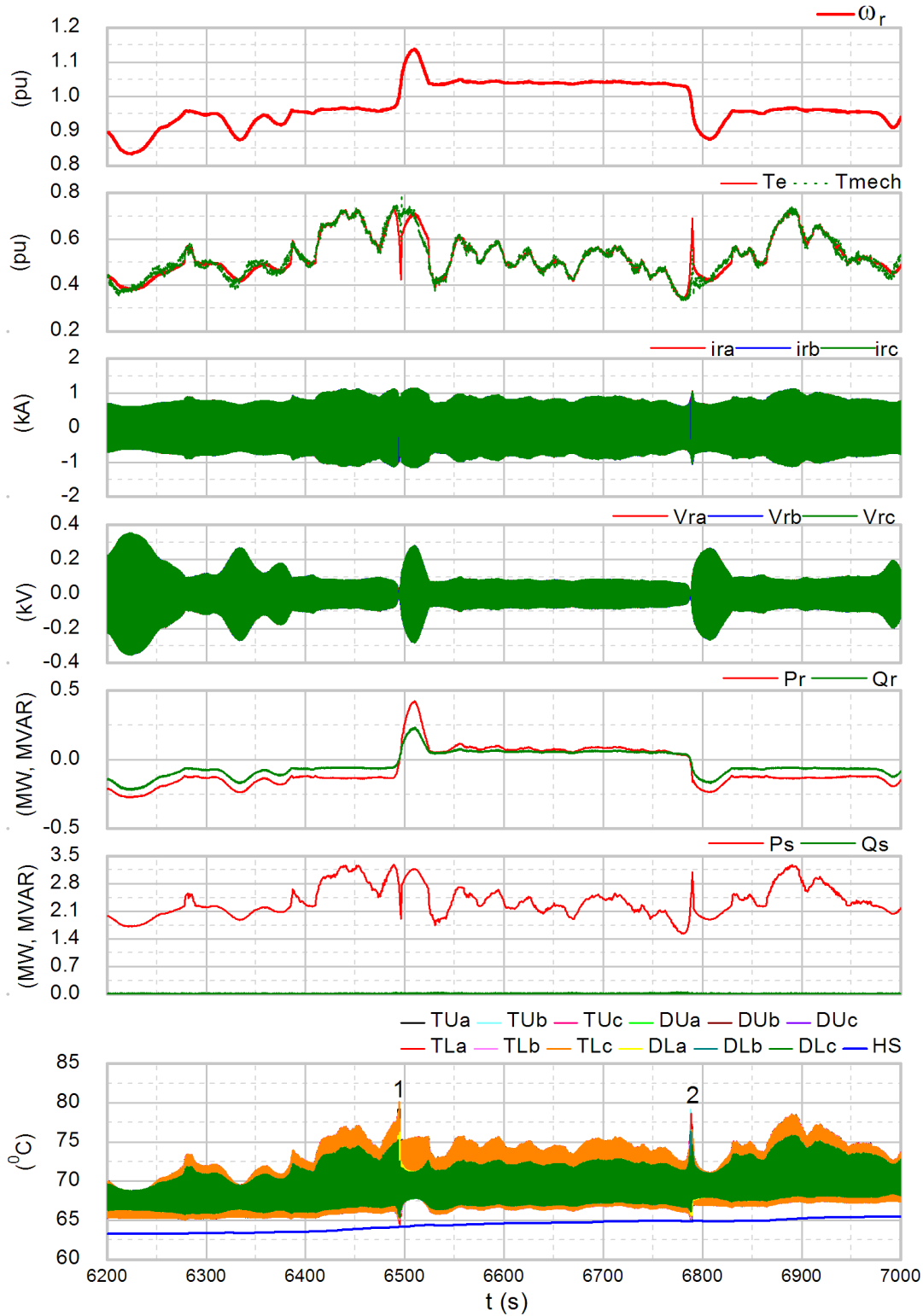


Figure 6.35 RSC electrical and thermal responses under 10% wind turbulences using the modified controller

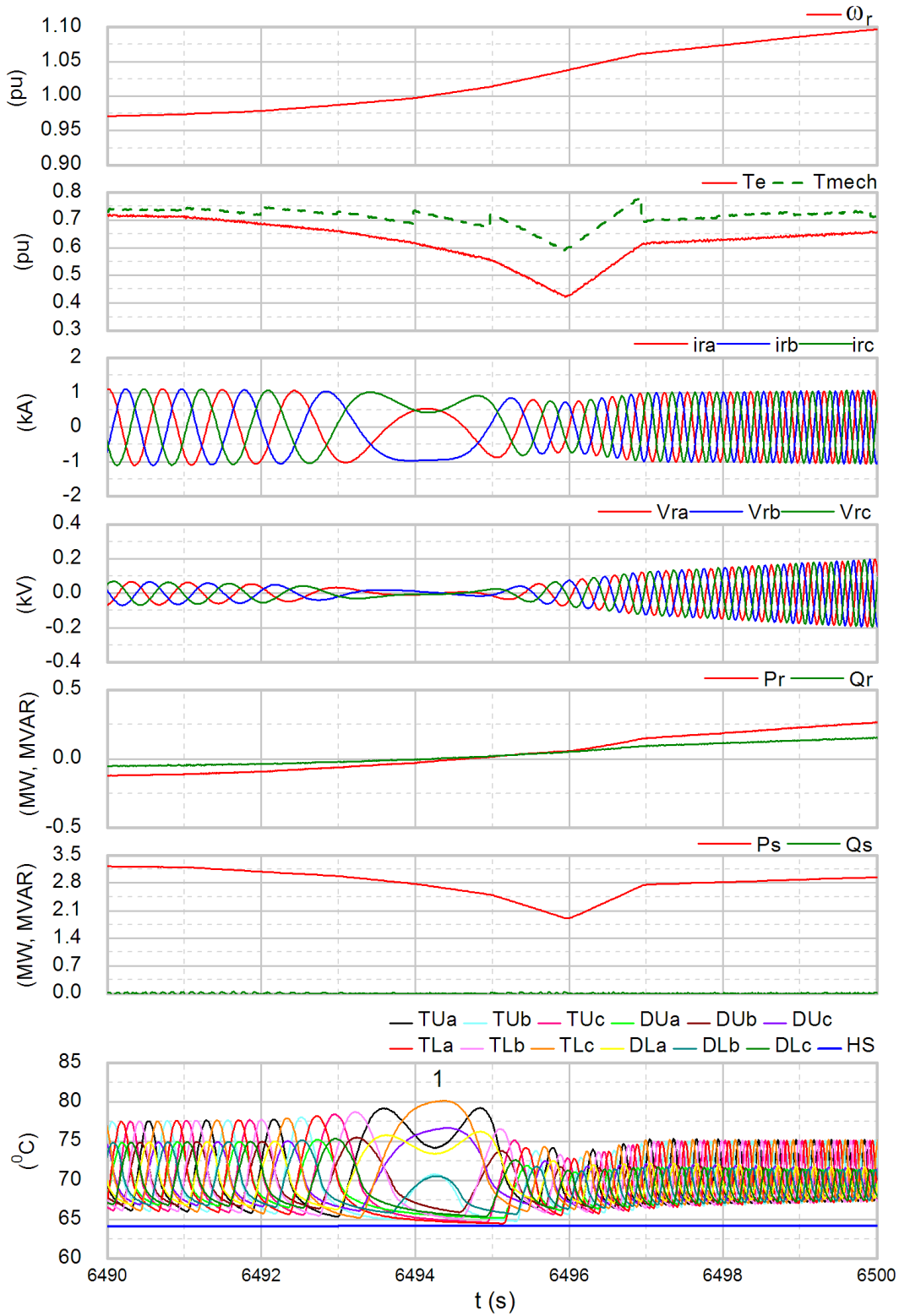


Figure 6.36 Magnified graph of the RSC performances in the first controller transition

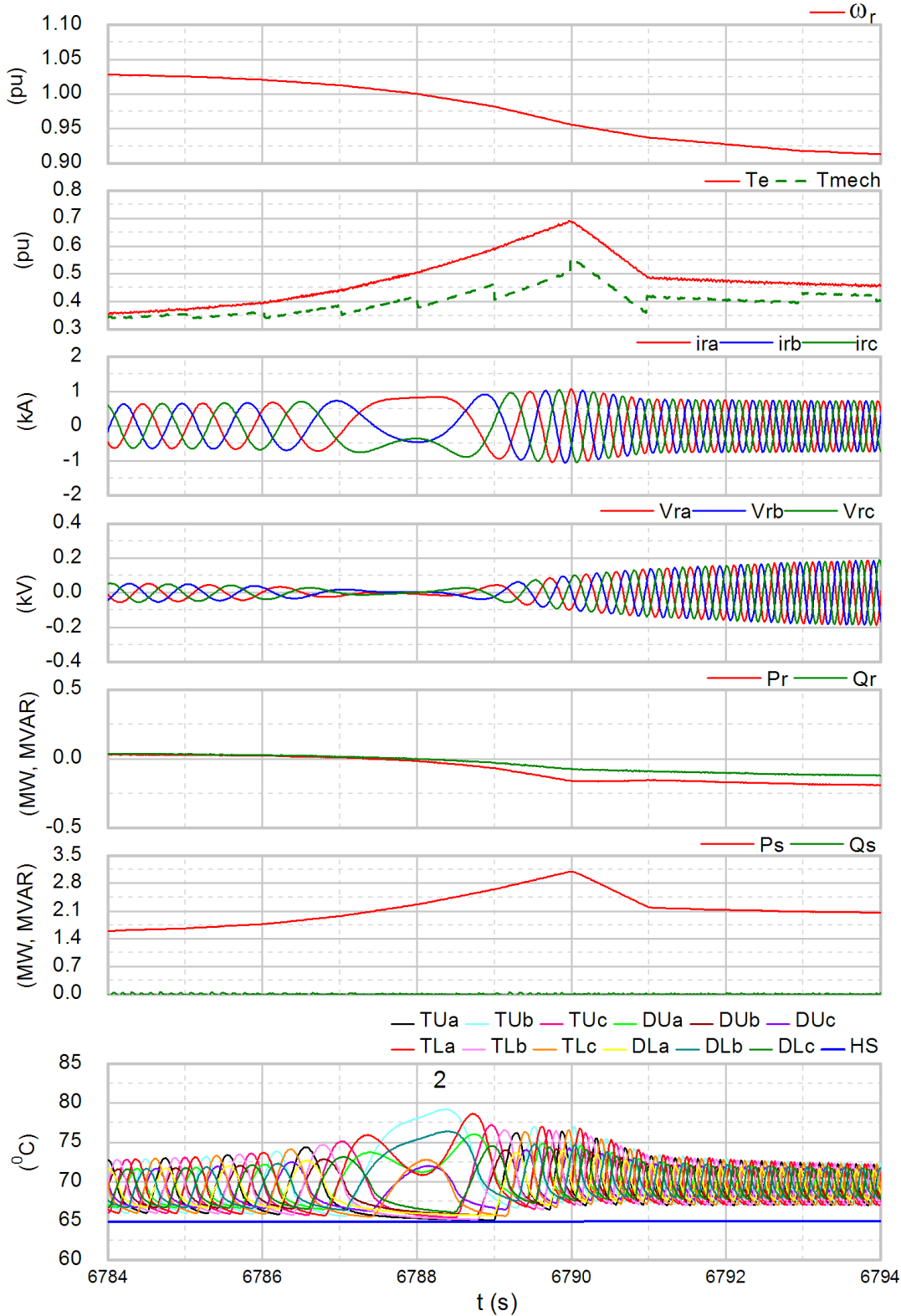


Figure 6.37 Magnified graph of the RSC performances in the second controller transition

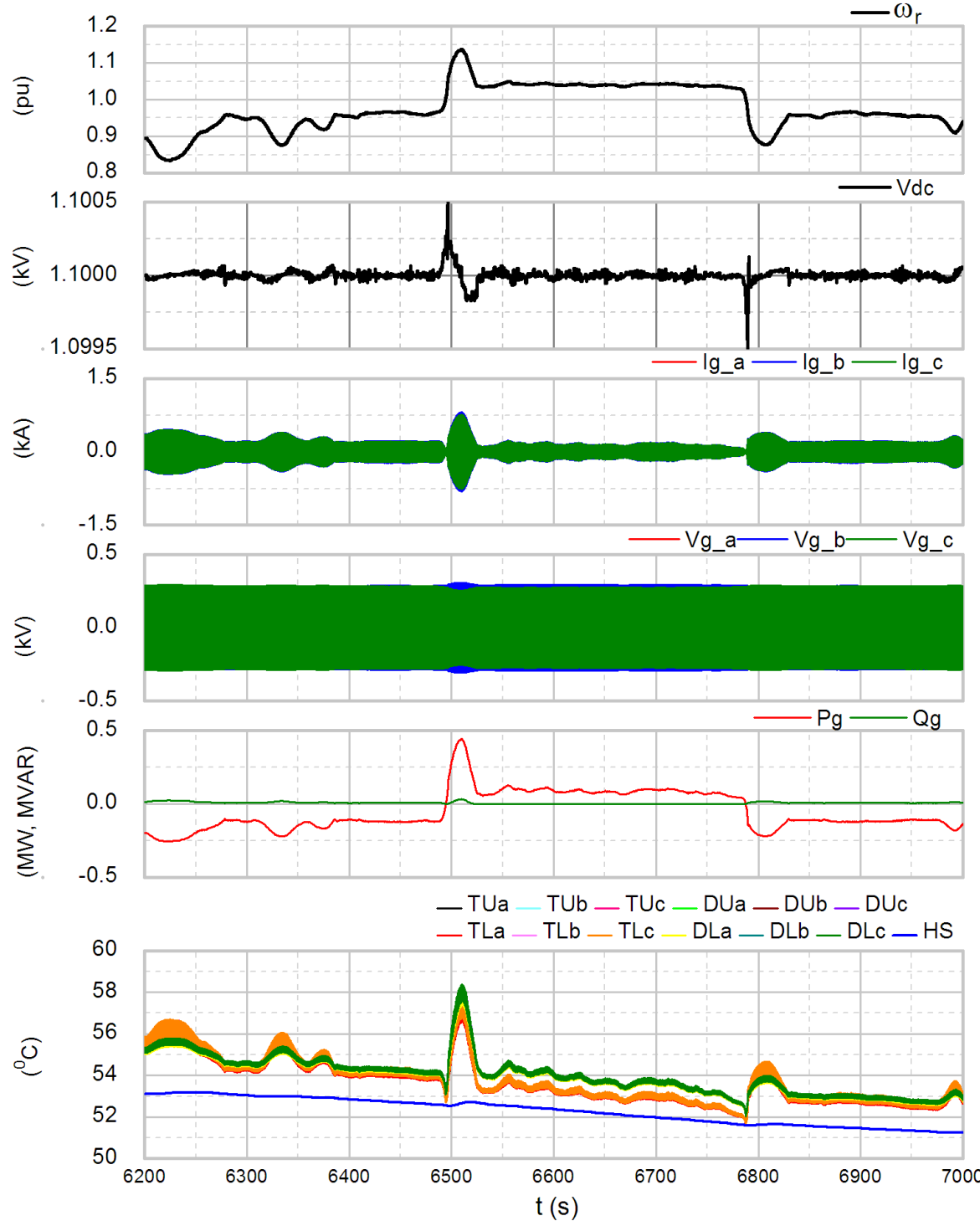


Figure 6.38 GSC electrical and thermal performances under 10% wind turbulences using the modified controller

6.7. Conclusions

In this chapter, a complete converter thermal model with loss prediction method is presented, considering the ratings in real applications. The accuracy of the model has been verified with the manufacturer's software. A quasi-instantaneous loss prediction method is adopted based on the switch-averaged converter model, which allows a larger simulation step without degradation of the accuracy. The simulation speed is hence increased essentially compared with the generic loss prediction method using the PWM gate signals. The RSC and GSC thermal network is developed for Semikron SKiiP module based on manufacturer's datasheet. The simulation shows only the Cauer network can give the correct transient thermal response when two (several) networks are to be cascaded. Therefore, for investigating the impacts of long-period load variation, a complete Cauer network including the power devices and heat-sink is required. For short period investigation such as grid fault, the device thermal model with a constant heat-sink temperature is sufficient.

Although large temperature swings near the synchronous operating point impose significant shear stress at the semiconductor layer interfaces, the mean temperature is lower compared to the rated operating point. Both the synchronous and the rated operating points are critical to the inverter and should be avoided for long duration operation. Determining which operating point matters more should take account of the converter dimensions and the average wind speed at the wind farm site.

The power devices can survive for a long period (minutes) for a torque demand to 1.8 times the rated torque. In the condition of grid voltage drop, the thermal stress can be reduced by an improved RSC controller tuning.

The system behaviour near the synchronous point is evaluated with 800s of variable wind speed data. It is demonstrated that the severe temperature swings in the RSC can be reduced with the modified control strategy. In the meantime, smoother electric and thermal responses are obtained.

The contributions of this chapter are the integrated dynamic electro-thermal model, highlighting the impact of electrical control tuning and evaluating performance integration with conventional and new turbine control.

Chapter 7. Conclusions and Recommendations for Further Work

The thesis focuses on improving the reliability of the DFIG wind turbine system through better control strategies, and shows methods to achieve reduced electrical and mechanical stresses. The results will be summarized in the following.

7.1. Power converter reliability and failure mechanisms

A literature study on power electronic converters used in wind energy has been carried out with the focus on the failure mechanisms and condition monitoring techniques. Today's market is dominated by the two-level back-to-back voltage source converter, while the multi-level converter is attracting more and more interest in high-rating applications.

The failure mechanism and reliability prediction methods for two critical components, the semiconductor device and the capacitor are discussed in detail. For the conventional wire-bonded IGBT (WBI), bond-wire lift-off and solder joint crack are the main failure driving factors. For the electrolytic capacitor, evaporation of the electrolyte during long-term operation is the most common factor resulting in aging. These failure mechanisms have been eliminated in the newer technology, i.e. the press-packed IGBT (PPI) and metallized polypropylene film (MPPF) capacitor. This makes them a more favourable choice compared with the conventional technologies due to higher reliability.

Condition monitoring (CM) for power electronics is still at an early stage. Parameter-based and model-based CM techniques have been summarized. Recent studies suggest that an effective way to achieve a real-time predictive CM would be to implement a combined wind turbine and power converter reliability model that can estimate the system health and lifetime during its operation.

7.2. DFIG wind turbine modelling and mathematical analysis

A comprehensive DFIG wind turbine is established in PSCAD/EMTDC, including the aerodynamic model, 2-mass shaft model and pitch control system. It is explained that the 2-mass shaft model can sufficiently characterise the system dynamics in this work and can be adopted for investigating the system dynamics and controller correlations.

The steady state model and the dynamic model with different reference frames, together with the vector control method for both the RSC and GSC were reviewed. Two kinds of converter models are presented - a full switched and a switch-averaged converter model. The former is better used for detailed analysis of fast electric transients, and the latter is suitable for investigating slower system dynamics. Typical wind turbine operating curves and the general pitch control strategies are also reviewed. The mathematical models for DFIG sub-systems are derived. These mathematical models are verified by PSCAD simulation and then are used to determine the controller gains for optimum performances.

The dc-link dynamics and wind turbine mechanical dynamics have been analysed in detail, with corresponding linear models derived. Such whole system analysis appears never to have been conducted to this detail before. The linear models have also been verified by PSCAD at different operating points. Based on this, the dc-link voltage and the grid current perturbations in response to an injected power step, and the blade angle and rotor speed variations in response to a wind speed step, have been evaluated for different controller gains.

The three most commonly used pitch controllers (P, PI and PID) were evaluated. A phase margin of approximately 75° and a gain margin larger than 10 dB are recommended for the system open-loop transfer function including the controller and actuator. This setting gives relatively fast response with no pitching overshoot. A rotor speed error always exists when using the P controller. In contrast, the PID controller can provide good error sensitivity when the derivative term is set sufficiently large. With variable wind speeds as found in practical conditions, the PI controller presents very similar performance to the PID controller. Due to the highly non-linearity of the wind turbine aerodynamic model, a gain scheduling technique is included in the controller design, in order to ensure consistent performance over the turbine's full operating region.

7.3. Controller coordination to improve fault ride-through capability

Several problems caused by a grid voltage drop have been dealt with. Firstly, the stator transient flux may introduce voltage and current transients several times higher than their rated values, and the long time it takes for the transient to vanish after the grid fault, only makes it worse. As a consequence, the converter control may be saturated, leading the control system to go unstable. Worse still, the converter can be damaged due to severe

electro-thermal stresses. A recently developed method – a demagnetizing current injection technique – has been applied to the model in a grid fault condition. The theoretical principle is to enforce a current component in phase with the stator flux in the RSC inner controller that helps the transient flux decay more quickly, along with the other electric transients (rotor voltage, current, power, electric torque and dc-link voltage). Besides, the influences of the controller tuning on the evolution of transient flux have been investigated to a more detailed level than in any other existing literature. In order to have the controller contribute positively to the flux decay, the proportional action should be far more significant than the integral action, which can only be achieved at a low frequency (10Hz). On the other hand, the controller bandwidths where low stability (or unstable response) presents itself during a grid fault in this study are found to be around 50 Hz, with 50 Hz being the worst case. An improved controller tuning method is proposed in this thesis. That is to set the d-loop at a lower frequency (10Hz). This produces a current component cancelling the natural flux. In contrast, if the q-loop is set at a higher frequency (150 Hz), this provides a high noise rejection property in the q-loop and therefore results in smaller transients in the total rotor current and electric torque. Compared with a conventional control scheme, this coordinated d-q controller tuning not only helps the system remain stable during a grid voltage drop, but also allows flexible setting of the q-loop bandwidth, and thus is convenient to insert a damping controller.

Secondly, dc-link voltage fluctuations are usually present in cases of a torque demand change or grid fault, where unequal instantaneous powers are induced at the two sides of the dc-link. From simulation, it is better to set the dc-link control speed to ten times the RSC electric torque control speed. This results in a fast response speed (thus smaller dc-link voltage ripple) without much increase in the grid current. The feed-forward compensation method proposed in recent research is also applied [98, 99]. Here the compensating term used is the perturbation of RSC injected power. This helps to improve the dc-link control performance by making the voltage transients decay faster, but the initial peak value remains the same. Both the methods discussed above have one thing in common: they reduce the dc-link fluctuations at the cost of increased grid current. Therefore, effective implementation of these methods needs to consider converter current limits.

Thirdly, simulations of the hardware protection techniques in PSCAD have been presented for severe voltage dips. In this case, the RSC will be by-passed and be set in an open circuit state. Meanwhile, both the outer and inner loops of the RSC controller are frozen by setting their inputs to zero. For a deeper voltage sag (0% remaining voltage for example), the dc-chopper should be used in combination with crowbar protection, in order to prevent the dc-link voltage continuing to rise before the crowbar releases.

Last but most importantly, a controller coordination method for the overall control system has been proposed in order to minimize shaft oscillations. Additionally, an overall bandwidth segmentation method has been proposed. The interaction between the mechanical and electrical subsystems has been represented by three-layers of cascaded control loops including the pitch control, damping control and the electric torque control. The dynamics are determined through root-locus analysis. If no damping control is used, then the electric torque control must be responsible for damping the shaft oscillations and thus should be set with a larger time constant. Otherwise, the time constant should be sufficiently small in order to avoid interference with the damping control. A strategy of implementing the damping control in coordination with crowbar protection during a grid fault has been proposed. This method only needs the damping control to be engaged when necessary (during and/or several seconds after the fault) and also it does not require wind speed measurement.

7.4. Power converter thermal modelling

A recent study shows that for a DFIG wind turbine, both the synchronous and the rated operating speed are considered as the most life-time consuming operating points for the power converter [6, 21, 101]. A complete converter electro-thermal model with loss prediction algorithm has been developed in PSCAD. This was used in combination with the DFIG wind turbine and full-switched converter model to obtain the instantaneous temperature of the power device under different operating conditions and control strategies. A faster loss prediction method is also proposed based on the switch-averaged model. All the parameters needed are from the manufacturer's datasheet. The simulated loss and transient thermal response from PSCAD have been verified by Semisel – software developed by Semikron for the power device loss and temperature prediction.

The switch-averaged model substantially increases the simulation speed without degradation of accuracy.

The device instantaneous junction temperatures are simulated for different operation conditions such as electric torque overload for minutes, grid voltage drop, and variable wind speeds that lasts 800s with 10% turbulence. The simulations show that in the case of a sudden electric torque demand increase, it can take several minutes for the power device to be heated up to the maximum temperature it can endure (150 °C). In the case of a grid fault, an improved d-q controller tuning can alleviate the device temperature of the GSC. A modified wind turbine control strategy is employed, which significantly reduces deep temperature cycling.

7.5. Suggestions for further work

This research considers that the wind turbine is connected to a strong grid, where using reactive power compensation to support the voltage is not required after a fault. In the next stage of research, a weak grid should be considered. In order to regulate the reactive power, an extra voltage control loop needs to be added to the RSC/GSC reactive power loop (d-loop). In this case, its bandwidth segmentation and coordinated use of the RSC and GSC to achieve reactive power regulation during and after a grid fault needs further investigation.

The RSC current controller tuning method proposed in this research can be a solution for a balanced three-phase voltage drop. Whether it would have the same effect in an unbalanced fault condition needs to be examined in the future work.

The popular PI controller is considered in this study. An important task for future work would be applying advanced control methods with multi-inputs and multi-outputs (MIMO) to the DFIG wind turbine model. Such a controller can be designed with disturbance accommodation techniques and observers for system state estimation. The performances of such advanced controllers can be evaluated and compared with the conventional controller.

The most important next step of this research is to establish a power device physics-of-failure model or lifetime model. It would be very useful to combine such a

lifetime model with the electro-thermal model developed in this research, to conduct quantitative analysis on the stress factors and the lifetime affected by different operating states and control methods. More powerful simulation software is required in order to simulate the entire operating time of the power device. More and more interest should be paid to new technologies such as the PPI and MPPF capacitors. As they are gradually replacing the conventional technologies for wind turbine applications, better understanding of their failure mechanisms is required so that an effective improvement strategy can be developed.

In the future work, it would be appreciated that a small-scaled test rig including both the DFIG machine and the converter can be built in the laboratory, in order to validate the theoretical research.

7.6. Associated publications

To date, one journal and three conference papers have been stemmed from this research, which are

- T. Lei, M. Barnes, A.C. Smith, "Thermal cycling evaluation for DFIG wind turbine power converter based on joint modelling", Presented at *Energy Conversion Congress and Exposition (ECCE)*, Denver, 2013.
- T. Lei, M. Barnes, and M. Ozakturk, "Doubly-fed induction generator wind turbine modelling for detailed electromagnetic system studies," published by *Renewable Power Generation, IET RPG*, vol. 7(2), 2013.
- T. Lei, M. Barnes, A.C. Smith, "DFIG wind turbine control system co-ordination to improve drive-train reliability", Presented at *European Wind Energy Association Conference (EWEA)*, Vienna, 2013
- T. Lei, M. Ozakturk, and M. Barnes, "Modelling and analysis of DFIG wind turbine system in PSCAD/EMTDC", Presented at *Power Electronics, Machines and Drives (PEMD)*, Bristol, 2012.

References

- [1] UK Renewable Energy Roadmap Update 2013. Available: https://www.gov.uk/government/uploads/system/uploads/attachment_data/file/255182/UK_Renewable_Energy_Roadmap_-_5_November_-_FINAL_DOCUMENT_FOR_PUBLICATION.pdf, Accessed on 26,03,2004.
- [2] M. Liserre, R. Cárdenas, M. Molinas, and J. Rodriguez, "Overview of Multi-MW Wind Turbines and Wind Parks," *IEEE Transactions on Industrial Electronics*, vol. 58(4), pp. 1081-1095, 2011.
- [3] A. Hansen and L. Hansen, "Wind turbine concept market penetration over 10 years (1995-2004)," *Wind Energy*, vol. 10(1), pp. 81-97, 2007.
- [4] H. Li and Z. Chen, "Overview of different wind generator systems and their comparisons," *Renewable Power Generation, IET*, vol. 2(2), pp. 123-138, 2008.
- [5] H. Polinder, D.-J. Bang, H. Li, and Z. Chen, "Concept report on generator topologies, mechanical and electromagnetic optimization," Delft University of Technology & Aalborg University, D1B2.b.1, 2007.
- [6] M. Bartram, J. von Bloh, and R. W. De Doncker, "Doubly-fed-machines in wind-turbine systems: is this application limiting the lifetime of IGBT-frequency-converters," in *35th Annual IEEE Power Electronics Specialists Conference (PESC)*, pp. 2583-2587, 04. 2004.
- [7] SUPERGEN Wind Website [Online]. Available: <http://www.supergen-wind.org.uk/index.html>. Accessed on 22nd, Mar. 2014
- [8] J. M. Carrasco, L. G. Franquelo, J. T. Bialasiewicz, E. Galvan, R. C. P. Guisado, M. A. M. Prats, J. I. Leon, and N. Moreno-Alfonso, "Power electronic systems for the grid integration of renewable energy sources: a survey," *IEEE Transactions on Industrial Electronics*, vol. 53(4), pp. 1002-1016, 2006.
- [9] L. H. Hansen, L. Helle, F. Blaabjerg, E. Ritchie, S. Munk, H. Bindner, P. Sørensen, and B. Bak-jensen, "Conceptual survey of generators and power electronics for wind turbines," National Renewable Energy Laboratory, Golden, Co (US) Risø-R-1205 (EN), 2011.
- [10] H. Arabian-Hoseynabadi, H. Oraee, and P. J. Tavner, "Failure modes and effects analysis (FMEA) for wind turbines," *International Journal of Electrical Power & Energy Systems*, vol. 32(7), pp. 817-824, 2010.
- [11] F. Spinato, P. J. Tavner, and G. J. W. v. Bussel, "Reliability-growth analysis of wind turbines from fleet field data," in *Proceedings of Advances in Risk and Reliability Technology Symposium (AR2TS)*, Loughborough, 2007.
- [12] S. Faulstich, B. Hahn, P. Lyding, and P. Tavner, "Reliability of offshore turbines—identifying risks by onshore experience," Fraunhofer institute for wind energy and energy system technology (IWES), Kassel, Germany 2009.
- [13] G. Hassan, Gamesa, and Alstom Ecotecnia, "Methodology and results of the reliawind reliability field study," presented at the Scientific Track, EWEC, Warsaw, 2010.
- [14] M. Wilkinson and G. Hendriks. Report on wind turbine reliability profiles. *Relia Wind-Work package Wp1 - Field data reliability analysis*. Available: http://www.reliawind.eu/files/file-inline/110502_Reliawind_Deliverable_D.1.3_ReliabilityProfilesResults.pdf, Accessed on 14/03/2011.
- [15] F. Blaabjerg, M. Liserre, and K. Ma, "Power electronics converters for wind turbine systems," in *Energy Conversion Congress and Exposition (ECCE)*, pp. 281-290, 2011.

- [16] F. Blaabjerg, M. Liserre, and M. Ke, "Power electronics converters for wind turbine systems," *IEEE Transactions on Industry Applications*, vol. 48(2), pp. 708-719, 2012.
- [17] S. Kouro, M. Malinowski, K. Gopakumar, J. Pou, L. G. Franquelo, B. Wu, J. Rodriguez, M. A. Pérez, and J. I. Leon, "Recent advances and industrial applications of multilevel converters," *IEEE Transactions on Industrial Electronics*, vol. 57(8), pp. 2553-2580, 2010.
- [18] G. Abad, M. A. Rodriguez, and J. Poza, "Three-level NPC converter-based predictive direct power control of the doubly fed induction machine at low constant switching frequency," *IEEE Transactions on Industrial Electronics*, vol. 55(12), pp. 4417-4429, 2008.
- [19] R. C. Portillo, M. M. Prats, J. I. León, J. A. Sánchez, J. M. Carrasco, E. Galván, and L. G. Franquelo, "Modeling strategy for back-to-back three-level converters applied to high-power wind turbines," *IEEE Transactions on Industrial Electronics*, vol. 53(5), pp. 1483-1491, 2006.
- [20] C. Zhe, J. M. Guerrero, and F. Blaabjerg, "A review of the state of the art of power electronics for wind turbines," *IEEE Transactions on Power Electronics*, vol. 24(8), pp. 1859-1875, 2009.
- [21] F. Fuchs and A. Mertens, "Steady state lifetime estimation of the power semiconductors in the rotor side converter of a 2 MW DFIG wind turbine via power cycling capability analysis," in *Proceedings of the European Conference on Power Electronics and Applications (EPE)*, pp. 1-8, 2011.
- [22] "Reliability prediction of electronic equipment," *Military Handbook 217 F*, Feb. 28 1995.
- [23] A. Wintrich, U. Nicolai, W. Tursky, and T. Reimann. (2011). *Application manual power semiconductors*. Available: http://www.semikron.com/skcompub/en/SEMIKRON_Application_Manual_Power_Semiconductors_.pdf
- [24] M. Rahimo and S. Klaka, "High voltage semiconductor technologies," presented at the 13th European Conference on Power Electronics and Applications (EPE), Barcelona, Sep. 2009.
- [25] A. Kopta, M. Rahimo, U. Schlapbach, and D. Schneider, "A 6.5kV IGBT module with very high safe operating area," in *Industry Applications Society*, Hong Kong: ABB Switzerland Ltd., pp. 12-17, 2005.
- [26] M. Winkelkemper, F. Wildner, and P. K. Steimer, "6 MVA five-level hybrid converter for wind power," in *Power Electronics Specialists Conference (PESC), IEEE*, pp. 4532-4538, 2008.
- [27] M. D. Manjrekar, P. K. Steimer, and T. A. Lipo, "Hybrid multilevel power conversion system: a competitive solution for high-power applications," *IEEE Transactions on Industry Applications*, vol. 36(3), pp. 834-841, 2000.
- [28] J. H. Fabian, S. Hartmann, and A. Hamidi, "Analysis of insulation failure modes in high power IGBT modules," in *Fourtieth IAS Annual Meeting on Industry Applications Conference*, pp. 799-805 Vol. 2, 2005.
- [29] J. M. Thebaud, E. Woïrgard, C. Zardini, and K. H. Sommer, "Extensive fatigue investigation of solder joints in IGBT high power modules," in *Proceedings of Electronic Components & Technology Conference* pp. 1436-1442, 2000.
- [30] H. Ye, M. Lin, and C. Basaran, "Failure modes and FEM analysis of power electronic packaging," *Finite Elements in Analysis and Design*, vol. 38(7), pp. 601-612, 2002.

- [31] C. Busca, R. Teodorescu, F. Blaabjerg, S. Munk-Nielsen, L. Helle, T. Abeyasekera, and P. Rodriguez, "An overview of the reliability prediction related aspects of high power IGBTs in wind power applications," *Microelectronics Reliability*, vol. 51(9–11), pp. 1903-1907, 2011.
- [32] S. Yang, D. Xiang, A. Bryant, P. Mawby, L. Ran, and P. Tavner, "Condition monitoring for device reliability in power electronic converters: a review," *IEEE Transactions on Power Electronics*, vol. 25(11), pp. 2734-2752, 2010.
- [33] O. S. Senturk, L. Helle, S. Munk-Nielsen, P. Rodriguez, and R. Teodorescu, "Converter structure-based power loss and static thermal modeling of the press-pack IGBT-based three-level ANPC and HB VSCs applied to Multi-MW wind turbines," in *Energy Conversion Congress and Exposition (ECCE)*, pp. 2778-2785, 2010.
- [34] F. Wakeman, G. Li, and A. Golland, "New family of 4.5kV press-pack IGBTs," in *Proceedings of PCIM*, Nuremberg, Germany, June, 2005.
- [35] R. Kaushik and S. Timothy, *Power Electronics, The Engineering Handbook*, 2nd ed. R. C. Dorf, Ed.: CRC Press, 2004.
- [36] D. Montanari, K. Saarinen, F. Scagliarini, D. Zeidler, M. Niskala, and C. Nender, "Film capacitors for automotive and industrial applications," presented at the CARTS Europe, Simpsonville, Oct. 2008.
- [37] M. Salcone and J. Bond, "Selecting film bus link capacitors for high performance inverter applications," in *IEEE International Electric Machines and Drives Conference (IEMDC)* pp. 1692-1699, 2009.
- [38] L. Kwang-Woon, K. Myungchul, Y. Jangho, L. Sang Bin, and Y. Ji-Yoon, "Condition monitoring of dc-link electrolytic capacitors in adjustable-speed drives," *IEEE Transactions on Industry Applications*, vol. 44(5), pp. 1606-1613, 2008.
- [39] M. J. Cushing, D. E. Mortin, T. J. Stadterman, and A. Malhotra, "Comparison of electronics-reliability assessment approaches," *IEEE Transactions on Reliability*, vol. 42(4), pp. 542-546, 1993.
- [40] G. Terzulli. Film technology to replace electrolytic technology in wind power applications. Available: <http://www.element14.com/community/servlet/JiveServlet/previewBody/27977-102-1-77163/FilminWindPower.pdf>, Accessed on 2011, 02.04.2014.
- [41] A. Lahyani, P. Venet, G. Grellet, and P. J. Viverge, "Failure prediction of electrolytic capacitors during operation of a switchmode power supply," *IEEE Transactions on Power Electronics*, vol. 13(6), pp. 1199-1207, 1998.
- [42] E. Wolfgang, "Examples for failures in power electronics systems," in *EPE Tutorial 'Reliability of power electronic systems'*, Nuremberg, Germany, Apr. 2007.
- [43] P. J. Tavner, S. Faulstich, B. Hahn, and G. J. W. van Bussel, "Reliability and availability of wind turbine electrical and electronic components," *EPE journal.*, vol. 20(4), 2011.
- [44] S. Barbati. Common reliability analysis methods and procedures. Available: http://www.reliawind.eu/files/publications/pdf_17.pdf, Accessed on 02.04.2004.
- [45] D. Kastha and B. K. Bose, "Investigation of fault modes of voltage-fed inverter system for induction motor drive," *IEEE Transactions on Industry Applications*, vol. 30(4), pp. 1028-1038, 1994.
- [46] R. Peugeot, S. Courtine, and J. P. Rognon, "Fault detection and isolation on a PWM inverter by knowledge-based model," *IEEE Transactions on Industry Applications*, vol. 34(6), pp. 1318-1326, 1998.

- [47] F. W. Fuchs, "Some diagnosis methods for voltage source inverters in variable speed drives with induction machines - a survey," in *The 29th Annual Conference of the IEEE Industrial Electronics Society (IECON)*, pp. 1378-1385, Nov. 2003.
- [48] X. Kaigui, J. Zefu, and L. Wenyuan, "Effect of wind speed on wind turbine power converter reliability," *IEEE Transactions on Industrial Electronics*, vol. 27(1), pp. 96-104, 2012.
- [49] B. Li, M. Li, K. Chen, and C. Smidts, "Integrating software into PRA: A software-related failure mode taxonomy," *Society for Risk Analysis*, vol. 26(4), pp. 997-1012, 2006.
- [50] C. Kulkarni, G. Biswas, C. Jose, and G. Kai, "Prognostics techniques for capacitor degradation and health monitoring," in *Proceedings of The Maintenance & Reliability Conference, MARCON*, Knoxville, TN, 03.2011.
- [51] M. L. Gasperi, "Life prediction modeling of bus capacitors in AC variable frequency drives," *IEEE Transactions on Industry Applications*, pp. 1430 - 1435, Dec. 2005.
- [52] C. Yaow-Ming, C. Ming-Wei, and W. Hsu-Chin, "Electrolytic capacitor failure prediction of LC filter for switching-mode power converters," in *Fortieth IAS Annual Meeting Industry Applications Conference*, pp. 1464-1469 Vol. 2, 2005.
- [53] J. R. Laghari and W. J. Sarjeant, "Energy storage pulsed power capacitor technology," *IEEE Transactions on Power Electronics*, vol. 7(1), pp. 251 - 257, 25-28 Jun 1990 1992.
- [54] B. Lu and S. K. Sharma, "A Literature review of IGBT fault diagnostic and protection methods for power inverters," *IEEE Transactions on Industry Applications*, vol. 56(6), pp. 1770-1777, 2009.
- [55] D. A. Murdock, J. E. R. Torres, J. J. Connors, and R. D. Lorenz, "Active thermal control of power electronic modules," *IEEE Transactions on Industry Applications*, vol. 42(2), pp. 552-558, 2006.
- [56] M. Ciappa and W. Fichtner, "Lifetime prediction of IGBT modules for traction applications," in *Proceedings of 38th Annual IEEE International Reliability Physics Symposium*, pp. 210-216, 2000.
- [57] V. Blasko, R. Lukaszewski, and R. Sladky, "On line thermal model and thermal management strategy of a three phase voltage source inverter," in *34th IAS Annual Meeting on IEEE Industry Applications Conference*, pp. 1423-1431 vol.2, 1999.
- [58] E. A. Amerasekera and F. N. Najm, *Failure mechanisms in semiconductor devices*, 2nd ed., New York: Wiley, June 1997.
- [59] C. Duvvury, J. Rodriguez, C. Jones, and M. Smayling, "Device integration for ESD robustness of high voltage power MOSFETs," in *Technical Digest of International Electron Devices Meeting (IEDM)*, pp. 407-410, 1994.
- [60] K. Kameda, "Motor driving device having MOSFET and motor having MOSFET," United States Patent US7352144 B2, Apr.1 2006, Apr. 2006. Available: <https://docs.google.com/a/google.com/viewer?url=www.google.com/patents/US7352144.pdf>
- [61] J. Lutz, "IGBT-Modules: Design for reliability," in *13th European Conference on Power Electronics and Applications (EPE)* pp. 1-3, 2009.
- [62] M. Ciappa, "Selected failure mechanisms of modern power modules," *Microelectronics Reliability*, vol. 42(4-5), pp. 653-667, 2002.
- [63] G. M. Buiatti, J. A. Martin-Ramos, A. M. R. Amaral, P. Dworakowski, and A. Cardoso, "Condition monitoring of metallized polypropylene film capacitors in railway power trains," *IEEE Transactions on Instrumentation and Measurement*, vol. 58(10), pp. 3796-3805, 2009.

- [64] W. J. Sarjeant, F. W. MacDougall, D. W. Larson, and I. Kohlberg, "Energy storage capacitors: aging, and diagnostic approaches for life validation," *IEEE Transactions on Magnetics*, vol. 33(1), pp. 501-506, 1997.
- [65] M. Musallam, C. M. Johnson, Y. Chunyan, C. Bailey, and M. Mermet-Guyennet, "Real-time life consumption power modules prognosis using on-line rainflow algorithm in metro applications," in *Energy Conversion Congress and Exposition (ECCE)*, pp. 970-977, 2010.
- [66] M. Held, P. Jacob, G. Nicoletti, P. Scacco, and M. H. Poech, "Fast power cycling test of IGBT modules in traction application," in *International Conference on Power Electronics and Drive Systems*, pp. 425-430 vol.1, 1997.
- [67] C. Busca, "Modeling lifetime of high power IGBTs in wind power applications - An overview," in *IEEE International Symposium on Industrial Electronics (ISIE)*, pp. 1408-1413, 2011.
- [68] P. Hansen and P. McCluskey, "Failure models in power device interconnects," in *European Conference on Power Electronics and Applications*, pp. 1-9, 2007.
- [69] M. Hao and W. Linguo, "Fault diagnosis and failure prediction of aluminum electrolytic capacitors in power electronic converters," in *31st Annual Conference of IEEE Industrial Electronics Society (IECON)*, pp. 1-6, 2005.
- [70] J. A. Lauber, "Aluminum electrolytic capacitors- Reliability, expected life and shelf capability," Sprague Technical Paper TP83-9, 1985.10 1985.
- [71] M. Musallam and C. M. Johnson, "Impact of different control schemes on the life consumption of power electronic modules for variable speed wind turbines," in *Proceedings of the European Conference on Power Electronics and Applications*, pp. 1-9, 2011.
- [72] V. Akhmatov, "Analysis of dynamic behaviour of electric power systems with large amount of wind power," PhD Thesis, Electric Power Engineering, Ørsted-DTU, Technical University of Denmark, 2003.
- [73] G. Abad, J. s. Lo'pez, M. A. Rodr'iguez, L. Marroyo, and G. Iwanski, *Doubly fed induction machine: Modeling and control for wind energy generation*: Wiley, 2011.
- [74] A. D. Hansen, P. Sørensen, F. Iov, and F. Blaabjerg, "Control of variable speed wind turbines with doubly-fed induction generators," *Wind Engineering*, vol. 28(4), pp. 411-432, 2004.
- [75] S. Heier, *Grid integration of wind energy conversion systems*, Chicester, UK: John Wiley & Sons Ltd, 1998.
- [76] J. F. Walker and N.Jenkins, *Wind energy technology*, Chicester, UK: John Wiley & Sons Ltd., 2002.
- [77] P. M. Anderson and A. Bose, "Stability simulation of wind turbine systems," *IEEE Transactions on Power Apparatus and Systems*, vol. PAS-102(12), pp. 3791-3795, 1983.
- [78] J. G. Slootweg, "Wind power modelling and impact on power system dynamics," PhD Thesis, Faculty of Electrical engineering, mathematics and computer science, Delft University of Technology, Nov. 2003.
- [79] J. G. Slootweg, S. W. H. De Haan, H. Polinder, and W. L. Kling, "General model for representing variable speed wind turbines in power system dynamics simulations," *IEEE Transactions on Power Systems*, vol. 18(1), pp. 144-151, 2003.
- [80] S. M. Muyeen, M. H. Ali, R. Takahashi, T. Murata, J. Tamura, Y. Tomaki, A. Sakahara, and E. Sasano, "Comparative study on transient stability analysis of wind turbine generator system using different drive train models," *IET Renewable Power Generation*, vol. 1(2), pp. 131-141, 2007.

- [81] G. Pannell, "Grid fault ride through for wind turbine doubly-fed induction generators," PhD Thesis, Newcastle University, 2008.
- [82] B. Hopfensperger, D. Atkinson, and R. Lakin, "Stator-flux-oriented control of a doubly-fed induction machine with and without position encoder," in *IEE Proceedings-Electric Power Applications*, pp. 241-250, Jul, 2000.
- [83] A. T. Bryant, P. A. Mawby, P. R. Palmer, E. Santi, and J. L. Hudgins, "Exploration of Power Device Reliability Using Compact Device Models and Fast Electrothermal Simulation," *IEEE Transactions on Industry Applications*, vol. 44(3), pp. 894-903, 2008.
- [84] RePower 5M wind turbine technical brochure [Online]. Available: http://www.repower.de/fileadmin/download/produkte/RE_PP_5M_uk.pdf. Accessed on Dec. 18, 2013
- [85] V. Akhmatov, "Variable-speed wind turbines with doubly-fed induction Generators, Part I: Modelling in Dynamic Simulation Tools," *Wind Engineering*, vol. 26(2), pp. 85-108, 2002.
- [86] M. H. Hansen, A. Hansen, T. J. Larsen, S. Øy, P. Sørensen, and P. Fuglsang, "Control design for a pitch-regulated, variable speed wind turbine," RISO National Laboratory, Roskilde Denmark Risø-R-1500(EN), 2005.
- [87] E. A. Bossanyi, *The Design of closed loop controllers for wind turbines* vol. 3: John Wiley & Sons, Ltd., 2000.
- [88] M. M. Hand, "Variable-speed wind turbine controller systematic design methodology: a comparison of non-linear and linear model-based designs," National Renewable Energy Laboratory, Golden, Co (US) NREL/TP-500-25540, Jul. 1999.
- [89] A. D. Wright, "Modern control design for flexible wind turbines," National Renewable Energy Laboratory, Golden, Colorado NREL/TP-500-35816, July 2004.
- [90] B. C. Kuo and D. C. Hanselman, *Matlab tools for control system analysis and design*, Englewood Cliffs, New Jersey: Prentice-Hall, Inc., 1994.
- [91] R. D. Lorenz and P. B. Schmidt, "Synchronized motion control for process automation," presented at the Industry Applications Society Annual Meeting, 1989.
- [92] C. L. Phillips and R. D. Harbor, *Feedback control systems*, 4th ed., Prentice Hall, Upper Saddle River, New Jersey, Tom Robbins, 2000.
- [93] D. J. Leith and W. E. Leithead, "Application of nonlinear control to a HAWT," in *Proceedings of the Third IEEE Conference on Control Applications*, pp. 245-250 vol.1, 1994.
- [94] J. Lopez, E. Gubia, E. Olea, J. Ruiz, and L. Marroyo, "Ride through of wind turbines with doubly fed induction generator under symmetrical voltage dips," *IEEE Transactions on Industrial Electronics*, vol. 56(10), pp. 4246-4254, 2009.
- [95] D. Xiang, L. Ran, P. J. Tavner, and S. Yang, "Control of a doubly fed induction generator in a wind turbine during grid fault ride-through," *IEEE Transactions on Energy Conversion*, vol. 21(3), pp. 652-662, 2006.
- [96] J. Lopez, P. Sanchis, E. Gubia, A. Ursua, L. Marroyo, and X. Roboam, "Control of doubly fed induction generator under symmetrical voltage dips," in *IEEE International Symposium on Industrial Electronics (ISIE)*, pp. 2456-2462, 2008.
- [97] A. D. Hansen and G. Michalke, "Fault ride-through capability of DFIG wind turbines," *Renewable Energy*, vol. 32(9), pp. 1594-1610, 2007.

- [98] L. Yang, Z. Xu, J. Ostergaard, Z. Y. Dong, and K. P. Wong, "Advanced control strategy of DFIG wind turbines for power system fault ride through," *IEEE Transactions on Power Systems*, vol. 27(2), pp. 713-722, 2012.
- [99] J. Yao, H. Li, Y. Liao, and Z. Chen, "An improved control strategy of limiting the dc-link voltage fluctuation for a doubly fed induction wind generator," *IEEE Transactions on Power Electronics*, vol. 23(3), pp. 1205-1213, 2008.
- [100] F. K. A. Lima, A. Luna, P. Rodriguez, E. H. Watanabe, and F. Blaabjerg, "Rotor voltage dynamics in the doubly fed induction generator during grid faults," *IEEE Transactions on Power Electronics*, vol. 25(1), pp. 118-130, 2010.
- [101] M. Bruns, B. Rabelo, and W. Hofmann, "Investigation of doubly-fed induction generator drives behaviour at synchronous operating point in wind turbines," in *13th European Conference on Power Electronics and Applications (EPE)*, pp. 1-10, 2009.
- [102] W. Lixiang, R. J. Kerkman, R. A. Lukaszewski, L. Haihui, and Y. Zhenhuan, "Analysis of IGBT power cycling capabilities used in doubly fed induction generator wind power system," *IEEE Transactions on Industry Applications*, vol. 47(4), pp. 1794-1801, 2011.
- [103] A. Isidori, F. M. Rossi, and F. Blaabjerg, "Thermal loading and reliability of 10 MW multilevel wind power converter at different wind roughness classes," *IEEE Transactions On Industry Applications*, vol. 50(1), pp. 484 - 494, Jan.-Feb. 2014.
- [104] C. Luo, H. Banakar, B. Shen, and O. Boon-Teck, "Strategies to smooth wind power fluctuations of wind turbine generator," *IEEE Transactions on Energy Conversion*, vol. 22(2), pp. 341-349, 2007.
- [105] K. Ma, M. Liserre, and F. Blaabjerg, "Reactive power influence on the thermal cycling of multi-MW wind power inverter," *IEEE Transactions on Industry Applications*, vol. 49(2), pp. 922-930, 2013.
- [106] T. Poller, T. Basler, M. Hernes, S. D. Arco, and J. Lutz, "Mechanical analysis of press-pack IGBTs," *Microelectronics Reliability*, vol. 52(9-10), pp. 2397-2402, 2012.
- [107] A. Pirondi, G. Nicoletto, P. Cova, M. Pasqualetti, M. Portesine, and P. E. Zani, "Thermo-mechanical simulation of a multichip press-packed IGBT," *Solid-State Electronics*, vol. 42(12), pp. 2303-2307, 1998.
- [108] A. Pirondi, G. Nicoletto, P. Cova, M. Pasqualetti, and M. Portesine, "Thermo-mechanical finite element analysis in press-packed IGBT design," *Microelectronics Reliability*, vol. 40(7), pp. 1163-1172, 2000.
- [109] Y. Chan-Su, P. Malberti, M. Ciappa, and W. Fichtner, "Thermal component model for electrothermal analysis of IGBT module systems," *IEEE Transactions on Electron Devices*, vol. 24(3), pp. 401-406, 2001.
- [110] U. Drofenik and J. W. Kolar, "Thermal analysis of a multi-chip Si/SiC-power module for realization of a bridge leg of a 10 kW Vienna rectifier," in *The 25th International Telecommunications Energy Conference (INTELEC)*, pp. 826-833, 2003.
- [111] N. Pluschke, "State-of-the-art Power Module Design for Renewable Energy Application," *Journal of International Council on Electrical Engineering*, vol. 2(1), pp. 79-83, 2012.
- [112] A. Petersson, "Analysis, modelling and control of doubly-fed induction generators for wind turbines," PhD Thesis, Chalmers University of Technology, Goteborg, Sweden, 2005.
- [113] *Wind turbines*. I. Al-Bahadly, Ed., Janeza Trdine 9, 51000 Rijeka, Croatia: InTech, 2011.

- [114] S. Chondrogiannis, "Technical aspects of offshore wind farms employing doubly-fed induction generators," PhD Thesis, University of Manchester, 2007.
- [115] SEMIKRON, SEMISTACK Renewable Energy [Online]. Available: http://www.semikron.com/skcompub/en/semistack_renewable_energy-2770.htm. Accessed on 11,08,2013
- [116] SEMIKRON, SKiiP 2013 GB172-4DW V3 datasheet [Online]. Available: http://www.semikron.com/products/data/cur/assets/SKiiP_2013_GB172_4DW_V3_20450248.pdf. Accessed on 11,08,2013
- [117] J. W. Kolar, F. C. Zach, and F. Casanellas, "Losses in PWM inverters using IGBTs," *IEE Proceedings - Electric Power Applications*, vol. 142(4), pp. 285-288, 1995.
- [118] M. H. Bierhoff and F. W. Fuchs, "Semiconductor losses in voltage source and current source IGBT converters based on analytical derivation," in *35th Annual Power Electronics Specialists Conference (PESC)* pp. 2836-2842 Vol.4, 2004.
- [119] O. Al-Naseem, R. W. Erickson, and P. Carlin, "Prediction of switching loss variations by averaged switch modeling," presented at the 15th Annual IEEE Applied Power Electronics Conference and Exposition (APEC), New Orleans, LA, 2000.
- [120] L. K. Mestha and P. D. Evans, "Analysis of on-state losses in PWM inverters," *IEE Proceedings - Electric Power Applications*, vol. 136(4), pp. 189-195, 1989.
- [121] U. Drofenik and J. W. Kolar, "A general scheme for calculating switching and conduction-losses of power semiconductors in numerical circuit simulations of power electronic systems," in *5th Int. Power Electronics Conf. (IPEC)*, Niigata, Japan, pp. 1604-1610, April 2005.
- [122] A. R. Hefner, "A dynamic electro-thermal model for the IGBT," *IEEE Transactions on Industry Applications*, vol. 30(2), pp. 394-405, 1994.
- [123] J. Holtz, "Pulsewidth modulation-a survey," *IEEE Transactions on Industrial Electronics*, vol. 39(5), pp. 410-420, 1992.
- [124] F. Blaabjerg, J. K. Pedersen, S. Sigurjonsson, and A. Elkjaer, "An extended model of power losses in hard-switched IGBT-inverters," in *31st IAS Annual Meeting on Industry Applications*, , pp. 1454-1463 vol.3, 1996.
- [125] S. Munk-Nielsen, L. N. Tutelea, and U. Jaeger, "Simulation with ideal switch models combined with measured loss data provides a good estimate of power loss," in *IEEE Industry Applications Conference*, pp. 2915-2922 vol.5, 2000.
- [126] P. Alemi and L. Dong-Choon, "Power loss comparison in two- and three-level PWM converters," in *8th International Conference on Power Electronics and ECCE Asia (ICPE & ECCE)* pp. 1452-1457, 2011.
- [127] A. D. Rajapakse, A. M. Gole, and P. L. Wilson, "Electromagnetic transients simulation models for accurate representation of switching losses and thermal performance in power electronic systems," *IEEE Transactions on Power Delivery*, vol. 20(1), pp. 319-327, 2005.
- [128] P. E. Bagnoli, C. E. Casarosa, M. Ciampi, and E. Dallago, "Thermal resistance analysis by induced transient (TRAIT) method for power electronic devices thermal characterization. I. Fundamentals and theory," *IEEE Transactions on Power Electronics*, vol. 13(6), pp. 1208-1219, 1998.
- [129] Y. C. Gerstenmaier, W. Kiffe, and G. Wachutka, "Combination of thermal subsystems modeled by rapid circuit transformation," presented at the 13th International Workshop on THERMINIC, 2007.
- [130] H. A. Mantooth and A. R. Hefner, "Electrothermal simulation of an IGBT PWM inverter," *IEEE Transactions on Power Electronics*, vol. 12(3), pp. 474-484, 1997.

- [131] W. E. Leithead and B. Connor, "Control of variable speed wind turbines: Design task," *International Journal of Control*, vol. 73(13), pp. 1189-1212, 2000.

Appendix A. DFIG Wind Turbine Model Parameters

A.1. General parameters

Mechanical parameters of the wind turbine:

Parameter	Value	Unit
Nominal turbine power P_T	5	MW
Turbine rotor radius R	63	m
Air density ρ	1.1225	kg/m ³
Nominal wind speed V_W	12	m/s
Cut-in wind speed	4	m/s
Variable speed range ($\Omega_{T,min} - \Omega_{T,nom}$)	7.0 – 12.1 (+15%)	rpm
Optimum tip-speed ratio λ_{opt}	6.3	-
Maximum power coefficient $C_{p,max}$	0.44	-
Optimum torque coefficient k_{opt}	0.55	pu
Turbine rotor inertia H_T	3	s
Generator rotor inertia H_G	0.5	s
Spring constant K_S	0.7	pu/el·rad
Turbine rotor self-damping D_T	0.020	pu
Generator rotor self-damping D_G	0.031	pu
Mutual damping between two mass D_S	3	pu
Optimum torque coefficient k_{opt}	0.550	pu

DFIG machine parameters

Parameter	Value	Unit
Machine rating P_s	4.5	MW
Synchronous speed ω_s	314	rad/s
Pole pair number pp	3	-
Rotor/stator turn ratio n	2.5	-
Stator winding leakage inductance $L_{\sigma s}$	0.0924	pu
Rotor winding leakage inductance $L_{\sigma r}$	0.0996	pu
Magnetizing inductance L_m	3.953	pu
Stator resistance R_s	0.00488	pu
Rotor resistance R_r	0.00549	Pu

Transformer parameters

Parameter	Value	Unit
Stator-connected winding voltage (L-L, RMS) V_1	1	kV
GSC-connected winding voltage (L-L, RMS) V_2	0.4	kV
Grid-connected winding voltage (L-L, RMS) V_3	33	kV
Magnetizing inductance L_m	0.08	pu
Transformer inductance: stator-converter $L_{tr,12}$	0.001	pu
Transformer inductance: stator-external grid $L_{tr,13}$	0.08	pu
Transformer inductance: grid – converter $L_{tr,23}$	0.08	pu
No-load losses $P_{loss,no}$	0.01	pu
Copper losses P_{cu}	0.01	pu

DC-link parameters

Parameter	Value	Unit	
dc-bus capacitor C_{dc_link}	3.5	pu	
Nominal dc-link voltage V_{dc}	1.2	kV	
Coupling impedance of the GSC (Base voltage = 0.4kV)	L_{gsc0} R_{gsc}	1 0.017	pu pu
Coupling impedance of the RSC (Base voltage = 1kV)	L_{rsc} R_{rsc}	0.2 0	pu pu

Other machine parameters

Stator self-inductance:

$$L_s = L_{\sigma s} + L_m + L_{12} + L_{13} = 0.0924 pu + 3.95 pu + 0.001 + 0.08 = 4.13 pu$$

Rotor self-inductance:

$$L_r = L_{\sigma r} + L_m + L_{rsc} = 0.0996 pu + 3.95 pu + 0.2 pu = 4.25 pu$$

Total coupling inductance to grid side (per 0.4 kV base):

$$L_{gsc} = L_{gsc0} + L_{23} + L_{12} = 1 pu + 0.08 pu + 0.001 = 1.081 pu$$

Total self damping of the rotational shaft $D_r = D_T + D_G = (0.02 + 0.03) pu = 0.05 pu$

Total shaft inertia constant: $H_r = H_T + H_G = 3.5 sec$

A.2. Transformation from per unit values

Base Power: $S_{base} = 4.5MW$

Base angular frequency: $\omega_{base} = \omega_s = 2\pi f = 314rad / s$

Machine-side circuit parameters (per 1kV base):

Base voltage: $V_{base,1} = V_{s_LL_rms} = 1kV$

Base current $I_{base,1} = I_{s_rms} = \frac{S_{base}}{\sqrt{3}V_{base,1}} = \frac{4.5MW}{\sqrt{3} \times 1kV} = 2.60kA$

($V_{s_LL_rms}$: Line-to-Line rms stator voltage, I_{s_rms} :Rated stator rms current,)

Base impedance $Z_{base,1} = \frac{V_{base,1}^2}{S_{base}} = \frac{(1kV)^2}{4.5MVA} = 0.22\Omega$

According to $Z = \frac{1}{2\pi fC} = 2\pi fL$, the base value of the capacitance and inductance are

$$C_{base,1} = \frac{1}{2\pi fX_{C-base,1}} = 0.014F \qquad L_{base,1} = \frac{X_{L-base,1}}{2\pi f} = 7.07 \times 10^{-4} H$$

Therefore, the real magnitudes of the parameters can be found

$$C_{dc_link} = 3.5 pu \times C_{base,1} = 0.05F$$

$$L_m = 3.95 pu \times L_{base,1} = 2.80mH \qquad L_{rsc} = 0.2 pu \times L_{base,1} = 1.42 \times 10^{-4} H$$

$$R_s = 0.00488 pu \times X_{base,1} = 1.08m\Omega \quad R_r = 0.00549 pu \times X_{base,1} = 1.22m\Omega$$

$$L_s = 4.13 pu \times L_{base,1} = 2.92mH \qquad L_r = 4.25 pu \times L_{base,1} = 3.01mH$$

$$\sigma L_r = \left(1 - \frac{L_m^2}{L_s L_r}\right) L_r = \left(1 - \frac{2.80^2}{2.92 \times 3.01}\right) \times 3.01 = 3.27 \times 10^{-4} H$$

Grid-side circuit parameters (per 0.4kV base):

Base voltage: $V_{base,2} = V_{g_LL_rms} = 0.4kV$

Base current $I_{base,2} = \frac{S_{base}}{\sqrt{3}V_{base,2}} = \frac{4.5MW}{\sqrt{3} \times 0.4kV} = 6.50kA$

($V_{g_LL_rms}$: Line-to-Line rms Grid-side terminal voltage)

$$\text{Base impedance: } Z_{base,2} = \frac{V_{base,2}^2}{S_{base}} = \frac{(0.4kV)^2}{4.5MVA} = 0.0356\Omega$$

$$\text{Base inductance: } L_{base,2} = \frac{X_{L-base,2}}{2\pi f} = 1.132 \times 10^{-4} H$$

Real magnitudes of the parameters

$$L_{gsc0} = 1pu \times L_{base,2} = 1.13 \times 10^{-4} H \quad L_{gsc} = 1.08pu \times L_{base,2} = 1.22 \times 10^{-4} H$$

$$R_{gsc} = 0.017pu \times X_{base,2} = 6.04 \times 10^{-4} \Omega$$

Mechanical parameters

Base values seen at the generator rotor (high speed shaft):

$$\Omega'_{m,base} = \frac{\omega_s}{pp} = \frac{314rad/s}{3} = 105rad/s$$

$$T'_{m,base} = \frac{P_{base}}{\Omega'_{m,base}} = \frac{4.5MW}{104.72rad/s} = 4.30 \times 10^4 N \cdot m$$

$$J'_{base} = \frac{P}{\frac{1}{2}\Omega_m^2} = 8.21 \times 10^2 kg \cdot m^2$$

$$K'_{s,base} = D'_{base} = \frac{T'_{m,base}}{\Omega'_{m,base}} = \frac{42971.8N \cdot m}{104.7rad/s} = 4.10 \times 10^2 N \cdot m / (rad/s)$$

$$k'_{opt,base} = \frac{T'_{m,base}}{\Omega_{m,base}^2} = \frac{P_{base}}{\Omega_{m,base}^3} = \frac{4.5MW}{(\pi \times 50 / (3rad/s))^3} = 3.92N \cdot m \cdot s^2 / rad^2$$

Base values seen at the turbine rotor (low speed shaft)

$$\Omega_{m,base} = \Omega'_{m,base} / G = 1.08rad/s$$

$$T_{m,base} = T'_{m,base} \cdot G = 4.17 \times 10^6 N \cdot m$$

$$J_{base} = G^2 \cdot J'_{base} = 7.72 \times 10^6 kg \cdot m^2$$

$$D_{base} = G^2 \cdot D'_{base} = 3.86 \times 10^6 N \cdot m / (rad/s)$$

$$K_{s,base} = G^2 \cdot K'_{s,base} = 3.86 \times 10^6 N \cdot m / (rad/s)$$

$$k_{opt,base} = G^3 \cdot k'_{opt,base} = 3.58 \times 10^6 N \cdot m \cdot s^2 / rad^2$$

Real parameters referred to the turbine rotor (low speed shaft)

$$J_T = H_T \cdot J_{base} = 2.32 \times 10^7 \text{ kg} \cdot \text{m}^2$$

$$J_G = H_G \cdot J_{base} = 3.86 \times 10^6 \text{ kg} \cdot \text{m}^2$$

$$J_r = J_T + J_G = 2.70 \times 10^7 \text{ kg} \cdot \text{m}^2$$

$$K_s = K_{s,base} \cdot K_{s,pu} = 8.49 \times 10^8 \text{ N} \cdot \text{m} / (\text{rad} / \text{s})$$

$$D_T = D_{base} \cdot D_{T,pu} = 7.72 \times 10^4 \text{ N} \cdot \text{m} / (\text{rad} / \text{s})$$

$$D_G = D_{base} \cdot D_{G,pu} = 1.20 \times 10^5 \text{ N} \cdot \text{m} / (\text{rad} / \text{s})$$

$$D_r = D_T + D_G = 1.97 \times 10^5 \text{ N} \cdot \text{m} / (\text{rad} / \text{s})$$

$$D_s = D_{base} \cdot D_{s,pu} = 1.16 \times 10^7 \text{ N} \cdot \text{m} / (\text{rad} / \text{s})$$

$$k_{opt} = k_{opt,base} \cdot k_{opt,pu} = 1.97 \times 10^6 \text{ N} \cdot \text{m} \cdot \text{s}^2 / \text{rad}^2$$

Appendix B. DFIG Controller Tuning and Model Verification

B.1. RSC current loop

The closed-loop transfer function of RSC current control is given by

$$\frac{i_{r-dq}}{i_{r-dq}^*} = \frac{\frac{k_p}{\sigma L_r} s + \frac{k_i}{\sigma L_r}}{s^2 + \frac{R_r + k_p}{\sigma L_r} s + \frac{k_i}{\sigma L_r}} \approx \frac{\omega_n^2}{s^2 + 2\xi \cdot \omega_n s + \omega_n^2}$$

Hence $k_p = 2\xi \cdot \omega_n \cdot \sigma L_r - R_r$, $k_i = \omega_n^2 \cdot \sigma L_r$. Step responses are obtained for different damping values at the same frequency ($f_n=10\text{Hz}$) in figure B.1, where the damping value is increased from 0.7 to 2.5 in 0.2 steps. The corresponding controller gains are listed in table B.1. The rated rotor current and voltage are respectively 1.1kA and 0.36kV. The responses shown in the figure are obtained for illustration of the controller parameters' impacts on the overshoot and settling time.

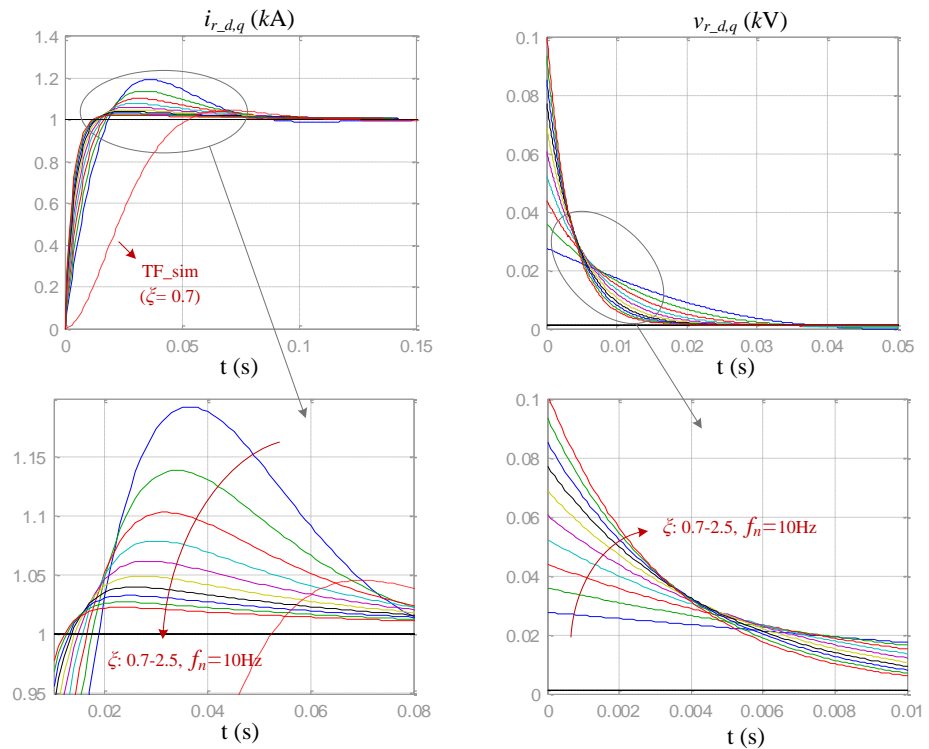


Figure B.1 Step responses of i_r and v_r to 1kA step in i_r^* with different damping values

	$\omega_n = 10\text{Hz}$									
ξ	0.7	0.9	1.1	1.3	1.5	1.7	1.9	2.1	2.3	2.5
k_p	0.0276	0.0358	0.0440	0.0522	0.0605	0.0687	0.0769	0.0851	0.0934	0.1016
k_i	1.292									
	$\xi=1.2$									
ω_n	10 Hz	50Hz			100Hz		200Hz		500Hz	
k_p	0.0481	0.246			0.492		0.986		2.47	
k_i	1.292	32.30			129.2		516.9		3230	

Table B.1. RSC current controller parameters with varying damping and frequency

The parameters highlighted in red are used for model verification, i.e. where $\omega_n= 10\text{Hz}$ and $\xi=1.2$. This delivers the transfer function

$$TF_{cl} = \frac{i_{r_dq}}{i_{r_dq}^*} = \frac{147.1s + 3948}{s^2 + 150.8s + 3948}$$

The corresponding controller parameters (marked in red in table B.1) are set in PSCAD, and the response (denoted as 'Model') is compared with closed-loop transfer function ('TF'). Here the current references are generated by electric torque and reactive power using the feed-forward control.

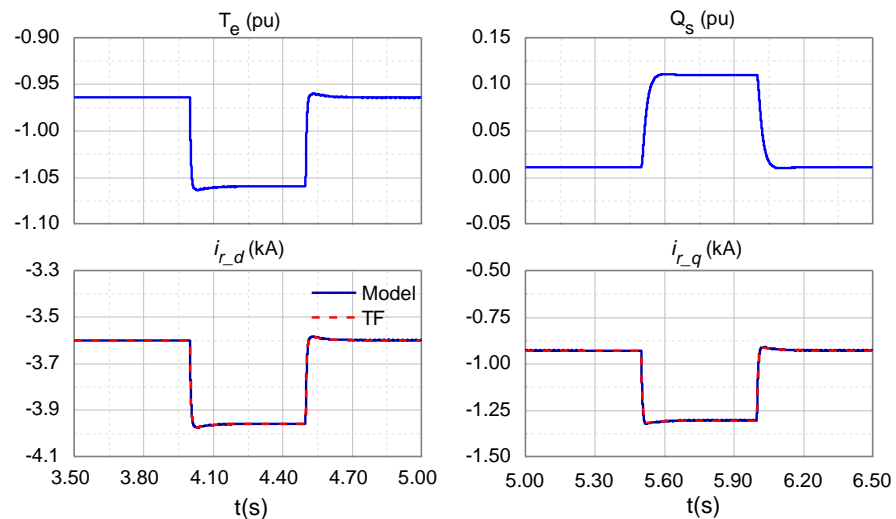


Figure B.2 Verification of the rotor current control system with 0.1 pu step in electric torque (left) and reactive power (right)

The time constant of the inner control loop is obtained as:

$$\tau_i = \frac{1}{\xi \cdot \omega_n} = 0.0133s.$$

B.2. RSC power loop

The closed loop transfer functions are given by

$$\begin{aligned} \frac{Q_s}{Q_s^*} &= \frac{p_1 \cdot s + 1}{\left(\frac{1}{m_1 k_i} + p_1\right)s + 1} \approx \frac{1}{\tau \cdot s + 1} \\ \frac{T_e}{T_e^*} &= \frac{p_2 \cdot s + 1}{\left(\frac{1}{m_2 k_i} + p_2\right)s + 1} \approx \frac{1}{\tau \cdot s + 1} \end{aligned} \quad (6.28)$$

with $m_1 = \frac{3\sqrt{2}}{2} \times \frac{L_m}{L_s} \times V_s = 1.173$, $m_2 = \frac{3}{2} \times \frac{L_m}{L_s} \times \psi_s = 3.735$, $p = \frac{k_p}{k_i}$. Let $p = 0.01$, the step responses with different time constants are obtained as depicted in Figure B.3.

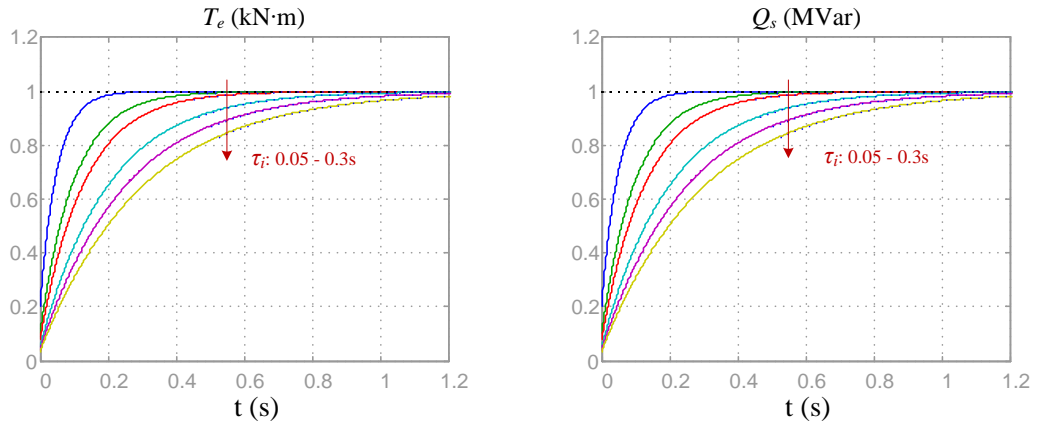


Figure B.3 Power loop responses to a 1 kNm step in electric torque (left) and 1 MVar step in reactive power (right) with different damping values

The RSC outer loop's time constant $\tau_i = \frac{1}{mk_i} + p$ should be much larger than the inner loop. Let $\tau_i = 0.1s$, then the full-closed loop transfer functions can be derived as:

$$TF_{FCL} = \frac{Q_s^*}{Q_s} = \frac{T_e^*}{T_e} = \frac{0.01s + 1}{0.1s + 1}$$

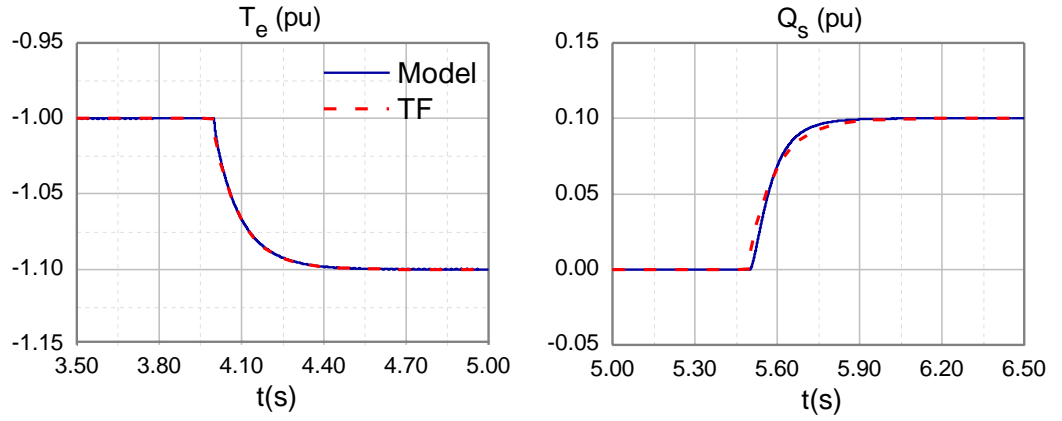


Figure B.4 Verification of the RSC power control loops with a 1 pu step in electric torque (left) and 0.1 pu step in reactive power (right)

	T _e controller $p = 0.01$					
τ_i	0.05s	0.1s	0.15s	0.2s	0.25s	0.3s
k_p	0.213	0.0947	0.0609	0.0448	0.0355	0.0294
k_i	21.3	9.47	6.09	4.48	3.55	2.94
	Q _s controller $p = 0.01$					
τ_i	0.05s	0.1s	0.13s	0.2s	0.25s	0.3s
k_p	0.0669	0.0297	0.0223	0.0141	0.0112	0.00923
k_i	6.69	2.97	2.23	1.41	1.12	0.923

Table B.2. RSC outer-loop controller parameters with varying time constants

B.3. GSC current loop

The closed-loop transfer function is given by

$$\frac{i_g}{i_g^*} = \frac{\frac{k_p}{L_{gsc}}s + \frac{k_i}{L_{gsc}}}{s^2 + \frac{(R_{gsc} + k_p)}{L_{gsc}}s + \frac{k_i}{L_{gsc}}} \approx \frac{\omega_n^2}{s^2 + 2\xi\omega_n s + \omega_n^2}$$

Here $k_p = 2\xi \cdot \omega_n \cdot L_{gsc} - R_{gsc}$, $k_i = \omega_n^2 \cdot L_{gsc}$

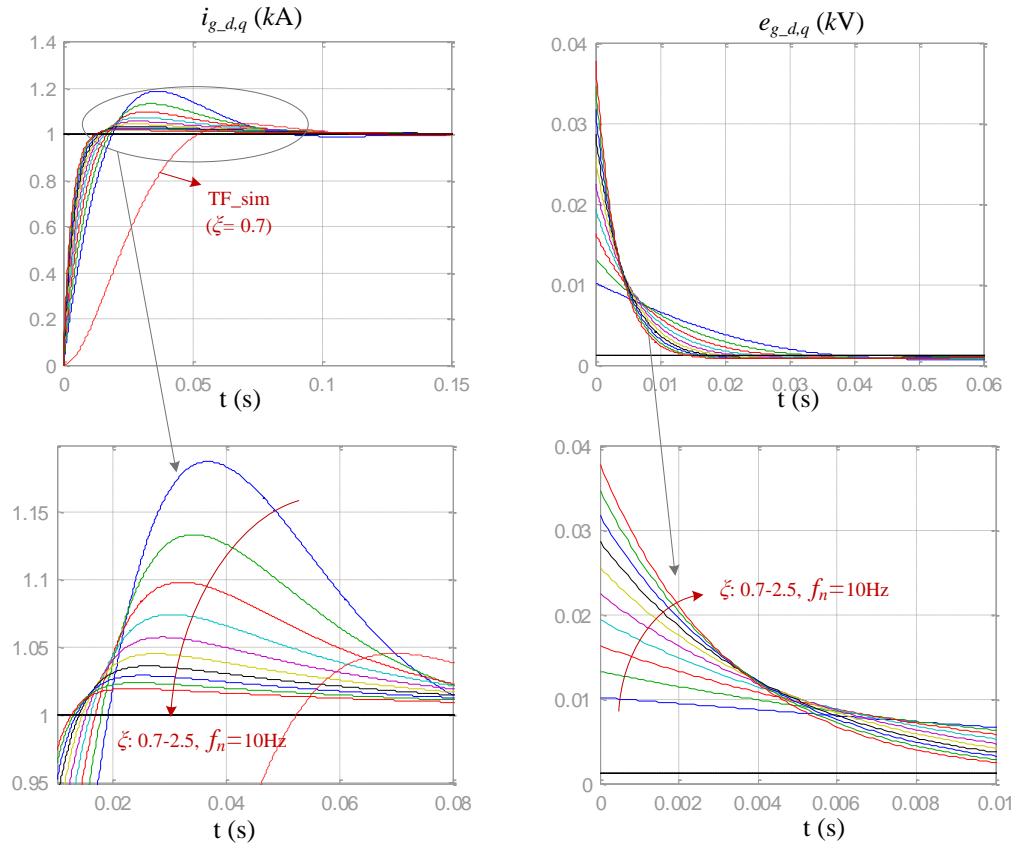


Figure B.5 Step responses of i_g and e_g to a 1 kA step in $i_{g_d,q}^*$ with different damping values

	$\omega_n = 10\text{Hz}$									
ξ	0.7	0.9	1.1	1.3	1.5	1.7	1.9	2.1	2.3	2.5
k_p	0.01015	0.0132	0.0163	0.0194	0.0224	0.0255	0.0286	0.0317	0.0347	0.0378
k_i	0.4825									
	$\xi = 1.6$									
ω_n	10 Hz		50Hz		100Hz		200Hz		500Hz	
k_p	0.0301		0.152		0.306		0.613		1.535	
k_i	0.482		12.1		48.3		193.0		1206	

Table B.3. GSC current controller parameters with varying damping and frequency

Substituting $\omega_n= 10\text{Hz}$ and $\xi=1.6$. the closed loop transfer function is derived as:

$$TF_{cl} = \frac{i_{r_dq}}{i_{r_dq}^*} = \frac{196.1s + 3948}{s^2 + 201.1s + 3948}$$

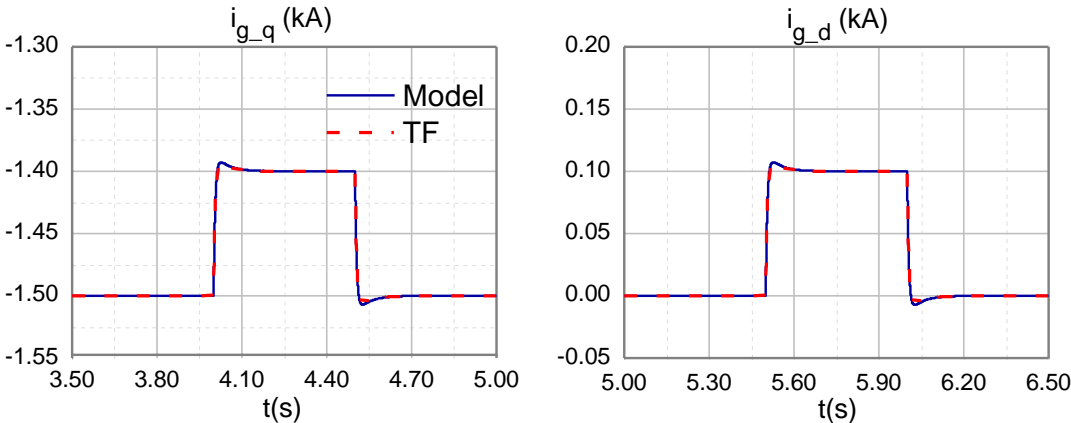


Figure B.6 Verification of the GSC inner-loop model with 1.4 kA step in $i_{g_q}^*$ and 0.1 kA step in $i_{g_d}^*$

Appendix C. Pitch Controller Tuning and Simulation Results

C.1. Proportional-only controller tuning

The compensator function including the controller and actuator is

$$Con \cdot Act(s) = \frac{k_p}{\tau_i s + 1}$$

Let $k_p = 100$, τ_i increases from 0s to 0.8s at 0.1s step

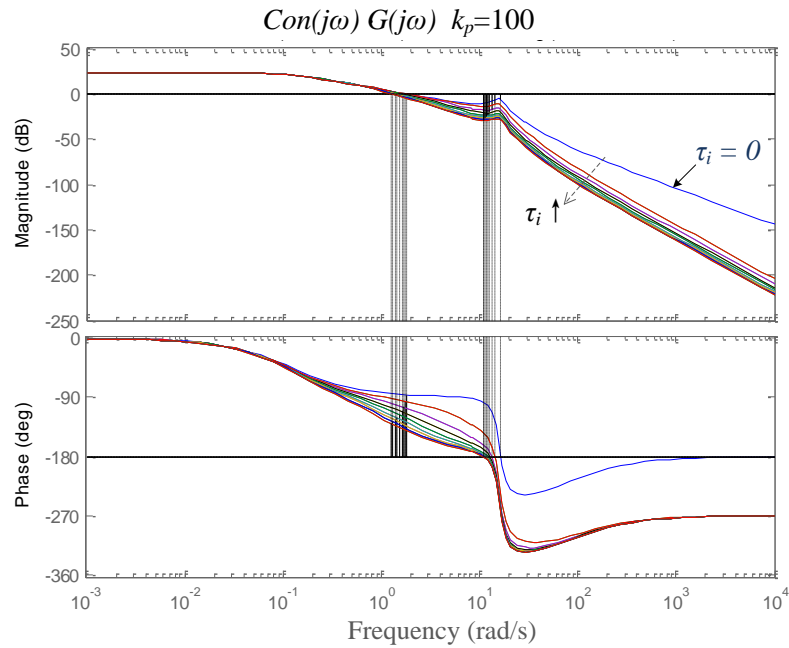


Figure C.1 Frequency responses with varying actuator time constants ($k_p=100$)

τ_i (s)	0	0.1	0.2	0.3	0.4	0.5	0.6	0.7	0.8
GM (dB)	8.03	13.3	19.1	22.7	25.2	27.2	28.7	29.9	31
PM (degrees)	94.6	86.3	78.8	72.6	67.5	63.3	59.9	57	54.6
ω_c (rad/s)	1.49	1.48	1.43	1.38	1.32	1.26	1.20	1.15	1.11

Table C.1. Stability margins with different actuator time constants ($k_p=100$)

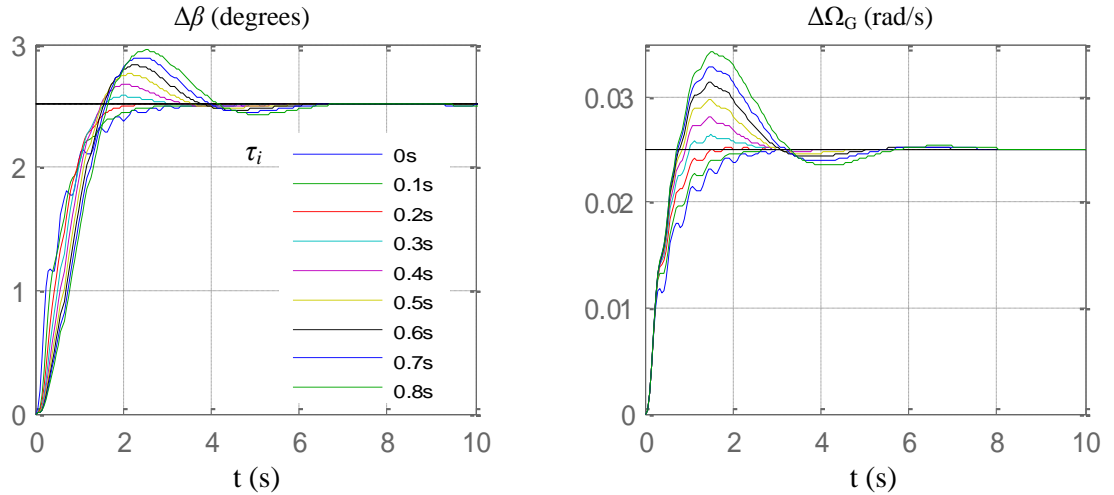


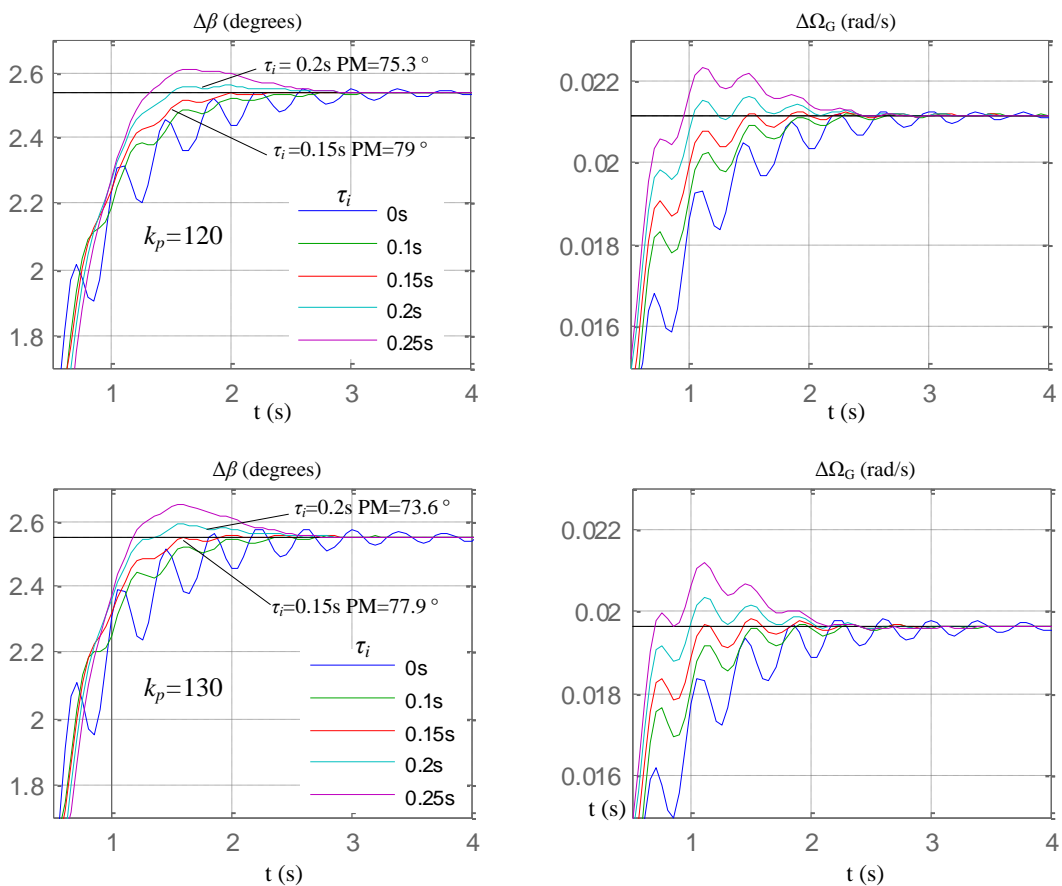
Figure C.2 Step responses to a 1 m/s step in wind speed with different actuator time constants ($k_p=100$)

From the above results, for the actuator's time constant larger than 0.3s, the cut-off frequency is smaller than 1.4rad/s, causing a decrease in the PM of more than 20° . Therefore, in the following tests, larger gain values are used with τ_i narrowed down to 0.1s – 0.25s.

τ_i (s)	0	0.1	0.15	0.2	0.25
GM (dB)	6.44	11.7	15	17.5	19.5
PM (degrees)	93.8	83.83	79	75.3	71.6
ω_c (rad/s)	1.80	1.77	1.74	1.70	1.66
Poles of the characteristic function	-0.8946 $\pm 16.0955i$	-1.4563 $\pm 15.4941i$	-1.6131 $\pm 15.5769i$	-1.6804 $\pm 15.6466i$	-1.7133 $\pm 15.6960i$
	-1.8782	-8.3376 -2.4171	-3.5539 \pm 0.7985i	-2.6533 \pm 1.6777i	-2.1203 \pm 1.8264i

Table C.2. System characteristics with different actuator time constants ($k_p=120$)

τ_i (s)	0	0.1	0.15	0.2	0.25
GM (dB)	5.7	11.0	14.3	16.8	18.8
PM (degrees)	93.5	82.7	77.9	73.6	69.9
ω_c (rad/s)	1.96	1.92	1.88	1.83	1.78
Poles of the characteristic function	$-0.8234 \pm 16.1165i$	$-1.4261 \pm 15.4581i$	$-1.5981 \pm 15.5471i$	$-1.6719 \pm 15.6229i$	$-1.7080 \pm 15.6767i$
	-2.0205	-2.6858 -8.1294	-3.5689 \pm 1.2741i	-2.6617 \pm 1.8899i	-2.1256 \pm 1.9862i

 Table C.3. System characteristics with different actuator time constants ($k_p=130$)

 Figure C.3 Step responses to a 1m/s step in wind speed with different actuator time constants ($k_p=120-130$)

As can be seen from Tables C.2 and C.3, including the actuator introduces another pole. As actuator time constant increases, the new pair of poles moves away from the real axis, and approaches the imaginary axis, indicating less damping. For $\tau_i > 0.15$ s, an overshoot occurs in the step response (As seen in Figure C.3). Therefore, the actuator time constant is set at $\tau_i = 0.15$ s. Increasing the controller gain further will reduce the error in the rotor

speed (Figure C.4). However, the PM will also be reduced, and large oscillations will be present at the initial transient in both the pitch angle and the rotor speed. It can be observed that the maximum gain without any overshoot is $k_p = 150$

k_p	130	150	170	190	210	220
GM (dB)	14.3	13.0	11.9	11.0	10.1	9.7
PM (degrees)	77.9	75.3	72.8	70.53	68.4	67.4
ω_c (rad/s)	1.88	2.15	2.42	2.69	2.95	3.08

Table C.4. Stability margins with different gain values ($\tau_i=0.15s$)

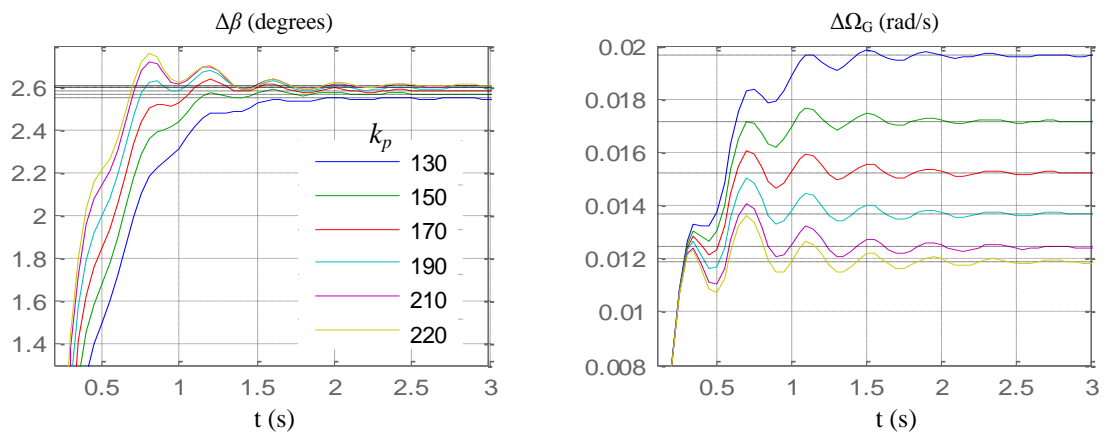


Figure C.4 Step responses to a 1m/s step in wind speed with different gains ($\tau_i=0.15s$)

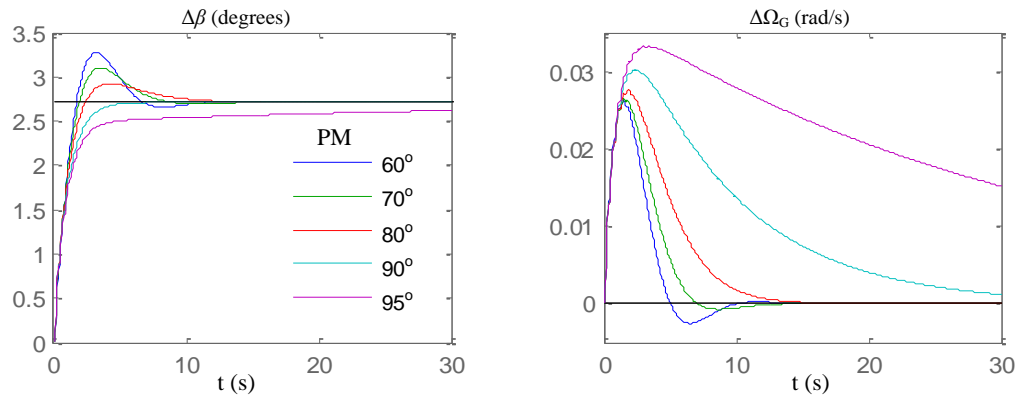
C.2. Proportional-integral controller tuning

Firstly, the PI controller is used without the actuator:

$$Con(s) = \frac{k_p s + k_i}{s}$$

The cross-over frequency is fixed at $\omega_c = 1\text{rad/s}$. Here ω_{01} is the cut-off frequency of the PI controller.

PM (degrees)	60	70	80	90	95
GM (dB)	13.18	12.30	11.73	11.46	11.40
k_i	40.59	30.59	19.65	8.12	2.24
ω_{01} (rad/s)	0.71	0.51	0.30	0.12	0.03

 Table C.5. System specifications with different PMs ($\omega_c=1\text{rad/s}$)

 Figure C.5 Step responses to a 1m/s step in wind speed with different PMs ($\omega_c=1\text{rad/s}$)

For a P -only controller without the actuator, an overshoot occurs when the PM is smaller than 90° (see Table C.1 – C.3, at $\tau_i = 0\text{s}$). Therefore $\phi_m=90^\circ$ is adopted in the design of PI controller. A larger PM means a smaller k_i , hence a longer settling time (as seen in Table C.5 and Figure C.5.), whilst a smaller PM may deteriorate stability.

ω_c (rad/s)	0.5	1	1.5	2	2.5	3
GM (dB)	17.45	11.46	7.98	5.54	3.68	2.19
k_i	4.08	8.12	12.08	15.88	19.40	22.46
ω_{01} (rad/s)	0.12					

 Table C.6. System specifications with different cross-over frequencies (PM = 90°)

The PI controller allows the flexibility of choosing the cross-over frequency ω_c . From Table C.6 and Figure C.6, a larger cross-over frequency ω_c increases the integral gain k_i , and thus accelerates the response speed. However, it reduces the GM and leads to oscillations. Adding an actuator will help to improve this phenomenon, as will be presented in the next paragraphs. From Figure C.6, a cross-over frequency larger than 1.5rad/s shows no significant improvement in the response speed, but only increases the oscillation amplitude.

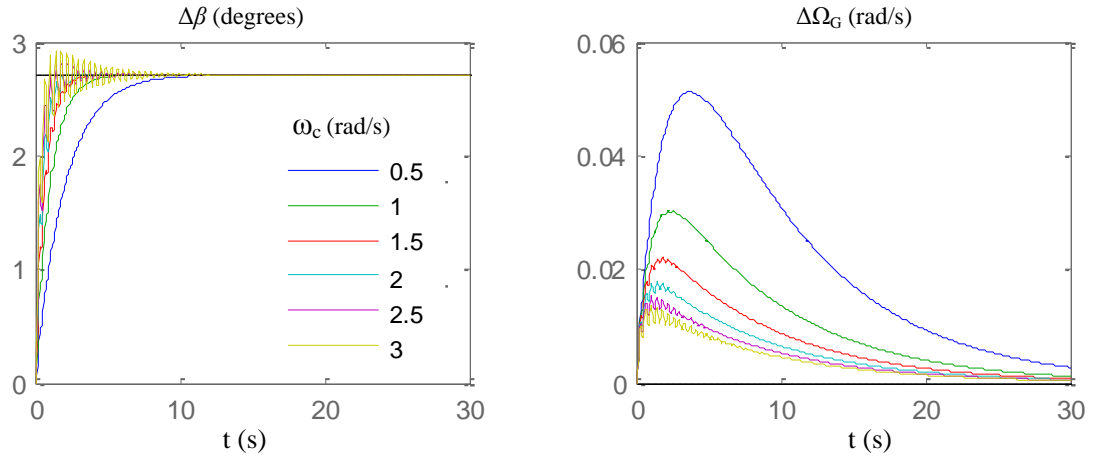


Figure C.6 Step responses to a 1m/s step in wind speed with different ω_c (PM = 90°)

Now by including the actuator, the compensator becomes

$$Con(s)Act(s) = \frac{k_p s + k_i}{s} \frac{1}{\tau_i s + 1}$$

Several cross-over frequencies from 1.5 rad/s to 3 rad/s are evaluated as listed in Table C.7, with different actuator time constants. A larger actuator time constant improves the system GM but reduces the PM. Taking the above factors into consideration, the controller parameters are determined as highlighted in red. The step responses with the corresponding controller settings are presented in Figure C.7.

Appendix C – Pitch Controller Tuning and Simulation Results

$\omega_c = 1.5 \text{ rad/s}$					
τ_i (s)	0	0.15	0.2	0.25	0.3
GM (dB)	8.0	16.6	19.1	21.1	22.7
PM (degrees)	90	77.6	73.9	70.6	67.5
ω_{c1} (rad/s)	1.50	1.46	1.44	1.41	1.38
$\omega_c = 2 \text{ rad/s}$					
τ_i (s)	0	0.15	0.2	0.25	0.3
GM (dB)	5.5	14.1	16.6	18.7	20.3
PM (degrees)	90	73.9	69.5	65.6	62.2
ω_{c1} (rad/s)	2.0	1.92	1.87	1.82	1.76
$\omega_c = 2.5 \text{ rad/s}$					
τ_i (s)	0	0.15	0.2	0.25	0.3
GM (dB)	3.7	12.3	14.8	16.8	18.4
PM (degrees)	90	70.6	65.5	61.4	57.8
ω_c (rad/s)	2.5	2.35	2.27	2.18	2.10
$\omega_c = 3 \text{ rad/s}$					
τ_i (s)	0	0.15	0.2	0.25	0.3
GM (dB)	2.2	10.8	13.3	15.3	16.9
PM (degrees)	90	67.6	62.3	57.9	52.3
ω_{c1} (rad/s)	3	2.76	2.63	2.51	2.40

Table C.7. System characteristics with varying actuator time constant and ω_c

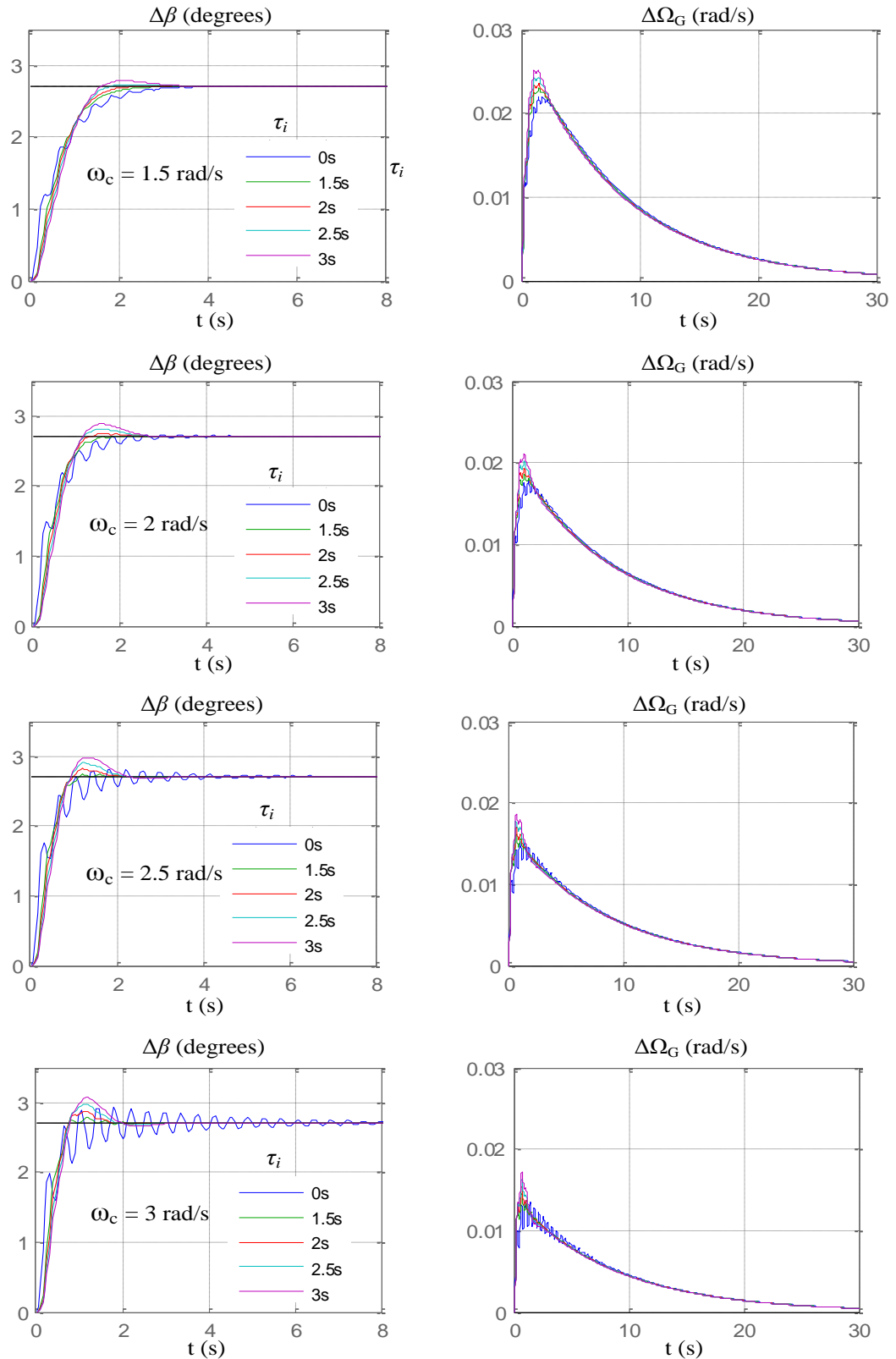


Figure C.7 Step responses to a 1m/s step in wind speed with different actuator time constants and cross-over frequencies

C.3. Sensitivity and gain scheduling

V_w	β	$dT/d\Omega_r$ (γ)	$dT/d\beta$ (ζ)	dT/dV_w (η)	k_p	k_i	k_d
(m/s)	(degrees)	Nm/rad s	Nm/degrees	N s	-	-	-
13	0.727	-0.308	-0.0401	0.1088	132.6	16	0.033
14	5.35	-0.2403	-0.0146	0.0949	364.8	34.67	0.033
15	10.88	-0.3947	-0.0215	0.1016	247.1	37.6	0.033
16	15.03	-0.5344	-0.029	0.1063	183.5	37.42	0.033
17	18.33	-0.6693	-0.037	0.11	143.7	36.47	0.033
18	21.04	-0.8034	-0.0458	0.1133	116.3	35.29	0.033
19	23.32	-0.9391	-0.0553	0.1164	96.26	34.07	0.033
20	25.28	-1.0779	-0.0657	0.1193	78.73	32.47	0.033
21	26.97	-1.2198	-0.0769	0.1222	69.22	31.7	0.033
22	28.47	-1.3663	-0.0891	0.125	59.72	30.6	0.033
23	29.79	-1.5168	-0.1023	0.1279	52.03	29.56	0.033
24	30.98	-1.6721	-0.1165	0.1307	45.67	28.58	0.033
25	32.04	-1.8317	-0.1318	0.1336	40.39	27.67	0.033

Table C.8. Variation of turbine sensitivities with operating points and the corresponding controller gain settings